The effects of neo-adjuvant chemotherapy on myeloid cells in high-grade serous ovarian cancer metastases

Owen Mortimer Heath

Thesis submitted in partial fulfilment of the requirements of the degree of

Doctor of Philosophy (PhD)

at Barts and the London School of Medicine and Dentistry,
Queen Mary University of London

Barts Cancer Institute
Queen Mary University of London
Charterhouse Square
London
EC1M 6BQ
United Kingdom

2019

Statement of originality

I, Owen Mortimer Heath, confirm that the research included within this thesis is my own work or that where it has been carried out in collaboration with, or supported by others, that this is duly acknowledged below and my contribution indicated. Previously published material is also acknowledged below.

I attest that I have exercised reasonable care to ensure that the work is original, and does not to the best of my knowledge break any UK law, infringe any third party's copyright or other Intellectual Property Right, or contain any confidential material.
I accept that the College has the right to use plagiarism detection software to check the electronic version of the thesis.

I confirm that this thesis has not been previously submitted for the award of a degree by this or any other university.

Signature:

Date:

Details of Collaborations and Publications

- Academic contribution, clinical mentorship and supervision provided throughout this project by Mr. Desmond Barton, St. George's Hospital NHS Trust, UK.
- Patients were consented and samples collected by Mr. Desmond Barton assisted by Ms. Samar Elorbany, St. George's Hospital NHS Trust, UK.
- Patients were consented and samples collected by Barts Gynae Tissue Bank directed by Dr. Michelle Lockley, Barts Cancer Institute, Queen Mary University of London, UK.
- Bioinformatic analysis of the RNA-sequencing data were performed by Dr. Eleni Maniati, Barts Cancer Institute, Queen Mary University of London, London, UK.
- Assessment and analysis of histopathology was supervised by Dr. Jacqueline McDermott, UCL Cancer Institute, London, UK.
- All mouse experiments were run with the support of Mr. Colin Pegrum and the Biological Services Unit team, Barts Cancer Institute, Queen Mary University of London, UK.
- A final mouse survival experiment was managed by Dr. Chiara Berlato, Barts Cancer Institute, Queen Mary University of London, London, UK.
- Macrophage culture and staining protocols were shared by Caterina Trevisan, University of Padova, Italy and Dr Laura Lecker, Barts Cancer Institute, Queen Mary University of London, UK.
- Protocols and reagents for the proximity ligation assay were kindly provided by Dr. Alessandro Annibaldi, Barts Cancer Institute, Queen Mary University of London, UK.
- Flow cytometry gating strategies and antibodies were kindly provided by Prof. Joachim Schultze, Limes Institute, University of Bonn, Germany.
- Flow cytometry and flow sorting was support by the staff on the Flow Laboratory led by Dr. Becki Pike, Queen Mary University of London, UK.

Conference poster presentation at the AACR Annual Meeting 2019, Atlanta, USA (Poster 1103).

This work was supported by a Wellcome Trust Clinical Research Fellowship Training Award (201118/Z/16/Z) and a CRUK Clinical Bursary Award (C56096/A21222).

Abstract

Many tumours have abundant macrophage populations. Tumour-associated macrophages (TAMs) frequently have tumour promoting roles and high tumour infiltrates are associated with poor clinical outcome. TAMs are highly plastic cells and their activation state is shaped by the integration of multiple stimuli in the context of specific tissue environments. Following chemotherapy TAMs can antagonise or promote therapeutic response; these opposite effects are largely determined by TAM activation state.

To understand the impact of chemotherapy on TAMs in high-grade serous ovarian cancer (HGSOC) I assessed TAM populations in human biopsy samples pre and post-chemotherapy as well as in murine HGSOC models harbouring a relevant mutational profile.

I find chemotherapy results in a reorganisation of TAMs within the omental tumour microenvironment (TME) of human and murine HGSOC. TAMs expressing markers known to associate with disease progression decrease following chemotherapy. Additionally, TAMs upregulate inflammasome pathways and TLR signalling following chemotherapy. I show macrophages are killed by carboplatin *in vitro* and non-viable TAM increase in human and murine HGSOC following chemotherapy. Interestingly, macrophages cleave caspase-3 and gasdermin E following carboplatin treatment, this implicates chemotherapy in driving inflammatory cell death (pyroptosis) in TAMs. Using a novel murine model of HGSOC relapse after first-line chemotherapy, I demonstrate CSF-1Ri-mediated TAM depletion post-chemotherapy in mice worsened survival to relapse. Furthermore, in patient samples high TAM density post-chemotherapy associated with improved survival.

Overall these results suggest chemotherapy promotes an anti-tumour TAM phenotype. TAM pyroptosis may be an important mechanism in chemotherapy-mediated enhancement of innate immunity. These results provide a rationale for treatments that re-program TAMs after chemotherapy in women with HGSOC.

Acknowledgements

First of all, I would like to thank Professor Fran Balkwill for inspiring me with her passion and enthusiasm for science and her knowledge and determination to develop new treatments for patients with ovarian cancer. It has been a privilege to be part of your lab. Thank you for all you have taught me over the last three and a half years and for your unyielding support.

I am indebted Mr. Desmond Barton for providing the catalyst to undertake this period of research training. I thank you for your unfaltering support over the duration of the PhD, both practically and academically and for providing a surgical training, which I am sure will define the rest of my career.

To everyone in the lab a huge thank you for all your help with my experiments, to listening to my ideas and providing revelry and solace in equal measure through the many highs and lows of life in the lab. Your friendship, humour and kindness which have made every day in the lab enjoyable: Dr. Ganga Gopinathan, Dr. Chiara Berlato, Dr. Eleni Maniati, Dr. Jacqueline McDermott, Ms. Anissa Lakhani, Mr. Colin Pegrum, Dr. Laura Lecker, Dr. Agata Krygowska, Dr. Juliana Candido, Dr. Robin Delane-smith, Dr. Oliver Pearce and Dr. Anne Montfort, Dr. Bea Malacrida, Dr. Florian Laforêts, Dr. Michael-John Devlin, Ms. Samar Elorbany and Dr. Bella Kotantaki. In particular I would like to thank Dr. Ganga Gopinathan for all her help initially with the mice. Mr. Colin Pegrum and Ms. Anissa Lakhani for all your help with running the mouse experiments, Dr. Chiara Berlato and Dr. Anne Montfort for teaching me flow cytometry and Dr. Eleni Maniati for her ‘wizardry’ with the bioinformatic analyses.

I thank Alice for your inexhaustible patience, kindness and humour throughout this time, including submitting a funding application while you were in labour with Iris, which is how this all started! Iris and Arthur for your limitless stimulation.

Finally, I thank all the patients being treated for ovarian cancer who have provided samples to support this research, without which this work would not have been possible.

•

For Alice, Iris and Arthur

Table of Contents

Table of Figures

List of Tables

Abbreviations

% v/v	Percent volume/volume
% w/v	Percent weight/volume
°C	Degrees Celsius
A700	Alexa Fluor® 700
APC	Allophycocyanin
AKT	Protein kinase B
ANOVA	Analysis of variance
APC	Antigen presenting cells
a.u.	Arbitrary unit
AUC	Area under curve
B cells	Bone-marrow derived lymphocytes
BCA	Bicinchoninic acid
BCR	B cell receptor
BRCA	Breast cancer susceptibility gene
BSA	Bovine serum albumin
BV	Brilliant Violet™
C	Cytosine
CAR	Chimeric antigen receptor
CCNE1	Cyclin E1
CCR2	C-C chemokine receptor 2
CD	Cluster of differentiation
CIC	Cortical inclusion cyst
CSF-1	Colony stimulating factor-1
CSF-1R	Macrophage colony-stimulating factor 1 receptor
CTLA-4	Cytotoxic T-lymphocyte antigen-4
Cy	Cyanine
CyTOF	Time of flight cytometry
DMEM	Dulbecco's modified eagle medium
DMSO	Dimethyl Sulfoxide
ECL	Enhanced chemiluminescence
ECM	Extracellular matrix
ECOG	Eastern cooperative oncology group
EDTA	Ethylenediaminetetraacetic acid
EGF	Epidermal growth factor
EGFR	Epidermal growth factor receptor
ELISA	Enzyme-linked immunosorbent assay
EMT	Epithelial-to-mesenchymal transition
EOC	Epithelial ovarian cancer
ERK	Extracellular signal-regulated kinase
FACS	Fluorescence-activated cell sorting
FBS	Fetal bovine serum
FC	Flow cytometry
FFPE	Formalin fixed, paraffin-embedded
FITC	Fluorescein isothiocyanate
FoxP3	Forkhead box P3
FSC-A	Forward scatter area

FSC-H	Forward scatter height
FTE	Fallopian tube epithelium
FVD	Fixable viability dye
H&E	Haematoxylin and eosin
HDR	Homologous DNA repair
HGF	Hepatocyte growth factor
HGSOC	High-grade serous ovarian cancer
HRP	Horseradish peroxidase
IDS	Interval debulking surgery
IF	Immunofluorescence
IFN	Interferon
IGF	Insulin-like growth factor
IHC	Immunohistochemistry
IL	Interleukin
ip / IP	Intraperitoneal
IV	Intravenous
iNOS	Inducible nitric oxide synthase
kDa	Kilo Dalton
LPS	Lipopolysaccharide
M	Molar
MCSF	Macrophage colony stimulating factor
MDM	Monocyte-derived macrophages
MFI	Mean fluorescent intensity
MHC	Histocompatibility complex
MMP	Matrix metalloproteinases
mRNA	Messenger RNA
NaCl	Sodium chloride
NACT	Neo-adjuvant chemotherapy
NF1	Neurofibromatosis type 1
NF-κB	Nuclear factor kappa-light-chain-enhancer of activated B cells
NK cells	Natural killer cells
NSAID	Non-steroidal anti-inflammatory drug
OD	Optical density
OSE	Ovarian surface epithelium
p	Phosphorylated
PARP	Poly (adenosine diphosphate [ADP]-ribose) polymerase
Pax8	Paired homeobox protein 8
PBMC	Peripheral blood mononucleated cell
PBS	Dulbecco's phosphate buffered saline
PC	Principal component
PCA	Principal component analysis
PD1	Programmed cell death protein 1
PD-L1	Programmed cell death protein ligand 1
PDS	Primary debulking surgery
PE	Phycoerythrin
Pen/strep	Penicillin/streptomycin
PerCP	Peridinin Chlorophyll Protein Complex
PFA	Paraformaldehyde

PLA	Proximity ligation assay
RB1	Retinoblastoma protein
rh	Recombinant human
RIPA	Complete radioimmunoprecipitation assay
RPMI	Roswell Park Memorial Institute
SD	Standard deviation
SCS	Secondary cytoreductive surgery
SEM	Standard error of mean
SSC-A	Side scatter area
SSC-W	Side scatter width
STAT	Signal transducer and activator of transcription
STIC	Serous tubal intraepithelial lesions
STR	Short tandem repeated
SVF	Stromal vascular fraction
T cells	Thymus-derived lymphocytes
TAMs	Tumour-associated macrophages
TBS	Tris-buffered saline
TCR	T cell receptor
TGFβ	TGF beta
TIL	Tumour infiltrating lymphocyte
TLR	Toll-like receptors
TMA	Tissue microarray
TME	Tumour microenvironment
TNF	Tumour necrosis factor
Treg	Regulatory T cell
VEGF	Vascular endothelial growth factor
VEGFR	Vascular endothelial growth factor receptor
WNT	Wingless
WT1	Wilms tumour 1

Chapter 1
Introduction

The aim of this thesis is to understand the effects of chemotherapy on tumour associated macrophages (TAMs) in high-grade serous ovarian cancer (HGSOC) metastases.

1.1 Epithelial ovarian cancer

1.1.1 Epidemiology of ovarian cancer

In 2012 there were 238,700 new diagnoses of ovarian cancer and 151,900 deaths worldwide from this disease[1]. In the United Kingdom it is estimated that there are 7,000 newly diagnosed cases and 4,200 deaths per year[2]. Ovarian cancer is more common in Western countries were it represents the most lethal gynaecological malignancy and the fifth most common cancer in women[1]. The most recent figure for overall five year survival in the England was 42.9%[3]. This dismal figure is largely due to presentation at an advanced stage; over two thirds of patients present with disease disseminated within or beyond the abdominal cavity (FIGO stage III/VI). Survival is directly linked to stage at diagnosis: in early stage disease confined to the ovaries (FIGO stage I) the 5 year survival is 90%, compared to 4% for stage VI[4].

The most commonly reported symptoms of ovarian cancer include pelvic pain, weight gain, abdominal bloating and a change in bowel habit. The non-specific nature of these symptoms frequently results in a delay in diagnosis and highlights the importance of early investigation of such symptoms, particularly in post-menopausal women, to exclude gynaecological pathology[5].

1.1.2 Classification of epithelial ovarian cancer

Historically, epithelial ovarian cancers (EOCs) were defined solely by morphological features and categorised into four main subtypes; serous, endometrioid, mucinous and clear cell cancers. Due the preponderance of HGSOC, EOC was generally regarded as a single disease with differences between other histological subtypes obscured[6]. Furthermore, as EOC generally presents clinically with a large pelvic mass involving the ovaries this was taken as evidence to suggest a common ovarian origin[6].

Molecular biology has revolutionised our understanding of EOC and has brought about a shift in classifying ovarian cancers based solely on histological features to an approach encompassing molecular and genetic differences. Significant progress has been made in identifying the genes that are commonly mutated in ovarian cancers; these include *KRAS*, *PIK3CA*, *TP53*, *BRCA1* and *BRCA2*[2]. It is now understood that these lesions are distributed unequally between the various histological subtypes of ovarian cancer. Microarray analyses have shown that EOC is a constellation of distinct diseases that are

frequently more similar to cancers arising in other organs than they are to one another[7]. For example, clear cell carcinoma of the ovary is more similar to renal cell carcinoma than to serous ovarian cancer[8]. When the common ovarian histological subtypes are compared, only high-grade serous and high-grade endometrioid tumours appear similar, and indeed these are indistinguishable by gene expression profiling, suggesting that high-grade endometrioid tumours may not be a separate entity[9,10].

1.1.3 Origin and pathogenesis of HGSOC

In the absence of a precursor lesion seen within the ovary, previously held theories of the pathogenesis of HGSOC assumed the ovarian surface epithelium (OSE) was the site of origin of this disease. The OSE is composed of a single layer of epithelial cells and originates from the mesoderlike. It was considered that either 'incessant ovulation' causing continuous disruption to the OSE, or the invagination of the OSE within ovarian stroma, resulting in cortical inclusion cysts (CICs), initiated malignant transformation[12].

Recent histopathological observations have challenged this view, strongly suggesting that in many cases the cells of the distal fallopian tube epithelium (FTE) are the progenitors of this disease[13,14]. The FTE is a columnar epithelium composed of ciliated and secretory cells[11]. The secretory cells produce tubular fluid and the ciliated cells mediate oocyte transport towards the uterus[15]. Callahan *et al.* were the first to demonstrate the presence of serous tubal intraepithelial neoplasia (STIC) lesions as well as occult serous tumours arising in the fallopian tube in patients with germline BRCA mutations undergoing risk reducing surgery[16]. Leading on from this discovery, STIC lesions were identified in 50-60% of patients with HGSOC in non-BRCA patients[17]. Finding identical p53 mutations within STIC lesions and the concomitant HGSOC, strongly supports the FTE as an initiating site of this disease[13]. Furthermore, gene expression studies comparing HGSOC to OSE and FTE brushings from healthy tissues found that the expression profile of the FTE but not the OSE significantly correlated with that of HGSOC[18]. Foci of cells harbouring p53 mutations, termed 'p53 signatures', have been demonstrated in histologically normal fallopian tubes and currently represent the earliest detectable event associated with HGSOC precursor lesions[7]. Overall these data suggest that the distal fallopian tube is the initiating site for many HGSOCs and that p53 mutation is the earliest event in the pathogenesis of this disease. Ectopic implantation of FTE (known as endosalpingiosis) or CIC formation followed by tubal-type differentiation are proposed as mechanisms to explain 'non-tubal' HGSOC, where there is no evidence of fallopian tube involvement[19].

1.1.4 Mutational landscape of HGSOC

Key genetic drivers of HGSOC progression have been identified. The high rate of *TP53* mutation in HGSOC suggests that this is an essential event in the pathogenesis of this disease[7]. BRCA mutations are also important in the pathogenesis of HGSOC. In the Cancer Genome Atlas Network HGSOC study 96% of the cases had a *TP53* mutation and *BRCA1* and *BRCA2* were either mutated in the germline in 9% and 8% of cases respectively, somatic mutations accounted for 3% of cases[20].

BRCA genes regulate the homologous DNA repair (HDR) pathway, which is required to repair DNA double-strand breaks[21]. The presence of *BRAC1* or *BRAC2* germline mutation results in a 30% to 70% lifetime risk respectively of developing HGSOC by the age 70[7]. Somatic mutations and inactivation of other components of the HDR pathway such as *BRIP1*, *BARD1*, *RAD51B* and *RAD51C,* are also found in HGSOC biopsies[22–25]. The "BRCAness" phenotype is used to describe mutations affecting HDR[26]. The frequent deficiency in HDR pathway renders HGSOC susceptible to platinum-based chemotherapy, which induces DNA damage[27]. The treatment effect can be enhanced when combined with poly (adenosine diphosphate[ADP]-ribose) polymerase (PARP) inhibitors, which additionally inactivate the DNA repair capability of cancer cells[28].

Among HDR proficient HGSOCs, approximately 30% of patients have an amplification of *Cyclin E1* (*CCNE1*), which regulates G1-S-phase transition during cell cycle progression[29]. Loss of neurofibromatosis type 1 (*NF1*), a negative regulator of the oncogene *RAS*[30], occurs in 17%, loss of retinoblastoma protein (*RB1*), an inhibitor of cellular proliferation, in 15% and loss of *PTEN* in 6% of HGSOC patients[29]. PTEN is a phosphatase that inhibits cell proliferation through the PI3K pathway[31]. Additionally, loss of *PTEN* defines a subgroup of ovarian cancers with significantly worse prognosis[31].

A cardinal feature of HGSOC is genomic structural variations with amplifications and deletions of DNA. This chromosome instability results in inactivation of tumour suppressor genes, via deletions or through gene breakage. A proposed model for the molecular pathogenesis of HGSOC is the loss of p53 and BRCA function leading to defects in homologous recombination pathways resulting in chromosomal and widespread copy number variation[7]. These initial events drive tumour development and promote further genetic lesions in the evolving tumour (Figure 1.1).

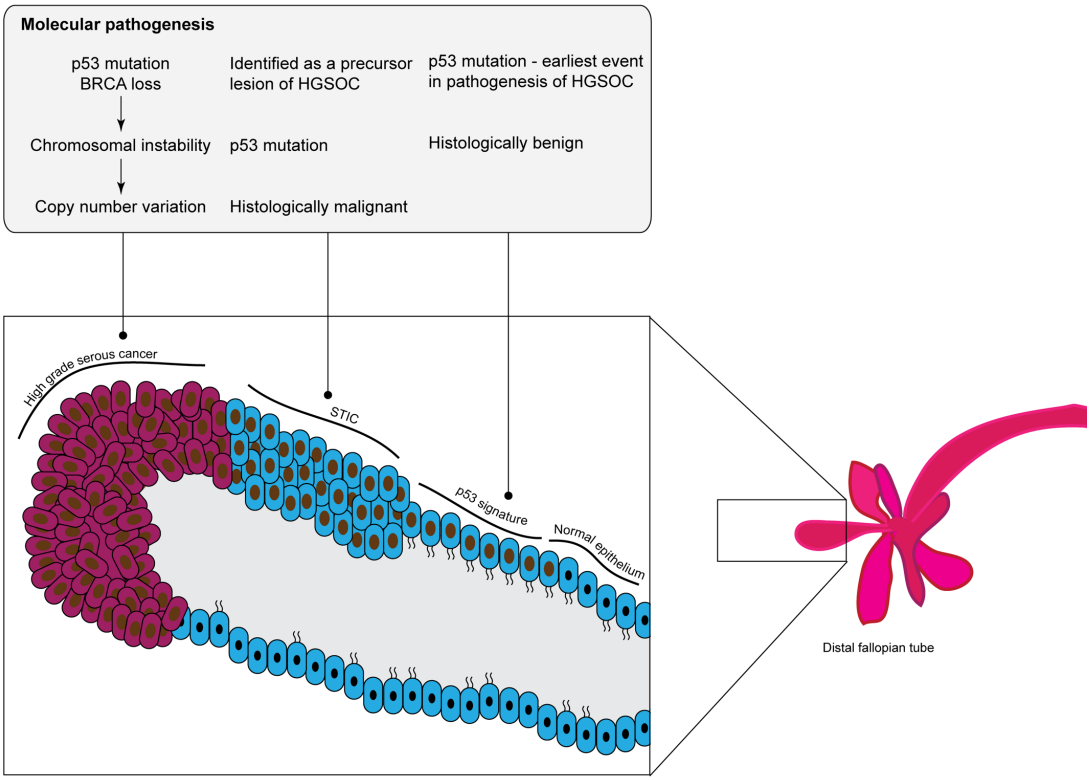

Figure 1.1 Diagrammatic representation of the cellular and molecular pathogenesis of HGSOC.

1.1.5 Molecular subtypes of HGSOC

Tothill *at al.* defined four molecular subtypes of HGSOC based on gene expression: C1 (mesenchymal), C2 (immunoreactive), C4 (differentiated) and C5 (proliferative)[9]. These subtypes associated with differences in clinical outcome. The mesenchymal subtype (C1) is characterised by an enhanced stromal gene signature. C1 tumours show extensive infiltration of activated fibroblasts, an epithelial-to-mesenchymal transition (EMT) gene signature and are associated with the worst survival amongst all of the subtypes[9,32]. The immunoreactive subtype (C2) is characterised by an extensive infiltration of intratumoural T cells, this was associated with enhanced overall survival[9]. C4 (differentiated) tumours have a low stromal response and share characteristics with serous borderline tumours, which have an intermediate prognosis[9,32]. Finally, the C5 (proliferative) subtype shows low expression of differentiation markers and low immune cell counts[9,32]. Tumours of this subtype display upregulation of extracellular matrix (ECM)-related genes, developmental transcription factors, oncogenic stem cell-associated genes associated with cell mobility[9,32]. The C5 subtype was associated with worse survival similar to the C1 subtype[9,32]. The four subtypes highlight the importance of the tumour microenvironment in the pathogenesis of HGSOC. These data demonstrate that transcriptional signatures of the immune infiltrate and stromal compartment of the tumour microenvironment can predict clinical outcome and

potentially dictate response to therapies[33,34].

1.2 Treatment of HGSOC

The majority of patients with ovarian cancer are treated with the combination of surgery and chemotherapy. Surgery provides the functions of diagnosis, staging, cytoreduction and palliation and includes total abdominal hysterectomy, bilateral salpingo-oophorectomy, omentectomy, inspection of peritoneal surfaces with biopsy or removal of any areas suspicious of disease and consideration of para-aortic and pelvic lymph node dissection. Surgery should be performed by a trained gynaecological oncology surgeon with the goal of no residual disease. Surgery undertaken in specialist centres by gynaecological oncologists increases the proportion of cases achieving 'optimal' cytoreduction, defined as <2cm of residual disease[35] and improved survival[36].

Primary debulking surgery (PDS) followed by adjuvant chemotherapy has been established as the standard of clinical care since the 1980s[37]. The aim of surgery is to achieve maximal disease clearance. Many studies have shown that the volume of residual disease following cytoreductive surgery predicts survival. The first of which was by Griffiths *et al.* in 1975 where cytoreduction to ≤1.5cm residual disease resulted in significantly improved survival[38]. The definition of what constitutes 'ideal' cytoreduction has evolved over time and is now taken to mean no macroscopically identifiable disease (R0). Aletti *et al.* showed that survival is significantly improved in patients with R0 disease resection compared to patients with any identifiable residual disease[39]. In contemporary clinical practice R0 resection after PDS is still the most important prognostic factor for survival[40–46]. There has been debate regarding the value of routine systematic pelvic and para-aortic lymphadenectomy in patients without obvious nodal involvement achieving R0 resection. Recently the LION trail showed that lymphadenectomy under these circumstances was not associated with improved survival and was associated with increased morbidity[47].

Neoadjuvant chemotherapy (NACT) followed by interval debulking surgery (IDS) was developed as an alternative treatment option in patients where it was deemed to be difficult to achieve complete tumour resection at PDS[48]. Two large randomized controlled trials have demonstrated non-inferiority of NACT-IDS to PDS in terms of patient survival[45,49]. Furthermore, lower operative morbidity has been reported in patients undergoing NACT-IDS compared to PDS[49]. However, both trials have attracted considerable criticism centred on the low R0 attainment rates and low survival in both trials[37]. To address these concerns the TRUST trial is currently recruiting which will randomise patients to either NACT-IDS or PDS from centres reporting greater then 50%

R0 resection rates. Patient selection to NACT-IDS *vs* PDS still remains an area of controversy. The EORTC 55971 trial showed a better overall survival in patients undergoing PDS with small volume stage 3 disease (<5cm metastases) in comparison NACT-IDS improved overall survival in stage 4 disease[45]. Based on these data strategies to select patients for IDS or PDS have been suggested[50]. Further research is needed to clarify the best way to select patients for IDS/PDS. Within the UK these decisions are made in the context of dedicated multi-disciplinary teams, MDTs.

The intravenous administration of carboplatin (area under the curve [AUC] 5-6) and paclitaxel 175mg/m^2 over 3 hours every three weeks is considered standard first-line chemotherapy for EOC[37]. The current standard recommendation is to give a total of six cycles of chemotherapy[37]. A Japanese study showed enhanced PFS when paclitaxel was administered weekly at a dose of 80mg/m^2 [51]. However, this 'dose-dense' approach has not shown benefit in other studies predominately in Western patient populations, suggesting that pharmacogenomic influences may explain these differences.

A number of trials have shown benefit of intraperitoneal (IP) administration of chemotherapy where cytoreduction to <1cm residual disease was achieved after PDS[52–54]. However, these studies have been criticised due to differences in the overall chemotherapy dose patients received in the different arms of the study. Furthermore, GOG252 which randomised patients to IP chemotherapy and bevacizumab or intravenous (IV) chemotherapy and bevacizumab showed no benefit of IP over IV administration[55]. This has led to the suggestions that additional benefits of IP chemotherapy are due to higher overall doses of chemotherapy administered rather than the mode of delivery. However, further investigation is needed.

A further development in the treatment of HGSOC is hyperthermic intraperitoneal chemotherapy (HIPEC)[56,57]. In 2017 two trials reported the outcome of HIPEC after NACT-IDS. The van Dreil *et al.* study showed a significant survival benefit of HIPEC whereas the Lim *et al.* study did not show survival benefit[56,57]. Therefore, further research is needed to understand if there is benefit from this approach.

1.2.1 Mechanism of action of chemotherapy

1.2.1.1 Carboplatin

Carboplatin [cisdiammine(1,1-cyclobutane dicarboxylato)platinum(II)] is a second-generation platinum drug developed to reduce the dose limiting toxicities (neuro and ototoxicity) associated with cisplatin[58]. Carboplatin enters the cell by diffusion; however a variety of membrane transporter proteins can also affect cellular accumulation of the

drug. One such protein is the copper transporter-1 (CTR1), which can facilitate the transport of carboplatin into cells. CTR1$^{-/-}$ murine fibroblasts were less sensitive to carboplatin treatment than wildtype cells[59]. Other transporter molecules (ATP7A and ATP7B) may be involved in sequestering cisplatin or enhancing drug efflux from the cell thus preventing cytotoxicity[60]. Indeed, downregulation of CTR1 and upregulation of ATP7A and ATP7B are mechanisms of acquired chemotherapy resistance[58,61]. Once inside cells, carboplatin is hydrolysed; this results in reactive carboplatin species that are able to bind DNA permitting the formation of inter-strand cross-links between guanine bases. Carboplatin mediated inter-strand cross linking results in significant distortion of the DNA double helix[58]. This DNA lesion is the principle cytotoxic effect of carboplatin, inhibiting DNA synthesis and mitosis and inducing apoptosis[58,62].

1.2.1.2 Paclitaxel

Paclitaxel was originally extracted from the bark of the Western Yew, *Taxes brevifolia*[63]. Paclitaxel has a complex chemical structure and is extremely hydrophobic making it a difficult drug to formulate for human administration. The vehicle used in current medical practice is a mixture of ethanol and cremophor which is associated with sensitivity reactions, necessitating pre-medication with corticosteroids and antihistamines in some patients[64].

The most important cytotoxic effect of paclitaxel is the inhibition of tubulin depolymerisation, which results in stabilisation of the microtubular cytoskeleton[65]. These effects become manifest during mitosis and result in dysregulation of the cell cycle, mitotic failure and cell death. Cell death is mediated by a prolonged block in mitosis. Mitotic block is dependent on the formation of the spindle assembly checkpoint (SAC) a protein complex that forms to ensure correct attachment of chromosomes to the mitotic spindle before anaphase commences. Prolonged activation of the SAC triggers cell death[65]. It is suggested that altered microtubule dynamics caused by paclitaxel treatment result in tension defects that activate SAC[66]. The protein aroura B is important in this regard, as inhibiting aroura B abrogates paclitaxel mediated cell cycle arrest[67].

1.2.2 Targeted therapies

1.2.2.1 Anti-angiogenic

Anti-angiogenic therapy is now routinely used in the treatment of HGSOC in many countries. Bevacizumab, a humanised monoclonal antibody to VEGF-A, can prevent angiogenesis and therefore disrupt tumour growth[68]. The ICON 7[69] and GOG 218[70] trials showed an increase in progression free survival, but not overall survival, with the addition of bevacizumab maintenance therapy to standard first-line chemotherapy with

carboplatin and paclitaxel[69,70]. This resulted in approval for this drug as a maintenance therapy in Europe[68].

Other antiangiogenic therapies aim to inhibit the VEGF receptor. A large range of other anti-angiogenic drugs are being tested, the most promising of which is cediranib[68]. Cediranib is an orally active small molecule tyrosine kinase inhibitor of the VEGF receptor[68]. Cediranib increases PFS in combination with chemotherapy or as maintenance therapy[71]. Furthermore, this drug has antitumor activity as a single-agent in platinum sensitive and resistant recurrent disease[72,73].

1.2.2.2 PARP inhibitors

PARP inhibitors (PARPi) represent an important new therapeutic approach in HGSOC. Approximately half of all HGSOC tumours have defects in DNA repair mechanisms, in particular the homologous recombination pathway which is essential for the repair of double stranded DNA breaks. *BRCA1* or *BRCA2* mutations are most frequently implicated in this process however, mutations in other HDR pathways or functional inactivation via methylation may also be responsible[37]. Homologous-recombination deficiency (HRD) results in an over-reliance of tumour cells on other DNA repair pathways, including base-excision repair which is dependent on the PARP proteins. Inhibition of PARP results in tumour cell death as the result of synthetic lethality[68].

Olaparib was the first PARPi used in HGSOC patients[74]. Phase I and II clinical trials have shown impressive clinical responses in patients with BRCA mutated and BRCA wild-type recurrent HGSOC[68]. In the context of platinum-sensitive HGSOC recurrence, objective response rates of 60% were seen in BRCA mutated tumours compared to 50% in BRCA wild-type tumours[75]. A phase 2 clinical trial assessing olaparib as maintenance therapy in patients with platinum-sensitive, relapsed disease showed an increase in progression free survival but with no changes in overall survival[27]. In patients with *BRCA1* and *BRCA2* mutations, median PFS was significantly extended in the olaparib group compared to the placebo group (11.2 *vs* 4.3 months). For *BRCA* wild-type patients the differences in survival were less pronounced, however there was still significantly improved PFS in olaparib compared to placebo treated patients (7.4 *vs* 5.5 months respectively)[76]. The SOLO2 trail confirmed the benefit of olaparib maintenance therapy in platinum-sensitive relapsed HGSOC[77]. These studies resulted in olaparib being approved for use as a maintenance therapy in platinum-sensitive recurrent disease with *BRCA1* or *BRCA2* mutations. Two other PARP inhibitors, rucaparib and niraparib, have also been granted regulatory approval for patients with relapsed ovarian cancer, irrespective of BRCA-mutation status or platinum-sensitivity[68]. The phase III NOVA study showed benefit of niraparib in women with a complete or partial response to platinum-

based chemotherapy. In this study BRCA patients treated with niraparib had significantly increased PFS (21 vs 5.5 months) compared to (9.3 vs 3.9 months) in the non-BRCA wild type patients[78]. Similar benefits of rucaparib maintenance therapy in platinum-sensitive recurrences were shown in the ARIEL3 study[79].

PARPi have been recently shown to have benefit as a front-line treatment of HGSOC. In December 2018 the FDA granted approval for olaprarib to be used as maintenance therapy in BRCA mutated platinum sensitive HGSOC[37]. This was on the basis of a phase III study, SOLO1, which showed a 70% lower risk of disease progression or death in patients treated with olaparib compared to placebo[80].

1.2.2.3 Immunotherapies

To date there are no approved immune therapies for ovarian cancer[81]. Immunotherapeutic approaches, most notably inhibiting immune check point pathways, have resulted in dramatic and durable responses in a range of tumour types (melanoma, NSCLC and renal cancers)[82]. Compared to these cancer types, the response of ovarian cancer to checkpoint blockade has been modest[81]. The best response reported by Hamanishi *et al.* was 15% in a study of 20 heavily pre-treated platinum-resistant ovarian cancer patients[83]. In this study there was one complete response and two partial responses with an overall disease control rate was 45%[83]. Treatment of 124 patients with the anti-PD1 avelumab resulted in 12 partial responses (ORR, 9.7%) with 55 patients showing stable disease[84]. The KEYNOTE-028 phase 1b trial treated 26 recurrent EOC patients with pembrolizumab with one complete response and two partial responses and six patients with stable disease[85]. Despite overall modest responses in combined studies of EOC, data relating to clear cell ovarian cancers show more encouraging responses[37]. A portfolio of clinical trials assessing the value of checkpoint blockade in ovarian cancer alongside standard chemotherapies (Javelin Ovarian 100), as maintenance therapy in the context of platinum sensitive (ATALANTE), and platinum resistant relapse (Javelin Ovarian 200) and in combination with bevacizumab (NRG-GY009) are currently recruiting[81,82].

Other immunotherapeutic approaches include the use of adoptive T cell transfer. In this approach tumour reactive T cell subsets are expanded *ex vivo* and re-infused into patients. Furthermore, T cells can be genetically modified to express a 'chimeric antigen receptor' which encodes a tumour antigen binding domain linked to a costimulatory molecule[81]. These approaches have proved successful in the treatment of melanoma and B cell lymphoblastic leukaemia with response rates of 50-70%[86]. To date are few reported studies of adoptive T cell transfer in ovarian cancer. In a small study Fujita *et al.* showed that when TILs propagated from resected tumours were administered after

chemotherapy the three year-survival was 100% compared to 67% in patients who did not receive TILs[87]. Several trials in ovarian cancer patients are ongoing using TILs and engineered T cells targeting the tumour associated proteins MUC16, mesothelin and NY-ESO-1[81,86].

1.2.3 Recurrent HGSOC

The majority of patients respond to primary chemotherapy but will, however, typically relapse and eventually go on to develop chemotherapy resistant disease[37]. Approximately 10% of patients do not respond to primary chemotherapy, suggesting intrinsic resistance also operates in a subset of patients[88]. The mechanisms of chemotherapy resistance are not completely understood but may include epithelial to mesenchymal transition, drug efflux mechanisms, cell cycle arrest, apoptosis block with up regulation of TGFβ, WNT and NOTCH signalling[89]. Significant effort has been expended to define a stem cell population that may be able to regenerate tumours after a complete response to chemotherapy. However, studies to date have demonstrated stemness markers to show variable expression in ovarian cancer[90].

Patch *et al.* performed whole genome sequencing in primary refractory/resistant, primary sensitive and matched acquired resistant HGSOC biopsies from ninety-two patients[91]. This study suggested that inactivation of *RB1*, *NF1*, *RAD51B* and *PTEN* genes was associated with acquired resistance as were reversions in germline *BRCA1/2* mutations[91]. Furthermore, overexpression of MDR1 was associated with acquired chemotherapy resistance[91]. Primary resistance was associated with CCNE1 amplification[91]. More recently RNA-sequencing of sixty-six matched primary and relapsed HGSOC biopsies has demonstrated heterogeneity between primary and recurrent samples based on differential expression of a panel of genes involved in immune activation and matrix remodelling pathways[92]. This study classified tumours into 'immune active' and 'immune silent' groups; at relapse some tumours shared the same immune status as the primary tumour, whereas other tumours switched immune status[92]. This demonstrates the complexity and heterogeneity of the tumour microenvironment between relapsed and primary tumours.

Secondary cytoreductive surgery should be considered at relapse for appropriate patients[37,93]. The Arbeitsgemeinschaft Gynaekologische Onkologie (AGO) group developed the Descriptive Evaluation of preoperative Selection KriTeria for OPerability in recurrent OVARian cancer (DESKTOP OVAR) algorithm to predict patients that would benefit from secondary debulking surgery (SDS)[94]. Patients with a first recurrence of EOC with a platinum-free interval of greater then 6 months, in whom complete

cytoreduction was achieved in the first debulking procedure, ascites less the 500ml and a ECOG performance status of 0 represent of group of patients who will benefit from SDS and chemotherapy compared to chemotherapy alone[37]. Other clinical algorithms to predict complete SDS are the Tian Risk Model[95] and the Slone Memorial Kettering criteria[96].

If surgical intervention is not an option, systemic chemotherapy is administered to control the disease for as long as possible. The various options for subsequent lines of chemotherapy will be based on the time to recurrence, patient characteristics and the disease biology.

1.3 The tumour microenvironment of HGSOC

Malignant cells acquire mutations in oncogenes or tumour suppressor genes that serve to initiate tumour development. However, it is now established that malignant cells rely on resident and recruited populations of non-transformed host cells to promote tumour evolution[97]. This diverse ecology of cells includes endothelial cells, pericytes, fibroblasts, mesothelial cells and infiltrating immune cells which, with their soluble mediators and the extracellular matrix, form the tumour microenvironment (TME)[97]. Therefore, tumours can be considered 'rogue organs', where intracellular communication is mediated by networks of cytokines, chemokines and growth factors along with changes in the physical properties of the tissue[98].

A common feature of virtually all TMEs is a prominent immune cell infiltrate. As proposed by Dunn *et al.* early in the process of tumour development malignant cells may be 'visible' to the immune system and can be 'eliminated' by $CD8^+$ cytotoxic T cells[99]. However, under the effects of continued immune pressure, malignant cell clones become 'immuno-edited', this results in the selection of malignant cells that can 'escape' immune surveillance. Crucially neoplastic cells that escape immune detection also acquire capabilities to subvert the host immune response to promote tumour progression and metastasis[100].

The immune infiltrate is however pliable and this has been successfully leveraged therapeutically for example by checkpoint blockade, adoptive cell transfer and vaccine therapies[101]. Indeed, heavily immune infiltrated tumours, compared to immune excluded tumours, are more amenable to control by a range of therapies and associate with improved patient survival. Understanding the mechanisms and regulatory circuits that generate immunosuppression in the TME and how this can be mitigated therapeutically is therefore important.

1.3.1 Pre-chemotherapy

1.3.1.1 Lymphocytes

In HGSOC tumour infiltrating lymphocytes (TILs) robustly associate with improved survival, this reflects findings in other epithelial cancers. Critical to prognosis of TILs in HGSOC is the balance of effector to regulatory T cell subsets[33].

Zhang *et al.* were the first to show that high $CD3^+$ T cell density within ovarian tumours correlated with increased progression free and overall survival[34]. In this study 186 stage III/IV EOC patients were studied. Within this cohort the major histological subtypes of EOC were represented. CD3 expression was assessed by IHC, in 55% of cases there were significant intratumoural $CD3^+$ infiltrates and 39% of cases lacked $CD3^+$ such infiltrates[34]. $CD3^+$ infiltrates were seen both in the stroma and the malignant cell areas of the biopsy. The five year survival rate was 38% in patients whose tumours contained T cell infiltrates and only 4.5% in patients whose tumours contained few T cells[34]. Interestingly, T cell infiltrates were also positively correlated with optimal surgical cytoreduction. However in multi-variate analysis, both $CD3^+$ T cell density and the extent of residual disease were independent predictors of overall and progression free survival[34]. Tumours richly infiltrated with T cells had higher expression of IFNγ, IL2, CCL21 and CCL22. Conversely, VEGF was higher in tumours with fewer T cells suggesting that secreted factors determine TIL density which has a significant effects on patient prognsosis[34]. This finding was confirmed by Raspollini *et al.*[102] and Tomsova *et al.*[103].

Woo *et al.* were the first to show that ovarian cancers contained $CD4^+CD25^+$ T regulatory cells (Tregs) which secrete the immunosuppressive cytokine transforming growth factor-β (TGF-β)[104]. These cells additionally expressed the T regulatory markers; cytotoxic T-lymphocyte-associated antigen 4 (CTLA-4), forkhead box P3 (FoxP3) and glucocorticoid-induced TNFR-related protein (GITR)[104]. In a multivariate analysis Curiel *et al.* showed that Tregs correlated with poor overall survival in EOC[105]. This finding was further substantiated by Wolf *et al.*[106] who showed that a low FoxP3 expression associated with approximately a 60% reduced risk of death[106]. FoxP3 can also correlate with a positive outcome in EOC[107,108]. These findings may be explained by FoxP3 being an indicator of a strong $CD8^+$ T cell response. Alternatively, subsets of FoxP3 T cells may have pro-inflammatory functions as demonstrated by the production of IL-17[33].

Sato *et al.* showed that the ratio of $CD8^+$ T cells to Tregs was important in determining the prognosis in EOC[109]. In 117 Stage III disease patients a high $CD8^+$ to $FoxP3^+CD25^+$

T cell ratio within the malignant cell areas of biopsies correlated with longer survival compared to patients with a low intratumoural ratio. In this study and in contrast to Zhang *et al.*[34] intraepithelial $CD3^+$ T cells did not significantly correlate with survival[109]. Hamanishi *et al.* found that high intraepithelial $CD8^+$ T cells were correlated with better overall prognosis whereas stromal $CD8^+$ T cells did not[110]. High $CD8^+$ T cell density was inversely correlated with programmed death ligand 1 (PDL1) expression on tumour cells[110], providing evidence that checkpoint pathways are an important TIL-regulatory mechanism in EOC.

Overall these studies suggest that enhanced patient survival is positively correlated with increased $CD8^+$ T cell density. However, pathways inhibiting adaptive immunity are frequently active in the ovarian cancer TME. These include the PDL1 and other immunosuppressive pathways including, for example the expression of IDO-1 which is associated with T cell exhaustion[111]. Therefore, although there are cells capable of recognising and killing malignant cells, these functions are prevented[33].

Milne *et al.* showed that high $CD20^+$ B lymphocyte densities are associated with a positive prognosis in optimally debulked HSOC patients[107]. Over 40% of the 198 patients showed intraepithelial expression of CD20[107]. Furthermore, CD20 staining was strongly associated with both $CD4^+$ T cells and $CD8^+$ T cells and markers of T cell activation and effector functionality[107]. In contrast to this finding, Phuc Dong *et al.* showed high B cell numbers in EOC ascites was associated with a worse outcome in EOC[112]. The mechanisms underlying these effects are not clearly understood.

1.3.2 Post-chemotherapy

Our laboratory and others have studied the effects of chemotherapy on the TME of HGSOC. Böhm *et al.* reported T cell activation in omental metastases after NACT; $CD4^+$ T cells showed enhanced IFNγ production and antitumor Th1 gene signatures were increased[113]. In patients with 'good' response to NACT, T-cell activation was more pronounced and these biopsies contained significantly fewer stromal $FoxP3^+$ Treg cells[113]. This finding was supported by a reduction in a Treg cell gene signature in post *versus* pre-NACT samples that was also more pronounced in good responders[113]. A high proportion of T cells in biopsies expressed immune checkpoint molecules PD-1 and CTLA4. Indeed, PD-L1 levels were significantly increased after NACT[113]. Therefore, despite T cell activation following NACT, T cell response may be hampered by immunosuppressive circuits activated by chemotherapy. This suggests a rationale for chemo-immunotherapy combinational approaches in HGSOC. Furthermore, Montfort *et al.* showed NACT promoted B cells that were associated with an anti-tumour

response[114]. Collectively, these data suggest that NACT may promote an anti-tumoural TME.

Pölcher *et al.* showed that NACT was associated with increased $CD4^+$, $CD8^+$ and granzyme B^+ TILs, but that $FoxP3^+$ cell density was unaffected by chemotherapy[115]. This study was conducted on a mixed cohort of epithelial ovarian cancer biopsies rather than exclusively studying HGSOC, furthermore there may not have been consistency of the site studied. However, although $CD4^+$ and $CD8^+$ TIL density did not affect prognosis before chemotherapy, after chemotherapy infiltration granzyme B^+ cells showed a tendency to improved PFS[115]. Following chemotherapy low $FoxP3^+$ T regulatory cell density was associated with significantly improved OS and PFS[115]. Additionally, post-NACT a high granzyme B^+:$FoxP3^+$ cell ratio associated with enhanced progression free survival. This study also suggests that NACT can activate anti-tumoral effects within the TME. Peng *et al.* showed that $CD8^+$ TILs increased in ovarian cancer patients undergoing NACT[116]. Wouters *et al.* also reported a similar tend[117]. Overall these data suggest that NACT enhances $CD8^+$ cytotoxic TIL response and may diminish $FoxP3^+$ Tregs.

Recently, Lo *et al.* performed a detailed assessment of chemotherapy on immunologic changes in matched pre and post-chemotherapy HGSOC omental metastases. This study showed that NACT was associated with increased densities of $CD3^+$, $CD8^+$, $PD1^+$ and $CD20^+$ TIL with no significant changes in $CD79a^+CD138^+$ plasma cells or $CD68^+$ macrophages. Furthermore, $FoxP3^+PD\text{-}1^+$ Tregs, indoleamine 2,3-dioxygenase $(IDO)^+$ and $PDL1^+$ cell density did not change. This group defined three response patterns to NACT by hierarchical clustering. Tumours containing both high and low TIL densities showed increases in multiple immune markers post-chemotherapy and their resulting immune profile were indistinguishable. This finding was in contrast to TIL-negative tumours which generally remained negative following NACT. Despite the changes observed in TIL markers overall, TIL densities following chemotherapy showed no association with survival. Therefore NACT appeared to enhanced a pre-existing TIL response, yet this failed to overcome immunosuppression[118].

Overall these studies suggest that chemotherapy alters the TME of HGSOC to promote antitumor adaptive immunity, yet immunosuppressive functions are still dominant. However, the effects of chemotherapy on TAMs is largely unexplored in HGSOC. TAMs are one of the most numerous immune cells within HGSOC. As I will describe below, TAMs have prominent roles in mediating immunosuppression within the TME of HGSOC. Therefore, it is important to study the effect of chemotherapy on this cell type.

1.4 Tumour Associated Macrophages

1.4.1 Macrophage activation states

A characteristic hallmark of macrophages is diversity and plasticity of phenotype[119]. In 1990's terms 'classical' and 'alternate' activation were introduced to describe macrophage responses seen *in vitro* to IFNγ and IL-4 stimulation respectively[120]. 'Classical' and 'alternate' activation are two extremes of macrophage activation and clearly associated with differences in gene expression. Classical activation is now used interchangeably with IFNγ or TLR stimulated macrophages. Classically activated macrophages are characterised by the expression of high levels of proinflammatory cytokines (e.g. IL-12, IL-23), reactive oxygen species and promotion of a Th1 response[119,121]. These macrophages are able to kill tumour cells[122]. Alternately activated macrophages are characterised by the expression of scavenger receptor molecules, mannose and galactose receptor molecules[123]. These macrophages have trophic tissue functions promoting wound healing and fibrotic tissue responses but also tumour progression and spread[119,121].

In 2002 by Mills *et al.* proposed 'M1' and 'M2' macrophage activation states based upon differences in arginase metabolism seen in macrophages by C57BL/6 and BALB/c mice[124]. These states correlated with differences in Th1 and Th2 cell responses in the same strains. Based on this Mills *et al*. proposed M1 (inflammatory) and M2 (healing) states. Since this time these two nomenclatures have been used interchangeably in the literature to describe these two extremes of macrophage activation. Within tumour tissue macrophages are exposed to a range of stimuli that result in the attainment of distinct functional phenotypes. Conceptualising macrophage activation in this dichotomous manner is a restrictive and simplistic view of the complexity of macrophage polarisation and is an inaccurate description of macrophages residing in complex tissue enviroments[125]. That said, it is a useful concept as a descriptor of general skew of macrophage activation. In this thesis I will describe macrophages as resembling 'classically activated' or 'alternatively activated' states to describe these two extremes of macrophage activation.

1.4.2 TAMs within the tumour microenvironment

Tumours develop in contact with resident or recruited populations of immune cells. The ability of malignant cells to evade immune detection is regarded as a hallmark of cancer[126]. Tumorigenesis relies on the subversion of immune cells at an early stage in tumour evolution; macrophages are highly implicated in this process.

Many cancers have abundant macrophage populations[123,127,128]; macrophages frequently represent the most common host cell type. As a non-malignant lesion makes the transition to malignancy, macrophages accumulate and become progressively polarised from inflammatory (classically activated) to immunosuppressive (alternatively activated) phenotypes[128]. Key chemokines driving this process are IL-4 derived from malignant cell and T cells, CSF-1, GMCSF and TGF-β. The hallmark of TAM is an immunosuppressive phenotype which impacts on multiple aspects of tumour biology, promoting tumour growth and metastasis[123,127,128]. The presence of TAMs is generally associated with a poor prognosis in many solid tumours. This has been shown using conventional IHC to quantify cellular density and by inferring the presence of macrophages based on gene expression profiles[129]. Depleting or antagonising macrophages can limit tumour growth and dissemination in experimental models[119,129,130]. This may be via direct effects on tumour cells however *in vivo* models indicate that this effect is often via enhanced recruitment and effector function of $CD8^+$ cytotoxic T cells[119,129,130].

In the following sections I will describe the origins of TAM in the TME and the multiple mechanisms by which TAM drive tumour progression. I will then move on to describe the current literature on the effects of chemotherapy on TAMs followed by strategies that have been used to target TAMs therapeutically.

1.4.3 Origins of TAMs

In recent times it has become clear that in murine tissue under homeostasis macrophages can originate from two distinct sources: from $CX3CR1^+$ $cKit^+$ erythromyeloid progenitor cells that seed into tissues during embryonic development and from bone marrow (BM)-derived haemopoietic stem cell progenitors. Cells are seeded into tissues in two 'waves' during embryonic development, and derive from either the fetal yolk sac or the fetal liver (Figure 1.2). These cells are able to replicate in tissues to maintain macrophage populations. The relative contribution of cells from these two origins varies between tissues. In the brain for example microglial cells are derived exclusively from embryonic precursors with little contribution for BM-derived progenitors. In the colon the dominant population of macrophages dependent on continuous replacement from $Ly6C^+$ inflammatory monocytes of bone marrow origin[119,121]. In perhaps the majority of tissues mixed populations of macrophages with divergent origins exist e.g. pancreas, breast and lung. The relevance of these divergent origins is still to be explored although it appears that tissue-specific stimuli are key in determining macrophage phenotype irrespective of origin[131]. The majority of these studies have been conducted in the mouse, in comparison studies of macrophage origin in human subjects

is far less explored, however recent reports suggest the existence of macrophage populations from divergent origins in humans as well[132–134].

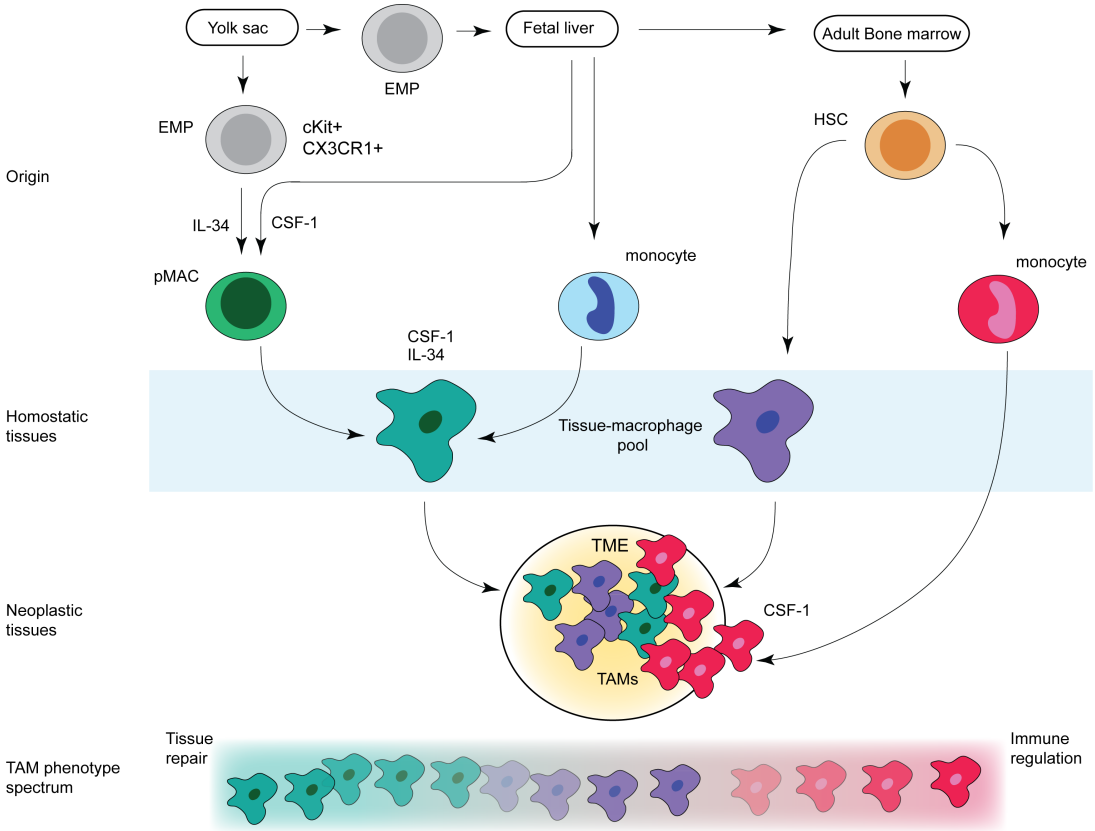

Figure 1.2 Macrophage origins. Studies in mice show macrophages arise from two divergent origins: i) from erythromyeloid progenitor cells (EMP) during embryonic and fetal development and ii) in adult life from haematopoietic stem cell (HSC) precursors produced in the bone marrow. Under homeostatic conditions macrophage populations from both these origins contribute to the tissue macrophage population, the relative contribution of these populations varies by tissue. Within in neoplastic tissue TAMs may also arise from both these origins furthermore TAM are also derived from recruited monocytes. Adapted from Cassetta and Pollard 2018[129] and Denardo and Ruffell[135].

Historically TAMs have been considered to derive principally from recruited BM-derived circulating monocytes that are recruited into malignant tissues. However, more recent data have called this assumption into question. In murine models of brain, lung and pancreatic cancer up to 50% of all TAMs were found to derive from tissue-resident populations[134,136,137]. Furthermore, these studies have suggested that embryonic-derived TAMs may have distinct phenotypes and functions compared to those derived from circulating monocytes. The relative contribution of macrophages of different origins to the TAM population is still debated and incompletely understood[138]. The majority of studies come from mouse cancer models, data relating to human TAMs are still rare. One recent paper addressing this deficit showed that 10-40% of TAMs in human PDAC expressed similar surface markers and transcriptional profiles to tissue resident TAM characterised in murine PDAC[139]. Furthermore, Cassetta *et al.* recently reported that TAM in endometrial and breast cancers were transcriptionally divergent compared to each other and compared to resident macrophages and monocyte precursors[133]. These

data suggest that cancer-specific microenvironments are responsible for driving myeloid cell pheneotype[133].

A myriad of cytokines, chemokines and chemotactic molecules may mediate the recruitment of monocytes from the blood into primary and metastatic tumours where they differentiate into TAMs[140]. Molecules that are important in this process in murine cancer models include CCL2, MIP1α, CCL4, CXCL12, IL1-β, IL6, VEGF, and CSF-1[140]. One of the most studied of these factors is the chemokine CCL2, which is expressed by tumour cells and macrophages in mouse and human cancers. CCL2 expression correlates with TAM number and poor prognosis.

CSF-1 is a major regulator of myeloid cells irrespective of developmental origin and is a chemoattractant for macrophages[128,141]. High intratumoral CSF-1 concentrations correlated with high TAM density and poor prognosis[133,142]. In the context of endometrial cancer, CSF-1 protein concentration within the tumour was an independent predictor of survival[143]. In murine models multiple studies show that pharmacological and genetic inhibition of CSF-1 signalling resulted in reduced TAM density and delayed tumour initiation, reduced tumour growth and metastasis[128,142]. These findings could be explained by interruption of CSF-1 signalling locally within the tumour, or as the result of systemic effects on the BM[128,129]. Lin *et al.* showed clear evidence for CSF-1 mediating local recruitment of macrophages via inducing gain-of-function mutations in CSF-1 in the mouse mammary tumour virus-polyoma middle tumour-antigen (MMTV-PyMT) model of breast cancer[144]. Expression of CSF-1 in the mammary epithelium resulted in macrophage recruitment which enhanced tumorigenesis, additionally this rescued loss-of function CSF-1 mutations, which were seen to delay tumour progression[144,145].

Chemotactic molecules activate signalling pathways that result in an inside-out conformational changes in integrins, including $\alpha4\beta1$[146,147]. As a result of this process monocytes are able to interact with the endothelial cells and mediated extravasation from the blood into tissues. One important signalling pathway in myeloid cells activated by a range of chemotactic molecules is PI3kγ[140]. Genetic or pharmacological inhibition of PI3kγ, the signalling components in this pathway or $\alpha4\beta1$ reduced TAM infiltration, tumour growth, and metastasis in a range of murine models[148–151]. As there is redundancy in the cytokine and chemokine networks recruiting TAM into tissues, targeting individual chemotactic molecules may not be as effective as targeting common down-stream signalling pathways[140].

Lineage tracing experiments in pancreatic ductal adenocarcinoma (PDAC) have shown

a proliferative TAM population of embryonic origin, distinct from BM derived cells[134]. Furthermore, cell proliferation within the TAM population has been shown in sarcoma and breast tumours[152–154]. This population of TAM derived from tissue resident cells is characterised by a unique set of markers in mice: these include CXCR3^{high}, MERTK^{+}, Siglec 1^{+}, CD64^{+} F480^{high}; whereas BM derived macrophages express integrin α4, L-selectin, Ly6C, and Nr4a1[140]. Furthermore, TAM in different tissue environments express specific transcription factors, for example Gata-6 expression is characteristic of peritoneal macrophages[140]. Transcriptomic analysis of adult and embryonic-derived TAM populations sorted from murine PDAC showed embryonic TAM associated with a fibrotic signature and upregulated collagens and cyclins; whereas BM derived cells were characterised by a gene signature of antigen presentation[134]. Clear understanding of markers associated with these populations in human tumours is lacking.

Feng *et al.* showed the differential contributions of resident and recruited TAM in a murine model of glioma. The glioma TAM population was a mixture of microglia, derived from embryonic precursors and macrophages recruited from BM-derived inflammatory Ly6C^{high} monocytes. Depleting CX3CR1 resulted in 'inflammatory' Ly6C^{high} monocyte recruitment which was associated with increased tumour incidence, decreased survival and decreased latency[155]. This suggested that recruited rather than resident myeloid cells may mediate protumoural functions in this model.

1.4.4 Roles of tumour associated macrophages

Within both the primary and metastatic sites of many tumours, TAMs promote tumour growth and development through multiple mechanisms including stimulation of angiogenesis, tumour cell invasion, cell mobility and extravasation at the metastatic site. This multiplicity of processes implicating TAM in the promotion of tumour development underscores the intense interest in therapeutic strategies to target TAMs[128,138] (Figure 1.3).

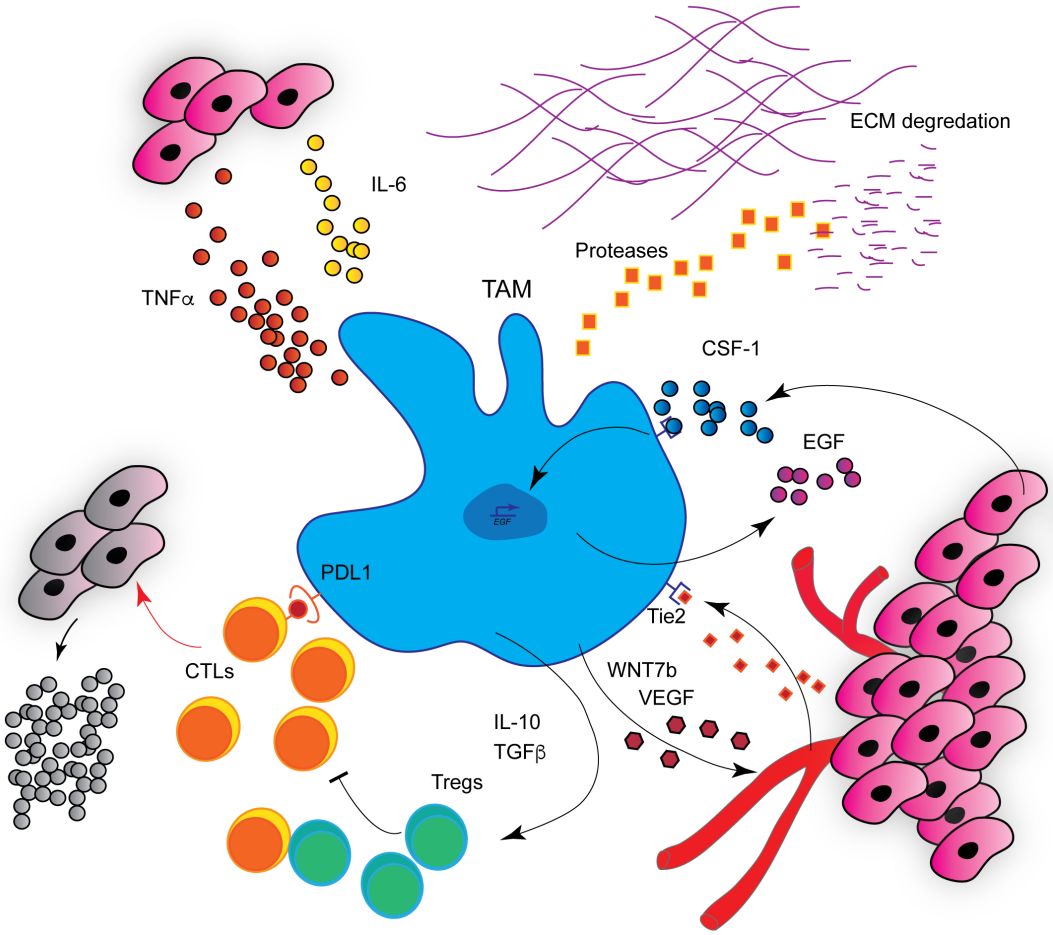

Figure 1.3 Diagrammatic representation of some of the known tumour promoting roles of TAMs. Macrophage production of IL-6 and TNF-α promote survival signalling in malignant cells. TAM mediate immunosuppression, directly or indirectly. TAMs promote angiogenesis via production of VEGF-A and WNT7b. TAM promote malignant cell invasion and metastasis via cytokine circuits and actions on the ECM. Adapted from Ruffell and Coussens 2015[156].

1.4.4.1 Angiogenesis

The development of a vasculature is a hallmark of tumour development and has been referred to as the 'angiogenic switch'[126]. TAMs regulated by CSF-1 are important in driving this process in a wide range of models; one of the most studied is the MMTV-PyMT breast carcinoma model[128]. In this model tumour angiogenesis was dependant on WNT7b secretion by TAMs resulting in VEGF-A production in endothelial cells[157,158]. Genetic deletion of WNT7b in macrophages resulted in failure of angiogenesis and in reduced tumour growth, invasion and metastasis[157]. A specific population of TAMs expressing the surface glycoprotein TIE2 is implicated in angiogenesis in a number of cancer models as shown by genetic ablation studies[159]. These TIE2 positive cells are frequently found on the abluminal side of vessels as the result of the interaction of TIE2 with its ligand ANG2 on endothelial cells[128]. Interestingly, these cells may also promote the invasion of cancer cells into the vasculature. Interfering with this vessel association through using an anti-ANG2 antibody or through conditional knockdown of TIE2 prevented angiogenesis[160]. CSF-1R is important in generating TIE2^{+} macrophages[161],

suggesting a link between these two molecules in driving angiogenesis[128].

1.4.4.2 Motility and intravasation

TAMs promote cancer cell motility and haematogenous dissemination. Wychoff *et al.* found that TAMs can drive unidirectional motility of tumour cells through a paracrine signalling loop involving CSF-1 derived from tumour cells and EGF derived from macrophages[162]. This mechanism was sufficient to enable tumour cell invasion of collagen gels[163]. Furthermore, this process has been directly visualised *in vivo* in the MMTV-PyMT model using multiphoton microscopy. Here, TAMs and tumour cells were observed to rapidly co-migrate along collagen fibres towards blood vessels[145]. In the perivascular space TAMs can 'open the gate' to allow tumour cell entry to the circulation[128]. TAMs can further promote the invasive capabilities of tumour cells for example by the production of secreted protein acidic and rich in cysteine (SPARC) which increases tumour cell integrin mediated ECM interaction and motility[164]. Furthermore cathepsins produced by TAMs result in matrix remodelling promoting tumour cell invasion[165,166] and TAM-derived TGFβ has been implicated in promoting EMT in tumour cells further facilitating mobility[128,167]. The trilogy of macrophages, malignant cells and endothelial cells has been termed the 'tumour microenvironment of metastasis' (TMEM) and can be identified as a histological marker for metastasis in human breast cancers[168].

Therefore, TAMs are implicated in promoting tumour growth via the induction of angiogenesis as well as promoting metastasis. Hence, targeting TAMs may facilitate both of these processes to be impacted simultaneously.

1.4.4.3 Immunosuppression

For tumours to evolve, evasion of the host immune response is essential. TAMs are important in this process, which is also mediated by Tregs and tumour cell driven immune evasion mechanisms[169,170]. Demonstrating this point, the ratio of Tregs and TAMs to $CD8^+$ cells is an important predictor of survival in breast cancer[171].

TAMs secrete a broad range of chemokines, cytokines and enzymes that foster immunosuppression via the inhibition of $CD4^+$ and $CD8^+$ T cell function or by the induction of regulatory T cell phenotypes[128]. For example, Curiel *et al.* showed that in human ovarian cancer TAMs can recruit Treg cells via production of IL22[105]. Schlecker *et al.* using murine models of melanoma showed that myeloid cell production of CCL3, CCL4 and CCL5 recruited Treg via CCR5 signalling[172]. Furthermore, TAM produce molecules that can induce Tregs, important amongst these are IL-10 and TGFβ[173].

Savage *et al.* showed that M2/alternatively activated (which expressed IL-10 at high levels) but not M1/classically activated human macrophages were able to induce Tregs, with a strong immunosuppressive phenotype[174]. Denning *et al.* show that macrophages in the lamina propria are able to induce Tregs via the production of IL-10 and TGFβ[175].

TAMs express a range of 'inhibitory' MHC molecules that are able to supress effector lymphocyte function. For example in mouse models HLA-G expression on tumour cells inhibits the activation of NK T cells via engagement of CD94[176]. In glioma this inhibitory signal can be provided by myeloid cells[177]. Likewise HLA-G expression on TAM can inhibit the activation of T cells[178]. Additionally, TAMs may inhibit intratumoural immune response via engagement of immune check point pathways. The most studied of these are mediated by PD1 and CTLA4 and are expressed on activated T-cells; stimulation of these receptors with their ligands, PDL-1/2 and CD80/CD86 respectively, inhibits T-cell responses. These pathways represent important mechanisms acting to limit immune responses and maintain homeostasis. Under the influence of HIF-1α signalling TAMs up regulate the expression of PDL-1[179]. It is difficult to define the importance of the TAM PDL-1 signal as this molecule is also expressed by tumour cells and other cells of the TME[128].

TAM can also mediate immunosuppression by influencing the metabolism of effector cells. TAM production of the enzyme arginase-1 results in the depletion of L-arginine from the TME of human and murine tumours. This can mediate immunosuppression by preventing the expression of the CD3γ chain, rendering T-cells unable to respond to antigen[180] in a murine lung cancer model. Furthermore, TAMs can produce the enzyme IDO which degrades L-tryptophan, this results in the production of immunosuppressive metabolites and the depletion of this amino acid from the TME which further contributes to T cell exhaustion[181,182].

1.4.4.4 Extravasation

As described above, TAM have critical roles in mediating tumour growth, development and invasion. Macrophages are also able to facilitate tumour cell extravasation at sites of metastasis by priming the so-called 'pre-metastatic niche'[183]. In lung cancer models, monocytes are recruited to the pre-metastatic niche by CCL2 gradients produced when micro-clots of tumour cells and platelets arrive in vessels[128]. The recruited monocytes differentiate into $CCR2^{+}$, $VEGFR1^{+}$ $Ly6C^{-}$ $F4/80^{+}$ macrophages (defined as metastasis associated macrophages, MAMs in this model). MAMs facilitate tumour cell extravasation into the tissue via the production of vascular permeability factors such as VEGF. Ablation of MAMs prevented tumour cell seeding and decreased metastasis growth[128,184].

1.4.5 TAM density and clinical outcome

The prognostic significance of TAMs has been studied in a wide range of human tumours[138]. High TAM density predicts poor patient prognosis[185], suggesting immunosuppressive actions of TAM, within many solid tumours. Indeed, an overall negative association of TAM density across a range of solid tumour types has been demonstrated in a large meta-analysis by Zhang *et al.*[186]. However, in colorectal, prostate and non-small cell lung cancer, high TAM density correlates with a favourable patient outcome[138].

In these studies, general myeloid markers or markers representative of specific macrophage polarisation states have been correlated with survival. CD68 is the most common pan-macrophage marker employed. Markers such as CD163, CD206 and CD204, which are regarded as markers of an alternatively activated phenotype have been assessed with similar results to CD68[187,188]. As will be discussed below, when interpreting these data it is important to consider the effects of chemotherapy on the TAM infiltrate. It is likely that the positive effects of TAMs on patient survival in CRC result from the effects of TAM on response to chemotherapy[138].

1.4.6 Tumour associated macrophages in ovarian cancer

In ovarian cancer multiple soluble mediators have been demonstrated as important in TAM polarisation and patient outcome. These include IL-6, IL-10, TGFβ and aracadonic acid[88,189]. Initial studies have shown ovarian TAMs to express markers suggesting an immunosuppressive alternatively activated phenotype, including CD163, CD204, CD206 and IL-10[190–192]. Although density of total macrophage populations quantified by CD68 have not been shown to predict patient outcome[193], clear evidence does exist that specific subsets of TAMs affect clinical outcome. For instance, Lan *et al.* showed that patients with tumours richly infiltrated with $CD163^+$ TAMs to have significantly reduced progression-free and overall survival[194]. TAM CD206/CD68 ratio predicts worse PFS[193], and, correspondingly, a high M1 (classically activated)/M2 (alternatively activated) ratio associated with improved survival[195]. Furthermore, Zhang *et al.* showed a high intra-tumoural, as opposed to stromal or whole tissue, M1 (classically activated)/M2 (alternatively activated) phenotypic ratio was associated with improved survival[196] suggesting localisation as well as phenotype to be clinically relevant. However, it should be noted that these studies are predominantly in mixed cohorts of ovarian cancer subtypes and the effects of chemotherapy on macrophage phenotype was not considered. A recent meta-analysis confirmed the association of poor prognosis with $CD163^+$ TAMs and improved prognosis with a high M1 (classically activated)/M2

(alternatively activated) ratio[197], further strengthening these data.

Transcriptomic assessment of TAMs from HGSOC ascites demonstrated a 'mixed' polarisation phenotype[198]. In this study TAM expression of CD163 was associated with early disease relapse, suggesting the importance of this population of TAM in promoting the tumours. Furthermore, transcriptomic assessment of TAMs and resident peritoneal macrophages has demonstrated a surprising similarity between these two populations. Interestingly, the most striking difference between these populations was an up regulation of ECM related genes in ovarian cancer ascites TAMs[199].

1.5 The effects of chemotherapy on TAM

Both clinical and experimental evidence show that chemotherapy can modify TAM phenotype and function within the TME of many tumours.

1.5.1 Clinical studies

Studying patient cohorts pre and post-chemotherapy shows that chemotherapy can modify the association of TAM density and patient outcome. This effect is exemplified in follicular lymphoma where $CD68^{+}$TAM density associated with favorable or unfavorable outcome in patients depending on the multi-agent chemotherapy administered[200,201]. In the post-treatment setting, following the rituximab, cyclophosphamide, doxorubicin, vincristine and prednisone regimen (R-CHOP) a high TAM density was associated with a favorable prognosis[202]. This effect was not seen however in patients treated with another chemotherapy regime which excludes doxorubicin: rituximab, cyclophosphamide, vincristine and prednisone (R-CPV)[203]. Hence, specifically doxorubicin treatment may engage antitumoral immune responses. Interestingly, doxorubicin can activate 'immunogenic' forms of cell death (see next section) which may provide a mechanism to explain these findings.

Di Caro *et al.* were the first to show the prognostic association of TAM density is impacted by chemotherapy exposure in solid tumours[188]. They studied PDAC patients with locally advanced cancers, who, following surgical resection, were either treated with adjuvant chemotherapy or did not receive additional treatment. High TAM density was associated with an extended disease free survival in patients treated with adjuvant gemcitabine, which negated the negative prognosis associated with high TAM density in patients who did not receive adjuvant chemotherapy[188]. Furthermore, Malesci *et al.* also showed that a high TAM density post-adjuvant 5-fluorouracil treatment was associated with favorable outcomes, however, this was not seen in untreated patients[181].

These data highlight that the prognostic significance of TAMs can be modified by exposure to chemotherapeutic agents and suggest that post-chemotherapy TAMs may adopt anti-tumour roles. This underscores the importance of considering the association of TAM density with clinical outcome in the context of chemotherapy. Moreover, most studies to date that have assessed the prognostic value of TAMs do not report the chemotherapy regimens used[204–206].

1.5.2 Experimental studies

Chemotherapy may affect macrophage function directly or indirectly[138]. For the last thirty years it has been known that tumour response to chemotherapy is at least in part dependent on myeloid cells. Mantovani *et al.* showed that tumour cell lines exposed to actinomycin D became susceptible to killing by monocytes; this phenomenon was termed drug dependant cellular cytotoxicity[207]. Building on this early work, the concept of 'immunogenic cell death' (ICD) was developed and suggests that in response to chemotherapy, tumour cells express alarm signals that then trigger immune responses[208]. For example, Ma *et al*. showed that doxorubicin exposure of tumour cells resulted in the release of ATP which recruited macrophage precursors that differentiated into antigen presenting cells capable of effective immune responses[209]. Indeed, ICD has been demonstrated in response to a range and suggests and immunological mechanisms may underlie the effects of many chemotherapies[208].

Trabectedin, a chemotherapy agent that binds DNA and causes cell cycle arrest acts, at least in part, via its effects on macrophages. Germano *et al.* showed that trabectedin, through interactions with DNA binding proteins, caused changes in genes encoding pro-inflammatory cytokines and chemokines in sarcoma xenografts and cell lines[210,211]. In a murine sarcoma model Germano *et al.* show that trabectedin activated caspase-8 mediated apoptosis selectively in monocytes/macrophages[212]. TAM depletion was demonstrated to be a mechanism underlying the effects of trabectedin in murine models. Furthermore, reduced TAM infiltration and decreased angiogenesis are observed in pre *vs* post-trabectedin treatment samples[211,212]. These data suggest TAM depletion may underlie the delayed yet prolonged effects of this drug on human tumours[212].

Further evidence showing the capability of TAM to mediate positive responsiveness to chemotherapy are made in the context of studies assessing the effects of the microbiome on TAM function. Lida *et al.* showed that priming of myeloid cells by microbiota components promoted the anti-tumoural effects of platinum chemotherapy in mouse tumour models[213]. Mice with formyl peptide receptor 1 (FPR1) dysfunction, a protein expressed in myeloid cells that functions as a DAMP sensor, have impaired responses

to anthracyclines[214]. The presence of loss-of-function mutations within the *FPR1* allele in human breast cancer is tied to an unfavourable response in patients with both breast and CRC following chemotherapy[214]. The above studies show that chemotherapy can alter the pro-tumoural phenotype of TAM in many tumour types to instead promote anti-tumoural immunity. However, under other conditions, TAMs can limit the effects of chemotherapy on tumour response. This dualistic effect of chemotherapy on TAM is perhaps not surprising given the plasticity of macrophages.

Enhancement of alternatively activated TAM phenotypes by chemotherapy reduces cytotoxic effects on malignant cells. In preclinical models this has been shown in the context of treatment with platinum compounds, paclitaxel and doxorubicin[215–221]. DeNardo *et al.* demonstrated that macrophages were recruited into murine breast tumours following paclitaxel treatment[222]. In this model abrogation of TAM recruitment using CSF-1R-antagonists enhanced response to chemotherapy, an effect that was dependent on $CD8^+$ T-cells[222]. Nakasone *et al.* also demonstrated that CCR2-dependent macrophage recruitment following chemotherapy in breast cancer models impaired response[220]. Hughes *et al.* showed that in a mouse tumour transplantation model M2 macrophages accumulated around vessels post-chemotherapy and promoted revascularization and relapse[223]. This was dependent on the CXCR4-CXCL12 axis[223]. Alberto Mantovani in his recent review[138] suggests two possible general mechanisms to explain negative impact of TAMs on chemotherapy response: in murine models chemotherapy induced tissue damage can trigger recruitment of immunosuppressive myeloid cells, or elicit a pro-tumorigenic type 17 T-helper-cell (Th17) skewed immune response promoted by IL1[138,218]. Alternatively, TAM may protect cancer stem cells from the cytotoxic effects of chemotherapy[138,216].

In conclusion, macrophage plasticity provides a platform to promote or limit the effects of chemotherapy, that is dependent on tumour type, chemotherapy and other host immune cells. Understanding how different chemotherapeutics interact with myeloid cells in different TMEs will enable rational approaches to targeting TAM in combination with chemotherapy be developed.

1.6 Targeting TAMs

Strategies to target macrophages in tumours fall into two broad categories, those blocking TAM recruitment and localisation within tumours and those that aim to functionally alter macrophages from a pro-tumour to anti-tumour phenotype[138]. I will provide an overview of both strategies and focus in more detail on CSF-1R pathway and its pharmacological blockade.

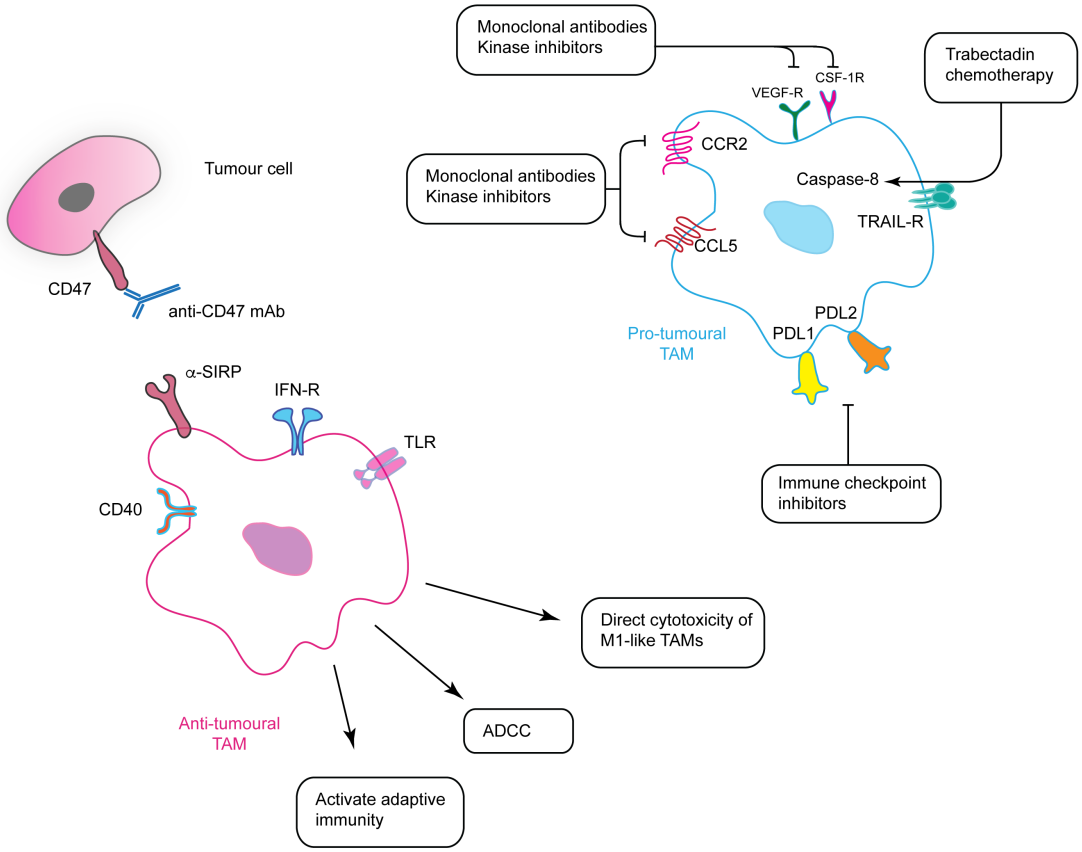

Figure 1.4 Macrophage-targeting treatment strategies in oncology. A range of therapeutic strategies have been explored that either deplete TAM or re-educate TAM towards anti-tumoural classically activated/M1-like functional programs (as described in the main text). Adapted from Mantovani 2017[138].

1.6.1 Targeting TAM recruitment

Multiple molecules are involved in the recruitment of TAM into tumours. Chemokines frequently act on multiple receptors and on different cell types and these features are a potential limitation to translating chemokine-targeting strategies in the clinic[138,224]. Targeting TAM via CCL2 reduces tumour growth and metastasis in a number of murine experimental models[225–229]. Concerns regarding this approach have been flagged with the observation of a rebound effect of monocyte/macrophage re-accumulation after drug withdrawal which enhanced metastasis development in murine breast cancer[230]. Despite this CCL2 antibodies have entered Phase 1 and 2 clinical testing[231–233]. A Phase 1 trial of carlumab, a fully human anti-CCL2 antibody, showed that the antibody was well tolerated, however there were no objective responses to treatment and only four of the thirty-three evaluable patients achieved durable disease stabilisation by RECIST criteria[233]. Furthermore, no objective responses were seen in a phase 2 study of carlumab in prostate cancer[231] and in a Phase 1b trial of carlumab in combination with chemotherapy no objective responses were observed[232]. In these studies only a transient suppression of CCL2 was followed with paradoxical increases in free CCL2 plasma

concentrations, which may underscore the lack of a clinical effect. This was in contrast with effects of an oral CCR2 antagonist PF-04136309, which engages the CCL2-CCR2 axis. This was evidenced by decreases in $CCR2^+$ blood monocytes and increases in $CCR2^+$ bone marrow monocytes in matched human samples[234], in keeping with the known role of this pathway in mediating monocytes egress from the bone marrow compartment. In a phase 1b human study, PF-04136309 has been used in patients with locally advanced PDAC who were not suitable candidates for surgery, alone and in combination with FOLFIRINOX (5-fluorouracil, folinic acid, irinotecan, and oxaliplatin) chemotherapy[234]. In this study, good safety profiles were observed and partial responses were seen in sixteen of thirty-three (49%) patients, compared with no objective responses in five patients treated with chemotherapy alone[234]. Therefore, targeting CCL2 may be a useful strategy.

1.6.1.1 Targeting TAM via CSF-1-Ri

Colony-stimulating factor 1 receptor (CSF-1R), is a cell-surface receptor for the cytokines CSF-1 and IL-34[235,236]. CSF-1R is predominately expressed by cells of the monocyte/macrophage lineage. Binding of ligand results in receptor dimerization and tyrosine kinase-mediated autophosphorylation of cytoplasmic tyrosine residues which creates binding sites for cytoplasmic proteins that activate phosphatidylinositol 3-kinase (PI3K) and extracellular regulated protein kinase 1/2 (ERK1/2) signalling pathways[141]. CSF-1 is the major growth and differentiation factor for the monocyte-macrophage lineage and is abundantly expressed by several tumour types[237]. IL-34, a second ligand for CSF-1R, also regulates macrophage recruitment to tissues[141]. CSF-1R is exclusively expressed by cells of the monocytic lineage and therefore represents a logical target to interfere with TAMs and their precursor cells[138]. As a tyrosine kinase CSF-1R represents an attractive therapeutic target. A number of small molecule CSF-1R inhibitors have been developed and tested in preclinical models, as well antibody antagonists[163,222,238–240].

CSF-1 and CSF-1R density in tissue is positively correlated with poor prognosis in a number of cancer types (breast, classical Hodgkin lymphoma, hepatocellular carcinoma)[138,241,242]. Inhibiting the CSF-1-CSF-1R axis has been investigated in a number of preclinical settings, both alone and in combination with conventional therapies[163,216,222,238,239,243]. The therapeutic antibody emactuzumab (RG7155) binds to the CSF-1R and prevents receptor dimerization, thereby preventing signalling[239]. Patients with diffuse type giant cell tumours (dt-GCTs) have shown objective responses to CSF-1R blockage with RG7155 and with PLX3397 (pexidartinib), a tyrosine kinase inhibitor of CSF-1R[239,244,245]. This disease is characterised by overexpression of CSF-1 and therefore serves as a 'model disease' for agents targeting the CSF-1-CSF-1R

axis[237]. In human dt-GCTs Ries *et al.* showed that RG7155 decreased TAM density and the circulating monocyte concentraion[239]. These effects were associated with an increase in the CD8:CD4 ratio within dt-GCT tumour tissues in five out of seven patients[239].

PLX3397, which is able to penetrate the blood brain barrier, has been tested in preclinical glioma models and was found to reduce glioma progression, tumour cell proliferation and tumour grade[246]. In patients with recurrent glioblastoma, PLX3397 decreased circulating monocyte populations, however no objective clinical responses were observed[247]. BLZ945, another small molecule inhibitor of CSF-1R, has also been studied in preclinical models of glioblastoma. In this setting BLZ945 treatment did not result in TAM depletion but caused a change in phenotype of TAM towards an anti-tumoural/classically activated phenotype[215]. In ovarian cancer, there have been few pre-clinical studies targeting TAM. Moughon *et al.* used GW2580, a small molecule inhibitor of CSF-1, to treat mice bearing ID8 tumours, which readily disseminate throughout the peritoneum[248]. GW2580 treatment decreased alternatively activated macrophage density in ascites and reduced ascites volume secondary to normalisation of the peritoneal vasculature[248]. However, a criticism of this study is the use of the ID8 model, which does not accurately recapitulate the genetic landscape of HGSOC (see also below). Lyons *et al.* used CSF-1Ri in combination with anti-VEGF and taxane chemotherapy, using HGSOC PDX models they found CSF-1Ri reduced VEGF resistance and enhanced anti-tumour effects[249]. These studies provide preliminary evidence to suggest that CSF-1Ri could be a valuable therapeutic approach in the context of ovarian cancer.

GW2580-mediated TAM depletion in a genetic model of gemcitabine-resistant PDAC enhanced activity of gemcitabine treatment[250]. TAM appeared to mediate resistance in tumour cells by upregulating cytidine deaminase, an enzyme that degrades the active form of gemcitabine[250]. In work carried out in our lab, Candido *et al.* used the CSF-1Ri AZD7507 to target TAM in a genetic model of PDAC[251]. AZD7507 treatment resulted in shrinkage of established tumours and increased survival in this model[251]. Malignant cell proliferation diminished, with increased cell death and an enhanced T cell immune response. TAM depletion rewired other features of the TME, for instance, there were significant decreases in several pro-tumor cytokines including IL-6 and IL-10 and chemokines such as CCL2 and CCL12 in AZD treated tumours[251].

Overall these data suggested that targeting the CSF-1-CSF-1R axis could be important in improving the therapeutic responses of conventional treatments. Based on these pre-clinical data, multiple clinical trials are currently in progress testing TAM-targeting agents

in combination with conventional treatment modalities and immunotherapies[135,138,237].

1.6.2 Activation of TAMs

Using bacterial products to promote immune responses to cancer represents the founding principle of immunotherapy, as pioneered by William Coley[252]. Indeed, microbial preparations (e.g. muramyl-dipeptide) prime macrophages for anti-tumour activity[253]. The clinical use of intravesical Bacillus Calmette-Guerin (BCG), in patients with recurrent urothelial malignancy, represents a clinical intervention inspired by this era of immunotherapy[138]. In addition to LPS, IFNγ is an inducer of classical macrophage polarization to a phenotype capable of tumour cell killing[138]. The therapeutic use of this cytokine has been tested in women with ovarian cancer both with advanced disease and after surgery in women with minimal residual disease[254,255]. Although in a very small study, Colombo *et al.* showed that in the context of small volume residual disease following cytoreductive surgery, IFNγ treatment resulted in tumour cell cytotoxicity and clinical responses[254]. These studies provide preliminary data to suggest that IFNγ-based immunotherapy and by extension M1/classically-activated macrophages may be useful in ovarian cancer.

CCL5 is a chemokine associated with functional reprogramming towards an M2 phenotype[138]. Halama *et al.* show in patients with advanced CRC, that targeting the CCL5-CCR5 axis resulted in objective clinical responses (60% partial responses, 80% disease control), although this was a very small cohort of patients[256]. This may represent another therapeutic strategy to alter macrophage phenotype[256].

CD40 agonists can reprogram alternatively activated TAM towards a classically activated phenotype. In a murine model of PDAC, treatment using an agonistic anti-CD40 mAb resulted in reprogramming of TAM toward classically-activated functions with reductions in tumour volumes[257]. On the basis of these findings a Phase 1 trial was undertaken which showed improved overall survival when CP-870,893 (a fully human CD40 agonist antibody) was administered in combination with gemcitabine and partial responses in four of twenty-two patients[258]. Interestingly, a recent study by Hoves *et al.* showed that CSF-1Ri treatment sensitises TAM to treatment with a CD40 agonist[259]. This resulted in a short-lived state of TAM activation which produced a proinflammatory cytokine milieu which enhanced T cell dependent immunity[259]. Therefore, multiple targeting approaches may be required to efficiently re-wire TAM immunosuppressive programs. This approach is being tested in an early phase clinical trial[138,259].

CD47 in an important negative regulator of phagocytosis, this molecule is broadly

expressed and has been regarded as a 'don't eat me' signal[260]. CD47 interacts with signal regulatory protein-α (SIRP-α) on macrophages and this prevents macrophage phagocytosis[260]. c-MYC drives the expression of this molecule which is expressed by virtually all cancers[261]. Inhibition of the CD47-SIRP-α interaction represents a mechanism of engaging anti-tumoral functions of TAMs. Advani *et al.* showed in a phase 1b clinical trial that blocking CD47-SIRP-α interaction using a humanized anti-CD47 antibody (Hu5F9-G4) along with anti-CD20 treatment had significant anti-tumor activity in lymphoma patients[262].

Reprogramming from an alternatively activated to a classically activated macrophage phenotype has been achieved using histidine-rich glycoprotein (HRG)[263]. This effect was associated with down regulation of placental growth factor (PlGF)[263]. EF-022, a modified form of the vitamin D binding receptor, is undergoing early clinical trials, based on evidence that it promotes classically activated repolarization[264]. Other agents that have shown potential to re-polarise TAM to a classically activated phenotype include PI3Kγ and BTK inhibitors[149,150]. In a preclinical model, PDAC treatment with a PI3Kγ inhibitor or a BTK inhibitor reset macrophages toward a classically activated phenotype that promoted $CD8^+$ T-cell cytotoxicity and resulted in reduced tumour growth[150].

1.7 Murine models of HGSOC

In order to develop improved treatments in ovarian cancer, pre-clinical murine models that accurately reflect the genetic, pathological and response to treatment characteristics are required. A diverse range of models have been developed to model ovarian cancer.

Human tumour xenograft models offer advantages of being able to study the effects of mutations or gene expression on human tumour progression, furthermore they allow the validation of therapeutic strategies. A crucial disadvantage is that these models use immunocompromised mice and therefore do not model the effects of immunity within the tumour[265]. Patient derived xenografts (PDX) models faithfully recapitulate the tumour mutational landscape and can be used to study the effects of therapeutic approaches on individual tumours. Again, these models are conducted in immunocompromised mice and therefore the effects of immunity and the full complement of the TME cannot be studied effectively in these models.

The ID8 model is widely used as a syngeneic model of HGSOC[266]. This model was generated by the multiple passage of mouse ovarian surface epithelial cells which underwent malignant transformation in culture. This model offers advantages in producing tumours in mice with an intact immune system. However, whole exome

sequencing has demonstrated that this models lacks any of the mutations implicated in driving HGSOC[267]. ID8 cells are *p53* and *brca-1/2* wildtype and are competent in double stranded DNA break repair[267]. Recently, clustered regularly interspaced short palindromic repeats (CRISPR) editing has been used to engineer ID8 cells that are *p53*$^{-/-}$*Brca1/2*$^{-/-}$; these cells displayed greater sensitivity to both platinum chemotherapy and PARPi[267,268].

More recently genetic engineered murine models (GEMM) have been developed to better reflect the genetic landscape of ovarian cancer. Furthermore, these models offer a number of additional advantages. First, they allow study of early events in tumour development and second, they are fully immunocompetent models and therefore allow study of the effects of the immune system within tumours, essential for studying the TME[265].

As discussed previously, HGSOC is characterised by a complex mutational landscape including frequent mutations in *TP53*, *BRCA1/2* and *RB1* and *PTEN*. Simian virus 40 (SV40) large T antigen binds and inactivates both *p53* and *pRb* and this was used as an early method for inhibiting both of these genes[265]. Expressing SV40 under the control of the promoter for a Müllarian specific gene (MISIIR) produced mice that developed poorly differentiated ovarian carcinomas[269]. This represented the first transgenic model of epithelial ovarian cancer. The major disadvantage of this model was that the mice were infertile and tumours sometimes occurred in new born mice[265].

Flesken-Nikitin *et al.* used cre conditional alleles in combinations with intrabursal injections of a cre-expressing adenovirus to target the mouse ovarian surface epithelium (MOSE)[270]. This approach was used to inactivate *Tp53* and *Rb1* within the MOSE which resulted in poorly differentiated ovarian tumours which metastasised to the lung, liver and contralateral ovary[270]. Mice with both *Rb* and *p53* knockout where much more efficient at producing tumours than single knockouts, although *p53* knockout alone was sufficient to induce tumour formation[265]. Szabova *et al.* further refined these approaches to generate a genetic model of HGSOC[271]. This was achieved by inhibition of *Rb* in concert with *Tp53* aberration (missense mutation or deletion) and inactivation of either *Brca-1* or *2*. This study demonstrated that loss of *Rb* was sufficient for tumourigenesis but additional inactivation of *p53* facilitated peritoneal dissemination and metastasis. Ovarian tumours from these models had a gene expression profile that recapitulates HGSOC[271]. This GEMM model was then used to generate orthotropic immunocompetent transplantable models, demonstrating the ability of this model to generate synchronised cohorts of mice suitable for preclinical study[272]. Using this model these tumours showed

response to single agent and combination treatment with cisplatin and olaparib based on Brca status[272].

In view of the finding of STICs as the likely precursor lesion of HGSOC, Perets *et al.* developed a HGSOC GEMM model that specifically targeted the fallopian tube secretory epithelial (FTE) cells by expression of cre recombinase from a *Pax8* promotor[273]. Using this system *Brca1* or *Brca2* were deleted in combination with *p53* and *Pten*[273]. This approach resulted in the development of fimbrial STIC lesions followed by HGSOC that progressed to an advanced stage with ovarian and peritoneal metastasis[273]. More recently Zhai *et al.* have used the *Ovgp1* promoter to control cre recombinase in the oviductal epithelium, the mouse equivalent to the fallopian tube epithelim[274]. Using this approach inactivation of combinations of *Brca1*, *Tp53*, *Rb1* and *Nf1* resulted in STIC formation and progression to HGSOC[274]. These models closely recapitulate the histological, genetic and biological features of HGSOC and as such are useful tools in understanding the pathogenesis as well as testing new strategies for prevention, detection and treatment of HGSOC[274]. However they have a mixed genetic background and the complex breeding protocols mean they are not suitable for extensive pre-clinical testing of immuno- and other biological therapies that target the TME[275].

1.8 Hypothesis and aims

The effect of chemotherapy on TAMs in HGSOC is incompletely understood. Previous work has shown that chemotherapy may enhance adaptive immune responses within the HGSOC TME, yet effector function may be limited by immunosuppression. TAMs are a major immunosuppressive force in the TME of HGSOC. Therefore, research into the effect chemotherapy has on TAMs in HGSOC may be important in understanding how chemotherapy modifies tumour immunity in this disease. This knowledge may facilitate the development of rational immunotherapies for HGSOC.

I hypothesise that targeting the recruitment, polarisation and effector function of TAMs may improve HGSOC response to chemotherapy as well as having independent anti-cancer activity.

This hypothesis will be investigated with the following objectives:

1. Explore macrophage phenotypes in metastases of human HGSOC and the influence of NACT on their activity, density and location (Chapters 3-5).
2. Explore macrophage phenotypes in mouse models of HGSOC and the influence of chemotherapy on their activity, density and location (Chapters 6, 7).

3. Determine the effects of macrophage-targeting agents on mouse models of HGSOC alone and in combination with chemotherapy (Chapter 8).
4. Explore the links between immunogenic cell death and macrophages after chemotherapy in HGSOC (Chapter 9).

Chapter 2
Materials and Methods

2.1 Buffers, solutions and reagents

Phosphate-buffered saline (PBS) (1x)

KCl 0.2 g/L, KH_2PO_4 0.2 g/L, NaCl 8.0 g/L, Na_2HPO_4-$7H_2O$ 2.16 g/L from Gibco (cat. no. 141-90-094, Gibco).

PBS-tween (PBST)

PBS 1x with the addition of 0.1% v/v Tween20 (cat. no. P7949, Sigma-Aldrich).

Blocking buffer (immunohistochemistry)

2.5% bovine serum albumin (BSA) (cat. no. A4503, Sigma-Aldrich) and 2.5% Goat serum (cat. no. B15-035, PAA) in PBS 1x.

Tris-buffered saline (TBS) (10x)

1.5M NaCl (cat. no. 71380, Sigma-Aldrich) and 200mM Trizma base (cat. no. T1503, Sigma-Aldrich) in deionised H2O, pH 7.6.

TBS-tween (1x)

1:10 dilution of TBS (10x) in deionised H_2O with 0.1% v/v Tween20 (cat. no. P7949, Sigma-Aldrich).

Complete radioimmunoprecipitation assay (RIPA) lysis buffer

RIPA buffer (cat. no. R0278, Sigma-Aldrich) supplemented with one tablet of protease inhibitor cocktail I (cat. no. 11836153001, Roche) per 10ml, and 1:100 phosphatase inhibitor cocktail II (cat. no. P5726, Sigma-Aldrich).

Bicinchoninic acid (BCA) assay reagent

4% (w/v) copper (II) sulphate (cat. no. C2284, Sigma-Aldrich) diluted 1:50 in BCA (cat. no. B9643, Sigma-Aldrich).

3-(N-morpholino)propanesulfonic acid (MOPS) running buffer

50ml NuPAGE® MOPS sodium dodecyl sulphate (SDS) running buffer (20x) (cat. no. NP0001, Thermo Fisher Scientific) in 950ml of deionised H_2O.

Transfer buffer

50ml NuPAGE® transfer buffer (20x) (cat. no. NP0006, Thermo Fisher Scientific) and 200 ml methanol (cat. no. 11976961, Thermo Fisher Scientific) in 750ml of deionised H_2O.

Blocking buffer (western blotting)

5% (w/v) non-fat dry milk (Marvel), in 1x TBST.

Fluorescence-activated cell sorting (FACS) buffer

Dulbecco's phosphate buffered saline (PBS) (cat. no. 141-90-094, Gibco), pH 7.2, 2.5% BSA (cat. no. A4503, Sigma-Aldrich) and 2 mM EDTA (cat. no. AM9262, Ambion).

Methyl green counterstain

0.5% (w/v) methyl green (cat. no. 67060, Sigma-Aldrich) dissolved in 0.1M sodium acetate trihydrate (cat. no. S8625, Sigma-Aldrich) in deionised H_2O, pH 4.6.

2.1.1 Antibodies

Antibody	Clone	Dilution	Company	Cat. No.
CD3 FITC	HIT3a	1:100	Biolegend	300306
CD19 FITC	SJ25C1	1:100	Biolegend	363008
CD20 FITC	2H7	1:100	Biolegend	302304
CD56 FITC	MEM-188	1:100	Biolegend	304604
CD66b FITC	G10F5	1:100	Biolegend	305104
Siglec8 FITC	7C9	1:100	Miltinyi Biotec	130-098-715
HLA-DR BV650	L243	1:100	Biolegend	307650
CD45 PerCP	2D1	1:100	Biolegend	368606
CD14 BV510	M5E2	1:100	Biolegend	301842
CD16 APC-Cy7	B73.1	1:100	Biolegend	360710
CD11c PE-Cy7	3.9	1:100	Biolegend	301608
CD1c A700	L161	1:100	Biolegend	331530
CD123 PE-CF594	7G3	1:100	BD Biosciences	562391
CD141 APC	M80	1:100	Biolegend	344106
CD163 PE	GHI/61	1:100	BD Biosciences	556018
CXCR1 PE	528728	1:100	R&D Systems	FAB5204P
CD206 PE	19.2	1:100	BD Biosciences	555954
CD209 PE	9E9A8	1:100	Biolegend	330106

Table 2.1 Antibodies used for flow cytometry in human samples.

Antibody	Clone	Dilution	Company	Cat. No.
CD45 BV785	30-F11	1:100	Biolegend	103149
CD3 PE-Cy7	145-2C11	1:50	Biolegend	100320
CD4 PE	RM4-4	1:200	Biolegend	116006
CD8 APC	53-6.7	1:200	eBioscience	17-0081-83
CD44 BV650	IM7	1:100	Biolegend	103049
CD62L BV605	MEL-14	1:100	Biolegend	104438
CD69 FITC	H1.2F3	1:100	Biolegend	104506
PD1 e450	RMP1-30	1:40	eBioscience	48-9981-82
CD11b A780	M1/70	1:100	eBioscience	47-0112-82
CD19 Percp5.5	eBio1D3	1:200	eBioscience	45-0193-82
CD11b BV650	M1/70	1:100	Biolegend	101239
Ly6G A700	RB6-8C5	1:200	eBioscience	56-5931-82
Ly6C Percp5.5	HK1.4	1:200	Biolegend	128012
F4/80 PE	BM8	1:100	Biolegend	123110
PDL1 BV421	10F.9G2	1:80	Biolegend	124315
MHCII APC/CY7	M5/114.15.2	1:200	Biolegend	107628
CD206 FITC	C068C2	1:100	Biolegend	141704
CD80 APC	16-10A1	1:100	eBioscience	17-0801-82
CD86 BV605	GL-1	1:100	Biolegend	105037

Table 2.2 Antibodies used for flow cytometry in mouse samples.

Antibody	Clone	Dilution	Company	Cat. No.
CD3 FITC	HIT3a	1:100	Biolegend	300306
CD19 FITC	SJ25C1	1:100	Biolegend	363008
CD20 FITC	2H7	1:100	Biolegend	302304
CD56 FITC	MEM-188	1:100	Biolegend	304604
CD66b FITC	G10F5	1:100	Biolegend	305104
Siglec8 FITC	7C9	1:100	Miltinyi Biotec	130-098-715
HLA-DR BV650	L243	1:100	Biolegend	307650
CD45 PerCP	2D1	1:100	Biolegend	368606
CD14 BV510	M5E2	1:100	Biolegend	301842

Table 2.3 Antibodies used for flow sorting of human samples.

Protein	Dilution	Species	Cat. no.	Company
CD68	1:8000	Mouse	M0814	Dako
TREML4	1:1100	Rabbit	ab204798	Abcam
PAX-8	1:400	Rabbit	NBP1-32440	Novus
Cleaved caspase-3	1:100	Rabbit	9664S	Cell Signalling
F4/80	1:100	Rat	MCA497	BioRad
CD206	1:100	Rat	MCA2235	BioRad
Rabbit IgG1 isotype control	Primary antibody dependent	Rabbit	AB-105-C	R&D Systems
Mouse IgG1 isotype control	Primary antibody dependent	Mouse	X0931	Dako
Rat IgG1 isotype control	Primary antibody dependent	Rat	14-4031-81	eBioscience

Table 2.4 Antibodies used for immunohistochemistry.

Antibody	Dilution	Species	Cat. no.	Company
NLRP3	1:100	Rabbit	bs-10021R	Bioss Antibodies
CD68	1:1000	Mouse	M0814	Dako
Anti-rabbit Alexa Fluor 488	1:1000	Goat	A11008	Life Technologies
Anti-mouse Alexa Fluor 568	1:1000	Goat	A21050	Life Technologies

Table 2.5 Antibodies used for immunofluorescence.

Antibody	Expected size [kDa]	Dilution	Species	Cat. no.	Company
β-actin	46	1:2000	Mouse	A1978	Sigma-Aldrich
Cleaved caspase-3	17, 19	1:1000	Rabbit	9664S	Cell Signalling
DFNA5	55	1:1000	Rabbit	ab215191	Abcam
Secondary anti-mouse	-	1:2000	Sheep	NXA931	GE Healthcare
Secondary anti-rabbit	-	1:2000	Donkey	NA9340V	GE Healthcare

Table 2.6 Antibodies used for western blotting.

Antibody	Dilution	Species	Cat. no.	Company
NLRP3	1:50	Mouse	AG-20B-0014-C100	AdipoGen
ASC	1:50	Rabbit	AG-25B-0006-C100	AdipoGen

Table 2.7 Antibodies used for proximity ligation assay.

2.2 Patients and samples

Institutional review board approval was granted for the Barts Gynae Tissue Bank to collect and store biological material and clinical information. Patients were treated at St. Bartholomew's Cancer Centre and St. George's Hospital (London, UK) between 2010 and 2019 and gave written informed consent (REC reference: 15/EE/0151).

2.3 Histology and Immunostaining

2.3.1 Single stain immunohistochemistry (IHC)

For immunohistochemical analysis, human tissue samples were fixed in 10% formalin solution (cat. no. HT501128, Sigma-Aldrich) for 24 - 72 hours in PBS at room temperature, dehydrated in 70% ethanol (cat. no. E/0650DF/17, Fisher Scientific) in H_2O, embedded in paraffin wax and sectioned by the Pathology Department, Barts Cancer Institute.

Paraffin embedded sections were cleared in two changes of xylene (cat. no. X/0100/17, Fisher Scientific) for 5 minutes, rehydrated through decreasing series of ethanol solutions (100%, 90%, 70% and 50% ethanol in H_2O) for 2 minutes each and rehydrated in H_2O for 3 minutes. Citrate-based Antigen unmasking solution (cat. no. H-3300, Vector Laboratories) was preheated to 100°C in a microwave and the slides were placed into the antigen retrieval buffer. The temperature of the antigen retrieval buffer was maintained at 100°C for 20 minutes using the microwave on a 'medium' power setting. Afterwards the slides were cooled down for 5 minutes with tap water and washed by submersion in 1x PBS. Sections were blocked for endogenous horseradish peroxidase (HRP) activity using 0.3% hydrogen peroxide (cat. no. H/1800/15, Fisher Scientific) in methanol (cat. no. M/4000/PB17, Fisher Scientific) for 10 minutes. Following submersion in 1x PBST for 5 minutes. Tissue sections were delimited using a hydrophobic pen (PAP pen, cat. no. H-4000, Vector Laboratories). Tissue sections were blocked with blocking buffer for 60 minutes at room temperature. The blocking buffer was then removed and primary antibody was applied diluted in blocking buffer (volume 100-250 µl depending on the size of the section). Primary antibodies were applied 60 minutes at room

temperature.

After three washes for 3 minutes each in 1x PBST, sections were incubated with an appropriate HRP conjugated secondary antibody Vector Impact Kit (H-4343, MP-63636, Vector Laboratories). Sections were then was three times for 3 minutes each in 1x PBST before addition of DAB chromogen followed by washing with tap water to stop further DAB development. Counterstaining was performed with haematoxylin (cat. no. GHS116, Sigma-Aldrich) for 20 seconds to obtain clear blue nuclear staining. Subsequently the sections were dehydrated briefly (7 dips) in 70% ethanol followed by 90% and 100% ethanol incubations for 1 minute followed by two xylene incubations for two minutes each. Sections were mounted in DPX resin (cat. no. 06522, Sigma-Aldrich) using 100 x 50 mm coverslips and left to dry over-night at room temperature prior to microscopic examination.

2.3.2 Staining of TMAs

HGSOC biopsy sections obtained from patients following neo-adjuvant chemotherapy and contained within a tissue microarray (TMA) were stained with anti-CD68 antibody (clone KP1, cat. no. M0814, Dako). Briefly, 4 µm sections were de-paraffinised and rehydrated, antigen retrieval was performed in a pressure cooker using citrate-based antigen unmasking solution (cat. no: H-3300, Vector Laboratories) followed by staining using an autostainer (Dako) using an ultrasensitive HRP Polymer Kit (Biogenex).

2.3.3 Pax-8/CD68 dual colour IHC

Paraffin embedded sections were cleared in two changes of xylene (cat. no. X/0100/17, Fisher Scientific) for 5 minutes, rehydrated through decreasing series of ethanol solutions (100%, 90%, 70% and 50% ethanol in H_2O) for 2 minutes each and rehydrated in H_2O for 3 minutes. Antigen unmasking solution (cat. no. H-3300, Vector Laboratories) was preheated to 100°C in a microwave and the slides were placed into the antigen retrieval buffer. The temperature of the antigen retrieval buffer was maintained at 100°C for 20 minutes using the microwave on a 'medium' power setting. Afterwards the slides were cooled down for 5 minutes with tap water and washed by submersion in 1x PBS. Sections were blocked for endogenous horseradish peroxidase (HRP) activity using 0.3% hydrogen peroxide (cat. no. H/1800/15, Fisher Scientific) in methanol (cat. no. M/4000/PB17, Fisher Scientific) for 10 minutes. Following submersion in 1x PBST for 5 minutes. Tissue sections were delimited using a hydrophobic pen (PAPpen, cat. no. H-4000, Vector Laboratories). Tissue sections were incubated with IHC blocking buffer for 60 minutes at room temperature. The blocking buffer was then removed and anti-CD68 antibody (Table 2.4) was applied diluted in IHC blocking buffer (volume 100-250 µl

depending on the size of the section) for 60 minutes at room temperature.

After three washes for 3 minutes each in 1x PBST, sections were incubated with ImmPRESS® HRP Anti-Mouse IgG (Peroxidase) Polymer Detection Kit (cat. no. MP-7402, Vector Laboratories) for 30 minutes at room temperature in accordance with the manufacture's instructions. Sections were then was three times for 5 minutes each in 1x PBST. Staining was revealed using the Liquid Dab+ Substrate Chromogen system (cat. no. K3468, Dako). Slides were the washed with tap water to stop colour development.

Slides were was washed by submersion in 1x PBS. Sections were blocked for horseradish peroxidase (HRP) activity using 0.3% hydrogen peroxide (cat. no. H/1800/15, Fisher Scientific) in methanol (cat. no. M/4000/PB17, Fisher Scientific) for 10 minutes. Following submersion in 1x PBST for 5 minutes. Tissue sections were incubated with IHC blocking buffer for 40 minutes at room temperature. The blocking buffer was then removed and anti-PAX-8 antibody (Table 2.4) was applied diluted in IHC blocking buffer (volume 100-250 µl depending on the size of the section) for 60 minutes at room temperature. After three washes for 3 minutes each in 1x PBST, sections were incubated with ImmPRESS® HRP Anti-Rabbit IgG (Peroxidase) Polymer Detection Kit (cat. no. MP-7415, Vector Laboratories) for 30 minutes at room temperature in accordance with the manufacture's instructions. Sections were then was three times for 5 minutes each in 1x PBST. Staining was revealed using the VIP Peroxidase (HRP) Substrate Kit (cat. no. SK-4600, Vector Laboratories). Slides were the washed with tap water to stop colour development.

Counterstaining was performed with methyl green applied for 10 minutes at 60°C. Subsequently the sections were dehydrated briefly (7 dips) in 70% ethanol followed by 90% and 100% ethanol incubations for 1 minute followed by two xylene incubations for two minutes each. Sections were mounted in DPX resin (cat. no. 06522, Sigma-Aldrich) using 100 x 50 mm coverslips and left to dry over-night at room temperature prior to microscopic examination.

2.3.4 Mouse Immunohistochemistry

Omental biopsy sections were fixed for 24 – 72 hours in 4% PFA and transferred to 70% ethanol prior to paraffin embedding. 4µm sections were cut by microtome in the Bart's Cancer Institute Pathology Department. Briefly, sections were de-paraffinised and rehydrated through an alcohol series, proteinase K (cat. no. P2308 Sigma-Aldrich) antigen retrieval was performed in $CaCl_2$ buffer at 37°C for 20 minutes. Endogenous peroxidase blocking was performed in 0.3% hydrogen peroxide in methanol for 20

minutes. Slides were incubated in IHC blocking buffer for 60 minutes at room temperature. Slides were then incubated with primary antbody (Table 2.4) followed by incubation with Impress anti-Rat IgG kit (cat. no: MP-7444, Vector Laboratories). Staining was revealed using the Liquid Dab+ Substrate Chromogen system (cat. no. K3468, Dako) followed by washing with tap water to stop further DAB development. Counterstaining was performed with haematoxylin (cat. no. GHS116, Sigma-Aldrich) for 20 seconds to obtain clear blue nuclear staining. Subsequently the sections were dehydrated briefly (7 dips) in 70% ethanol followed by 90% and 100% ethanol incubations for 1 minute followed by two xylene (cat. no. X/0100/17, Fisher Scientific) incubations for two minutes each. Sections were mounted in DPX resin (cat. no. 06522, Sigma-Aldrich) using 100 x 50 mm coverslips and left to dry over-night at room temperature prior to microscopic examination.

2.3.5 Haematoxylin and eosin (H&E)

Sections were stained with H&E by the Pathology department of the Barts Cancer Institute.

2.3.6 Digital quantification of IHC and H&E staining

Immunohistochemistry and H&E sections were imaged using the Panoramic digital slide scanner (3DHISTECH). Definiens® digital image analysis was used to quantify staining and determine location within tumour islands and stromal areas. Scanned images were imported into a Definiens® workspace. The entire tissue area sample or TMA core was selected manually. Within the tissue area 'regions of interest' (tumour and stroma areas) were selected using the built-in automated algorithms within the Definiens® software. The software-determined tumour and stromal separation for the entire tissue sample was reviewed (with the oversight of Consultant Gynaecological Pathologist, Dr. Jacqueline McDermott) prior to proceeding to analysis of the straining characteristics within the tumour and stromal areas of the biopsy.

2.4 Mouse models

FVB-NCrl and C57BL/6 wild type mice (aged 8-9 weeks) were purchased from Charles River Laboratories and were acclimatised for 1 week prior to the initiation of the studies. Mice were housed under sterile conditions in individually ventilated cages, a maximum of five per cage, fed with standard chow diet and water *ad libitum*, and maintained on an automatic 12 hour light cycle at 22–24°C. All studies were conducted using sterile techniques in accordance with the guidelines of the Animal Care Committee and the Procedures Project License (70/7411 and PBE3719B3).

60577, 30200 or HGS2 cells were grown in mouse cell line media (as below) [271,272]. At the commencement of the experiment mice received $1x10^7$ cells injected i.p. in 300µL PBS.

2.4.1 Chemotherapy treatment

Carboplatin (Hospira) and paclitaxel (Hospira) were obtained from the pharmacy at St. Bartholomew's Hospital, London, were dissolved in 0.9% NaCl, and were administered to mice i.p. in 300µL volume. Mice were treated with carboplatin 20mg/kg, paclitaxel 10mg/kg or the combination of carboplatin 20mg/kg + paclitaxel 10mg/kg, based on average weight of all mice in the experiment. Vehicle-treated controls were treated in an identical manner to chemotherapy treated mice and received either 0.9%Nacl or cremophor (cat. no. C5135, Sigma-Aldrich) / ethanol (cat. no. 51976, Sigma-Aldrich) (1:1) dissolved in 0.9%NaCl.

2.4.2 CSF-1Ri treatment

AZD7507 was obtained from AstraZeneca. AZD was dissolved in 0.5% (w/v) methyl cellulose (cat. no. M7027, Sigma-Aldrich) and 0.1% (v/v) Tween-80 (cat. no. P4780, Sigma-Aldrich) in deionised H_2O and administered to mice at 100mg/kg twice daily by oral gavage, based on an average weight of all mice in the experiment. Treatment was administered to mice on weekdays, on weekends no treatment was given. BLZ945 (cat. no. HY-12768, MedChemTronica) was dissolved in 10% sulfobutylether-β-cyclodextrin (cat. no. HY-17031, MedChemTronica) in deionised H_2O and administered to mice at 200mg/kg once daily by oral gavage. Treatment was administered to mice on weekdays, on weekends no treatment was given.

2.4.3 Survival end point determination

Mice were assessed daily and weighed twice weekly. Assessment of survival endpoint was based on 'moderate' severity as per the project license. The survival endpoint for mice was defined as a change in general health, specifically 15% body weight loss over 72 hours or 20% over any time period, or inability to ambulate, or hunched posture, or difficulty breathing or signs of hypothermia as well as signs of ascites or palpable tumours exceeding an estimated size of 1cm diameter. In survival experiments assessment of mice was made twice daily by the same individual to limit interobserver variability. Furthermore, in the majority of cases survival determinations were made by a trained animal technician who was not directly involved in the experimental design.

2.5 Flow cytometry

2.5.1 Human stromal vascular fraction extraction

Human omental biopsy specimens were received directly from the operating theatre from patients undergoing primary surgery or interval debulking surgery for confirmed or presumed HGSOC. Samples were processed as rapidly as possible and generally processing was completed within 5-7 hours from sample resection. Omental samples were treated enzymatically and mechanically to obtain a stromal vascular fraction (SVF). Samples were dissected into small pieces using a scalpel, incubated with collagenase D from *Clostridium histolyticum* 1mg/mL (cat. no. 11088866001, Roche) and DNAse I from bovine pancreas 25mg/mL (cat. no. D4513, Sigma-Aldrich) in 5% FBS RPMI (cat. no. R8758, Sigma-Aldrich) media for 30 minutes under agitation. The solution was then filtered through a 70µm strainer (cat. no. 352350, Falcon), followed by red blood cell lysis (cat. no. 555899, BD Biosciences) diluted 1:10 in water for 5 minutes, followed by washing with 5% FBS RPMI. The resulting cell suspension was stained with a panel of antibodies for flow cytometry analysis.

2.5.2 Human immunostaining for flow cytometry

SVF obtained from human samples were stained in FACS buffer for 30 minutes at 4°C in a V-bottomed 96-well plate (cat. no. 2605, Thermo Fisher). Cells were stained using the antibodies at the concentrations listed in Table 2.1. Cells were washed three times with 100µl PBS 1x and subsequently stained with FVD_{450nm} or DAPI (cat. no. 65-0863-14, eBioscience) at a dilution of 1:2000 (stock concentration: 5 mg/ml) in 50 µl PBS for 25 minutes at 4°C. After three washing steps with FACS buffer, the cells were fixed by adding 2% formalin (cat. no. HT501128, Sigma-Aldrich) in 1.25% BSA and 1mM EDTA in 1x PBS for 10 minutes at 4°C. After the fixation the cells were washed three times, centrifuged and transferred in a total volume of 100µl FACS buffer and analysed with on a LSR Fortessa II flow cytometer (BD Biosciences). Compensation was performed on DIVA software using One Comp eBeads (cat. no. 01-1111-42, eBiosciences) with the exception for FVD_{450nm}, which was compensated using the ArC^{TM} Amine Reactive Compensation Bead kit (cat. no. A10346, ThermoFisher Scientific). The results were analysed using FlowJo v10.2 (Treestar Inc.) with tSNE plugins installed.

2.5.3 Cell sorting of human samples

SVF obtained from human samples or human stained in FACS buffer for 30 minutes at 4°C. Cells were stained using the antibodies at the concentrations listed in Table 2.3. Cells were then stained with DAPI (cat. no. 422801, Biolegend) 1:2000 (stock concentration: 5 mg/ml) immediately prior to sorting. FITC-HLA-DR^{+}CD14^{+} cells were

then sorted using a FACSAria II cell sorter (BD Bioscience). Cells were sorted into 5% FBS RPMI 1640 media (cat. no. 21875-034, Gibco) maintained at 4°C. 0.25-2x10^6 cells were sorted per sample. A purity check was performed following sorting completion. Cell purities of >96% were obtained. Cells were them centrifuged at 1500rpm for 10 minutes at 4°C. Cells were then lysed in RLT buffer (cat. no. 1015750, Qiagen) supplemented with 1% β-mecaptoethanol (cat. no. M-6250, Sigma-Aldrich). The cell lysate was snap frozen on dry ice and stored at -80°C prior to RNA extraction.

2.5.4 Mouse stromal vascular fraction extraction

Mice were culled by cervical dislocation. A laparotomy was performed and the mouse greater omentum was dissected in its entirety from surrounding structures and placed in PBS at 4°C. Omenta were weighed using a AM100 analytical balance (Mettler). A 2-3mm biopsy of each resected omentum was taken at the centre and fixed in 4% PFA. The sample for digestion was then re-weighed. This sample was cut into pieces approximately 1 mm^2 and digested in Hanks Balanced Salt Solution (cat no. 9374543, Gibco) supplemented with Collagenase from *Clostridium histolyticum* (Sigma, cat. no. C9263) and DNAase I from bovine pancreas for 20 minutes on an rotational platform at 140rpm at 37°C. The resulting digest was then passed through a 70µm cell strainer and flushed with FACS buffer. The resulting cell suspension was centrifuged at 1500rpm for 10 minutes. Cells were then resuspended in FACS buffer and concentration and viability assayed using a Vi-CELL Analyser (Beckman Coulter).

2.5.5 Mouse immunostaining for flow cytometry

SVF obtained from murine omenta were stained in FACS buffer for 30 minutes at 4°C. Cells were stained using the antibodies at the concentrations listed in Table 2.2. Cells were then washed 3 times in PBS 1x and stained separately with FVD_{506nm} (cat. no. 65-0866-14, eBiosciences,) for 20 minutes in 100µL PBS at 4°C. Cells were then washed once in FACS buffer and were then fixed in 2% PFA in PBS containing 1.25% BSA and 1nM EDTA for 10 minutes at 4°C. After the fixation the cells were washed three times, centrifuged and transferred in a total volume of 100µl FACS buffer and analysed with on a LSR Fortessa II flow cytometer (BD Biosciences). Appropriate fluorescence minus one controls were used. Data analysis was performed in FlowJo v10.2 (Treestar Inc.) with tSNE plugins installed.

2.5.6 Cell sorting of murine samples

SVF obtained from murine tumour samples were stained in FACS buffer for 30 minutes at 4°C. Cells were stained using the antibodies at the concentrations listed in Table 2.2. Cells were then stained with DAPI (cat. no. 422801, Biolegend) 1:2000 (stock

concentration: 5 mg/ml) immediately prior to sorting. FITC-HLA-DR^{+}CD14^{+} cells were then sorted using a FACSAria II cell sorter (BD Bioscience). Cells were sorted into 5% FBS RPMI 1640 media (cat. no. 21875-034, Gibco) maintained at 4°C. 0.25-2x10^{6} cells were sorted per sample. A purity check was performed following sorting completion. Cell purities of >96% were obtained. Cells were them centrifuged at 1500rpm for 10 minutes at 4°C. Cells were then lysed in RLT buffer (cat. no. 1015750, Qiagen) supplemented with 1% β-mecaptoethanol (cat. no: M-6250, Sigma-Aldrich). The cell lysate was snap frozen on dry ice and stored at -80°C prior to RNA extraction.

2.5.7 t-distributed stochastic neighbour embedding (tSNE) analysis

tSNE analysis was performed using FlowJo v10.2 (Treestar Inc.). 2,500 CD45^{+} events for each sample were selected using the FlowJo downsample plugin. FACS data relating to an entire murine experiment were concatenated into a single .fcs data file. Within a FlowJo workspace dimensionality reduction was performed using the tSNE algorithm. The resulting tSNE plots were analysed using FlowJo v10.2 (Treestar Inc.).

2.6 RNA extraction

RNA was extracted from the FACS-sorted TAM population using the micro RNAEasy kit (cat. no. 74004, Qiagen) utilizing the on column DNAse digestion step as per the manufactures recommended protocol. RNA was eluted in 12µl volume. Purity and integrity was assessed using Nanodrop and RNA NanoChip (cat. no. 5067-1511, Agilent) and RIN (RNA integrity number) values were ≥8.60.

2.7 RNA sequencing

RNA Sequencing was carried out at the Wellcome Trust Centre for Human Genetics. Library preparation was with RNA-Seq Ribozero and sequencing was performed with HiSeq4000, 150bp read-length, paired-end, strand specific and a coverage of approximately 40 million reads per sample. Raw reads were aligned to the reference genome GRCh37 (hg19). The number of reads aligned to the exonic region of each gene were counted using htseq-count based on the Ensembl annotation. Only genes that achieved at least one read count per million reads (CPM) in at least 25% of the samples were kept. This led to 17,184 filtered genes in total, 13,259 of which were protein-coding genes. Conditional quantile normalisation (cqn) was performed counting for gene length and GC content and a log2 transformed RPKM expression matrix was generated. Differential expression analysis was performed using the edgeR R package. The generalized linear model (GLM) approach was used for the differential analysis. All bioinformatics and graphical analysis of the data was performed by Dr. Eleni Maniati in the statistical programming language R (version 3.1.3).

2.8 Cell lines and culture conditions

2.8.1 Human cell line culture

Human cell lines
G164
G33
AOCS1

Table 2.8 Human cell lines

Table 2.8 shows the human cell lines used in this project. Cells were grown in DMEM/F12 with Glutamax (cat.no 31331-093, Gibco) supplemented with 4% human serum (cat. no. H4522, Sigma-Aldrich) and 100ug/ml pen/strep (cat. no. 15140-122, Gibco) (G164) or 10% FBS (cat. no. SV30160.03, lot. no. RXL35906, HyClone) and 100ug/ml pen/strep (cat. no. 15140-122, Gibco) and ITS (cat. no. 51300-044, Gibco) (G33, AOCS1) on non-precoated tissue culture plastic. When splitting cells 0.5% trypsin-EDTA (cat. no. 15400-054, Gibco) diluted 1:10 in PBS was used.

2.8.2 Murine cell line culture

Mouse cell lines
30200
60577
HGS2

Table 2.9 Murine cell lines.

Two mouse HGSOC cell lines (30200 and 60577) were obtained in collaboration with the National Cancer Institute, USA[271,272]. Both mouse cell lines are *Rb*, *p53* and *Brca-1* deficient and therefore accurately recapitulate the genetic lesions of HGSOC[271,272]. HGS2 cell line was derived from the fallopian tube and ovary of a doxycycline-induced mouse from a GEMM[276] where *Pax8*-Cre drives inducible inactivation of *Brca2*, *Trp53,* and *Pten* (*Brca2*$^{-/-}$;*Trp53*$^{-/-}$;*Pten*$^{-/-}$) in the fallopian tube. Mouse cell lines were cultured in DMEM/F12 with Glutamax (cat. no. 31331-028, Gibco) supplemented with insulin, transferrin, sodium selenite, sodium pyruvate, hydrocortisone, EGF from murine submaxillary gland, FBS, penicillin, streptomycin and amphotericin B at the concentrations outlines in Table 2.10. Cells were grown at 37°C 5% CO_2 on non-precoated tissue culture plastic. When splitting cells 0.5% trypsin-EDTA (cat. no. 15400-054, Gibco) diluted 1:10 in PBS was used and inactivated with DMEM/F12 with Glutamax (cat. no. 31331-028, Gibco).

Supplement	Concentration	Catalogue number	Company
Fetal bovine serum	4% (v/v)	SV30160.03 Lot No: RXL35906	HyClone
Insulin	10ug/ml	51300-044	Gibco
transferrin	5.5ug/ml	51300-044	Gibco
sodium selenite	6.7ng/ml	51300-044	Gibco
sodium pyruvate	110ug/ml	51300-044	Gibco
hydrocortisone	0.5ug/ml	H0135	Sigma
Murine epidermal growth factor	0.2µg/ml	E4127	Sigma
Penicillin	200units/ml	15240-062, P4333	Gibco, Sigma
Streptomycin	200µg/ml	15240-062, P4333	Gibco, Sigma
Amphotericin B	0.25µg/ml	15240-062, P4333	Gibco, Sigma

Table 2.10 Supplements required for mouse cell line culture

Routine testing for mycoplasma contamination using the MycoAlert PLUS Mycoplasma Detection Kit (cat. no. LT07-710, Lonza) has been consistently negative.

2.8.3 Freezing and recovery of cell lines

Cells were frozen in 1ml 10% of dimethyl sulfoxide (DMSO) (cat. no. D2650, Sigma-Aldrich) in fetal bovine serum (cat. no. SV30160.03, lot. no. RXL35906, HyClone). Cells were stored at -80°C over-night prior to long-term storage in liquid nitrogen at -196°C. Cells were recovered from liquid nitrogen by thawing at 37°C prior to addition to 10ml DMEM/F12 medium with appropriate supplements. Cells were collected by centrifugation at 1400rpm for five minutes, re-suspended in DMEM/F12 medium with appropriate and added to a T75 culture flask (cat. no. CLS430641, Corning, Sigma-Aldrich).

2.9 *In vitro* cell viability assay

Cells were plated into 6 well plates at a density of $1x10^5$ cells/well. Media was replaced with media alone or media containing variable concentrations of carboplatin (Hospira) or paclitaxel (Hospira) obtained from St. Bartholomew's Hospital pharmacy. Cells were incubated with media supplemented with chemotherapeutic agent for 48 hours. The media was then aspirated and cells were fixed and stained in 70% ethanol (cat. no. 51976, Sigma-Aldrich) + 0.5% crystal violet (cat. no. C0775, Sigma-Aldrich). Plates were washed and air-dried. The resulting crystal violet staining was dissolved in 10% acetic acid (cat. no. W200603, Sigma-Aldrich) and transferred to an optically clear 96 well plate (cat. no. 3690, Costar). The optical density at 595nm (OD_{595}) was quantified using a plate

reader (Dynex Technologies).

OD_{595} measurements for each concertation of chemotherapeutic agent were normalised to the media only control and plotter in Prism v7.0 and curves were fitted using the 'log(agonist) *vs* response - variable slope' equation.

2.10 Terminal deoxynucleotide transferase dUTP nick end labelling (TUNEL) Assay

The Novus Biologicals APO-BRDU-IHC reagent kit (cat no. NBP2-31164, Novus Biologicals) was used in accordance with the manufacturer's instructions following the staining protocol for paraffin embedded tissue. 4µm sections of FFPE tissue were cut by the Bart's Cancer Institute Pathology Department. Kit positive control in addition to a tissue positive control section, produced by incubation of sections for 30 mins with 1ug/ml DNAse in 1xPBS + 1mM $MgSO_4$, were stained within the experiment. Sections were de-paraffinised in xylene (cat. no. X/0100/17, Fisher Scientific) and rehydrated through an ethanol (cat. no. E/0650DF/17, Fisher Scientific) series (100%, 90%, 80%, 70%) and washed in PBS. Slides were then incubated with proteinase K solution for 20mins at RT. Slides were then washed in PBS followed by endogenous peroxidase blocking by incubating slides with 3% hydrogen peroxide in methanol for 5 minutes at toom temperature followed by washing in PBS. Slides where then equilibrated in reaction buffer followed by addition of labelling reaction (reaction buffer, TdT enzyme, Br-dUTP and distilled water), the sections were then incubated in a humidified chamber for 1.5 hours at 37˚C. The slides were then washed in 1x PBS followed by incubation with Blocking buffer for 10mins at room temperature. Following this, slides were incubated with biotinylated BrDU antibody for 1.5 hours at room temperature. The slides were washed in PBS followed by incubation with 1x conjugate solution for 30 minutes at room temperature. After washing in PBS the slides were incubated with DAB for 15 minutes, slides were washed in water followed by counterstaining with methyl green. Slides were then cover slipped using permanent mountant (cat. no. 06522, Sigma-Aldrich). Sections were then imaged on an Axiophot microscope (Zeiss).

2.11 Cytokines MSD V PLEX Assay

Lysates were analysed on a V-PLEX Proinflammatory panel 1 (human) kit (cat. no. K15049, Mesoscale), according to manufacturer's instructions. Briefly, the plate was washed three times with Wash buffer, 50 µl of sample and the calibration curve were added and incubated for two hours. The plate washed again three times with Wash buffer, then the detection antibody was added and incubated for two hours. Following three washes with Wash buffer, 150 µl of 2X Read buffer were added, and the plate was

analysed on MDS QuickPlex SQ 120 (Mesoscale).

2.12 Proximity ligation assay (PLA)

The PLA assay was performed using the Duolink PLA Fluorescence kit (cat. nos. DUO92002, DUO92004, DUO92014, Sigma-Aldrich) Cells were grown on 13mm glass coverslips (VWR). Prior to starting the PLA assay cells were fixed in 10% formal saline (cat. no. HT501128, Sigma-Aldrich) for 10 minutes at toom temperature. The cells were then washed three times in PBS at room temperature and stored in PBS at 4C. Cells were permeabilised in 0.5% Triton-X100 (cat. no. T8787, Sigma-Aldrich.) in PBS (cat. no. D8537, Sigma-Aldrich) for 10 minutes at room temperature. Cells were then washed blocked in 5% BSA (A4503, Sigma-Aldrich) in PBS for 60 minutes at room temperature. Following this, cells were incubated with primary antibodies (see table 2.7) overnight at 4°C. Cells were then washed three time in 0.1% Triton-X100 in PBS for 10 minutes each wash. The cells were then incubated with PLA probes (DUO92002, DUO92004, Sigma-Aldrich) for 60 minutes at room temperature. The cells were then washed three times with 0.1% triton x-100 for five minutes each. The ligation reaction was then applied to the cell and the cells were incubated at 37°C in a humidity chamber for 30 minutes. Following this the cells were washed twice in 0.1% triton X100 for 3 minutes each. The polymerisation reaction was then applied to the cells and the cells were incubated at 37°C in a humidity chamber for 100 minutes in the dark. The cells were then washed three times in 0.1% Triton X-100 for 5 minutes each wash. Cells were then stained with 1µg/ml DAPI (cat. no. 40043, Biotium) applied to cells for 3 minutes followed by three five-minute washes in PBS. The coverslips were then mounted on Polysine glass slides (cat. no. 631-0107, VWR) using FluorSave reagent (cat. no. 345789, Calbiochem). Slides were stored at 4°C in the dark. Cells were imaged the next day on a LSM 710 confocal microscope. Approximately 30 cells were images using 63x objective under oil immersion. LSM files were exported and analysed in Fiji v1.2 software.

2.12.1 Quantification of PLA signals

LSM files were opened in Fiji v1.2. Regions of interest were drawn manually around each cell based on the position of the nucleus and the green fluoresces within the cell. Within the green channel of the image the “find maxima” process was used to isolate the green specs individual points. For each ROI the number of maxima points was counted by the software and manually recorded. The sample settings were used across all samples in the analysis.

2.13 Leucocyte cone monocyte isolation

Human blood from anonymous healthy donors were obtained from leucocyte cones from the NHS Blood and Transplant service. Leucocyte cones contain leukocytes that are collected as a by-product from individuals donating platelets via apheresis. To isolate peripheral blood mononucleated cells (PBMCs), blood was diluted 1:10 with PBS (cat. no. D8537, Sigma Aldrich) and a total volume of 25ml of diluted blood was overlaid onto 15ml Ficoll-Paque PLUS (cat. no. 17-1440-03 AG, GE Healthcare) at room temperature. The samples were centrifuged at 2600rpm for 20 minutes at room temperature without braking. PBMCs located at the interface of the Ficoll and the plasma were collected and centrifuged at 300g for 10 minutes with interim washes with PBS for three times. The cells were counted and an appropriate volume (20µl beads per 10^7 cells) of $CD14^+$ beads (cat. no. 130-050-201, Miltenyi) was added to the cells and incubated for 15 minutes at 4°C. According to the manufacturer's instructions, $CD14^+$ monocytes were isolated from PBMCs by labelling with CD14 microbeads (cat. no. 130-050-201, Miltenyi) and magnetic isolation on LS columns (cat. no. 130-042-401, Miltenyi). Subsequently the cells were seeded onto 6-well plates at a seeding density of 1.5 million per well in RPMI-1640 (cat. no. 31870-074, Invitrogen) supplemented with 10% foetal calf serum (FCS) cat. no. SV30160.03, lot. no. RXL35906, HyClone), 100 µg/ml penicillin/streptomycin (pen/strep) (cat. no. 15140-122, Gibco) and 100 ng/ml recombinant human (rh) macrophage colony stimulating factor (MCSF) 1 (cat. no. 574806, Biolegend). Monocytes were differentiated to macrophages for seven days and cell surface marker expression was assessed by flow cytometry to check for $CD14^+$ cell purity. For macrophage re-plating, the cells were washed with PBS and incubated with cell dissociation buffer (cat. no. 13151014, Gibco) for 15 minutes at 37°C. For complete detachment the cells were scraped of the tissue culture plastic using a cell scraper (cat. no. 353085, Falcon) and washed twice with PBS before reseeding at the desired cell concentration or staining for flow cytometry analysis.

2.13.1 Monocyte differentiation and polarisation

Differentiated macrophages (monocytes incubated for seven days in 100 ng/ml rhMCSF [cat. no. 574806, Biolegend]), were treated with various recombinant human cytokines to polarise them towards a pro- or anti-inflammatory phenotype. The cytokine concentrations used are listed in Table 2.11.

Cytokine	Concentration	Cat. no.	Company
IL-4	20ng/ml	200-04	Peprotech
IL-10	20ng/ml	200-10	Peprotech
IFNγ	10ng/ml	300-02	Peprotech
LPS	100ng/ml	L2630	Sigma Aldrich

Table 2.11 Recombinant human cytokines used for macrophage polarisation.

During all culture conditions 100ng/ml rhMCSF was added to the medium. The cells were stimulated for 72 hours. Cells were then detached for flow cytometric analysis or for protein lysates and medium was kept for MSD analysis (stored at -20°C).

2.14 Protein detection

2.14.1 Protein extraction

Cells were washed with cold PBS (cat. no. D8537, Sigma-Aldrich) and lysed with a RIPA cell lysis buffer (cat. no. R0278, Sigma-Alrich) containing 1:10 complete mini EDTA protease inhibitor (cat. no. 11836153001, Roche) and 1:100 phosphatase inhibitor cocktail (cat. no. P5726, Sigma-Alrich). Adherent cells were detached using a cell scraper (cat. no. 353085, Falcon) and the cell lysate was centrifuged at 4°C for 10 minutes at 13200 rpm. The protein supernatant was collected and the concentration was calculated using the BCA assay (see paragraph 2.14.2).

2.14.2 Bicinchroninic acid (BCA) assay

Protein standard concentrations were prepared using BSA (cat. no. A4503, Sigma-Aldrich) at a concentration of 0, 0.2, 0.4, 0.6, 0.8 and 1.0µg/µl. 10µl of each standard is measured in duplicates in a 96-well plate (cat. no.3599, Costar). The protein samples were diluted 1:5 and were measured in triplicates. 4% (w/v) copper (II) sulphate solution (cat. no. C2284, Sigma-Aldrich) was added to bicinchroninic acid (cat. no. B9643, Sigma-Aldrich) at a ratio of 1:50 and 200µl was added to each condition. The plate was incubated for 30 minutes at 37°C. Subsequently the absorbance was measured at 595nm using the Opsys MR plate reader (Dynex technology) and the Revelation Quicklink software.

2.14.3 Western blotting

Western blotting was performed using 10-well or 15-well 4-12% NuPAGE Bis-Tris pre-cast gels (cat. no. NP0335BOX (10-well), NP0336BOX (15-well), Invitrogen). 4x

NuPAGE LDS sample buffer (cat. no. NP0007, Invitrogen) and 10x NuPAGE sample reducing agent (cat. no. NP0009, Invitrogen) were added to 20-35µg protein to achieve a 1x dilution. Protein samples were heated to 70°C for 10 minutes and centrifuged prior to loading. Gel electrophoresis was performed using an XCell SureLock mini-cell (cat. no. EI0001, ThermoFisher Scientific) system. The gel was run at 150V for 1.5 hours (first 30 minutes at 90V) in 1x MOPS SDS running buffer (cat. no. NP0001, Invitrogen). The running buffer of the inner chamber was supplemented with NuPAGE anti-oxidant solution (cat. no. NP0005, Invitrogen) at a dilution 1:400. 7µl of ColorPlus pre-stained protein ladder (cat. no. P7711S, New England Biolabs) were used to visualise the protein weight [kDa]. After running the gel, the resolved proteins were transferred onto a PolyScreen® polyvinyl fluoride hybridisation transfer membrane (cat. no. NEF1002001PK, Perkin Elmer). The mini Trans-Blot cell (Biorad) transfer cassette was built of a sandwich of the gel placed next to a methanol (cat. no. 11976961, Thermo Fisher Scientific) activated PVDF membrane, lined by two Whatman chromatography papers (cat. no. 3030-6189, Whatman) on each side and surrounded by Scotch-Brite pads. The tray holding the sandwich was placed into the transfer tank, cooled by an ice pack, and the chamber was filled with 1x NuPAGE transfer buffer (cat. no. NP0006-1, Invitrogen). The protein transfer was performed at 100V for 1.5 hours.

2.14.4 Immunodetection

Non-specific antibody binding was inhibited using 5% skimmed milk powder (Marvel) in 1x TBST. The membrane was blocked for one hour at room temperature on a shaker. The primary antibody (see) was diluted in blocking buffer and the membrane was incubated over-night at 4°C. After three times five-minute washing steps in 1x TBST the membrane was incubated with a secondary antibody conjugated to HRP (see Table 2.12) for one hour at room temperature. Following additional three times five-minute washes in 1x TBST the HRP activity was visualised with Amersham enhanced chemiluminescence (ECL) Western Blotting Detection Reagent (cat. no. RPN2232, GE Healthcare) or the Luminata Forte Western HRP substrate (cat. no. WBLUF0500, Millipore) and the Amersham Imager 600 (GE Healthcare).

2.14.5 Immunofluorescence staining

Cells grown on glass slides were washed with PBS, fixed in 10% formalin (cat. no. HT501128, Sigma-Aldrich) for 10 minutes and stored in PBS (cat. no. D8537, Sigma-Aldrich) at 4°C prior to staining. Cells were permeabilised for 15 minutes in PBS solution containing 0.2% (v/v) Triton-X100 (cat. no. T8787, Sigma Aldrich) and blocked in PBS solution supplemented with 2% BSA (cat. no. A4503, Sigma-Aldrich) for one hour at

room temperature. Samples were incubated with primary antibody (see Table 2.5) in PBS containing 2% BSA at room temperature for one hour. Glass slides were then rinsed three times with PBS for five minutes and the secondary detection antibody (see Table 2.5) at a 1:1000 dilution was incubated for one hour at room temperature. Cells were counterstained with 1µg/ml DAPI (cat. no. 40043, Biotium) and washed three times in PBS for 10 minutes in order to remove excess dye. Glass slides were mounted using FluorSave Reagent (cat. no. 34589, Calbiochem) and, once dried, analysed using a Zeiss 710 confocal microscope (Zeiss).

2.15 Statistical Analysis

Graphic representation of data and statistical analysis was performed in the programme Prism Version 7.0. Data was tested for normality using the Kolmogorov-Smirnov test. If the data was normally distributed an unpaired Student's *t*-test was used for analysis of differences between two groups. Non-parametric data was tested using a Mann-Whitney test. For multivariate data analysis, one or two-way analysis of variance (ANOVA) was used for assessment of group differences with Turkey's post-test applied. Kaplan Meier curves were used to show survival and Log-rank Mantel-Cox test applied to assess for differences. A p-value below 0.05 was used to define significance.

Chapter 3

The effects of chemotherapy on TAM density and localisation in HGSOC patients

3.1 Background

The aim of this thesis is to investigate the effects of chemotherapy on myeloid cells in the tumour microenvironment of HGSOC. As described in detail in Chapter 1, there are conflicting reports on the effects of chemotherapy on TAM density. For instance, DeNardo *et al.* showed recruitment of macrophages into breast tumours following paclitaxel treatment[222] and Nakasone *et al.* demonstrated that CCR2-dependent macrophage recruitment following chemotherapy[220]. However, other studies have shown either depletion or no change in TAM density following chemotherapy[188,277–279].

The omentum is the disease site studied throughout this thesis. This was chosen as it represents the most common metastatic site of HGSOC and is the principle site of disease studied in the lab[113,114,280]. Furthermore, omentum is routinely used for percutaneous diagnostic biopsy and its surgical accessibility means it can be resected separately from the pelvic mass, allowing rapid tissue processing following surgical devascularisation.

3.2 Patient cohorts

The gold standard treatment for advanced ovarian cancer has been primary cytoreductive surgery followed by adjuvant chemotherapy[281]. More recently clinical evidence supports NACT followed by interval cytoreductive surgery[49]. In this thesis I have studied matched omental biopsies from patients with FIGO stage IIIC and stage IV HGSOC, before and after NACT using a tissue resource collected by Dr. Steffen Böhm[113] (Table 3.1). This fully annotated set of human samples allows for correlations between clinical data, myeloid cell density and phenotype. Additionally, I have used a cohort of unmatched omental samples obtained from treatment naïve patients or from patients who received NACT (Table 3.2). These samples were provided under ethical approval from Barts Cancer Institute Tissue Bank and St. George's Hospital, London.

Patient ID	Histology	Stage	Chemotherapy regime	Pre/Post
G4	High-grade serous carcinoma of the ovary	3C	Carboplatin + Paclitaxel	Matched Pre and Post
G17	High-grade serous carcinoma of the ovary	3C	Carboplatin + Paclitaxel	Matched Pre and Post
G29	High-grade serous carcinoma of the ovary	3C	Carboplatin + Paclitaxel	Matched Pre and Post
G57	High-grade serous carcinoma of the ovary	3C	Carboplatin + Paclitaxel	Matched Pre and Post
G61	High-grade serous carcinoma of the ovary	3C	Carboplatin + Paclitaxel	Matched Pre and Post
G64	High-grade serous carcinoma of the ovary	3C	Carboplatin + Paclitaxel+ Bevacizumab	Matched Pre and Post
G67	High-grade serous carcinoma of the ovary	3C	Carboplatin + Paclitaxel	Matched Pre and Post
G68	High-grade serous carcinoma of the ovary	4	Carboplatin + Paclitaxel	Matched Pre and Post
G75	High-grade serous carcinoma of the ovary	3C	Carboplatin + Paclitaxel	Matched Pre and Post
G77	High-grade serous carcinoma of the ovary	3C	Carboplatin + Paclitaxel	Matched Pre and Post
G95	High-grade serous carcinoma of the ovary	3C	Carboplatin + Paclitaxel	Matched Pre and Post
G98	High-grade serous carcinoma of the ovary	3C	Carboplatin + Paclitaxel	Matched Pre and Post
G100	High-grade serous carcinoma of the ovary	3C	Carboplatin + Paclitaxel	Matched Pre and Post
G102	High-grade serous primary peritoneal carcinoma	3C	Carboplatin + Paclitaxel	Matched Pre and Post
G105	High-grade serous carcinoma of the ovary	3C	Carboplatin + Paclitaxel	Matched Pre and Post
G109	High-grade serous carcinoma of the ovary	4	Carboplatin + Paclitaxel	Matched Pre and Post
G117	High-grade serous carcinoma of the ovary	3C	Carboplatin + Paclitaxel	Matched Pre and Post
G118	High-grade serous carcinoma of the ovary	3C	Carboplatin + Paclitaxel	Matched Pre and Post
G119	High-grade serous carcinoma of the ovary	3C	Carboplatin + Paclitaxel	Matched Pre and Post
G120	High-grade serous carcinoma of the ovary	3C	Carboplatin + Paclitaxel	Matched Pre and Post
G127	High-grade serous carcinoma of the ovary	4	Carboplatin + Paclitaxel+ Bevacizumab	Matched Pre and Post
G128	High-grade serous carcinoma of the ovary	3C	Carboplatin + Paclitaxel+ Bevacizumab	Matched Pre and Post
G132	High-grade serous carcinoma of the ovary	3C	Carboplatin + Paclitaxel+ Bevacizumab	Matched Pre and Post
G135	High-grade serous carcinoma of the ovary	4	Carboplatin + Paclitaxel+ Bevacizumab	Matched Pre and Post
G139	High-grade serous carcinoma of the ovary	4	Carboplatin + Paclitaxel	Matched Pre and Post
G143	High-grade serous carcinoma of the ovary	3C	Carboplatin + Paclitaxel	Matched Pre and Post

Table 3.1 Clinical characteristics of patients from whom matched biopsies are used in this thesis. Patient ID, description of histological diagnosis, FIGO stage, chemotherapy regime and pre/post-chemotherapy status are listed for each patient.

Patient ID	Histology	Stage	Chemotherapy regime	Pre/Post ChemoRx
G159	High-grade serous ovarian/tubal carcinoma	3C	Carboplatin + Paclitaxel	Post
G161	High-grade serous carcinoma of the ovary	3C	Carboplatin + Paclitaxel + Bevacizumab	Post
G163	High-grade serous carcinoma of the ovary	3C	Carboplatin + Paclitaxel	Pre
G164	High-grade serous carcinoma of the ovary	3C	Carboplatin + Paclitaxel	Post
G165	High-grade serous carcinoma of the ovary	3C	Carboplatin + Paclitaxel	Post
G166	High-grade serous carcinoma of the ovary	3C	Carboplatin + Paclitaxel	Post
G168	High-grade serous carcinoma of the ovary	4	Carboplatin + Paclitaxel	Pre
G172	High-grade serous carcinoma of the ovary	4	Carboplatin + Paclitaxel + Bevacizumab	Post
G173	High-grade serous carcinoma of the ovary	4	Carboplatin + Paclitaxel + Bevacizumab	Post
G178	High-grade serous carcinoma of the ovary	4	Carboplatin + Paclitaxel + Bevacizumab	Post
G181	High-grade serous carcinoma of the ovary	3B	Carboplatin + Paclitaxel	Pre
G184	High-grade serous carcinoma of the ovary	3C	Carboplatin + Paclitaxel	Pre
G192	High-grade serous carcinoma of the ovary	3C	Carboplatin + Paclitaxel	Pre
G195	High-grade serous carcinoma of the ovary	3C	Carboplatin + Paclitaxel	Post
G196	High-grade serous carcinoma of the ovary	4	Carboplatin + Paclitaxel	Post
G197	High-grade serous carcinoma of the ovary	4	Carboplatin + Paclitaxel + Bevacizumab	Post
G204	High-grade serous carcinoma of the ovary	3C	Carboplatin + Paclitaxel	Pre
G208	High-grade serous carcinoma of the ovary	4	Carboplatin + Paclitaxel + Bevacizumab	Post
G209	High-grade serous carcinoma of the ovary	3C	Carboplatin + Paclitaxel + Bevacizumab	Post
G214	High-grade serous carcinoma of the ovary	3C	Carboplatin + Paclitaxel	Post
G220	High-grade serous carcinoma of the ovary	3C	Carboplatin + Paclitaxel + Bevacizumab	Post
G221	High-grade serous carcinoma of the ovary	4	Carboplatin + Paclitaxel + Bevacizumab	Post
G275	High-grade serous carcinoma of the ovary	3C	Carboplatin + Paclitaxel + Bevacizumab	Pre
G276	High-grade serous carcinoma of the ovary	4	Carboplatin	Post
G278	High-grade serous carcinoma of the ovary	4	Carboplatin + Paclitaxel	Post
G301	High-grade serous carcinoma of the ovary	4	Carboplatin + Paclitaxel	Post
G302	High-grade serous carcinoma of the ovary	4	Carboplatin + Paclitaxel	Post
G338	High-grade serous carcinoma of the ovary	4	Carboplatin + Paclitaxel	Post
G343	High-grade serous carcinoma of the ovary	3C	Carboplatin + Paclitaxel	Pre
G347	High-grade serous carcinoma of the ovary	3C	Carboplatin + Paclitaxel	Pre
G351	High-grade serous carcinoma of the ovary	4	Carboplatin + Paclitaxel	Post
SG0001	Mucinous cystadenoma of instinal type	n/a	n/a	n/a
SG0004	High-grade serous carcinoma of the ovary	3C	Carboplatin + Paclitaxel + Bevacizumab	Post
SG0005	High-grade serous carcinoma of the ovary	3C	Carboplatin + Paclitaxel + Bevacizumab	Post
SG0008	Endometrioid adenocarcinoma of the endometrium	1	n/a	n/a
SG0011	High-grade serous carcinoma of the ovary	3C	Carboplatin + Paclitaxel + Bevacizumab	Post
SG0012	High-grade serous carcinoma of the ovary	3C	Referred ouside SGH	Pre
SG0013	High-grade serous carcinoma of the ovary	3C	Carboplatin + Paclitaxel	Pre
SG0014	Mucinous cystadenoma of instinal type	n/a	n/a	n/a
SG0017	High-grade serous carcinoma of the endometrium	1	n/a	n/a
SG0018	High-grade serous carcinoma of the ovary	2	n/a	n/a
SG0020	High-grade serous carcinoma of the ovary	3C	Referred ouside SGH	Post
SG0021	High-grade serous carcinoma of the ovary	3C	Carboplatin + Paclitaxel	Pre
SG0024	High-grade serous carcinoma of the ovary	3C	Carboplatin + Paclitaxel	Pre
SG0026	High-grade serous carcinoma of the ovary	3C	Carboplatin + Paclitaxel + Bevacizumab	Pre
SG0027	High-grade serous carcinoma of the ovary	4	Carboplatin + Paclitaxel	Pre
SG0028	High-grade serous carcinoma of the ovary	4	Carboplatin + Paclitaxel	Post
SG0029	High-grade serous carcinoma of the ovary	4	Carboplatin + Paclitaxel	Post

Table 3.2 Clinical characteristics of patients from whom non-matched biopsies are used in this thesis. Patient ID, description of histological diagnosis, FIGO stage, chemotherapy regime and pre/post-chemotherapy status are listed for each patient.

3.3 Quantification of macrophage density pre- and post-chemotherapy in human HGSOC metastases

The effect of chemotherapy on TAM density in HGSOC has not been determined. Therefore, I set out to measure the effects of NACT on TAM density and location within human HGSOC omental metastases. Expecting significant heterogeneity between patient samples I used a cohort of twenty-six matched pre and post-NACT biopsy samples to control for inter-patient variability, as described above. Post-chemotherapy samples were contained in a tissue microarray (TMA) whereas pre-chemotherapy samples were sections of the diagnostic percutaneous core biopsy from the omentum. The TMA cores were 1.2 mm in diameter and multiple cores were taken from each tissue sample (three-six per patient) from different areas of the tumour (e.g. invasive margin, tumour core).

I stained these sections for CD68, as a pan-macrophage marker[171] and used Definiens® digital analysis software to quantify CD68 staining within malignant cell islands and stromal areas of the biopsies. Definiens® was used to perform automated tumour-stromal separation. The results of the software tumour-stroma separation were reviewed and manually corrected were necessary. Assessment of CD68 staining was then performed within the tumour and stromal areas of the biopsy. During optimisation of the Definiens® analysis I found that quantification as $CD68^+$ cells/mm^2 would not be accurate due to the CD68 staining pattern. $CD68^+$ cells were large with cytoplasmic extensions, this resulted in multiple bleb-like structures seen in cross-section which were counted as individual cells by the software. Therefore, I quantified the $CD68^+$ staining as a percentage of the malignant cell area, the stromal area or the entire TMA core/tissue area. Figure 3.1 shows Definiens® digital analysis of a single TMA core from a patient biopsy showing tumour and stroma separation and detection of $CD68^+$ staining.

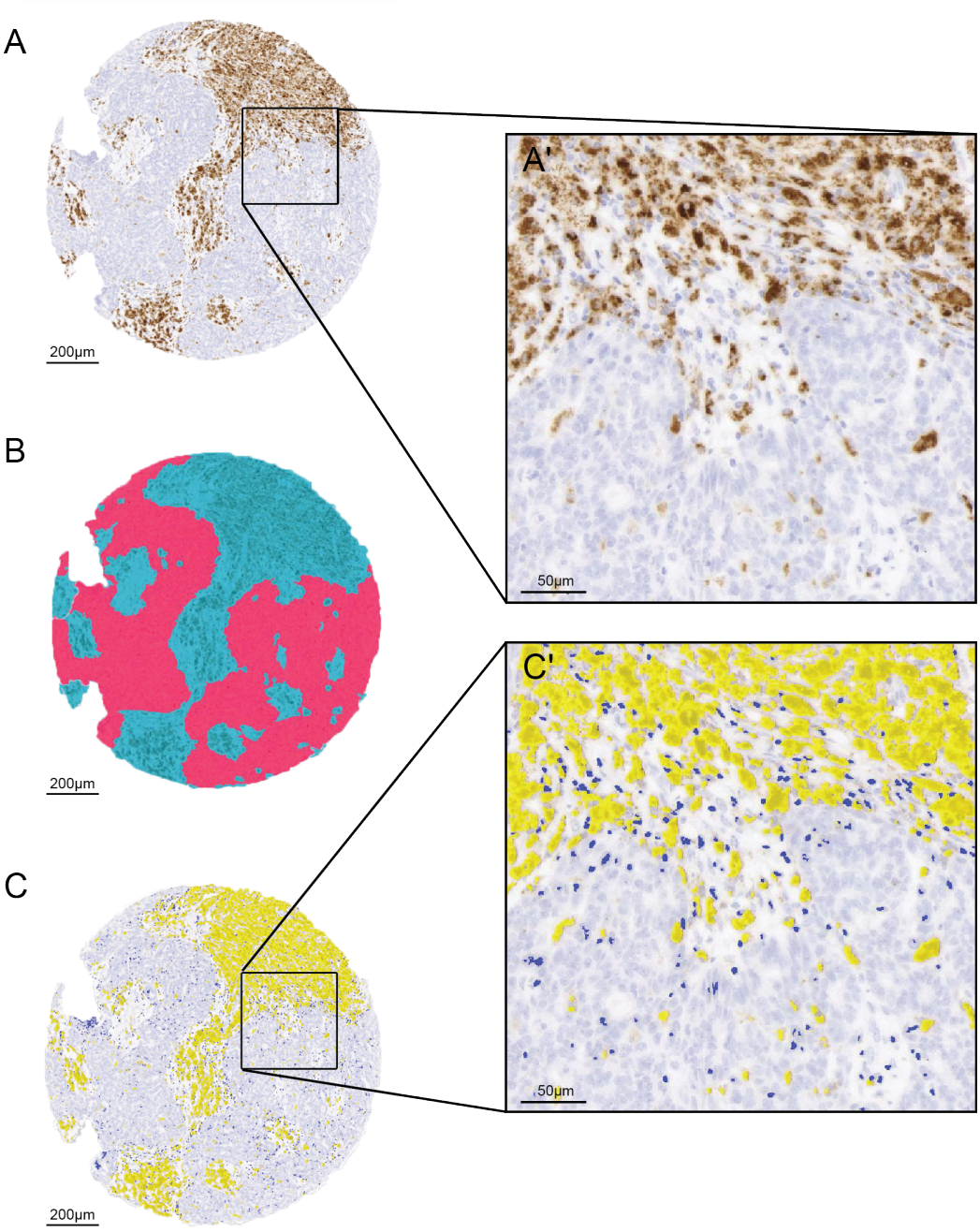

Figure 3.1 Definiens® digital analysis of human HGSOC omental metastases stained with an anti-CD68 antibody. A TMA core from a single HGSOC biopsy sample from a patient who received NACT is shown. **A** Original stained section, **A'** area of TMA core as marked by rectangle depicted at x20 magnification. **B** Core overlaid with areas assigned as malignant cell islands (red) and as adjacent stroma (green). **C** Core overlaid with areas assigned as positive CD68 staining (yellow), analysed within both tumour and stromal areas and darkly counterstained nuclei (blue). **C'** area of TMA core as marked by rectangle depicted at x20 magnification. Scale bars, A-C: 200µm; A', C': 50µm.

Figure 3.2 shows the result for the Definiens® analysis. Counting within the entire tissue sample, there was no difference in $CD68^+$ area in treatment naïve compared with samples post-NACT. However, there were differences when the malignant cell and stromal areas of the biopsy were considered separately. Values for $CD68^+$ area did not

change after NACT in the stromal areas. In contrast, within malignant cell islands there was a significant reduction in the mean CD68$^+$ area following NACT compared to pre-treatment samples (7.88 *vs* 1.01% p<0.0001). These changes resulted a higher TAM density in the stroma compared to the malignant cell areas following NACT (3.94 *vs* 1.01% p=0.02).

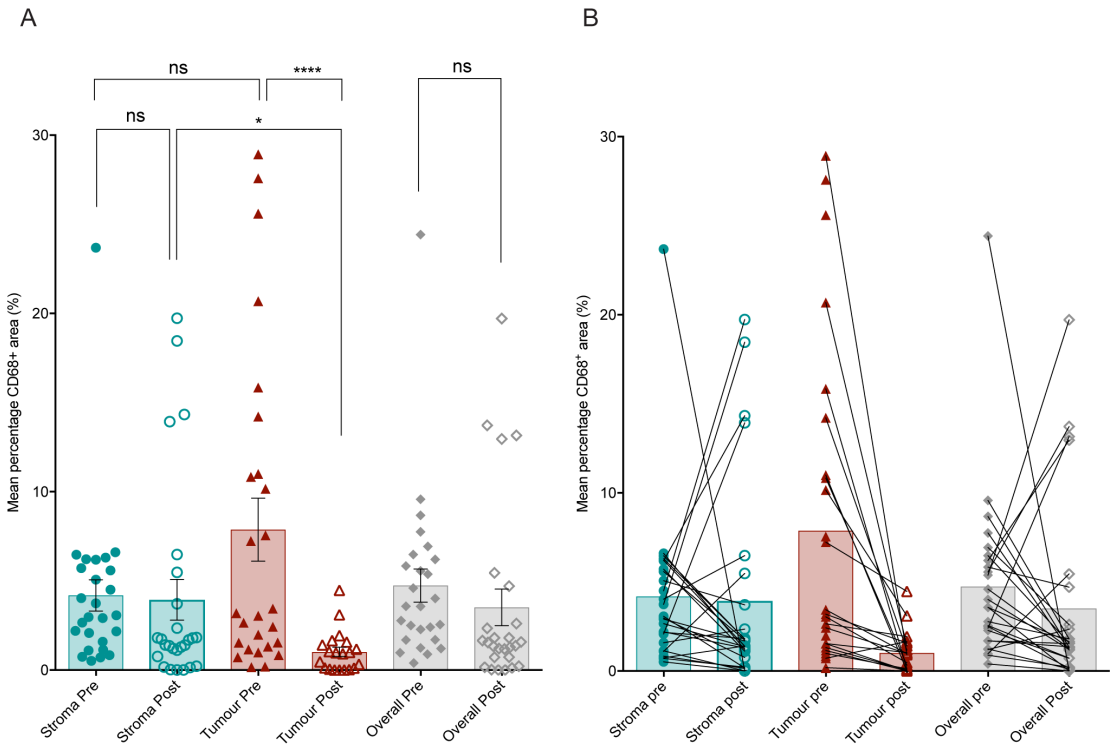

Figure 3.2 Quantification of CD68 density within tumour, stromal and whole biopsy areas in matched pre- and post-NACT human HGSOC omental metastases. A Mean percentage area of CD68 staining within stromal areas (green circles; pre-chemotherapy filled circles, post-chemotherapy unfilled circles), malignant cell islands (red triangle; pre-chemotherapy filled triangles, post-chemotherapy unfilled triangles), and the biopsy overall (grey diamonds; pre-chemotherapy filled diamonds, post-chemotherapy unfilled diamonds) was quantified by Definiens® digital analysis in matched pre and post-chemotherapy human HGSOC biopsy samples from the omentum. Data presented from twenty-six matched pre and post-NACT biopsy samples, error bars represent SEM and individual data points are overlaid. Wilcoxon matched-pairs signed rank test p-values for matched analyses and Mann-Whitney U test p-values for unmatched analyses are shown. **B** Data presented showing matched sample pairs. Significant p-values shown; ****<0.0001, *<0.05.

3.4 Tissue features in pre and post-chemotherapy human HGSOC biopsy sections

As seen in Figure 3.2 the stromal CD68$^+$ area was greatly increased in four of the patients. A core from one of these patients is shown in Figure 3.1. The striking increase in stromal CD68$^+$ area in this subset of patients suggested that macrophages may not be uniformly distributed through the tissue and that macrophage density may not have been fully captured as a result of limited sampling of the tissue in the post-NACT TMAs.

In order to explore this further, I studied the effects of chemotherapy in HGSOC omental metastases using unmatched larger tissue sections from a different patient cohort. I

performed dual colour immunohistochemistry, staining malignant cells with an anti-PAX8 antibody and TAMs with an anti-CD68 antibody. I observed large clusters of macrophages frequently surrounding or in close proximity to viable-appearing malignant cells. This pattern of staining was frequently seen post-NACT but rarely in pre-treatment samples. I used the term stromal macrophage 'lakes' to describe these areas (Figure 3.3).

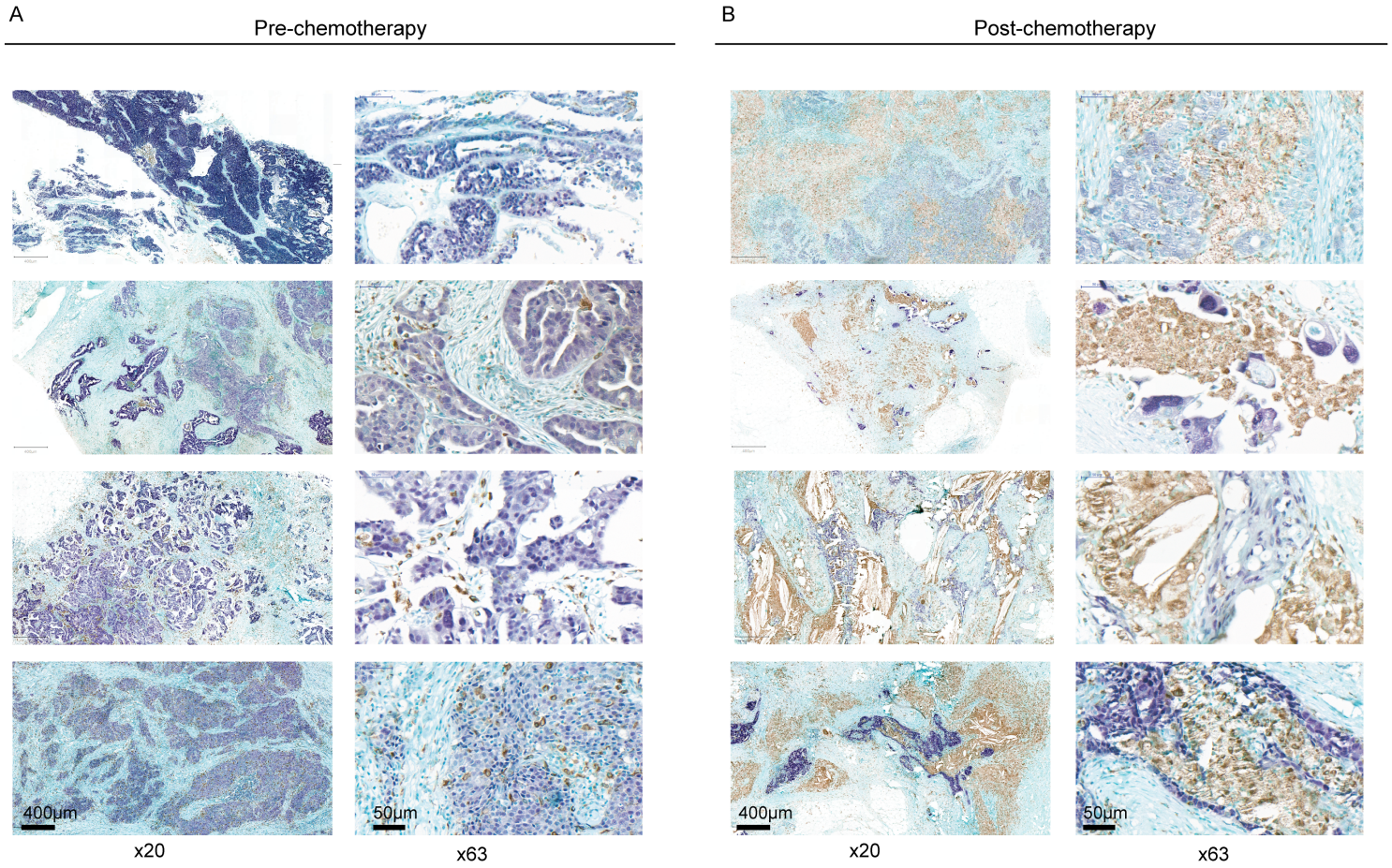

Figure 3.3 Dual colour immunohistochemistry of human HGSOC metastases. Representative images of dual colour immunohistochemistry staining malignant cells with an anti-PAX8 antibody (purple) and myeloid cells with an anti-CD68 antibody (brown) from **A** four patients pre and **B** four patients post-chemotherapy. Images shown at x20 and x63 magnification. Scale bars; 400µm; 50µm.

I then quantified the macrophage lakes in a total of thirty-two unmatched HGSOC omental metastases; nine patients were pre-treatment and twenty-three patients had received chemotherapy. I defined macrophage lakes as areas of continuous $CD68^+$ staining >4000μm^2, 10,000μm^2 or >50,000μm^2 and quantified these in an unbiased manner across the entire tissue section. There were significantly more macrophage lakes within post-NACT tissues sections compared to pre-chemotherapy (Figure 3.4). Furthermore, no macrophage lake areas >50,000μm^2 were observed in pre-chemotherapy samples (Figure 3.4).

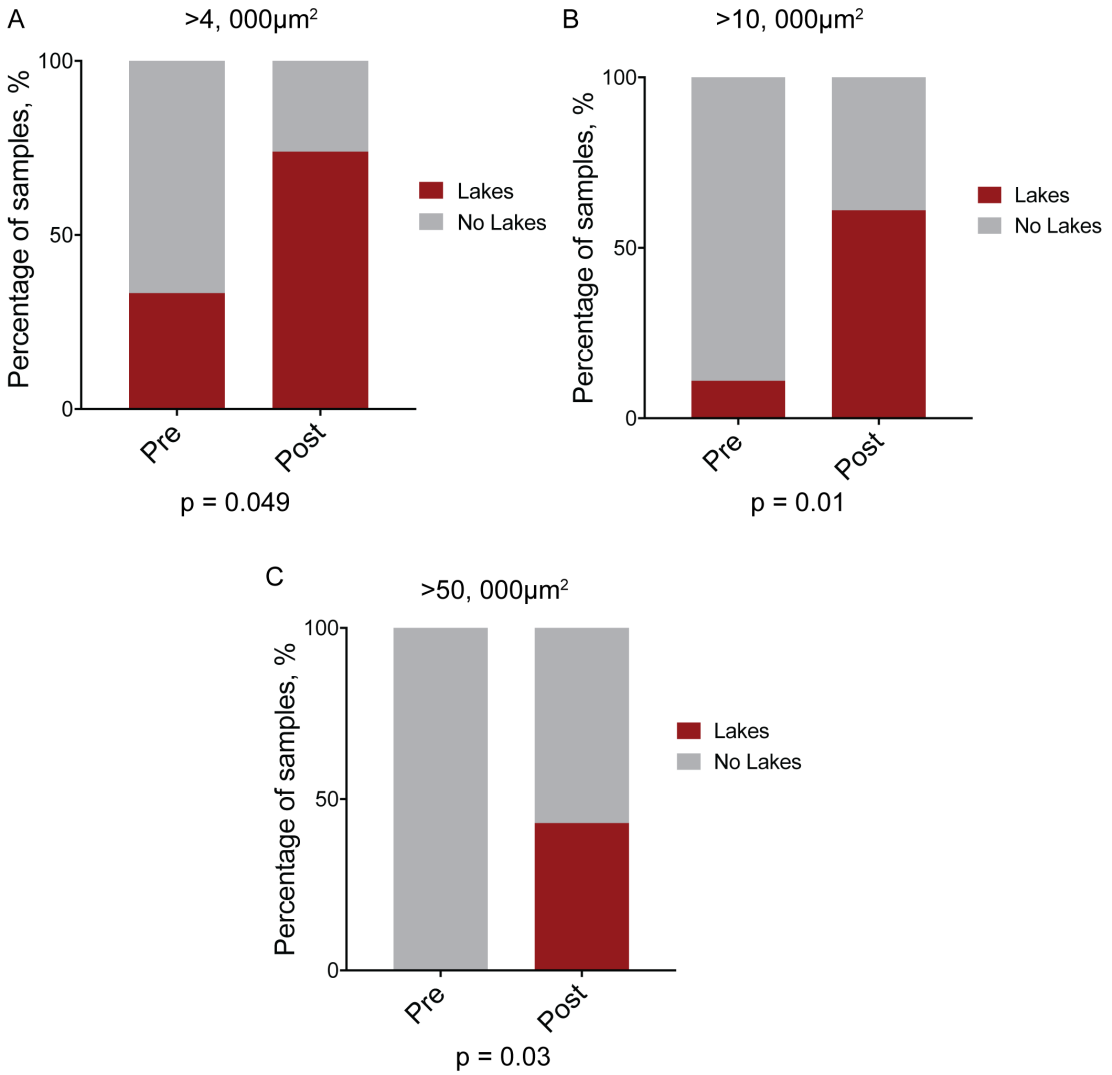

Figure 3.4 Quantification of 'macrophage lakes' within human HGSOC omental metastases. Macrophages lakes were quantified in human HGSOC omental metastases pre and post-chemotherapy. Macrophage lakes were defined as areas of continuous $CD68^+$ staining greater than **A** 4,000μm^2, **B** 10,000μm^2 and **C** 50,000μm^2. Data represent quantification of unmatched biopsies from nine patients pre and twenty-three patients post-chemotherapy. Fisher's exact test p-values are shown.

Taken together these data suggest widescale changes in the overall tissue architecture as the result of chemotherapy with non-homogenous localisation of macrophages within

the post-NACT microenvironment, in contrast to pre-chemotherapy biopsies.

3.5 CIBERSORT assessment of immune populations in pre and post-chemotherapy HGSOC omental metastases

CIBERSORT is an analytical tool developed by Newman *et al.* to provide an estimation of cells types in mixed populations of cells using gene expression data[282]. Using this approach Dr. Eleni Maniati (BCI Core Bioinformatics Service) compared the cellular composition of unmatched pre and post-chemotherapy HGSOC omental metastasis samples on which RNA-sequencing had been previously performed for a previous project in the lab. Treated samples were further sub-categorised into those having a good response and those have a bad response to NACT, as assessed by the chemotherapy response score (CRS)[280]. According to the CIBERSORT analysis, all tumours contained significant populations of naïve B cells, memory $CD4^+$ T cells, monocytes, M0 and M2 macrophages (Figure 3.5). Genes associated with $CD8^+$ T cells, resting dendritic cells, neutrophils and NK cells were variably expressed.

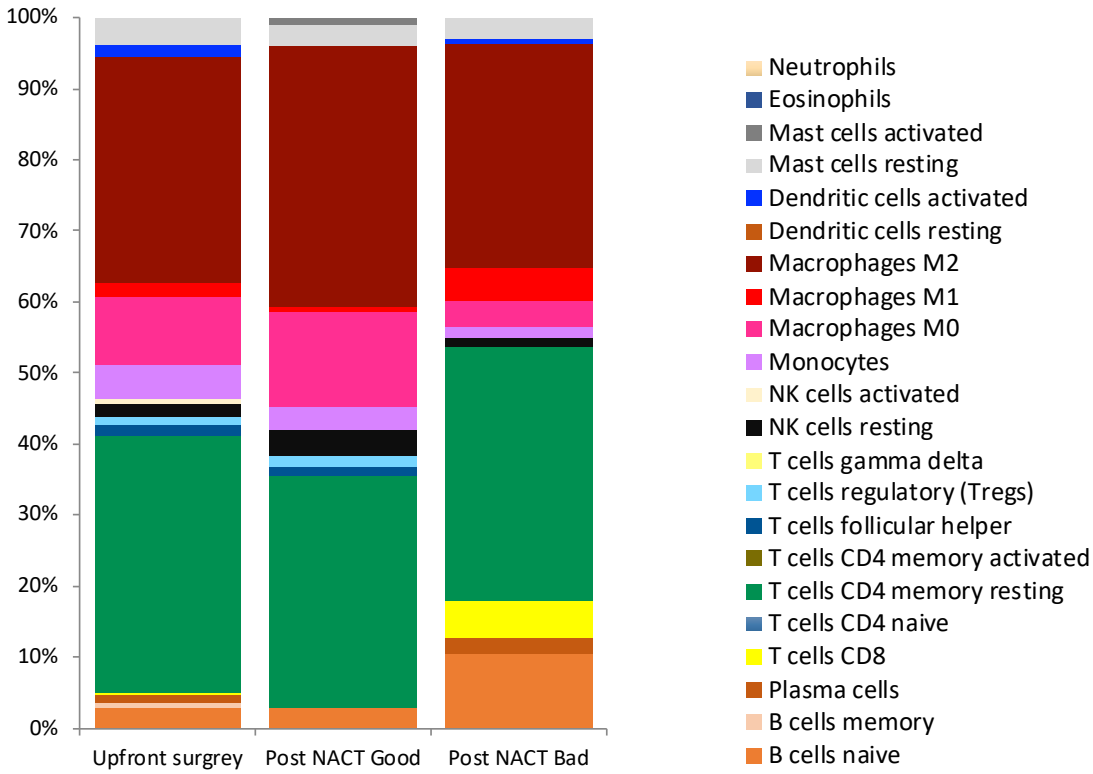

Figure 3.5 Proportions of immune cell populations estimated from human omental metastasis pre and post-NACT using CIBERSORT. Analysis performed on RNA-sequencing data derived from whole tumour preparations. Median values are shown representing four patients treated with upfront surgery, five patients post-NACT with a good response and seven patients post-NACT with a bad response.

In agreement with the IHC data there were no obvious changes in the global frequency of myeloid cell gene expression between untreated and post-NACT samples.

Interestingly, it appeared that bad responders had less macrophages and good responders had more macrophages compared to untreated samples. Furthermore, CIBERSORT provided information on macrophage phenotypes which will be described in more detail in Chapter 5. Bad responders to NACT appeared to have more M1/classically activated macrophages and less M0 macrophages compared to untreated samples. Conversely, good responses to NACT had less M1/classically activated macrophages and more M0 macrophages. There appeared to be overall little change in M2/alternatively activated macrophages between untreated and post-NACT patients and these cells represented the dominant myeloid phenotype. CIBERSORT additionally provided an analysis of the human HGSOC lymphocyte compartment, which has not been assessed in any other aspect of this thesis. Within the group of bad responders to NACT there was an increase in $CD8^+$ and naïve B cell gene expression.

CIBERSORT analysis supports the concept of little change in TAM frequency overall. Interestingly, clustering patients into good and bad responders to NACT suggests macrophages may promote beneficial response post-chemotherapy as overall, the expression of the macrophage signatures was higher in the good prognosis group.

3.6 Effects of TAM density on patient survival

Studies in mixed cohorts of ovarian cancer patients have not shown any clear prognostic implications of overall TAM density[186,197]. However, these studies have not accounted for the effects of chemotherapy on TAM. To investigate if TAM density affected overall survival I categorised patients with high or low $CD68^+$ TAM area and compared the pre- and post-NACT values with their overall survival. Figure 3.6 and Figure 3.7 show Kaplan Meier curves for patient survival stratified by overall, stromal or malignant cell area TAM density pre (Figure 3.6) and post-chemotherapy (Figure 3.7) using a cohort of thirty-three patient biopsy samples contained on the post-treatment TMAs.

Stratifying patient overall survival by TAM density above and below the median value showed no significant difference in survival outcome either before or after chemotherapy. To determine if there was any association of high compared to low TAM density on overall survival, I also compared survival in the upper quartile versus the lower quartile for $CD68^+$ TAM density. As can be seen in Figure 3.7 there was a significantly increased overall survival in patients with high compared to low $CD68^+$ TAM area following chemotherapy (log-rank $p=0.05$) and a near-significant trend ($p=0.08$) to improved survival within the stroma before chemotherapy. Interestingly, within the malignant cell areas there was a trend to reduced survival before NACT with no obvious difference after NACT. Overall these data, albeit on a small cohort of patients, suggest that high stromal

TAM density may confer positive influence on overall survival and furthermore, that TAM within the stromal and malignant cell areas of the HGSOC TME may have different associations with survival.

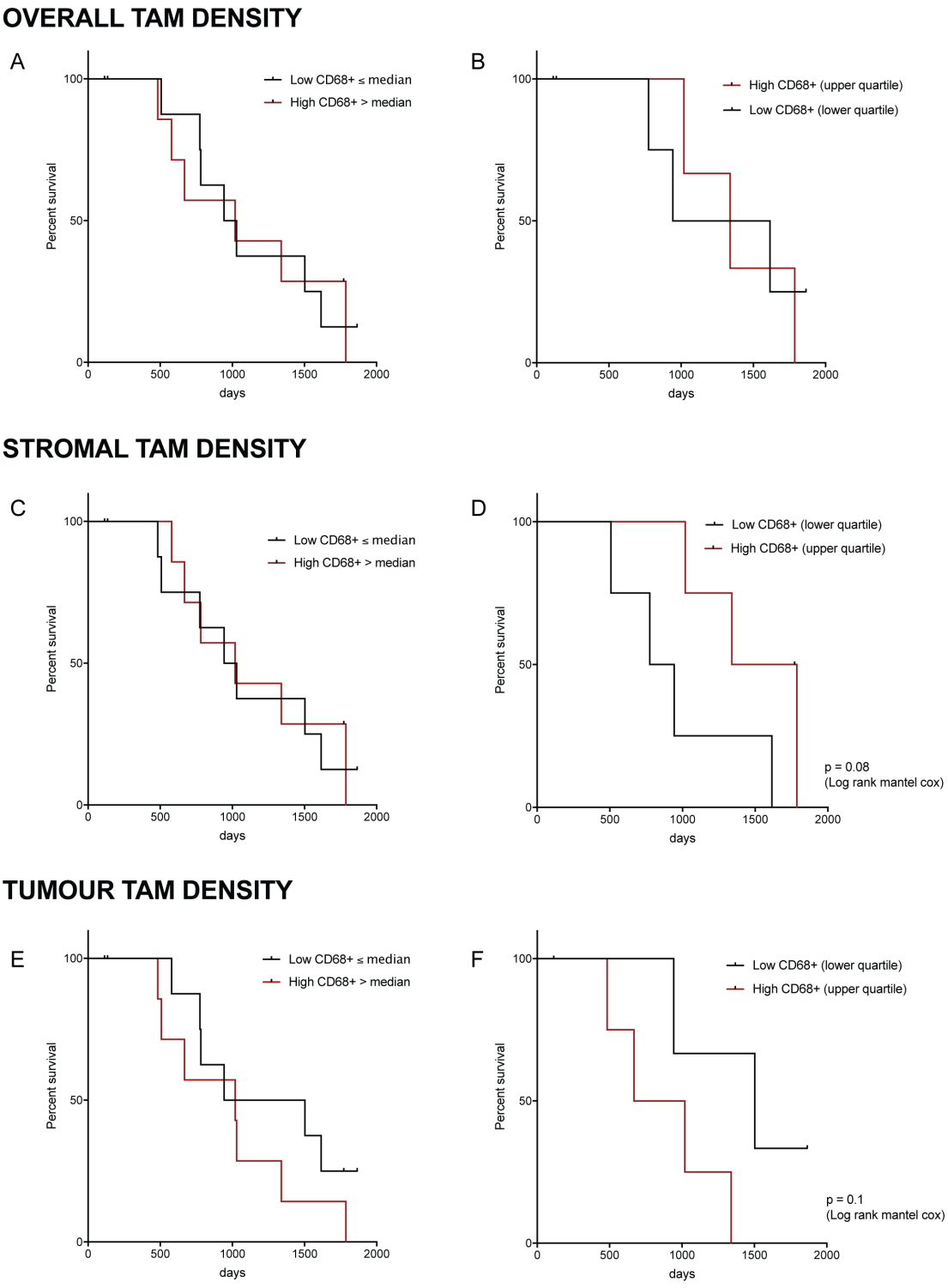

Figure 3.6 Overall survival of patients stratified by pre-chemotherapy TAM infiltrate. A,C,E Overall survival of HGSOC seventeen patients stratified by high (>median) or low (<median) $CD68^+$ percentage area. **B,D,F** Overall survival of nine HGSOC patients stratified by high (upper quartile) or low (lower quartile) $CD68^+$ percentage area **A,B** shows overall TAM density **C,D** shows stromal TAM density and **E,F** shows malignant cell density. Selected log-rank test p-values are shown.

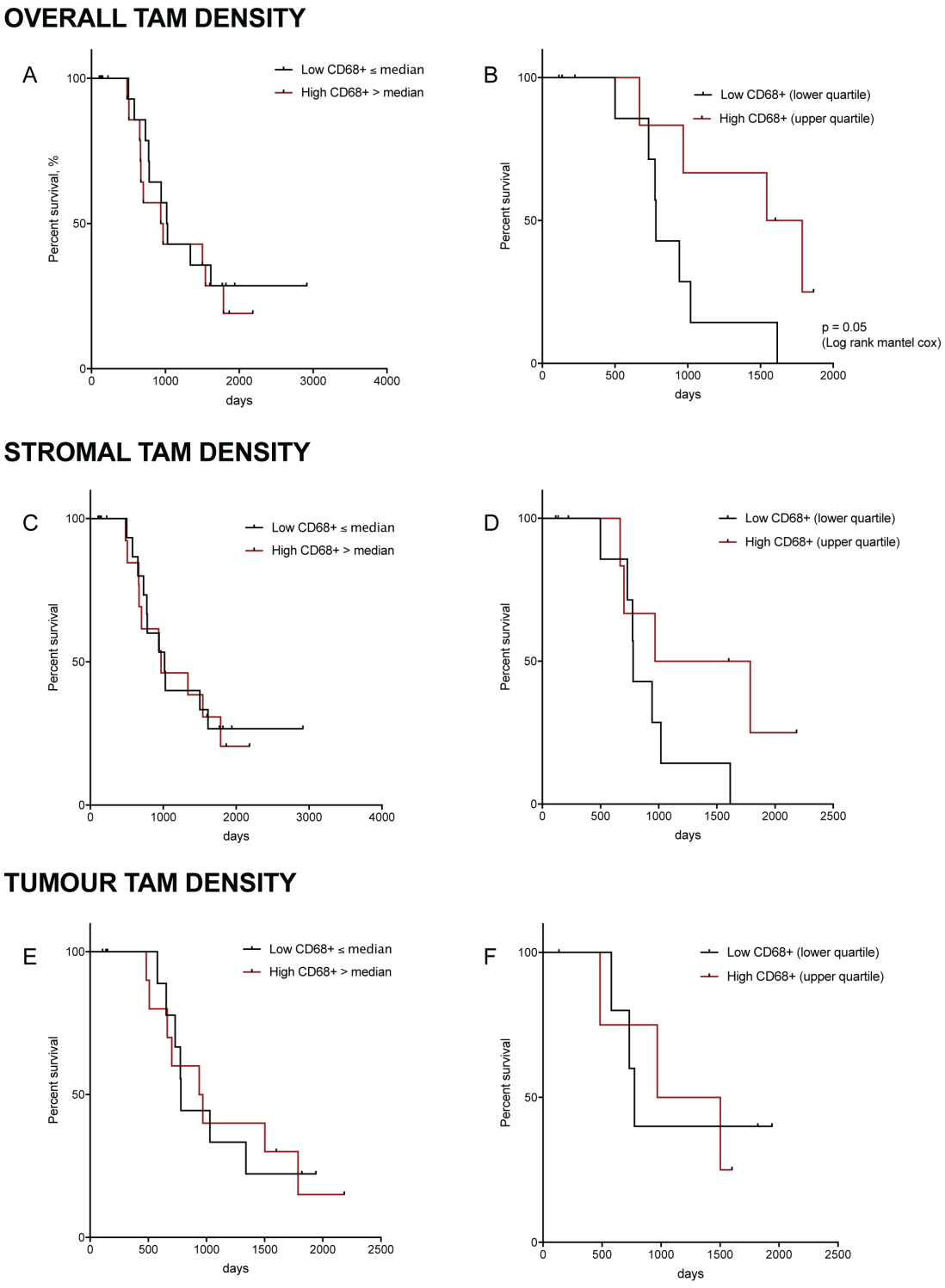

Figure 3.7 Overall survival of patients stratified by post-chemotherapy TAM infiltrate. A,C,E Overall survival of HGSOC thirty-three patients stratified by high (>median) or low (<median) $CD68^+$ percentage area. **B,D,F** Overall survival of sixteen HGSOC patients stratified by high (upper quartile) or low (lower quartile) $CD68^+$ percentage area **A,B** shows overall TAM density **C,D** shows stromal TAM density and **E,F** shows malignant cell density. Selected log-rank test p-values are shown.

3.7 Discussion

To date the role of TAMs in HGSOC has not been extensively studied[192]. No studies have addressed the effects of chemotherapy on ovarian cancer TAM density, phenotype or function *in vivo*, however, work in other cancer types suggests this could be a promising area to explore[156,220–222,283].

I observed striking differences in the microscopic appearance of HGSOC sections three weeks following NACT compared to untreated samples. In chemotherapy treated samples I frequently observed extensive immune infiltrates associated with extracellular matrix deposition extending through large areas of the biopsies. These areas measured up to 4mm^2 and were often in close proximity to or surrounding islands of apparently viable malignant cells. This was in contrast to pre-chemotherapy samples, where although there was evidence of an extensive immune infiltrate this was typically observed as scattered cells interspersed within the stroma or malignant cell islands. Assessment of cell morphology within these extensive immune infiltrates post-chemotherapy was suggestive of many of the cells being macrophages. This was confirmed by IHC using an anti-CD68 antibody.

I rereferred to these large clusters of macrophages as macrophage 'lakes'. Macrophage lakes were significantly more numerous in the stroma following NACT. A fibro-inflammatory response including infiltrating macrophages and 'foam' cells has been described as a tissue response to chemotherapy within omental HGSOC metastases[280]. Indeed, assessment of these infiltrates form a part of the chemotherapy response score (CRS) and are associated with a favourable response to chemotherapy (CRS3) when associated with a concomitant tumour cell response[280].

To minimise the effect of sample heterogeneity I used a cohort of matched untreated and post-NACT biopsies to study the effect chemotherapy on TAM density within HGSOC metastases. Digital quantification demonstrated a significant decrease in the CD68$^+$ area following NACT within the malignant cell islands compared to pre-treatment samples. Assessment of stromal areas demonstrated no significant differences in mean CD68$^+$ area following chemotherapy compared to pre-treatment samples. However, in four patients there was a marked increase in TAM density within the stroma which was reflected in the quantification of TAM density in the biopsy overall (Figure 3.2). A core relating to one of these patients is shown in Figure 3.1; the appearance of the stromal CD68 staining in this core is characteristic of a macrophage lake. It is likely therefore that TMA cores for these four patients sampled macrophage lakes. As the result of the relatively limited sampling of the TME combined with the non-uniform CD68 staining

pattern, the TMA analysis may not have completely captured the stromal response in all patients.

In other cancer types, studies have addressed the effects of chemotherapy on overall TAM density, although they have not compared malignant and stromal biopsy areas. These studies show conflicting results, in pancreatic ductal adenocarcinoma (PDAC) Di Caro *et al*. show trends toward reduction in $CD68^+$ TAM density at the tumour-stroma interface after chemotherapy[188]. In a murine sarcoma model Germano *et al.* show that trabectedin activated caspase-8 mediated apoptosis selectively in monocytes/macrophages[212]. TAM depletion was a mechanism underlying the effects of trabectedin in murine models. Also in mouse models, gemcitabine and 5-fluorouracil are able to deplete suppressive populations of myeloid cells[277–279]. In contrast to these studies showing either no change or a depletion of myeloid cells after chemotherapy, TAM recruitment following paclitaxel treatment was reported in mouse breast cancer models[220,222]. It is possible that different chemotherapeutic agents may effect TAM density differently[277].

To investigate if TAM density before or after chemotherapy affects patient survival I compared overall survival in cohorts of patients stratified by TAM density within the stroma, malignant cell islands and within the biopsy overall. Although comparing patients above and below the median did not show differences in survival, comparing high TAM infiltrate (upper quartile) with low TAM infiltrate (lower quartile) in the biopsy overall was associated with a significant increase in patient survival in this small cohort (Figure 3.7). It appeared that chemotherapy treatment potentiated this effect, suggesting the possibility of chemotherapy driving an anti-tumorigenic TAM phenotype within stromal TAM. In agreement with these findings, in patients with haematological malignancies[202], PDAC[188] and CRC[181], high TAM density after chemotherapy predicts enhanced survival.

The data presented here relate to a small number of patients and need to be confirmed in a larger cohort before robust conclusions can be drawn. However, in a study of 326 pre-treatment primary HGSOC biopsies by others in the lab, high levels of stromal $CD68^+$ cells significantly associated with increased overall survival (Montfort *et al.* manuscript under preparation). These data do not show that TAM are mechanistically involved in promoting a positive response to chemotherapy. TAM tissue density may be acting as a surrogate marker of patient response to therapy. Further experiments will be required to confirm these results and search for the molecular and cellular circuits within the TME underpinning these observations. Additionally, the TME is affected by the underlying genetic landscape of the tumour. Tothill *at al.* defined four molecular subtypes of HGSOC

based on gene expression: C1 (mesenchymal), C2 (immunoreactive), C4 (differentiated) and C5 (proliferative)[9]. These subtypes associated with differences in clinical outcome as well as differences in the TME. I have not sought to classify tumour based on gene expression, and it is likely that more samples would be needed to capture the genetic diversity of HGSOC then analysed in this study.

As noted above, published studies to date in ovarian cancer do not show total macrophage density to predict patient outcome[193]; however, specific TAM subsets differentiated phenotypically and spatially in tumours, do have associations with patient surival[193–195,197]. Zhang *et al.* showed that a high intra-tumoural, as opposed to stromal or whole tissue, M1 (classically activated)/M2 (alternatively activated) phenotype ratio was associated with improved survival[196] suggesting localisation as well as phenotype to be clinically relevant. However, it should be noted that these studies are in predominantly in mixed cohorts of ovarian cancer subtypes and crucially that the effects of chemotherapy on macrophage phenotype were not considered.

In conclusion these data demonstrate that at a time point on average three-four weeks following NACT, there are significant differences in the macrophage infiltrate, as measured by $CD68^+$ area, within the malignant cell and stromal areas of the biopsy compared to pre-treatment samples. There are preliminary data that high TAM density post-NACT in the omental biopsies may associate with greater overall survival. In the following two chapters I will examine the effects of chemotherapy on TAM phenotype by flow cytometry (Chapter 4) and on TAM pathways and processes using RNA-sequencing (Chapter 5).

Chapter 4

The effects of chemotherapy on myeloid cell phenotype within HGSOC omental metastases

4.1 Background

The aim of this chapter is to phenotype macrophages and dendritic cells (DCs) in pre and post-NACT samples by cell surface protein expression of canonical activation markers. In this chapter I have used flow cytometry (FC) to assess the phenotype of TAMs before and after chemotherapy.

It is established that TAM in ovarian cancer adopt an immunosuppressive (alternatively activated) phenotype, and express markers including CD163, CD204, CD206 and IL-10[190–192]. Densities of alternatively activated TAMs associate with a reduced patient survival, in keeping with their roles in limiting anti-tumour immunity. For example, patients with tumours richly infiltrated with $CD163^+$ TAMs have significantly reduced progression free and overall survival[194] and the CD206/CD68 TAM ratio predicted worse PFS[193]. Further confirming the importance of macrophage phenotype, a high M1 (classically activated)/M2 (alternatively activated) ratio associated with improved survival[195,196]. This suggests that macrophages in ovarian cancer may enhance or limit tumorigenesis depending on activation state. However, these studies were predominantly in mixed cohorts of ovarian cancer subtypes and the effects of chemotherapy on macrophage phenotype was not considered. A recent meta-analysis confirmed the association of poor prognosis with $CD163^+$ TAMs and improved prognosis with a high M1 (classically activated)/M2 (alternatively activated) ratio[197] in ovarian cancer, further strengthening these data.

In this chapter, immunostaining for FC analysis using a 'myeloid panel' of antibodies (see Materials and Methods) included assessment of DCs in addition to TAMs. FC assessment of the DC population was included to provide additional descriptions of these myeloid cells and allow for the study of the effects of chemotherapy on this cell type. DC are bone-marrow derived cells that have essential roles in antigen sensing and presentation and as such lie at the interface between innate and adaptive immunity[284]. Therefore, assessment of the effects of chemotherapy on DC subsets could be important.

4.2 Flow cytometry analysis of macrophages in human HGSOC omental metastases

I used multicolour FC to define myeloid cell populations and to phenotype TAM in omenta that were undiseased, and HGSOC omenta pre-treatment and following NACT. Figure 4.1 shows the gating strategy employed to define myeloid populations from human biopsy samples. To gate for TAMs, lineage markers (CD3, CD19, CD20, CD56, CD66b, Siglec8) were all stained with FITC conjugated antibodies, allowing exclusion of cells expressing these markers, by gating for the $FITC^-$ population. TAMs were defined as $CD45^+FITC^-HLA\text{-}DR^+$ cells. Given the possibility of other myeloid cells residing within the gate, most notably DCs, a further population of $CD14^+$TAMs was defined. Analysis of canonical surface makers were assessed within the TAM and $CD14^+$TAM populations.

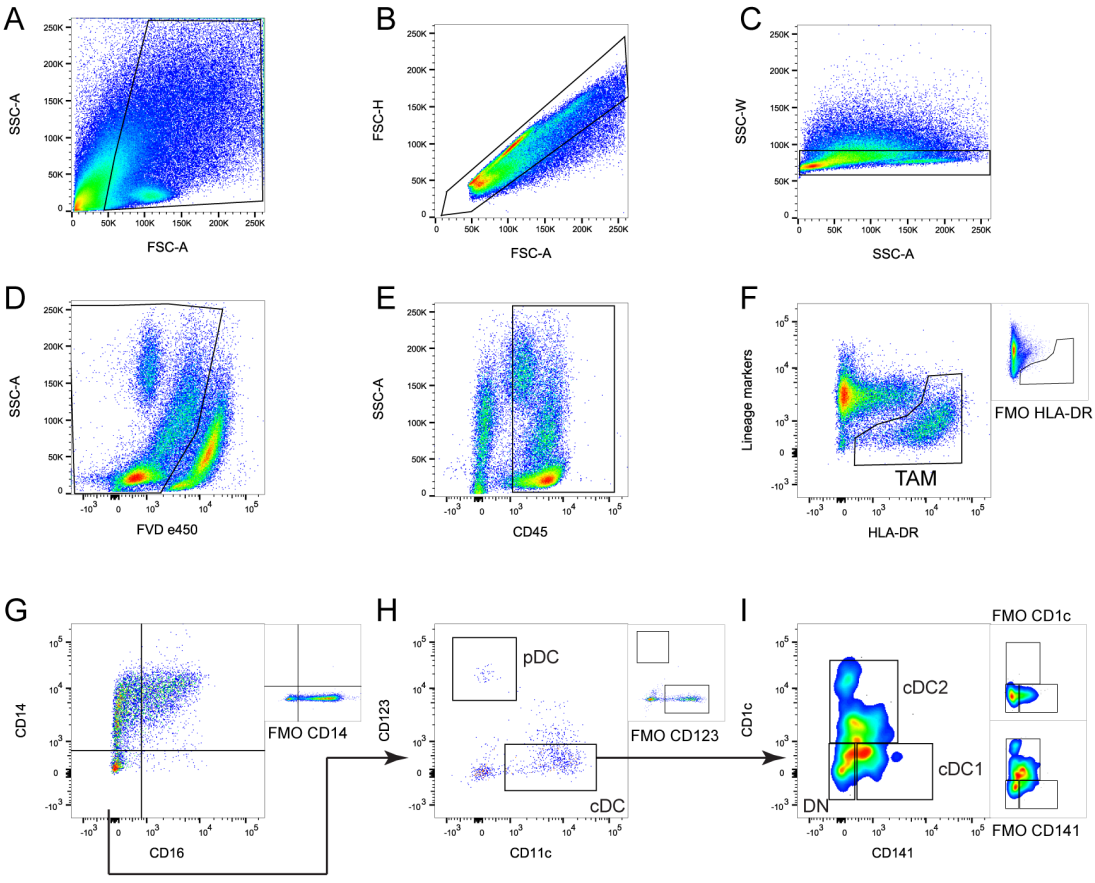

Figure 4.1 Multicolour flow cytometry gating strategy to characterise myeloid populations. Density plots shown from a representative patient sample showing the immunostained stromal vascular fraction from a human omental HGSOC metastasis. **A** Gating to exclude cellular debris, **B**, **C** sequential gating to exclude doublet cells, **D** sequential gating to exclude non-viable cells, **E** sequential gating for CD45 positive cells, **F** sequential gating for $FITC^-HLA\text{-}DR^+$ cells. Insert showing FMO for HLA-DR. **G** sequential gating for CD14 by CD16, insert showing FMO for CD14. **H** sequential gating for CD11c by CD123, insert showing FMO for CD123. **I** sequential gating for CD1c by CD141, inserts showing FMOs for CD1c and CD141. *FMO:* florescence minus one control, *FVD:* fixable viability dye, *SSC-A*: side scatter area, *SSC-W*: side scatter width, *FSC-A*: forward scatter area, *FSC-H*: forward scatter height.

A total of twenty-eight patient samples were analysed; nine patients treated by upfront surgery pre-chemotherapy and fourteen patients undergoing interval cytoreduction after three to six cycles of NACT. Additionally, omental samples from five patients with no omental disease or benign pathology were included (Table 4.2). There was a non-significant decrease in TAMs as a percentage of the $CD45^+$ infiltrate (23.60% *vs* 16.02% p=0.37) in patients undergoing interval cytoreductive surgery following chemotherapy compared to patients being treated with upfront surgery (Figure 4.2A). When the analysis was restricted to $CD14^+$TAMs, I again observed a non-significant reduction (21.19% *vs* 11.58% p=0.16) of this cell population relative the total $CD45^+$ population at interval cytoreductive surgery compared to upfront surgery (Figure 4.2B).

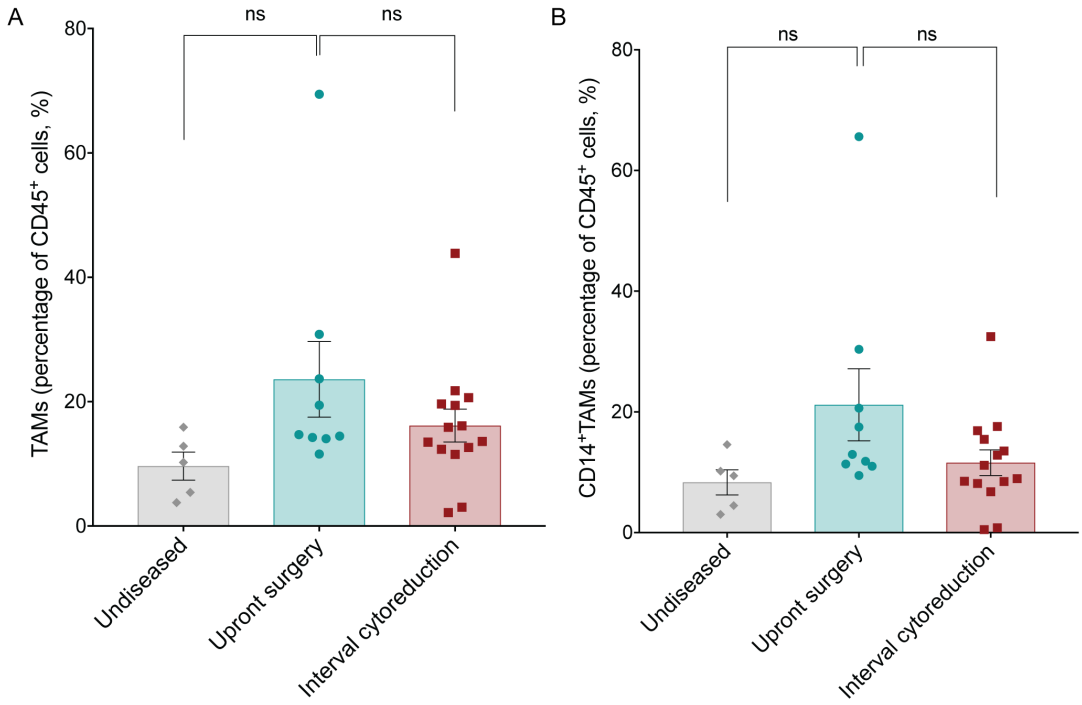

Figure 4.2 Effect of chemotherapy on the TAM infiltrate of human HGSOC omental metastases. Flow cytometry data demonstrating frequency of **A** TAMs ($FITC^-HLA\text{-}DR^+$) and **B** $CD14^+$ TAMs as a percentage of $CD45^+$ cells in fourteen patients having received NACT (red), nine patients treated with upfront surgery (green) and five patients with undiseased omenta (grey). Error bars represent SEM. One-way ANOVA with Turkey post hoc test was applied. ns denotes a non-significant p-value.

To study TAM phenotype pre and post-chemotherapy I assessed the surface expression of a panel of markers (CD163, CD206, CD209, CX3CR1). There was a significant reduction in $CD163^+$ (55% *vs* 32% p=0.006) and $CX3CR1^+$ (68% *vs* 25% p=0.003) TAMs in patients receiving chemotherapy compared to those treated with primary surgery (Figure 4.3A,B). Furthermore, there were trends to reduced expression of $CD206^+$ and $CD209^+$ TAMs following chemotherapy (Figure 4.3C,D).

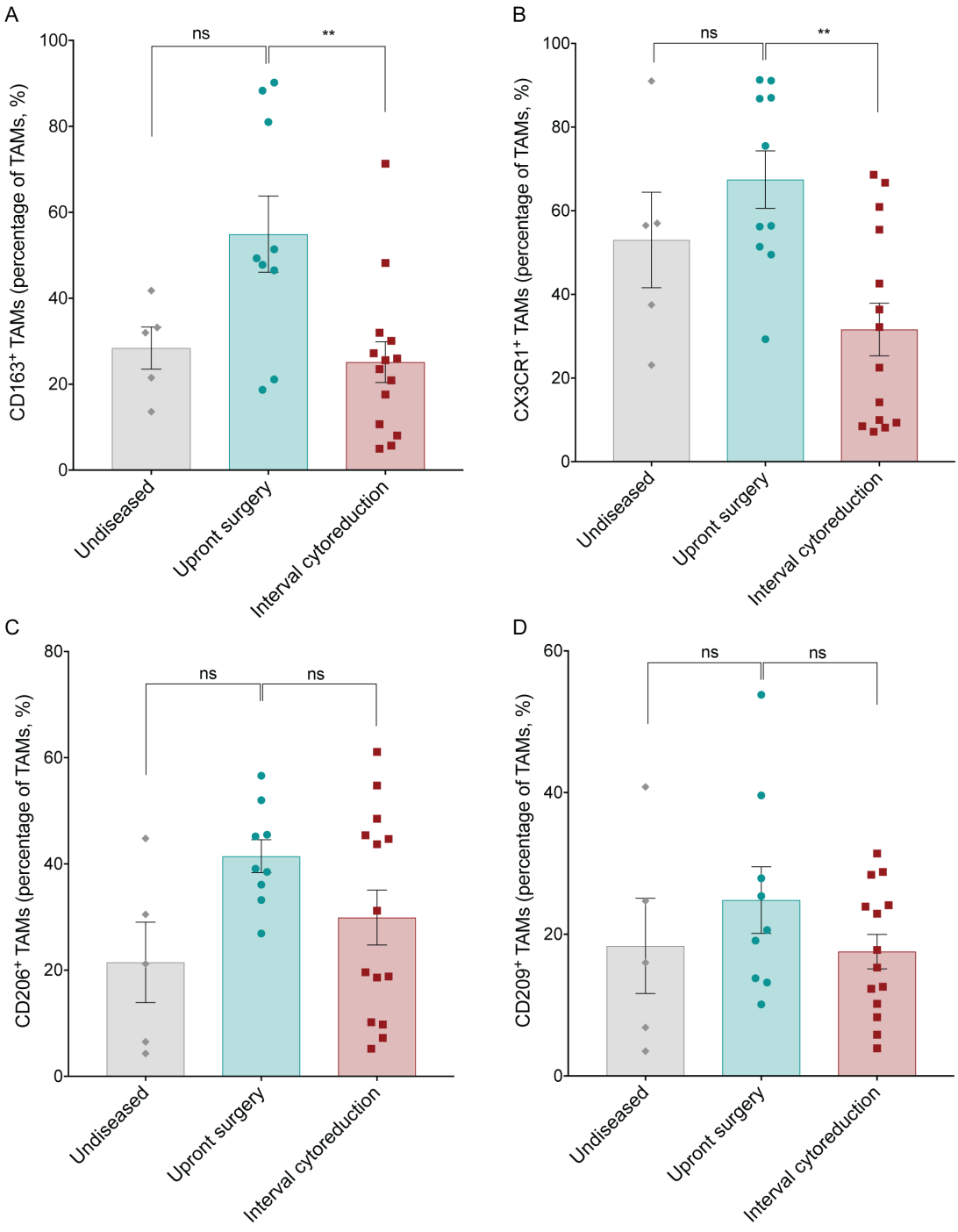

Figure 4.3 Effect of chemotherapy on TAM surface marker expression in human HGSOC omental metastases. Flow cytometry data demonstrating TAM ($FITC^{-}HLA\text{-}DR^{+}$) expression of **A** CD163, **B** CX3CR1 **C** CD206, **D** CD209, as a percentage of the TAM population in fourteen patients having received NACT (red), nine patients treated with upfront surgery (green) and five patients with undiseased omenta (grey). Error bars represent SEM. One-way ANOVA with Turkey's post-hoc test p-values are shown; ns = non-significant, ** <0.01.

Given that in Chapter 5 I will perform RNA-sequencing on $CD14^{+}$TAM I wished to explore any differences in activation marker expression within the $CD14^{+}$TAM population. These data show the same trends as seen within the TAM population (Figure 4.4). Again, I observed significant reductions of CD163 (62% *vs* 38% p = 0.02) and CX3CR1 (77% *vs* 42% p = 0.03) expression as a percentage of the $CD14^{+}$TAM population.

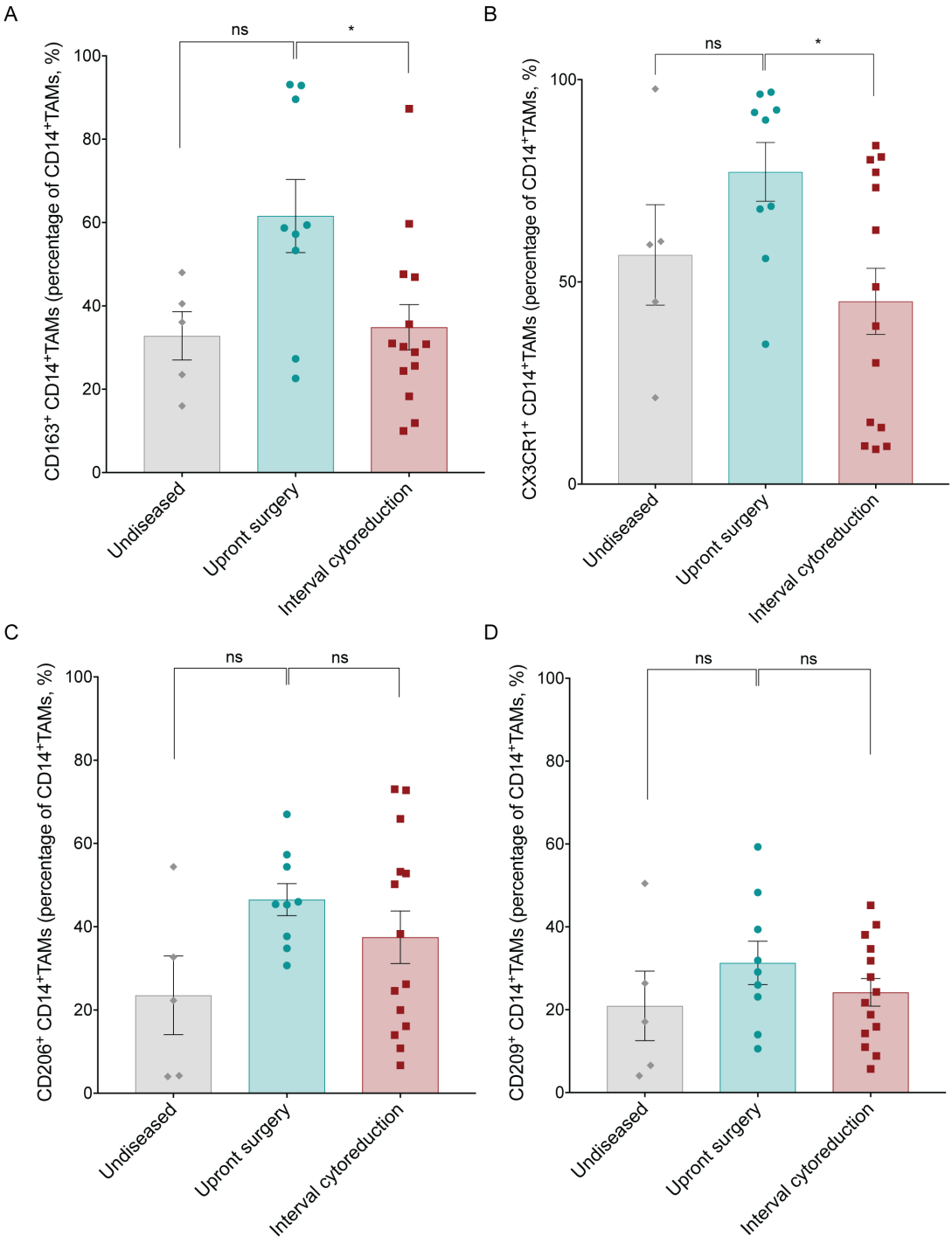

Figure 4.4 Effect of chemotherapy on CD14⁺TAM surface marker expression in human HGSOC omental metastases. Flow cytometry data demonstrating TAM (FITC⁻HLA-DR⁺) expression of **A** CD163, **B** CX3CR1, **C** CD206, **D** CD209 as a percentage of the TAM population in fourteen patients having received NACT (red), nine patients treated with upfront surgery (green) and five patients with undiseased omenta (grey). Error bars represent SEM. One-way ANOVA with Turkey's post-hoc test p values are shown; ns = non-significant, *<0.05.

To gain an understanding if these changes held at the level of the entire immune infiltrate, I quantified marker positive TAMs as a percentage of the CD45⁺ cell infiltrate. This demonstrated significant reductions CX3CR1⁺TAM (18% *vs* 5% p=0.016) (Figure 4.5) and near significant reductions of CD163⁺ (p=0.06) and CD206⁺ (p=0.09) TAMs as a

percentage of the total CD45$^+$ population. This suggests robust changes in TAM phenotype following chemotherapy discernible at the level of the entire immune infiltrate. The comparison to undiseased tissue suggests that TAM density and marker-positive TAM density was very similar to that seen after NACT. However, the data were not statistically significant between untreated and undiseased samples, due to the small number of patients in the undiseased group. However, based on the mean values with a larger sample size these differences are also likely to be significant. Taken together the data show that chemotherapy is acting to 'normalise' the TAM population towards that of undiseased tissue.

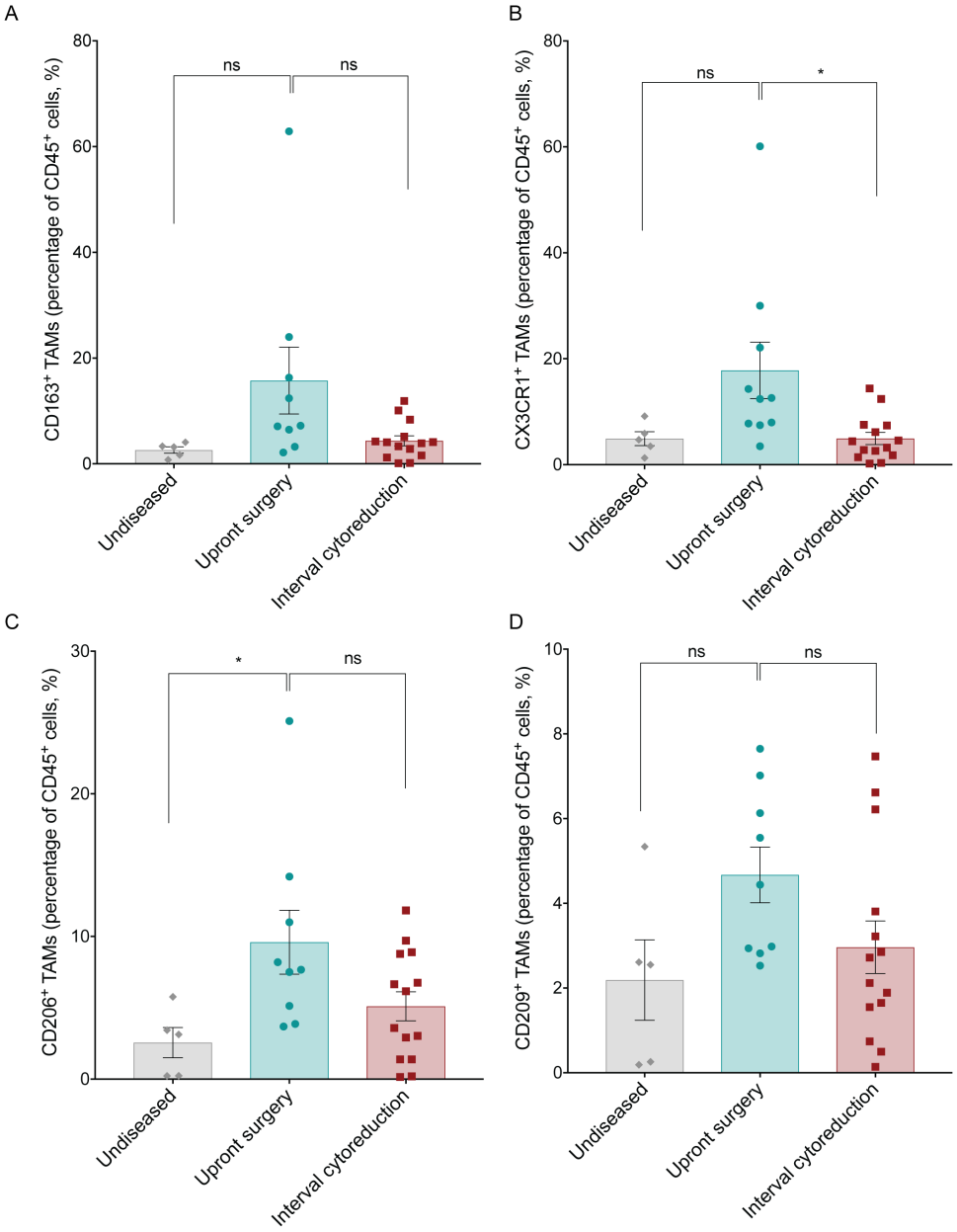

Figure 4.5 Effect of chemotherapy on TAM surface marker expression in human HGSOC omental metastases. Flow cytometry data demonstrating TAM (FITC$^-$HLA-DR$^+$) expression of **A** CD163, **B** CX3CR1 **C** CD206, **D** CD209, as a percentage of the CD45$^+$ cell population in fourteen patients having received NACT (red), nine patients treated with upfront surgery (green) and five patients with undiseased omenta (grey). Error bars represent SEM. One-way ANOVA with Turkey's post-hoc test p-values are shown; ns = non-significant, *<0.05.

Given the changes in the percentage of positive cells I wished to quantify the mean fluorescence intensity (MFI) values for these markers within the TAM population (Figure 4.6). I normalised MFI values to the fluorescent minus one control acquired at the same time to account for variation in cytometer laser calibration over time. These data recapitulated the percentage positive cell analysis and demonstrated significant reductions of CX3CR1 (8.22 a.u. *vs* 3.05 a.u. p=0.0008) and CD163 MFI (8.53 a.u *vs* 2.45 a.u. p=0.027). In view of the significant decrease in CD163, a marker of alternatively activated macrophages, I looked for reciprocal changes in markers of classical macrophage activation. However, I observed no significant difference in MFI value for the MHC Class II molecule HLA-DR (Figure 4.6A).

Taken together, these data show that chemotherapy alters the surface expression of canonical macrophage activation markers in omental metastases of HGSOC suggesting a change in macrophage phenotype.

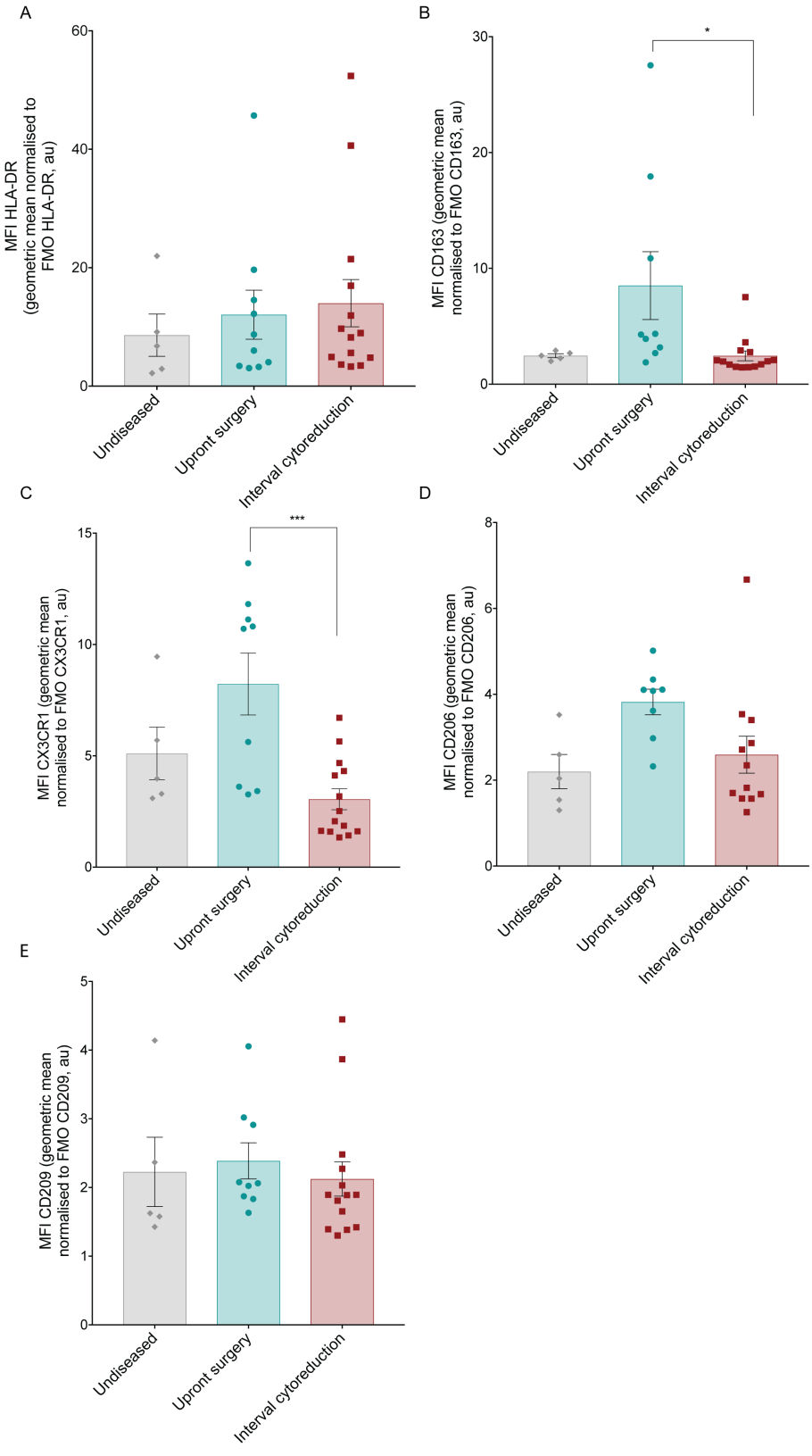

Figure 4.6 Effect of chemotherapy on TAM surface marker expression in human HGSOC omental metastases. Flow cytometry data demonstrating TAM ($FITC^{-}HLA\text{-}DR^{+}$) MFI of **A** HLA-DR, **B** CD163, **C** CX3CR1 **D** CD206, **E** CD209 in fourteen patients having received NACT (red), nine patients treated with upfront surgery (green) and five patients with undiseased omenta (grey). Error bars represent SEM. One-way ANOVA with Turkey's post-hoc test p-values are shown; ns = non-significant, *<0.05, ***<0.001.

4.2.1 Chemotherapy increases macrophage cell death

In Chapter 3 I found extensive stromal lakes of $CD68^+$ macrophages. However, as assessed by FC, viable TAMs showed a trend to a decrease in post-NACT samples compared to untreated samples (Figure 4.2). This discrepancy in my observations led me to consider that chemotherapy may increase cell death within the TAM population or render TAMs more susceptible to destruction during tissue processing. To investigate this possibility, I determined the number of non-viable TAMs for each patient sample. As shown in Figure 4.7 there was a significant increase in non-viable TAMs as a percentage of all TAMs in chemotherapy treated samples compared to untreated and undiseased samples. These data rely on gating dead cells which may non-specifically bind antibody and this is an acknowledged potential source of error. However, the differences between the groups suggests that there are more dead or dying TAMs post-NACT than in untreated samples which could potentially reside within stromal 'lakes'.

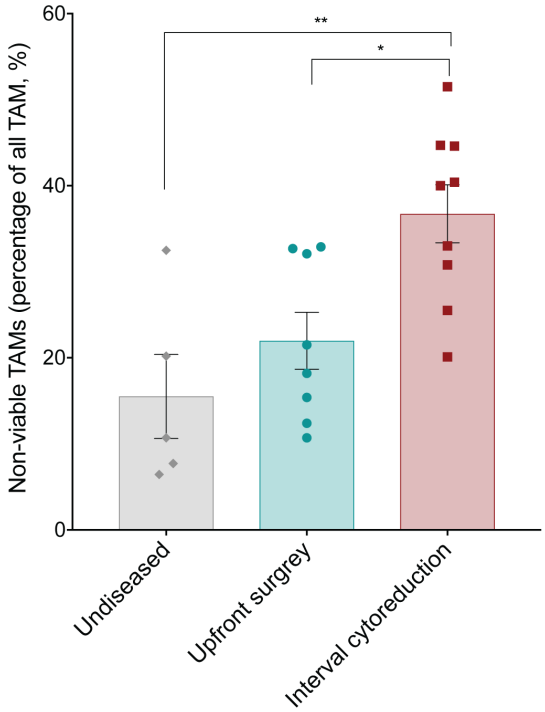

Figure 4.7 Assessment of non-viable TAMs in human HGSOC pre and post-chemotherapy and in uninvolved omentum. Flow cytometry data demonstrating non-viable (FVD positive) TAM ($FITC^-HLA\text{-}DR^+$) as a percentage of all TAMs in nine patients having received NACT (red), eight patients treated with upfront surgery (green) and five patients with undiseased omenta (grey). Error bars represent SEM. One-way ANOVA with Turkey's post-hoc test p-values are shown; *<0.05, **<0.01.

4.3 Effect of chemotherapy on CD14/CD16 myeloid subsets in HGSOC omental metastases

Subsets of human blood monocytes have been defined on the basis of CD14 and CD16 (FcγRIII) surface co-expression. 'Classical' monocytes are defined as $CD14^{++}CD16^{-}$ and these account for the majority (~90%) of circulating monocytes. Two $CD16^{+}$ monocyte subsets have been defined based on relative expression of CD16, these are $CD14^{+}CD16^{+}$ termed 'intermediate' monocytes and $CD14^{+}CD16^{++}$ termed 'non-classical' monocytes[285]. Non-classical monocytes are frequently expanded in pathological inflammatory states and Cassetta *et al.* show that non-classical monocytes are expanded in the patients with breast and endometrial cancer[133]. It is not completely understood if specific monocyte subsets give rise to different populations of macrophages within tissues. Clear differentiation of macrophage phenotypes based on CD14/CD16 expression has not been described, however, CD16 has been regarded as a marker of an inflammatory (classically activated) phenotype[286] and has been shown to be important in myeloid ADCC[287] and may be associated with improved outcome in CRC patients[288].

To gain an appreciation of how CD14 and CD16 markers changed between undiseased and pre- and post-chemotherapy diseased samples, I compared CD14 and CD16 co-expression within the TAM population in these three groups (Figure 4.8A). CD14 was expressed on a majority of HGOSC TAM, with less than five percent of the $CD45^{+}$ population being CD14-negative. $CD14^{+}CD16^{+}$ cells were expanded in pre-chemotherapy diseased samples compared to undiseased controls. In chemotherapy-treated samples there were no significant changes in $CD14^{+}CD16^{+}$ and $CD14^{+}CD16^{-}$ subsets compared to pre-treatment samples. However, there was a significant increase in $CD14^{-}CD16^{-}$ myeloid cells in post-treatment compared to pre-treatment samples. This suggests an expansion of DCs within the myeloid population post-chemotherapy.

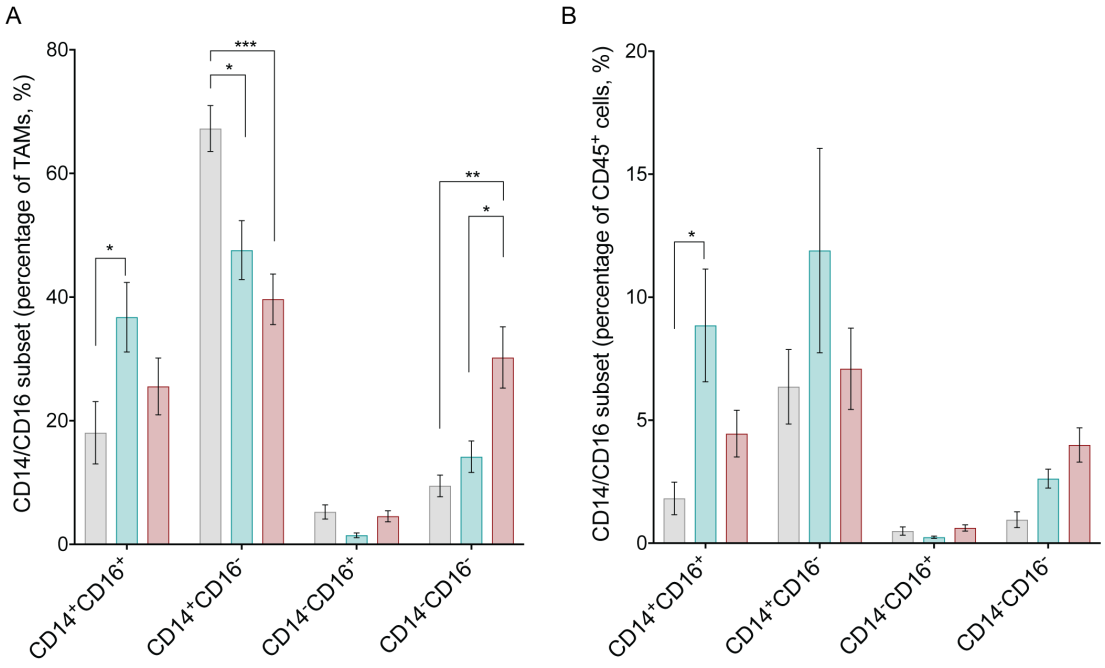

Figure 4.8 CD14/CD16 myeloid subsets with the HGSOC samples pre and post-chemotherapy and uninvolved tissues. Flow cytometry data on CD14/CD16 subsets as a percentage of **A** myeloid cells and **B** $CD45^+$ cells in fourteen patients having received NACT (red), nine patients treated with upfront surgery (green) and five patients with undiseased omenta (grey). Error bars represent SEM. Two-way ANOVA with Turkey's post-hoc test p-values are shown; ns = non-significant, *<0.05, **<0.01, ***<0.001.

4.4 Effect of chemotherapy on DCs in HGSOC omental metastases

I next divided the $CD14^-CD16^-$ population into conventional DC (cDC) and plasmocytoid DC (pDCs) populations on the basis of CD123 and CD11c expression (Figure 4.1). These results show that cDC represent the greater population of DC in both untreated and treated samples. Interestingly with chemotherapy exposure there was a significant increase in cDCs compared to untreated and undiseased samples (Figure 4.9).

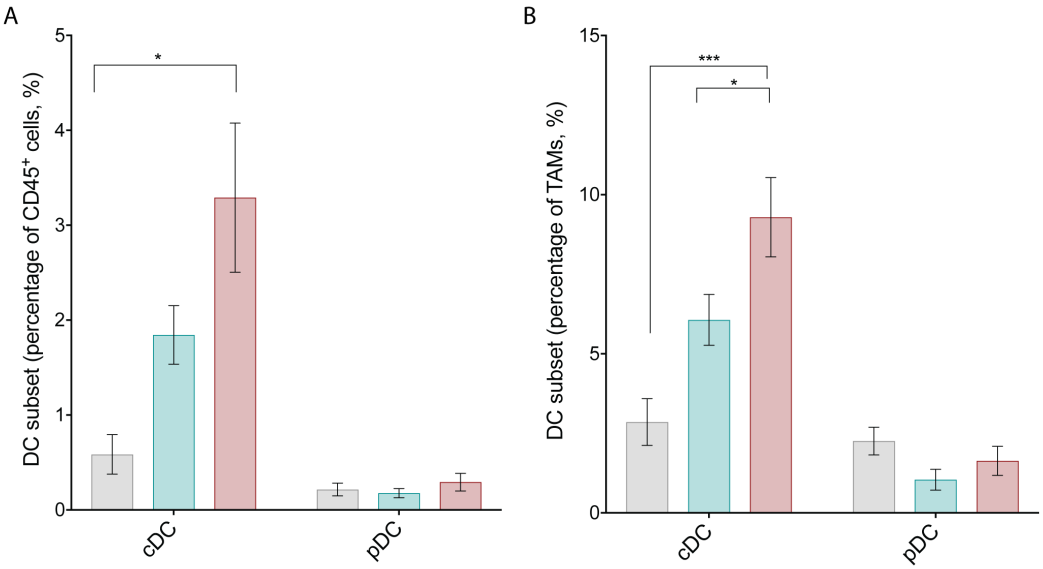

Figure 4.9 Dendritic cell phenotypes of HGSOC samples pre and post-chemotherapy and in uninvolved tissues. Flow cytometry data cDC ($CD14^-CD16^-CD123^-CD11c^+$) and pDC ($CD14^-CD16^-CD123^+CD11c^-$) as a percentage of **A** $CD45^+$ cells and **B** cells in the 'TAM gate' in fourteen patients having received NACT (red), nine patients treated with upfront surgery (green) and five patients with undiseased omenta (grey). Error bars represent SEM. Two-way ANOVA with Turkey's post-hoc test p-values are shown; ns = non-significant, *<0.05, **<0.01

Further characterisation within the cDC gate by CD141 and CD1c demonstrated the majority of the cDC gate to be $CD141^-CD1c^-$ (double negative, DN) cells and furthermore this population was significantly increased in chemotherapy treated compared to untreated samples (Figure 4.10).

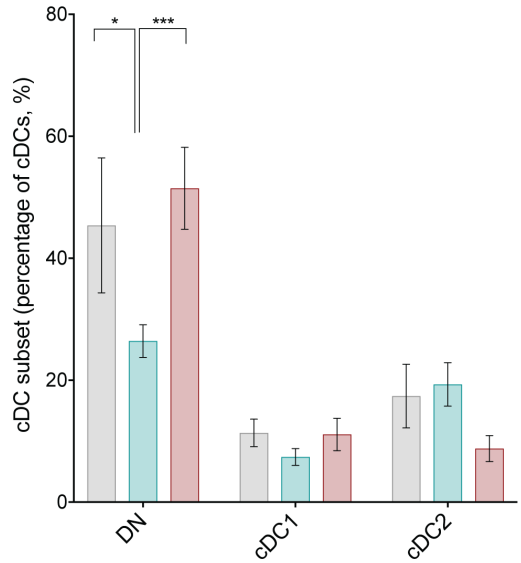

Figure 4.10 cDC phenotypes of HGSOC samples pre and post-chemotherapy and in uninvolved tissues. Flow cytometry data showing DN cells ($CD14^-CD16^-CD123^-CD11c^+CD141^-CD1c^-$), cDC1 ($CD14^-CD16^-CD123^-CD11c^+CD141^+CD1c^-$) and cDC2 ($CD14^-CD16^-CD123^-CD11c^+CD141^-CD1c^+$) as a percentage of cDC cells in fourteen patients having received NACT (red), nine patients treated with upfront surgery (green) and five patients with undiseased omenta (grey). Error bars represent SEM. Two-way ANOVA with Turkey's post-hoc test p-values are shown; *<0.05, ***<0.001.

In conclusion these data support an increase in dendritic cells post chemotherapy. $CD141^{-}CD1c^{-}$ cDCs appear to be the dominant DC phenotype within HGSOC and are significantly increased following chemotherapy exposure.

4.5 Discussion

In this chapter I first assessed TAM phenotype in HGSOC before and after chemotherapy and in undiseased omental tissue. I found a significant reduction in the surface protein expression of $CD163^{+}$ and $CX3CR1^{+}$ TAMs after chemotherapy compared to pre-chemotherapy samples (Figure 4.3A,B; Figure 4.4A,B). I also observed a decrease, although not statistically significant with this number of patients, in CD206 expression. This suggests that chemotherapy may alter TAM phenotype. As the last dose of chemotherapy was an average of three-four weeks preceding interval surgery, these data suggest durable changes of TAM phenotype.

Reduction of CD163 and CD206 surface expression suggests a change in TAM activation from an alternatively activated towards a classically activated phenotype. Interestingly, and consistent with these data, in human PDAC, $CD206^{+}$ TAMs significantly decreased following chemotherapy compared to untreated samples, suggesting that chemotherapy curbs the immunosuppressive microenvironment of this disease[188]. In HGSOC, CD163-high TAM were enriched for matrix pathways whereas CD163-low TAM were enriched for interferon signalling pathways[289]. CD163 expression is associated with decreased survival and a shorter time to relapse[197,198,289]. In contrast to my data, an *in vitro* study by Dijkgraaf *et al.* showed that platinum-based chemotherapy treatment of ovarian cancer cells lines co-cultured with monocytes enhanced M2 polarisation[217]. Furthermore, in murine models of breast cancer and in patient samples chemotherapy increased tumour promoting macrophages[220,222].

To assess for reciprocal changes in a marker of classical macrophage activation, I quantified MHC Class II expression. There was no significant difference in MHC Class II expression on TAM between pre and post-chemotherapy samples (Figure 4.6A). This suggests a change of macrophage phenotype distinct from the simplistic M1 (classically activated)-M2 (alternatively activated) model. Mirroring my data, Reinartz *et al.* showed that CD163 is highly expressed on HGSOC TAM, but did not associate clearly with other canonical M1 (classically activated)/M2 (alternatively activated) markers[198]. Therefore, selective reductions in CD163 expressing TAMs may be independent of an M1 (classically activated)/M2 (alternatively activated) phenotype change, yet reflect an anti-tumoural myeloid phenotype associated with improved patient outcome.

As discussed in Chapter 1 high CX3CR1 surface expression is a marker for self-renewing populations of macrophages in healthy tissue[290] and in tumour microenviroments[139] in mice. I observed CX3CR1 expression at higher levels in undiseased tissue than the other macrophage surface markers (~50% *vs* ~25% of the TAM population) (Figure 4.3B), which suggests this marker is associated with the tissue-resident population in the human omentum. In murine models of PDAC $CX3CR1^+$ tissue-resident macrophages were significantly enriched for matrix secretion and remodelling pathways, whereas recruited bone-marrow derived cells upregulated genes relating to antigen presentation[139]. I show chemotherapy causes a reduction in $CD163^+$ and $CX3CR1^+$ macrophages which have both been linked to roles in matrix remodelling and fibrosis. Collectively, these data suggest TAM phenotype following chemotherapy may be associated with improved clinical outcome in HGSOC; furthermore, chemotherapy may selectively deplete a tissue-resident macrophage-derived TAM population.

In Chapter 3 I observed chemotherapy-associated macrophage lakes, however, I observed no significant changes in TAM density by flow cytometry (Figure 4.2). This suggested that TAMs may be either dying as a result of chemotherapy exposure or being rendered more sensitive by tissue processing during FC. This finding fits with others that have shown increases in TAM death in inflammatory states[291]. M1/classically activated macrophages may be killed by their own NO production or via Fas-mediated processes[291]; this has led to the suggestion that classically activated macrophages may represent a terminal differentiation phenotype, with the natural endpoint of most of these cells being death within tissues[291].

$CD14^-CD16^-$ cells were significantly expanded with chemotherapy treatment compared to untreated and undiseased samples (Figure 4.8). This suggests chemotherapy resulted in an increase in DCs. Given the role of DCs as antigen presenting cells, DCs may expand in response to increased tumour antigen load following chemotherapy. Plasmacytoid DCs (pDCs) are characterised by expression of the surface marker CD123 in humans[284]. These cells have well-described roles in viral immunity and are rapid and potent producers of type I and type III IFNs[284]. Conventional DCs (cDCs) can be subdivided in to cCD1 and cDC2 cells on the basis of surface expression of CD141 and CD1c respectively[284]. cDC1 cells have particular roles of antigen cross presentation via MHC class I to $CD8^+$ T-cells cells whereas cDC2 cells are regarded as migratory and express TLRs, NOD and RIG-I-like receptors suggesting roles in response to diverse stimuli. They can secrete broad range of cytokines (IL1, IL8, IL-10, IL-12 and IL-23) but are low in the secretion of IFN.

In this analysis, cDC1 and cDC2 cells were very minor populations. The major dendritic cell population appeared to be double negative (DNcDC) for CD141 and CD1c. In support of this finding, in a recent study in head and neck cancer, DNcDC was the population most significantly expanded in malignant compared to benign tonsil[292]. Furthermore, transcriptomic profiling of these cells showed enrichment for IFN, IL6 and PGE_2 signalling pathways compared to this population in non-malignant tissue[292]. Given the importance of DCs in activating adaptive immune responses, coupled with their expansion seen after chemotherapy, my results suggest that chemotherapy creates the potential for enhancement of adaptive immunity in HGSOC. This finding expands previous work in our lab which has shown that NACT enhances adaptive anti-tumour immunity in HGSOC in studies of T and B cell populations [113,114].

In conclusion these results show significant downregulation of CD163 and CX3CR1 on the cell surface of TAMs in chemotherapy treated compared to chemotherapy naïve patients. Both these markers have been associated with extracellular matrix remodelling and are linked to poor prognosis in cancer TMEs. DC increased significantly after chemotherapy exposure. $CD141^{-}CD1c^{-}$cDC appear to be a dominant population of DC in the TME of HGSOC and expansion of this population accounted for the increases seen in this cell type overall.

In the next chapter I will build on these data and assess the HGSOC TAM transcriptome by RNA-sequencing before and after chemotherapy.

Chapter 5

The transcriptome of human HGSOC TAMs pre and post-chemotherapy

5.1 Background

RNA-sequencing allows for sensitive and accurate measurement of gene expression across the entire transcriptome. This approach offers advantages over gene microarrays by allowing global coverage of the transcriptome and is not limited by prior knowledge of gene function. TAMs are characterised by diversity and plasticity of function and phenotype; therefore RNA-sequencing offers the best approach to the assessment of TAM pathways and processes in a global and unbiased manner.

As discussed in Chapter 1, few studies have examined the transcriptome of TAMs in HGSOC[198,199,289,293,294] and these have used ascites-derived TAMs rather than TAMs from tumour samples. These publications report that TAM gene expression is more similar to that of resident peritoneal macrophages than to monocytes. The most significant differences in gene expression between TAMs and resident macrophages were in genes regulating extracellular matrix (ECM) formation and remodelling[199].

In this chapter I will explore the effects of chemotherapy on TAMs by performing RNA-sequencing of TAMs from human HGSOC omental metastases before treatment and following NACT.

5.2 Transcriptomic analysis of TAMs in HGSOC omental metastases

$CD14^+$ myeloid cells were obtained by fluorescent activated cell sorting (FACS) from human omental biopsy samples acquired at primary or interval cytoreductive surgery. Figure 5.1 shows the gating strategy employed from a representative biopsy sample. Within the FITC channel I stained for the lineage markers CD3, CD20, CD19, CD56, CD66b and Siglec 8. By gating for $FITC^-$ cells I was able to exclude cells expressing these markers. $CD14^+$TAMs were defined as cells being $CD45^+HLA\text{-}DR^+FITC^-CD14^+$ and were sorted as a bulk population obtaining between 250,000-750,000 cells per sample. $CD14^+$TAMs were chosen as the population to sequence to limit the analysis to TAMs and exclude $CD14^-$ myeloid cells, which would also be enriched for dendritic cells.

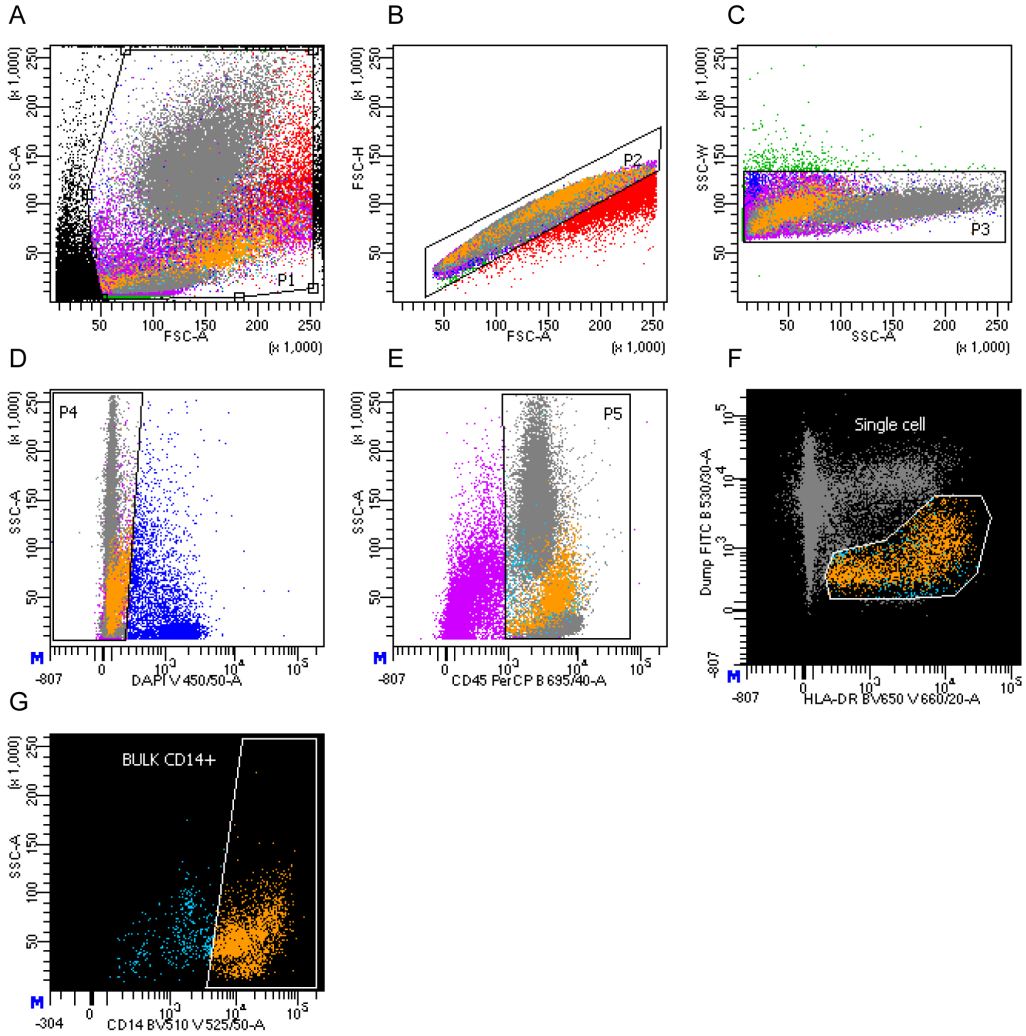

Figure 5.1 Multicolour flow cytometry gating strategy to sort TAMs for RNA-sequencing. Density plots from a representative patient sample showing the immuno-stained stromal vascular fraction from a human omental HGSOC metastasis. **A** Gating to exclude cellular debris, **B**, **C** sequential gating to exclude doublet cells, **D** sequential gating to exclude non-viable cells, **E** sequential gating for $CD45^+$ cells, **F** sequential gating for $FITC^-HLA\text{-}DR^+$ cells. **G** Sequential gating for $CD14^+$. $CD14^+$TAMs sorted as a bulk population. *SSC-A*: forward scatter area, *SSC-W*: side scatter width, *FSC-A*: forward scatter area, *FSC-H*: forward scatter height.

Immediately following sorting, TAMs were lysed and the lysates were stored at -80°C. RNA was extracted using established protocols. Prior to RNA-sequencing, RNA concentration, purity and integrity were assessed. Table 5.1 shows the RNA concentration and RNA integrity number (RIN) values obtained. These values showed that the RNA was of sufficient quality and concentration for sequencing. TAM RNA from seven post-NACT samples and five pre-treatment samples was sequenced on the HiSeq4000 with 30-40 million reads per sample at the Welcome Trust Centre for Human Genetics. Raw reads were aligned to the reference genome GRCh37 (hg19). The sequence-aligned data were then analysed by Dr. Eleni Maniati (BCI Core Bioinformatics Service).

Sample ID	RNA concentration (ng/ul)	260/280 absorbance ratio	260/230 absorbance ratio	RIN
SG0004	11.3	2	0.41	8.7
SG0005	27.3	2.24	0.31	8.6
SG0011	12.5	2	1.32	N/A
SG0012	29.3	2.02	0.99	10
SG0013	26.7	2.14	0.93	9.2
SG0020	43.5	1.96	1.56	8.4
SG0021	48.4	2.05	1.65	8.7
SG0024	57.5	2.02	1.37	9.3
SG0026	547.9	2.09	2.14	9.3
SG0027	48.7	1.93	0.66	8.4
SG0028	30.8	2.1	0.12	8.5
SG0029	73.9	1.77	1.29	9.3

Table 5.1 RNA quality analysis. Table summarising the RNA concentration obtained from TAMs flow sorted from HGSOC. 260/80 and 260/230 absorbance ratios are shown as is the RNA integrity number (RIN).

Only genes that achieved at least one read count per million reads (CPM) in at least 25% of the samples were kept. This led to 16,253 sufficiently quantified genes in total, 12,614 of which were protein coding genes. Figure 5.2 demonstrates, as expected, a high expression of macrophage genes relative to lineage genes of other cell types. Sample SG0012 and SG0026 had a higher epithelial cell gene expression profile (EPCAM, PAX8, WT1) compared to other samples, suggesting a possible contamination of these samples with malignant cells. However, overall these data demonstrate good quality of TAM sorting, with minimal contamination of other cell types.

		SG0012M_pre	SG0013M_pre	SG0021M_pre	SG0024M_pre	SG0026M_pre	SG0027M_post	SG0028M_post	SG0029M_post	SG0004M_post	SG0005M_post	SG0011M_post	SG0020M_post
Macrophage	CD14	8.89	9.81	9.48	8.93	9.51	9.05	8.88	9.23	9.47	8.71	9.32	9.59
	MARCO	8.17	8.46	4.34	5.06	2.87	7.09	6.53	6.35	6.90	3.97	7.07	7.07
	MSR1	8.97	8.84	7.17	7.42	8.77	7.33	7.56	8.05	8.79	4.71	6.92	7.33
	CD163	9.12	9.36	7.35	8.54	7.85	8.28	8.69	8.03	9.24	8.19	8.40	7.79
	EMP1	5.20	5.34	6.47	6.12	3.21	5.41	5.11	6.58	4.81	1.88	5.53	5.72
	CD68	-2.97	-1.97	-0.31	-2.57	-1.84	-1.88	-1.63	-0.54	-1.25	-0.79	-0.46	-0.74
Tcell	CD3E	ND	ND	ND	ND	ND	ND	ND	ND	ND	ND	ND	ND
	CD3G	ND	ND	ND	ND	ND	ND	ND	ND	ND	ND	ND	ND
	CD3D	-0.70	-2.15	-3.69	-3.91	-0.80	-1.69	-3.05	-2.49	-2.24	-3.46	-0.52	-3.86
	LCK	-0.79	-2.01	-4.03	-4.57	-1.33	-1.75	-4.75	-2.15	-2.79	-3.10	-0.77	-3.16
	LEF1	ND	ND	ND	ND	ND	ND	ND	ND	ND	ND	ND	ND
Bcell	CD19	ND	ND	ND	ND	ND	ND	ND	ND	ND	ND	ND	ND
	CR2	ND	ND	ND	ND	ND	ND	ND	ND	ND	ND	ND	ND
	TCL1A	ND	ND	ND	ND	ND	ND	ND	ND	ND	ND	ND	ND
	BACH2	-3.18	-1.84	-0.65	-1.61	-3.16	-2.26	-1.73	-1.96	-2.69	-2.06	-2.11	-0.91
Gr/cyte	MME	-2.95	-2.70	-1.82	-4.61	-5.71	-4.05	-1.20	-4.03	-4.40	-0.42	-0.67	-3.55
	IL8RA	ND	ND	ND	ND	ND	ND	ND	ND	ND	ND	ND	ND
	IL8RB	ND	ND	ND	ND	ND	ND	ND	ND	ND	ND	ND	ND
Mast	PRG2	ND	ND	ND	ND	ND	ND	ND	ND	ND	ND	ND	ND
	SIGLEC6	ND	ND	ND	ND	ND	ND	ND	ND	ND	ND	ND	ND
Epithel.	EPCAM	1.24	-4.70	-2.30	-0.50	2.80	-3.82	-2.56	-0.17	-0.68	-1.86	-5.19	-3.67
	PAX8	1.79	-0.82	-0.21	1.18	1.63	-0.87	-0.37	0.89	-0.16	-1.66	-0.17	-1.20
	WT1	1.75	-1.54	-1.85	-0.82	1.66	-2.16	-1.43	-1.17	-1.31	-2.01	-2.83	-2.50

Figure 5.2 Assessment of lineage genes expression in sorted myeloid populations. Log_2RPKM expression of the indicated genes in the twelve sequenced samples. Data demonstrate a high abundance of macrophage lineage genes compared to genes characteristic of other cell lineages. Colour gradient indicates high (red) to low (blue) gene expression range. ND = Not detected.

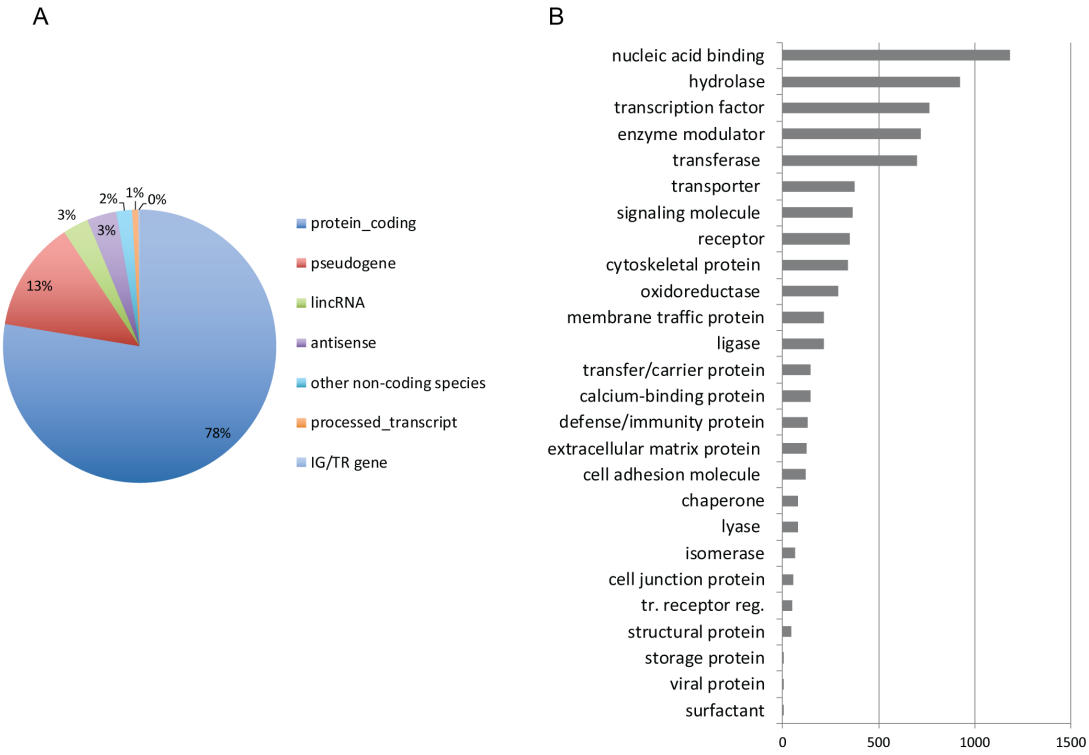

Figure 5.3 Distribution of RNA species and classification of protein coding genes. **A** distribution of RNA species and **B** classification of protein coding genes. Data represent the twelve patients included in this analysis.

Figure 5.3 shows the distribution of the RNA species and the classification of protein coding genes further confirming the quality of sequencing. Nucleic acid binding proteins were most abundant, other highly represented functional groups included receptors and signalling molecules. This is in keeping with TAM responding to multiple environmental stimuli in the TME of HGSOC. The coefficient of variation (square root of common dispersion) was 0.45 (Figure 5.4A). Although this is a large value, it is not atypical for human data generated from a small number of independent samples. Multidimensional scaling showed distances in terms of the biological co-efficiency of variation between samples, and provided an overview of the expressional differences between the samples (Figure 5.4B).

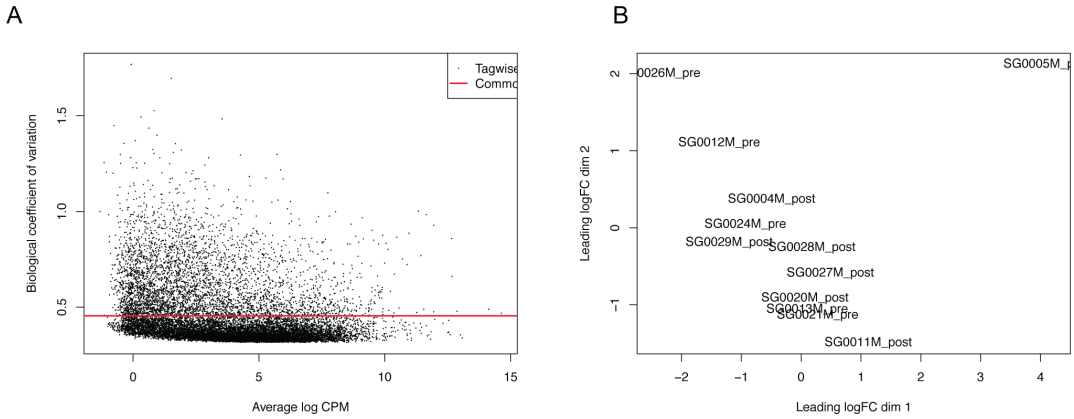

Figure 5.4 Assessment of biological variability within the data. A Scatter plot of tagwise dispersions against log_2 counts per million. **B** Multidimensional scaling plot shows distances in terms expression differences between samples.

Using protein coding genes, unsupervised clustering was performed by hierarchical cluster analysis. Only partial separation of the samples by chemotherapy status was observed (Figure 5.5). This could be explained by the low number of samples sequenced and the high degree of variability seen, especially in genes that were expressed at low levels (Figure 5.4).

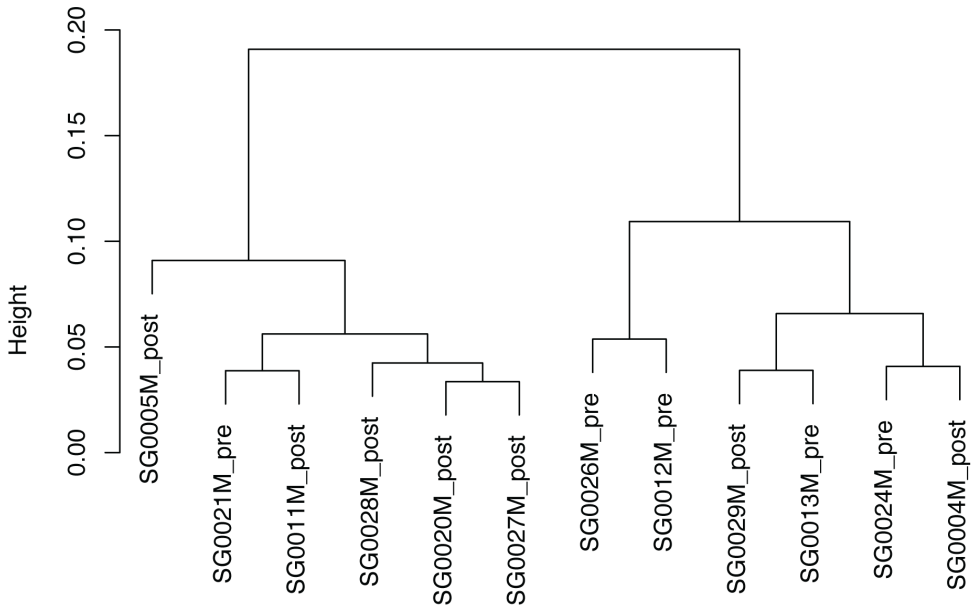

Figure 5.5 Hierarchical cluster analysis. Hierarchical cluster analysis performed on a Pearson's correlation matrix of normalized read counts. Data represents five patients pre-chemotherapy and seven patients post NACT.

Differential expression analysis was performed using a generalised linear model to subset genes with statistical significance (p-value < 0.05). There were 858 protein-coding genes with a statistically significant difference in HGSOC TAM post-NACT *vs* pre-chemotherapy. Of these 81 were up regulated and 777 down regulated post-NACT.

Figure 5.6 shows a heat map of the differentially expressed protein coding genes across the twelve samples. Figure 5.7 shows a volcano plot of the up- and down regulated genes in the analysis.

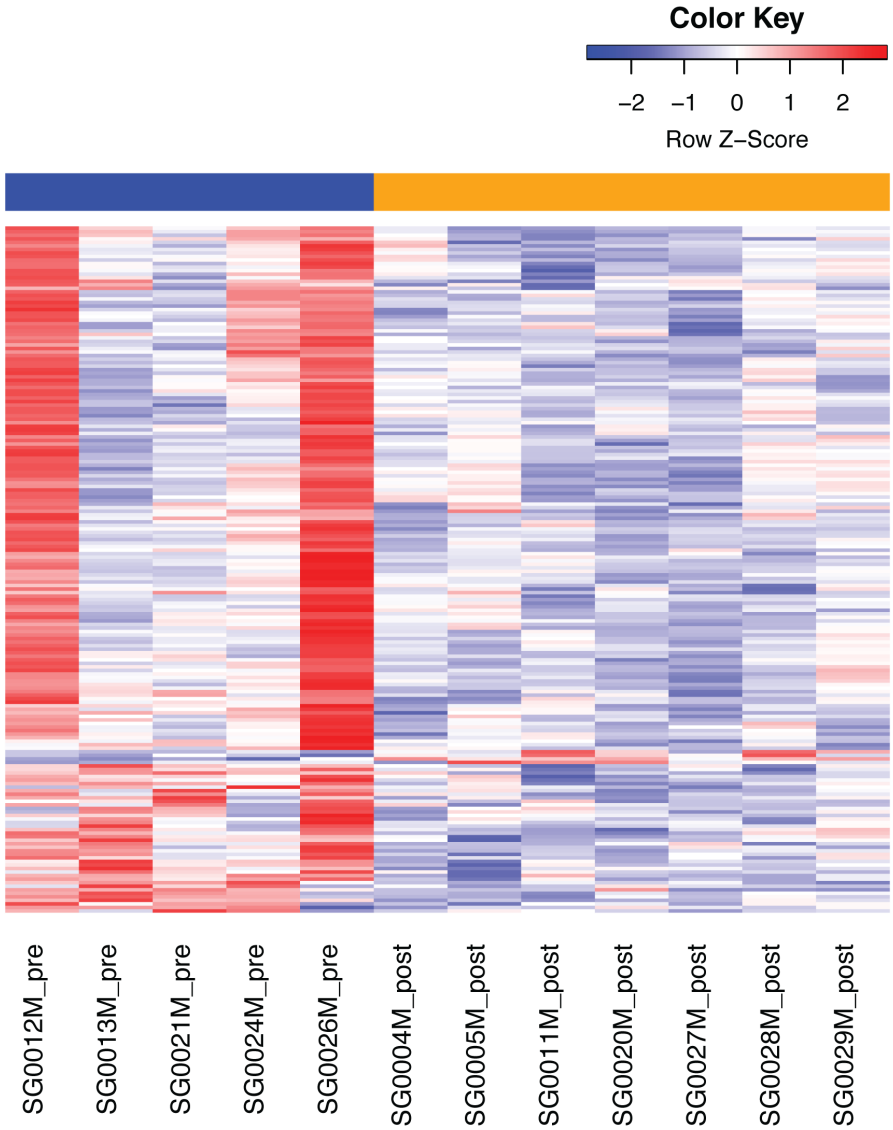

Figure 5.6 Heat map of differentially expressed protein coding genes. Data represents gene expression of five patients pre-chemotherapy (blue bar) and seven patients post neo-adjuvant chemotherapy (yellow bar). Color range indicates high (red) to low (blue) z-scores, which correspond to high and low expression levels respectively.

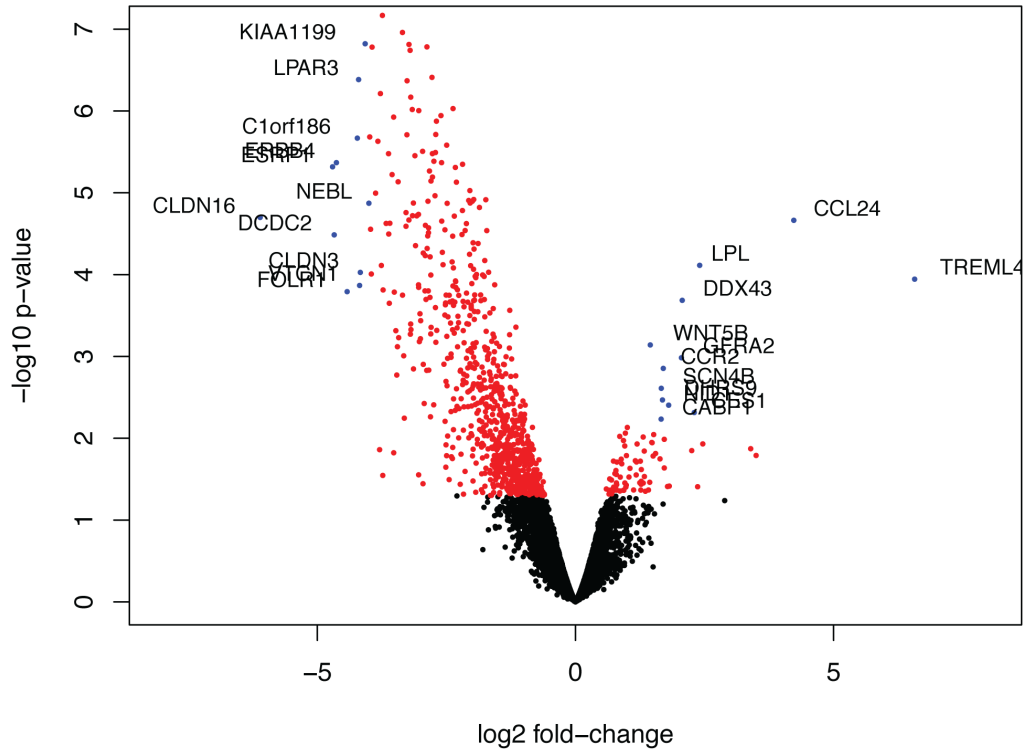

Figure 5.7 Volcano plot illustrating protein-coding genes that were differentially expressed in post *vs* pre-chemotherapy TAM. In red are statistically significant genes (p-value < 0.05). The names of upregulated genes with log_2FC >0 p< 0.05 (FDR <0.25) and downregulated genes log_2FC <-4 p< 0.05 (FDR <0.25) are also shown and marked in blue.

Gene name	Description	logFC	logCPM	LR
TREML4	triggering receptor expressed on myeloid cells-like 4	6.5695	1.0599	14.896
CCL24	chemokine (C-C motif) ligand 24	4.229	4.8958	18.035
RP11-219A15.1	Coiled-coil domain-containing protein 144A	3.4988	-0.092	5.7779
CCDC144A	coiled-coil domain containing 144A	3.3941	2.3834	6.1131
ZFP57	ZFP57 zinc finger protein	2.8902	0.6245	3.5993
FABP4	fatty acid binding protein 4, adipocyte	2.4662	5.5147	6.353
LPL	lipoprotein lipase	2.4057	6.499	15.631
NPIPB15	nuclear pore complex interacting protein family, member B15	2.3661	0.027	4.2559
CES1	carboxylesterase 1	2.301	3.102	7.9339
FOLR3	folate receptor 3 (gamma)	2.2521	1.6505	6.0196
DDX43	DEAD (Asp-Glu-Ala-Asp) box polypeptide 43	2.068	-0.634	13.775
GFRA2	GDNF family receptor alpha 2	2.0522	4.317	10.758
LAMP5	lysosomal-associated membrane protein family, member 5	1.8166	1.2796	4.286
NID1	nidogen 1	1.805	4.1353	8.3106
CLDN5	claudin 5	1.7832	0.545	4.2667
LGALS2	lectin, galactoside-binding, soluble, 2	1.7202	5.9085	5.1636
CPAMD8	C3 and PZP-like, alpha-2-macroglobulin domain containing 8	1.72	2.8332	6.582
CCR2	chemokine (C-C motif) receptor 2	1.7008	7.3355	10.206
DHRS9	dehydrogenase/reductase (SDR family) member 9	1.6849	4.2561	8.5782
SCN4B	sodium channel, voltage-gated, type IV, beta subunit	1.662	0.1742	9.1766

Table 5.2 Top up regulated genes following chemotherapy treatment in TAM. Table summarising the 20 most up regulated genes with the highest fold change. *logFC* log10 fold change, *logCPM* log10 counts per million, *LR* log ratio, p-value <0.05.

Gene name	Description	logFC	logCPM	LR
CLDN16	claudin 16	-6.109	3.0031	18.189
FGFR2	fibroblast growth factor receptor 2	-5.685	2.6003	35.576
ESRP1	epithelial splicing regulatory protein 1	-4.705	2.0191	20.91
DCDC2	doublecortin domain containing 2	-4.673	1.7523	17.255
ERBB4	v-erb-b2 avian erythroblastic leukemia viral oncogene homolog 4	-4.631	1.595	21.135
FOLR1	folate receptor 1 (adult)	-4.423	1.4843	14.233
C1orf186	chromosome 1 open reading frame 186	-4.226	2.2082	22.457
LPAR3	lysophosphatidic acid receptor 3	-4.201	2.0938	25.631
VTCN1	V-set domain containing T cell activation inhibitor 1	-4.182	2.1053	14.561
CLDN3	claudin 3	-4.168	1.856	15.254
KIAA1199	KIAA1199	-4.074	3.5179	27.579
NEBL	nebulette	-4.002	2.2437	18.951
WFDC2	WAP four-disulfide core domain 2	-3.985	1.7237	22.523
EMX2	empty spiracles homeobox 2	-3.969	-0.124	17.556
ERBB3	v-erb-b2 avian erythroblastic leukemia viral oncogene homolog 3	-3.955	2.2127	15.169
ESPN	espin	-3.94	-0.202	27.394
THSD4	thrombospondin, type I, domain containing 4	-3.872	3.9842	19.492
CDH3	cadherin 3, type 1, P-cadherin (placental)	-3.845	1.3482	30.389
CP	ceruloplasmin (ferroxidase)	-3.827	3.5801	22.288
BMP7	bone morphogenetic protein 7	-3.794	1.5583	6.0655

Table 5.3 Top down regulated genes following chemotherapy treatment in TAM. Table summarising the 20 most down regulated genes with the highest fold change. *logFC*: log10 fold change, *logCPM*: log10 counts per million, *LR*: log ratio, p-value < 0.05.

Table 5.2 and Table 5.3 summarise the top 20 up and down regulated genes following chemotherapy. The gene that showed the greatest fold change increase in expression was *TREML4* (triggering receptor expressed on myeloid cells-like 4), a positive regulator of TLR7 signalling. *CLDN16* (claudin 16), a component of tight junctions, was the gene showing the greatest fold change decrease in expression after chemotherapy.

Pathway analysis of the differentially expressed protein-coding genes was then performed using gene set enrichment analysis (GSEA) for gene ontology categories and canonical pathways (Figure 5.8). Amongst the top twenty significantly upregulated pathways in the post-NACT samples were activation of AKT/PI3K signaling, IL6 signaling, IL8 signaling, activation of the inflammasome and IL1β signaling. Top significantly down regulated pathways in the post-NACT TAM were ECM formation and remodeling, ECM interactions and signaling and cell cycle and proliferation pathways.

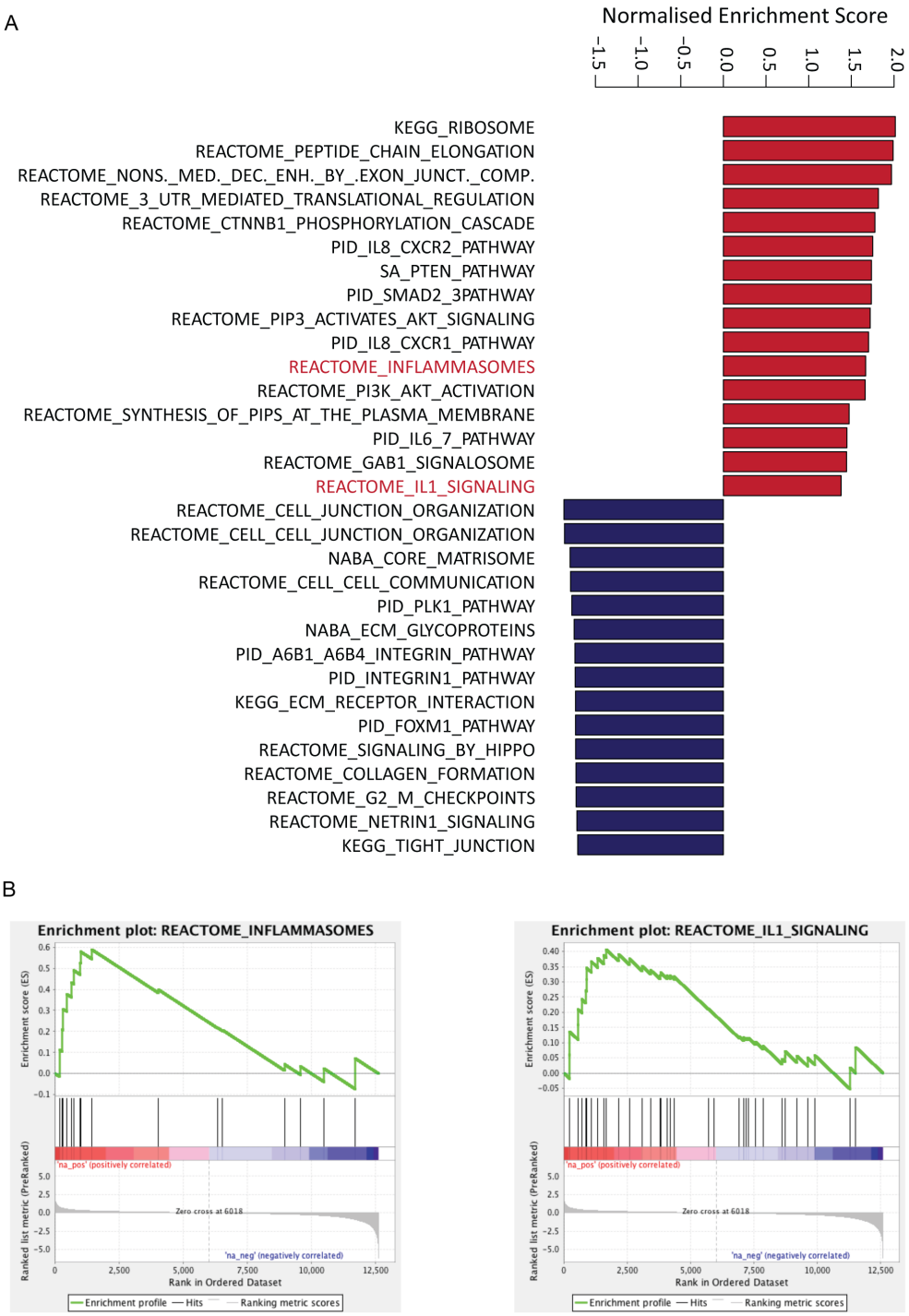

Figure 5.8 GSEA analysis of protein-coding genes differentially expressed in post-NACT *vs* treatment naïve TAMs. A Barplot shows the top enriched pathways following chemotherapy exposure (p-value <0.05). **B** Enrichment plots are illustrated for the inflammasome and IL1β signaling (highlighted in red in **A**). Positive enrichment scores correspond to upregulation in post-NACT samples, negative enrichment scores correspond to downregulation.

5.3 Comparing TAM chemotherapy-associated transcriptional reprogramming with a spectrum-model of macrophage activation

Xue *et al.* describe a spectrum-model of macrophage activation based on analysis of macrophage transcriptomes following exposure to different stimuli[295]. In this paper human $CD14^+$ monocyte-derived macrophages were stimulated *in vitro* with twenty-nine

discrete stimuli and RNA microarray analysis was performed. From this dataset forty-nine co-expressed gene modules were defined by a weighted correlation network analysis (WGCNA). To understand better TAM transcriptional reprogramming in response to chemotherapy treatment, I related the differentially expressed genes between chemotherapy treated and untreated TAMs to the spectrum-model WGCNA modules from the Xue *et al.* paper[295].

Figure 5.9 shows the correlation of the WGCNA modules with genes differentially expressed in TAM upon chemotherapy exposure. The most significantly positively correlated modules were “MEGreen”, “MESienna3”, “MEPaleturquiose” and “MEDarkgrey”. GSEA was then performed within each of these modules. In support of the pathway analysis performed previously, within these four modules pathways relating to IL1 response, TLR signalling, IFNγ signalling, positive regulation of NFκB signalling, antigen presentation, apoptosis and programmed cell death were significantly upregulated (Table 5.4, Table 5.5, Table 5.6, Table 5.7).

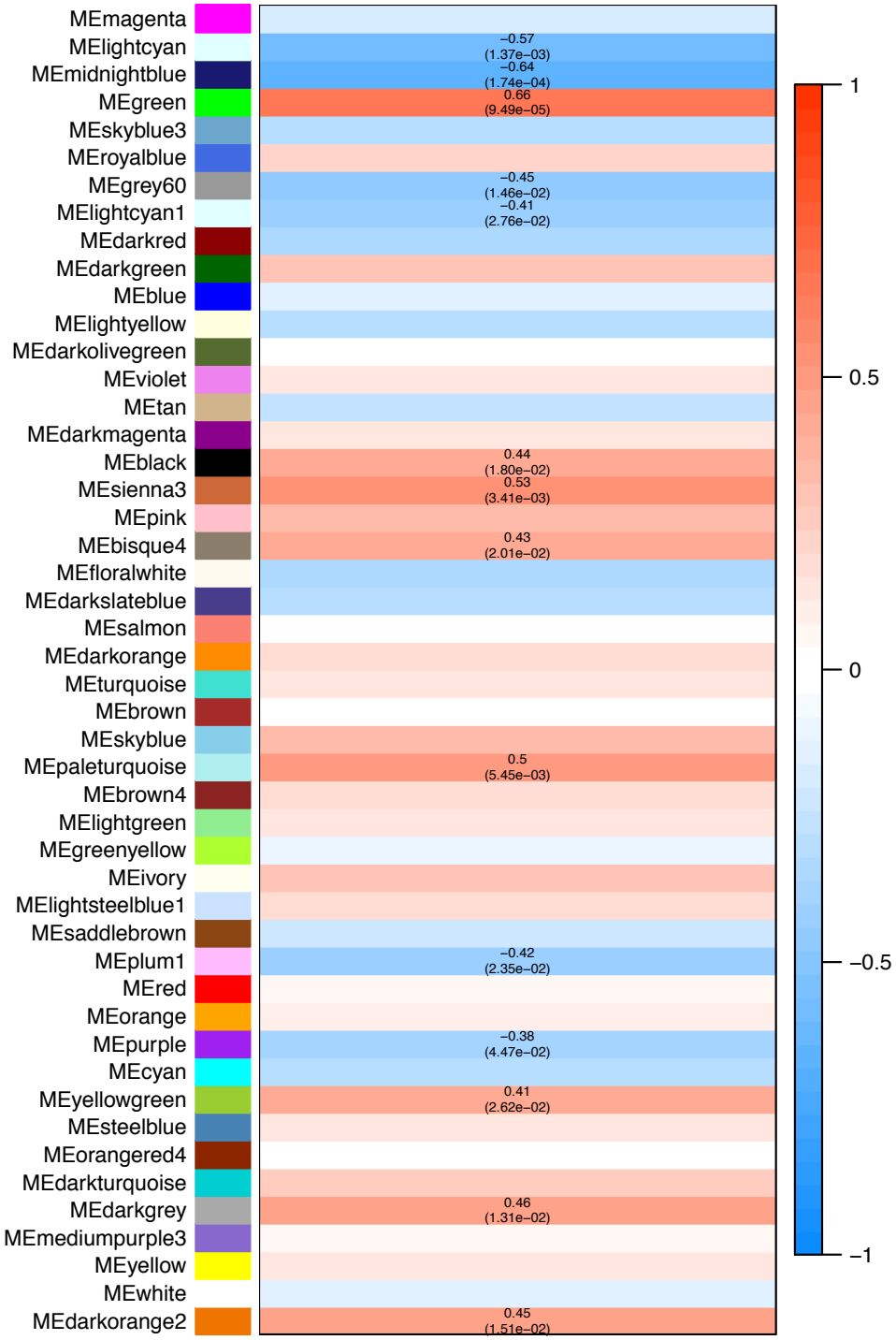

Figure 5.9 Heat map showing correlation between WGCNA module and HGSOC TAM genes differentially expressed genes following chemotherapy. Heatmap summarising the correlation of module eigengene (ME) values with the differentially expressed genes in TAM following chemotherapy treatment of human HGSOC. Each module of the forty-nine modules has been ascribed a unique colour and colours name. Red indicates a positive correlation, blue indicates a negative correlation. Significant p-values are indicated.

Pathway	Z-score
phosphorylation	6.64
synaptic vesicle fusion to presynaptic membrane	8.78
positive regulation of ATPase activity	5.53
vesicle docking	5.62
heme biosynthetic process	5.07
cellular sodium ion homeostasis	4.81
Golgi to plasma membrane transport	4.39
negative regulation of cysteine-type endopeptidase activity involved in apoptotic process	3.86
cellular response to nitrogen starvation	3.9
regulation of heart contraction	3.76
cellular response to reactive oxygen species	3.9
regulation of extrinsic apoptotic signaling pathway via death domain receptors	4.05
protein oligomerization	3.63
mitochondrion degradation	3.51
DNA methylation	3.51
phosphatidylinositol phosphorylation	3.44
activation of cysteine-type endopeptidase activity involved in apoptotic signaling pathway	3.63
response to interferon-gamma	3.39
nucleophagy	3.39
negative regulation of cyclin-dependent protein serine/threonine kinase activity	3.39

Table 5.4 Enrichment analysis for Gene Ontology Biological Processes on the genes clustering in the Green WCGNA module. Table summarises the z-scores for pathways upregulated in post-NACT samples (adj. p<0.05).

Pathway	Z-score
inflammatory response	7.94
signal transduction	5.28
intrinsic apoptotic signaling pathway in response to endoplasmic reticulum stress	8.05
amino acid transport	7.37
cellular response to interleukin-1	7.5
nucleotide-binding domain, leucine rich repeat containing receptor signaling pathway	6.47
chromosome segregation	4.99
toll-like receptor 2 signaling pathway	4.73
toll-like receptor 5 signaling pathway	5.08
toll-like receptor 9 signaling pathway	4.77
toll-like receptor 10 signaling pathway	5.08
response to endoplasmic reticulum stress	4.9
toll-like receptor TLR1:TLR2 signaling pathway	4.82
toll-like receptor TLR6:TLR2 signaling pathway	4.82
neurotrophin TRK receptor signaling pathway	4.38
positive regulation of NF-kappaB transcription factor activity	4.55
TRIF-dependent toll-like receptor signaling pathway	4.58
MyD88-dependent toll-like receptor signaling pathway	4.44
MyD88-independent toll-like receptor signaling pathway	4.51
toll-like receptor 3 signaling pathway	4.37

Table 5.5 Enrichment analysis for Gene Ontology Biological Processes on the genes clustering in the Sienna3 WCGNA module in post NACT samples. Table summarises the z-score for upregulated pathways (adj. p<0.05).

Pathway	Z-score
branching involved in ureteric bud morphogenesis	6.06
glycosaminoglycan biosynthetic process	6.39
cell cycle arrest	4.25
regulation of apoptotic process	4.08
signal transduction	3.51
proteasome-mediated ubiquitin-dependent protein catabolic process	3.68
central nervous system development	3.41
glycosaminoglycan metabolic process	3.3
negative regulation of cell growth	3.24
actin cytoskeleton organization	3.04
G2/M transition of mitotic cell cycle	2.89
protein ubiquitination	2.83
cell-cell signaling	2.63
extracellular matrix organization	2.1
carbohydrate metabolic process	1.93
cell proliferation	1.81
intracellular signal transduction	1.75

Table 5.6 Enrichment analysis for Gene Ontology Biological Processes on the genes clustering in the Paleturquiose WCGNA module. Table summarises the z-score for upregulated pathways in post-NACT samples (adj. $p<0.05$).

Pathway	Z-score
protein polyubiquitination	7.26
ubiquitin-dependent protein catabolic process	5.97
negative regulation of ubiquitin-protein ligase activity involved in mitotic cell cycle	5.83
positive regulation of ubiquitin-protein ligase activity involved in regulation of mitotic cell cycle transition	5.53
regulation of ubiquitin-protein ligase activity involved in mitotic cell cycle	5.34
membrane fusion	5.77
anaphase-promoting complex-dependent proteasomal ubiquitin-dependent protein catabolic process	5.09
protein K48-linked ubiquitination	5.16
regulation of cellular amino acid metabolic process	4.91
proton transport	4.64
retrograde transport, endosome to Golgi	4.44
proteasome-mediated ubiquitin-dependent protein catabolic process	4.1
ER to Golgi vesicle-mediated transport	4.18
DNA damage response, signal transduction by p53 class mediator resulting in cell cycle arrest	4.18
stimulatory C-type lectin receptor signaling pathway	3.89
antigen processing and presentation of exogenous peptide antigen via MHC class I, TAP-dependent	3.84
positive regulation of canonical Wnt signaling pathway	3.69
antigen processing and presentation of exogenous peptide antigen via MHC class I	3.71
G1/S transition of mitotic cell cycle	3.26
programmed cell death	3.16
peptidyl-tyrosine dephosphorylation	3.16

Table 5.7 Enrichment analysis for Gene Ontology Biological Processes on the genes clustering in the Darkgrey WCGNA module. Table summarises the z-score for pathways upregulated in post-NACT samples (adj. $p<0.05$).

I then examined which of the individual *in vitro* stimuli correlated most strongly with these four co-expressed gene modules. I observed that the gene profiles that are altered in macrophages upon chemotherapy significantly over-lapped with the gene changes that occur upon *in vitro* stimulation with IL4 and the fatty acids palmitic acid (PA) and stearic acid (SA) (Figure 5.10).

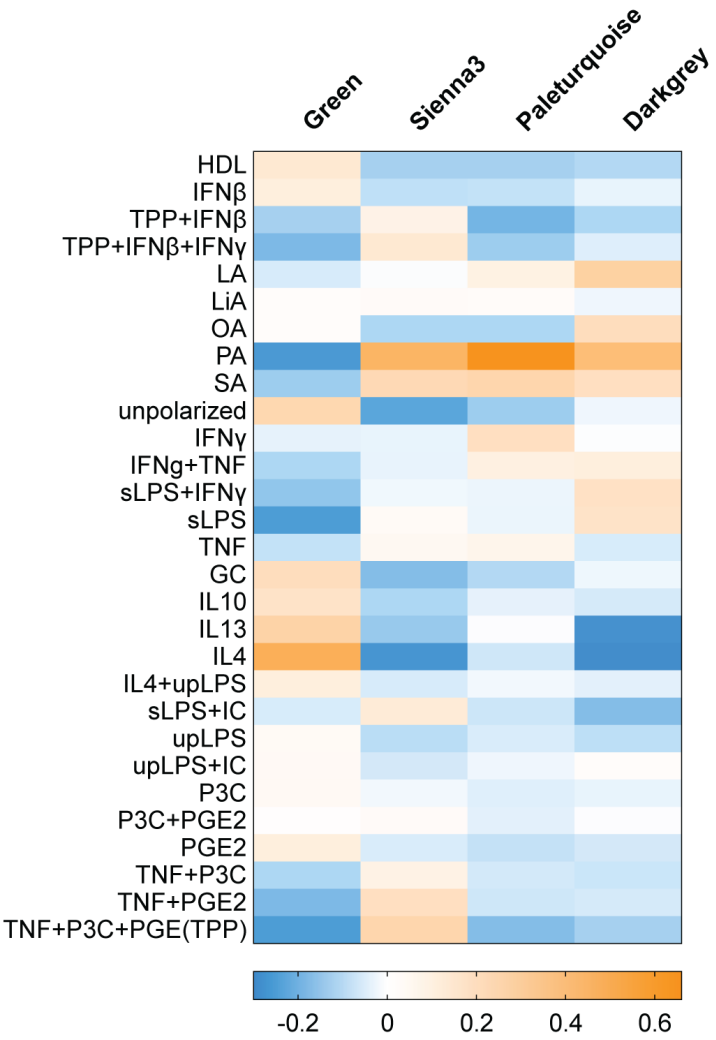

Figure 5.10 Correlation of WGCNA module with biological stimuli. Heatmap showing the correlation of module eigenvalues to biological stimulation conditions, for the four modules with the highest enrichment in differentially expressed genes following chemotherapy.

In summary these data suggest chemotherapy treatment of HGSOC results in transcriptional reprogramming of TAMs. There was enhancement of TLR signalling, T cell and eosinophil chemotaxis, lipid metabolism, inflammasome and IL1β signalling and declines in ECM formation and remodelling pathways. Overall these changes are not consistent with a strict M1 (classically activated)-M2 (alternatively activated)-axis re-polarisation as assessed by individual gene expression changes.

5.4 Discussion

I conducted RNA-sequencing to characterise the transcriptome of $CD14^{+}$TAMs sorted from HGSOC omental metastases from twelve patients, five pre-chemotherapy and seven following NACT. Unsupervised clustering analysis of protein coding genes showed pre and post-chemotherapy samples largely clustered in distinct groups with some interspersed samples (Figure 5.5). This partitioning suggests that chemotherapy

results in distinct changes in macrophage gene expression. The large degree of biological viability between samples (Figure 5.4) and the relatively small sample number from unmatched patients may underlie the lack of complete separation of samples by chemotherapy exposure.

The top unregulated gene was *TREML4*, a gene implicated in the immune responses of dead or dying cells. TREML4 is a member of the TREM family of proteins that are important in fine-tuning immune responses[296]. The protein is known to be highly expressed on macrophages and DCs[297]. Treml4 binds nucleic acids, late apoptotic and necrotic cells[297]. *Treml4* was specifically enriched in CD8α^+ DC *vs* CD8α^- DC, the former have particular roles in antigen presentation[297]. Ramirez-Ortiz *et al.* show that Treml4 positively regulated macrophage activation, by amplifying the TLR7-mediated production of inflammatory cytokines, such as type I interferons[298]. Furthermore, Hemmi *et al.* show that Treml4 enhances the presentation of antigens to CD4$^+$ and CD8$^+$ T cell *in vivo*[299]. Targeting Treml4 with a HER2-anti-treml4 fusion protein resulted in presentation of HER2 to CD4$^+$ and CD8$^+$ T cells and engagement of anti-tumour immunity in a transplantable breast cancer model[299]. These data collectively suggest that this protein has important roles in engaging adaptive immunity through the recognition and presentation of antigens from dead or dying cells. Therefore, this result suggests that macrophages, following chemotherapy, may be important activating immune responses to dying malignant cells via TREML4.

Also within the top ten upregulated genes post-chemotherapy were *CCL24* (chemokine C-C motif ligand 24), *FABP4* (fatty acid binding protein 4) and *LPL* (lipoprotein lipase). CCL24 is a known potent chemoattractant for resting T cells, eosinophils and neutrophils[300]. FABP4 is a known fatty acid binding protein with known roles in lipid transfer between adipocytes and tumour cells in omental metastasis[301]. LPL is essential in lipid metabolism. Upregulation of these genes may reflect switches in TAM metabolism as a result of normalisation of the fatty omental tissue post-chemotherapy. The most significantly down regulated gene was *CLDN16*, encoding CLDN16, a member of the claudin family of proteins, essential in the formation of tight junctions[302]. It is interesting that this was the most significantly downregulated gene as, to date, these proteins have no known roles within macrophages. Within the top ten down regulated genes was *LPAR3* (lysophosphatidic acid receptor 3). Interestingly, lysophosphatidic acid, a bioactive fatty acid, has tumour promoting activity in HGSOC correlating with genes regulating cellular mobility and migration as well as cell communication and signalling in HGSOC ascites[303]. *PDCD1* the gene encoding programmed cell death 1 (PD1) was also significantly down regulated in post-chemotherapy samples but was not in the top twenty

genes shown in Table 4.2. PD1 expression on macrophages inhibits phagocytosis[304], suggesting a possible mechanism by which chemotherapy may mediate increased phagocytosis by TAM.

Pathway analysis of the differentially expressed protein-coding genes was performed using GSEA for Gene Ontologies categories and canonical pathways. The most significantly enriched downregulated pathways were ECM deposition, remodeling and interaction along with cell cycle and proliferation pathways (Figure 5.8). Within the top significantly enriched pathways was activation of the inflammasome as well as IL1β, IL8 and PI3K/AKT signaling pathways. TLR signaling was also upregulated in the pathway analysis (not shown in Figure 5.8), fitting with the observation of *TREML4* being the top upregulated gene.

Enrichment of the linked processes of TLR, inflammasome and IL1β signaling suggests that chemotherapy may result in TLR activation with downstream inflammasome assembly and IL1β production. As the majority of HGSOCs are sensitive to first-line chemotherapy, increased TAM exposure to apoptotic/dying cancer cells shortly following chemotherapy is likely. As the TLR family have evolutionary conserved roles in recognizing DAMPs and PAMPs of diverse origin[305] upregulation of these pathways is in keeping with TAMs responding to dying cancer cells. These changes concomitant with highly significant decreases in ECM secretion, interaction and remodeling pathways which represent key functions of TAM in HGSOC and other cancers highlight radical TAM transcriptional re-programming following chemotherapy[139,289]. Overall these data suggest a skew away from classically described TAM functions towards an overall pro-inflammatory and potentially anti-tumoural phenotype.

Assessment of canonical macrophage activation makers demonstrated no significant changes in transcript expression across chemotherapy treated and untreated myeloid cells (*MRC1* [CD206], *CD163*, *HLA-DQ*, *CD80*, *CD86*, *iNOS*). This suggested that the changes observed upon chemotherapy exposure were not captured by the M1 (classically activated)-M2 (alternatively activated) paradigm. This is in keeping with studies of ascites-derived TAM obtained from HGSOC which demonstrated a 'mixed' TAM phenotype as assessed by the expression of canonical macrophage activation markers[198]. A comparison between TAM and resident peritoneal macrophages showed that CD163 was upregulated but M1/classically activated markers (MHC, iNOS, TLR) were also upregulated.

To further explore for changes in macrophage activation following chemotherapy

treatment I compared my data with a comprehensive transcriptome-based study of macrophage activation by Xue *et al.* To do this I determined which of the WGCNA modules described by Xue *et al.* most positively correlated with genes reflecting TAM chemotherapy exposure (Figure 5.9). Enrichment analysis within the four most correlated modules demonstrated pathways regulating TLR signalling, IL1β tissue response, programmed cell death and apoptosis (Table 5.4, Table 5.5, Table 5.6, Table 5.7). This analysis serves to validate my results in a much larger, independent dataset.

Finally I determined how biological stimuli interacted with the four modules most associated with TAM chemotherapy exposure. Interestingly in three of the four upregulated pathways the fatty acids palmitic and stearic acid were most correlated. Palmitic acid induces an inflammatory activation state in macrophages at physiological concentrations[306]. IL4 was correlated with the module "MEGreen", however, this module was not highly associated with alternatively activated-stimuli (IL4, 1L-10) in the Xue *et al.* dataset overall. Indeed, the most highly correlated modules to M2-stimuli were "MERed", "MEPlum", and "MESaddlebrown", whereas the most correlated modules to classically activated-stimuli (LPS, IFNγ) were "MEOrangered4", "MESteelblue" and "MEYellowgreen" – these modules were not significantly associated with transcriptional changes reflecting macrophage exposure to chemotherapy in my dataset. Although in this analysis I am comparing my data to a highly artificial system of macrophages exposed to single stimuli *in vitro*, the analysis does suggest changes in TAM transcriptional programs upon chemotherapy exposure distinct from the M1 (classically activated)-M2 (alternatively activated) axis. This conclusion is supported by Cassetta *et al.* who demonstrate breast and endometrial cancer TAMs did not display enrichment for an M2-gene signature, which suggests TAM phenotypes cannot be categorised in this simplistic manner[133].

The limitations of the data presented in this chapter include the small number of samples and the fact that significantly different mRNA expression levels have not been validated by protein expression. Further validation with IHC and *in situ* hybridisation with RNA scope should be undertaken to complete this aspect of the project.

These data lead me to conclude that chemotherapy treatment of HGSOC results in transcriptional reprogramming of TAMs, with features distinct from M1 (classically activated)-M2 (alternatively activated)-axis phenotypes and associated with a skew away from established pro-tumoural function, towards an antigen sensing, anti-tumour phenotype. This suggest that TAM chemotherapy exposure may foster overall antitumoral immunity in human HGSOC.

5.5 Overall summary of human data (Chapters 3-5)

- I found that NACT significantly decreased $CD68^+$ densities within malignant cell areas of HGSOC omental biopsies.
- Analysis of larger tissue sections revealed NACT promoted the formation of stromal macrophage 'lakes'.
- Stratifying patients by TAM density suggested enhanced survival in patients with high TAM density post-NACT.
- FC analysis of treatment naïve and post-NACT HGSOC samples showed decreases in $CD163^+$ and $CX3CR1^+$ TAM, an increase in non-viable TAMs and an increase in DCs.
- RNA-sequencing showed that NACT increased IL-1β, inflammasome and TLR pathways and decreased ECM, matrix remodelling and proliferation pathways in TAM.

Taken together, I conclude that at a time point three-four weeks after NACT, TAM and DC populations are more likely to aid than inhibit host anti-tumour responses.

In the next chapter I will ask if the effects of chemotherapy on myeloid cells can be reproduced in mouse models of HGSOC. I will use these models to gain further understanding of the effects of chemotherapy on TAMs and to provide a platform to explore the effects of TAM depletion in HGSOC.

Chapter 6

The effect of chemotherapy on the tumour microenvironment in murine HGSOC

6.1 Background

HGSOC is characterised by ubiquitous *TP53* mutations/deletions with frequent defects in genes regulating homologous recombination pathways[7,20]. A cardinal feature is widespread genome amplification and deletion[7].

In this thesis I have used three syngeneic injectable murine models that harbour many of the genetic features of human HGSOC: 60577, 30200 and HGS2. 60577 and 30200 cell lines were established from tumours from genetic models generated by adenoviral transfection of the ovarian surface epithelium in FVB mice[272]. HGS2 was generated from tumours derived from a different genetic model[273] that has been backcrossed to a Bl6 background in our lab. 60577 and 30200 cell lines are *Tp53*$^{-/-}$, *Brca-1*$^{-/-}$ and have inactivation of the pRb pathway. Both these cell lines, when injected intraperitoneally, produce tumours within the omentum, as well as miliary peritoneal deposits and large volume ascites when they reach an advanced stage. 60577 and 30200 models differ in latency, with 60577 tumours reaching an advanced stage in five-six weeks from cell injection, compared to eighteen-twenty weeks in the 30200 model. HGS2 is *Tp53*$^{-/-}$, *Pten*$^{-/-}$ and *Brca-2*$^{-/-}$. This model produces metastasis to the omentum and other peritoneal sites reaching an advanced stage in around twelve weeks.

Recently work in our lab has characterised the cellular, molecular, and biomechanical characteristics of these models and compared these data to patient biopsies (Maniati *et al.* submitted for publication). There were significant correlations in mRNA expression profiles, tissue modulus (a measure of material stiffness independent of sample dimension), host cell infiltrates, matrisome, vasculature and immune response pathways between the mouse and human TMEs showing that these models faithfully replicate features of human HGSOC. Although there were strong similarities between the models there were significant differences and potential therapeutic vulnerabilities. Overall the analyses show that multiple models are needed to capture the diverse therapeutic response of human HGSOC. Hence, I studied three of the synegeneic models in this thesis with differing transcriptional profiles, natural histories and from two different mouse backgrounds.

The models used here develop tumours in the murine omentum, as this is the site studied in patients in this thesis (Chapters 3-5) and in previous work in the lab[113,114,307]. In this chapter I will test the effects of carboplatin and paclitaxel chemotherapy on myeloid cell and lymphocyte cell number and phenotype in omental tumours and compare this to my findings in patients.

6.2 *In vitro* sensitivity of the 60577, 30200 and HGS2 cell line to chemotherapy

Before evaluating the effects of chemotherapy *in vivo*, I assessed the sensitivity of the 60577, 30200 and HGS2 mouse cell lines[272,273] to carboplatin and paclitaxel *in vitro* (Figure 6.1). IC_{50} values were similar between the three cell lines and were within the range described for human ovarian cancer cell lines[308,309].

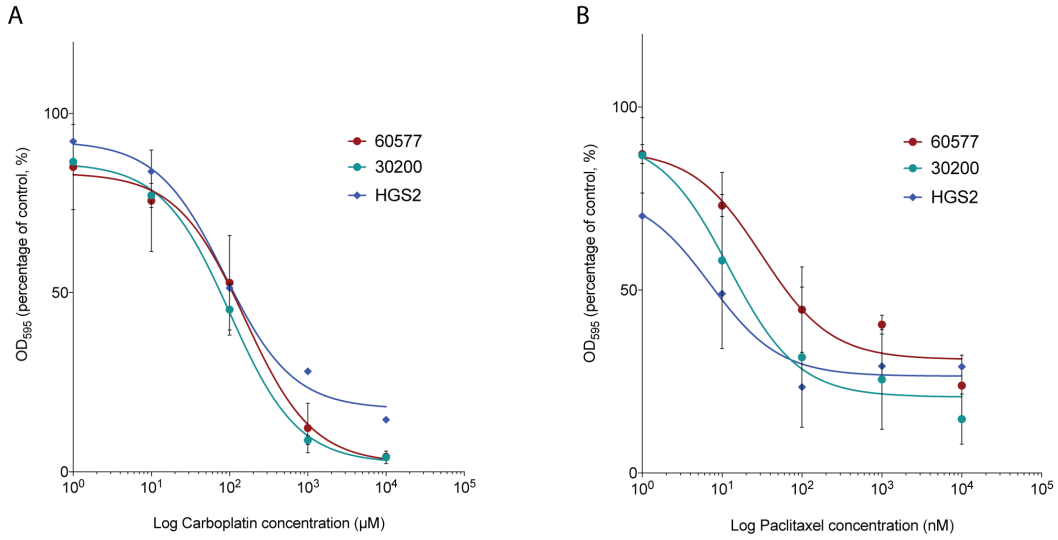

Figure 6.1 The effects of carboplatin and paclitaxel chemotherapy on the 60577, 30200 and HGS2 cell lines *in vitro*. OD_{595} measurements presented as mean with error bars representing SEM, data normalised to media-only control. **A** carboplatin treatment, **B** paclitaxel treatment. 30200 (green line), 60577 (red line) and HGS2 (blue) data combined from three separate experiments. IC_{50} values carboplatin: 60577=155μM, 30200=100μM HGS2=87μM; IC_{50} paclitaxel 60577=31nM, 30200=12nM HGS2=7nM.

6.3 Summary of mouse experiments in this chapter

In this chapter I present data from four mouse experiments conducted in three HGSOC models. Figure 6.2 describes the experimental outline for each mouse experiment. 60577 and 30200 models were treated with carboplatin and paclitaxel. HGS2 was only treated with carboplatin. To reflect the clinical situation of treating patients with disseminated disease, mice were treated when tumours were established in the peritoneum. The experimental time points chosen were determined by detailed natural histories of the models conducted previously in the lab.

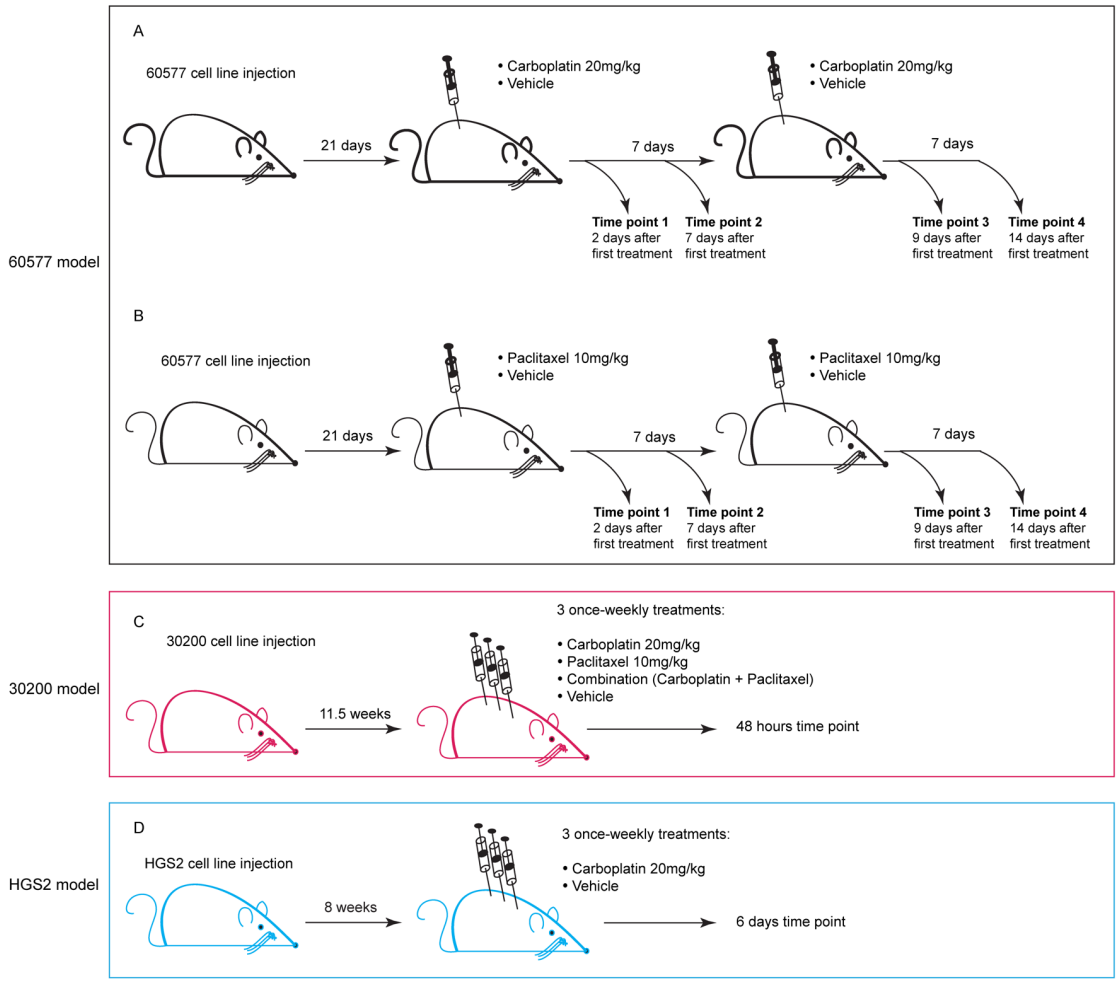

Figure 6.2 Schematic outline of all mouse experiments presented in this chapter. Box colour relates to murine model: 60577 model (black box), 30200 model (pink box), HGS2 model (blue box). **A**, **B** Time course experiment in 60577 model, mice were treated twenty-one days following cell injection with carboplatin, paclitaxel or vehicle, mice were culled at the time points indicated. **C** Time point experiment in the 30200 model, mice were treated 11.5 weeks following cell injection with carboplatin, paclitaxel or the combination of carboplatin and paclitaxel or vehicle. Mice were culled forty-eight hours after the final treatment. **D** Time point experiment in the HGS2 model, mice were treated eight weeks following cell injection with carboplatin or vehicle. Mice were culled six days after the final treatment. *OD:* once a day, *BD*: twice a day, *OG*: oral gavage.

6.4 Effects of chemotherapy on tumour growth and survival

I wanted to determine the individual contribution of carboplatin and paclitaxel on survival and TAM phenotype. Therefore, in the majority of experiments in this thesis mice were exposed to single-agent treatment with either carboplatin or paclitaxel, rather than receiving these drugs in combination. Response to treatment was assessed by measuring omental weight and determining mouse survival.

6.4.1 60577 model

The mouse omentum is a discrete structure that can be identified and dissected in its entirety[310,311]. Therefore, I used omental weight as a surrogate measure of the degree of tumour infiltration within this structure. Furthermore, due to the miliary nature of

peritoneal disease dissemination, attempting to measure total tumour burden in these models would have been difficult and inaccurate. The carboplatin and paclitaxel time-course experiments (Figure 6.2) allowed serial assessment of tumour (i.e. omental) weight through treatment in addition to the FC analysis. Figure 6.3 shows that 60577 tumours were highly sensitive to carboplatin treatment. Omental weight decreased throughout the experiment in carboplatin treated mice, whereas control omenta increased in weight due to disease progression. The differences in omental weight reached statistical significance at a time point forty-eight hours after the second treatment of carboplatin. This is in clear contrast to the treatment of the 60577 model with paclitaxel (Figure 6.4), here there is no significant difference in omental weight at any time point in the study.

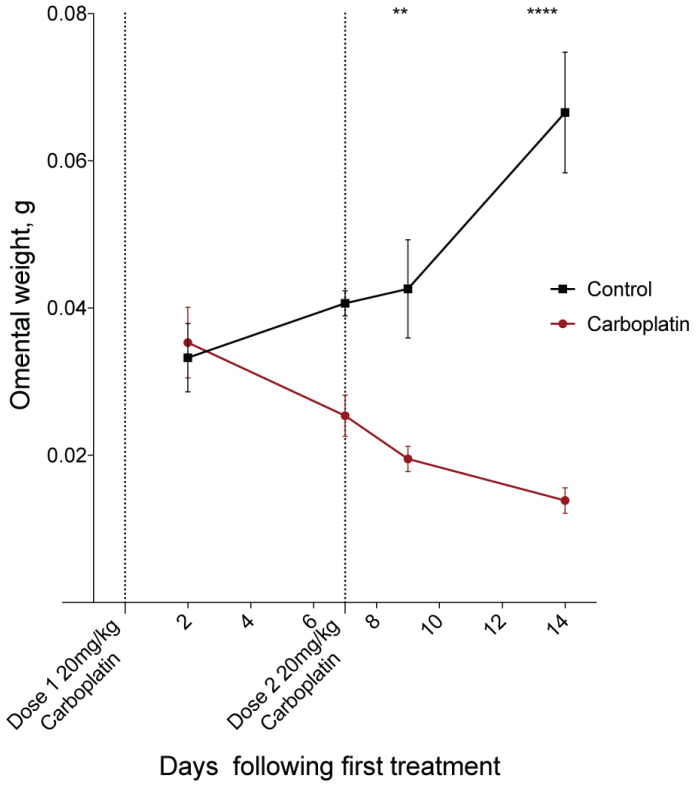

Figure 6.3 The effect of carboplatin on omental weight in the 60577 model. Omental weight of tumours from mice culled at time points two days, seven days, nine days and fourteen days following completion of carboplatin treatment. Data relate to a single experiment, five mice per group, the mean for each group is shown. Error bars represent SEM. Dashed lines indicate treatment scheduling. Significant two-way ANOVA p-values are shown; **<0.01, ****< 0.0001.

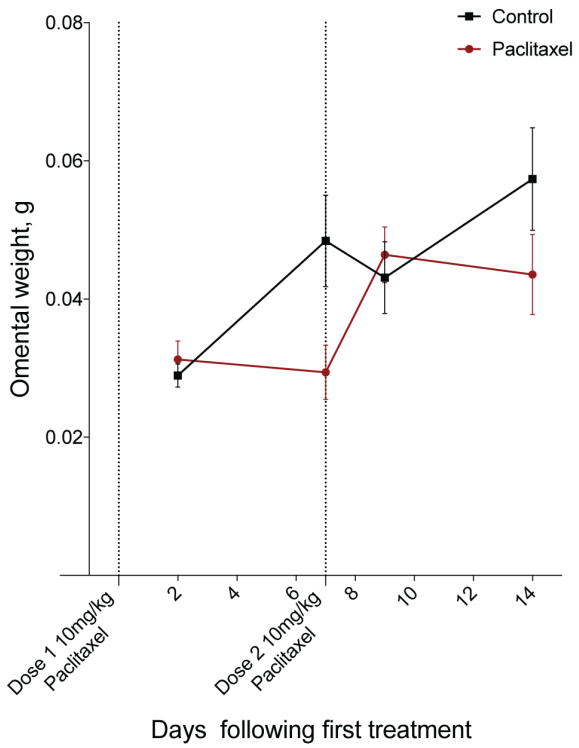

Figure 6.4 The effects of paclitaxel on omental weight in the 60577 model. Omental weight of tumours from mice culled at time points two days, seven days, nine days and fourteen days following completion of paclitaxel treatment. Data relate to a single experiment, five mice per group, the mean for each group is shown. Error bars represent SEM. Dashed lines indicate treatment scheduling.

In a further time point experiment in the 60577 model mice were treated with three doses of carboplatin, given at weekly intervals. Replicating features of treatment in patients, clinical signs of ascites resolved with carboplatin treatment. Mice proceeded to live without outward signs of disease for six weeks, resulting in significantly increased survival (Mantel-Cox log-rank $p<0.0001$) in carboplatin treated compared to vehicle-treated mice (Figure 6.5A). At this time point mice were culled and the omenta examined. Microscopically, there were small foci of malignant cells indicating the beginnings of tumour regrowth. Omenta from carboplatin treated mice weighed significantly less then omenta from vehicle-treated controls reaching humane endpoint (44.7mg *vs* 9.2mg $p<0.0001$). Overall these data suggest that 60577 tumours are highly sensitive to carboplatin but not paclitaxel chemotherapy *in vivo*. Furthermore, the effects of carboplatin treatment were long lived, persisting up to a time point six weeks following treatment.

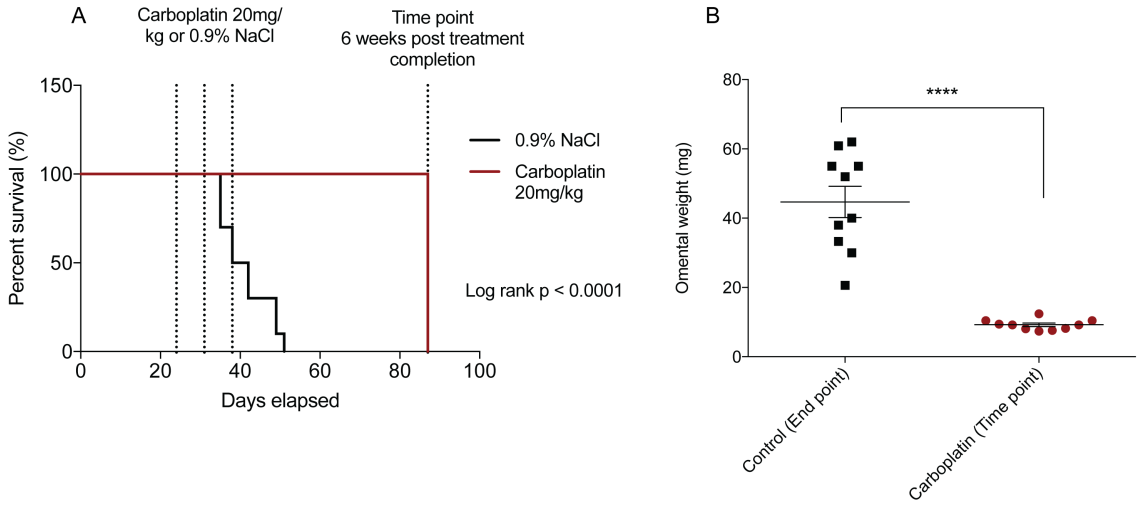

Figure 6.5 The effect of carboplatin treatment on the 60577 model. A Kaplan-Meier curves comparing mice treated with three once-weekly doses of carboplatin (red line) or 0.9% NaCl (black line). Dashed lines indicate treatment events and the time point when mice were culled. Log-rank (Mantel-Cox) p-value is shown. **B** Omental weight recorded for control mice succumbing to disease at endpoint and carboplatin treated mice culled six weeks post carboplatin treatment. Data relates to a single experiment, ten mice per group, the mean for each group is shown. Error bars represent SEM. Student's *t*-test is shown to compare means between groups, ****<0.0001.

6.4.2 30200 model

I next assessed the effects of carboplatin, paclitaxel and combination treatment in the 30200 model. Figure 6.6 shows the effects of treatment on the weight of omenta harvested forty-eight hours following three weekly treatments of chemotherapy. At this time point I observed a significant reduction (33.4mg *vs* 14.8mg p=0.043) in omental weight between carboplatin treated and paclitaxel treated mice. At this number of mice, there was a non-significant trend towards a reduction in omental weight in carboplatin and combination treated mice compared to vehicle-treated controls (Figure 6.6).

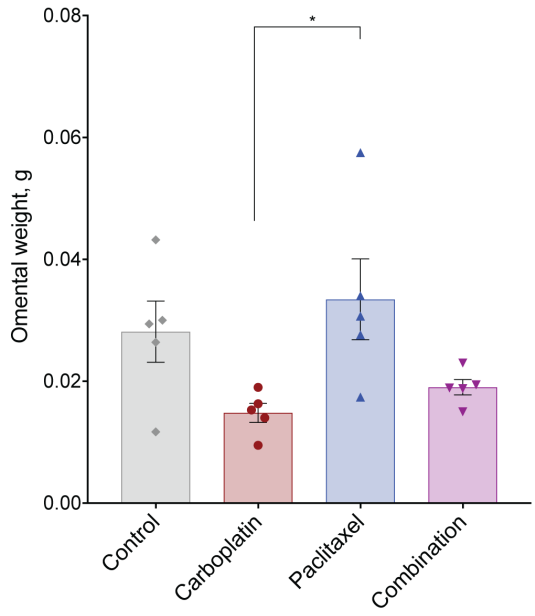

Figure 6.6 The effects of chemotherapy on 30200 tumour weight. Omental weight of tumours treated with carboplatin, paclitaxel, the combination of carboplatin and paclitaxel or vehicle from mice culled at a time point forty-eight hours following the last treatment. Data relates to a single experiment, five mice per group, the mean for each group is shown. Error bars represent SEM. Significant one-way ANOVA p-values are shown, *<0.05.

Assessment of survival in the 30200 model was undertaken, comparing paclitaxel and combination treated tumours to vehicle-treated controls. Due to limitations of the number of mice available, I did not assess the effects of carboplatin alone in this experiment. Treatment with paclitaxel alone extended median survival, however, this was not significantly different compared to vehicle-treated controls (median survival of 143 *vs* 126.5 days, Mantel-Cox log-rank p=0.19) (Figure 6.7). Treatment with the combination of paclitaxel and carboplatin significantly increased survival compared to control mice (median survival of 164 *vs* 126.5 days, Mantel-Cox log-rank p=0.012) (Figure 6.7), suggesting either increased sensitively of 30200 tumours to carboplatin or a synergistic action between these two drugs.

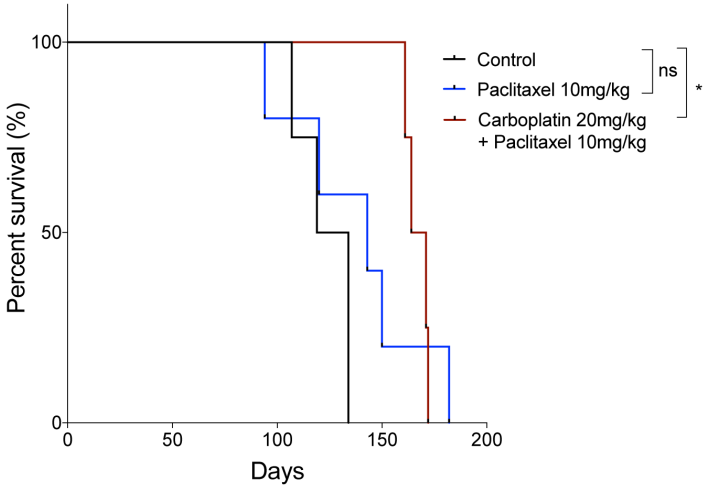

Figure 6.7 Effect of chemotherapy on survival in the 30200 model. Kaplan-Meier curves comparing mice treated with weekly paclitaxel i.p. injections (red line), carboplatin and paclitaxel combination treatment (blue line) or 0.9% NaCl (black line). Five mice per group. Log-rank (Mantel-Cox) p-values are indicated for survival differences between control and treated groups; ns denotes a non-significant p-value; *<0.05.

6.4.3 HGS2 model

I also used carboplatin to treat established HGS2 tumours. Mice again received three doses of carboplatin 20mg/kg administered weekly. Mice were culled at a time point one week after the completion of treatment. As seen in Figure 6.8B carboplatin treatment did not significantly affect tumour weight at this time point. However, carboplatin significantly increased survival compared to untreated controls (median survival of 105 *vs* 84 days, Mantel-Cox log-rank p=0.0027) (Figure 6.8A). Paclitaxel treatment was not tested in this model.

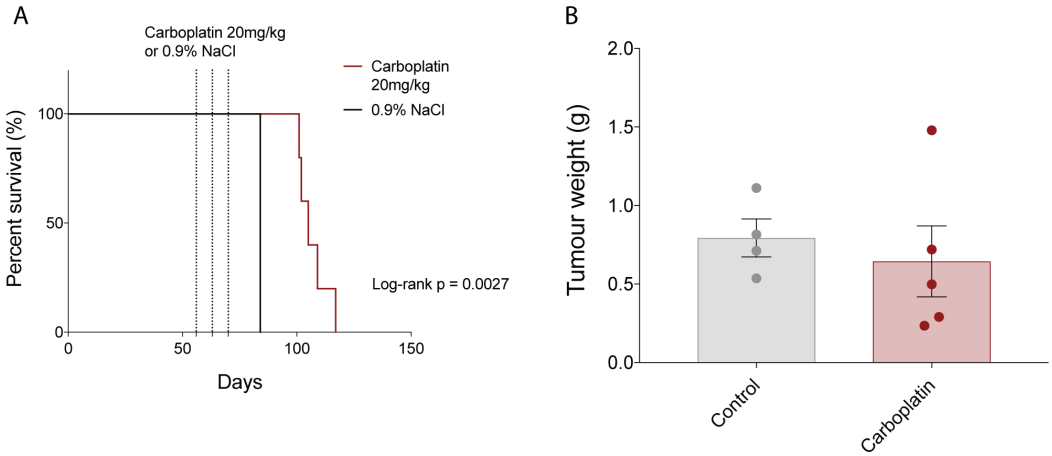

Figure 6.8 The effects of carboplatin treatment on the HGS2 model. A Kaplan-Meier curves comparing mice treated with three once-weekly doses of carboplatin (red line) or 0.9% NaCl (black line). Dashed lines indicate treatment events. Log-rank (Mantel-Cox) p-value is shown. **B** Total tumour weight recorded for mice succumbing to disease at endpoint. Data relate to a single experiment, four vehicle-treated mice and five carboplatin treated mice, the mean for each group is shown. Error bars represent SEM.

In summary, all models used in this thesis were sensitive to carboplatin or the combination of carboplatin and paclitaxel given as three weekly doses. However, there were obvious differences in the response of the models. 60577 tumours were clearly the most sensitive to carboplatin treatment with extension of survival in excess of six weeks, whereas in HGS2 tumours the difference in median survival was three weeks.

6.5 Characterisation of murine TAMs by flow cytometry

FC was used to assess the TAM populations of all three models. The gating strategy used is shown in Figure 6.9. Mouse TAMs initially were defined as $CD45^{+}Ly6C^{-}Ly6G^{-}$ $F4/80^{+}CD11b^{+}$ cells. However, there were two clearly identifiable sub-populations varying in $F4/80^{+}$ expression. I referred to these as $F4/80^{high}$ and $F4/80^{dim}$ cells (Figure 6.9G). Characterisation of these populations demonstrated differences in canonical macrophage marker expression. The majority of $F4/80^{dim}$ cells were negative for MHC class II (Figure 6.9Ga) and CD206 in contrast to the $F4/80^{high}$ population (Figure 6.9Gb). Furthermore, the $F4/80^{high}$ and $F4/80^{dim}$ populations differed in their forward and side scatter parameters (Figure 6.9Ga, Gb). To determine if $F4/80^{dim}$ cells were TAMs or represented another cell population, I sorted $F4/80^{high}$ and $F4/80^{dim}$ populations from 60577 tumours. H&E staining of the sorted populations showed that the $F4/80^{dim}$ gate contained a mixed population of cells, with nuclear features suggestive of eosinophils and myeloid cells (Figure 6.10A). The $F4/80^{high}$ gate contained only cells with a myeloid appearance (Figure 6.10B). Murine eosinophils have a ring-shaped nucleus[312] and myeloid cells typically have a kidney shaped nucleus[313]. This result, in combination with the flow cytometry analysis of the different populations showed that the $F4/80^{dim}$ population contains a large proportion of eosinophils.

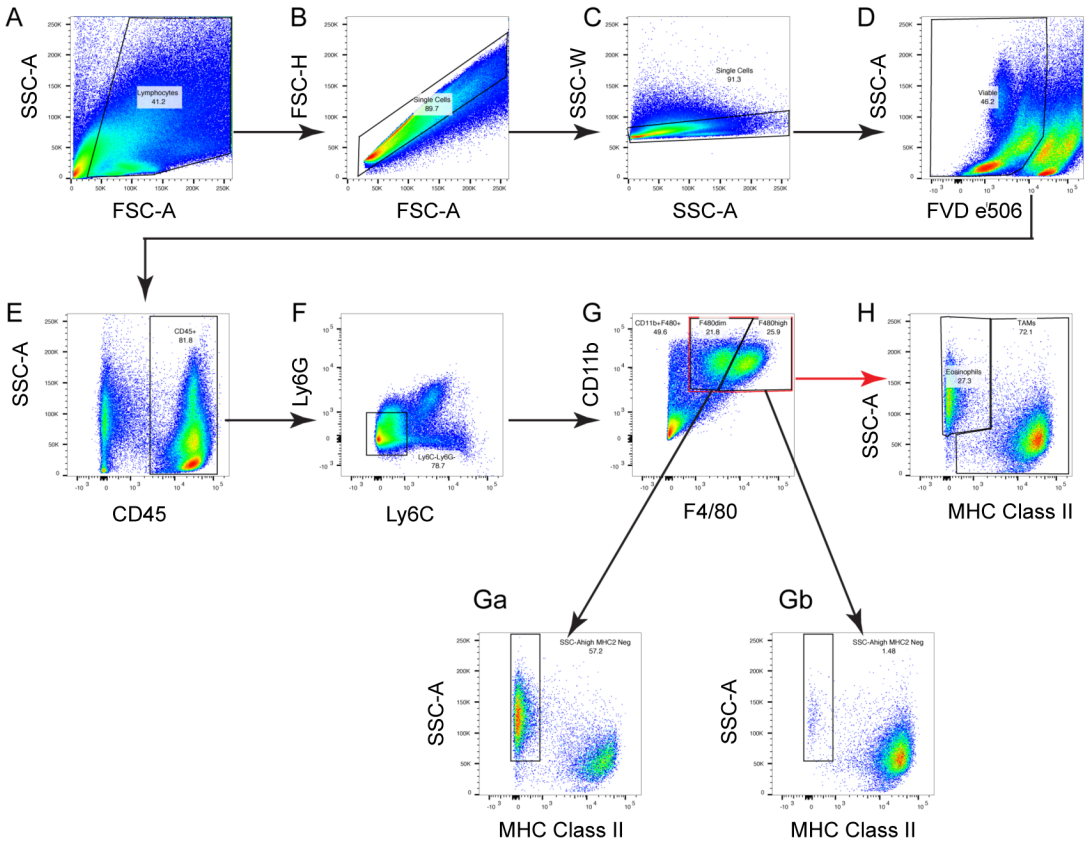

Figure 6.9 Multi-colour flow cytometry gating strategy to characterise murine TAM populations. Density plots from a representative immunostained murine HGSOC omental tumour. **A** Gating to exclude cellular debris, **B**, **C** sequential gating to exclude doublet cells, **D** sequential gating to exclude non-viable cells, **E** sequential gating for $CD45^+$ cells, **F** sequential gating for $Ly6C^-Ly6G^-$ cells **G** sequential gating for $F4/80^+CD11b^+$ cells showing $F4/80^{high}$ and $F4/80^{dim}$ population, **Ga** $F4/80^{dim}$ population showing MHC Class II and SSC-A parameters **Gb** $F4/80^{high}$ population showing MHC Class II and SSC-A parameters **H** Gating for eosinophils (SSC-A high MHC Class II negative cells) and TAMs (MHC Class II^+ cells) further assessment of TAM markers was made within this gate. SSC-A: side scatter area, SSC-W: side scatter width, FSC-A: forward scatter area, FSC-H: forward scatter height.

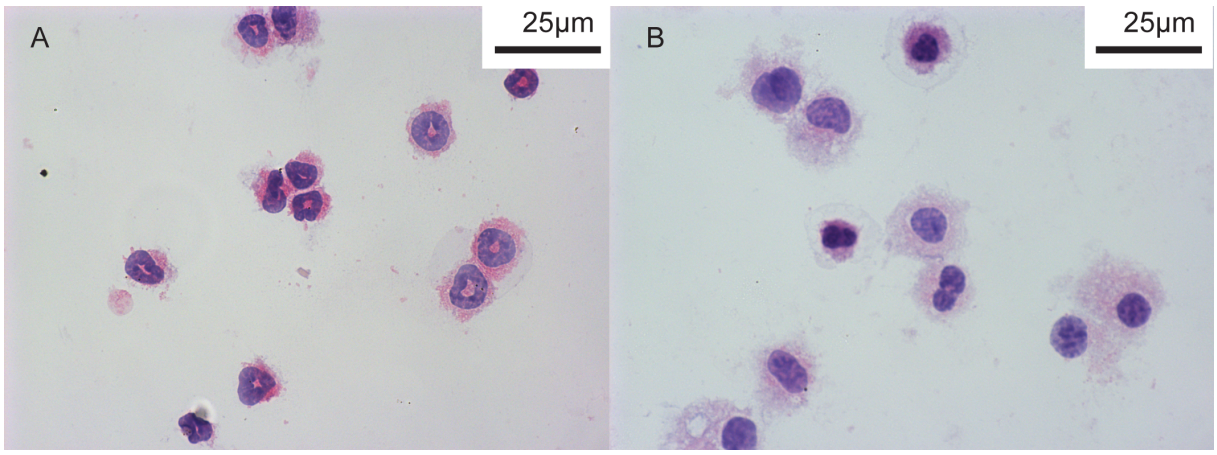

Figure 6.10 F4/80^{dim} and F4/80^{high} CD11b^{+}F4/80^{+} sub-populations contain different cell types. H&E staining of cytospun flow sorted F4/80^{dim} and F4/80^{high} cells, demonstrating differences in nuclear morphology and eosin uptake. Scale bar, 25µm

Examining H&E stained sections of murine tumours at high magnification showed the presence of eosinophilic cells with typical nuclear features of eosinophils, further supporting these observations (Figure 6.11).

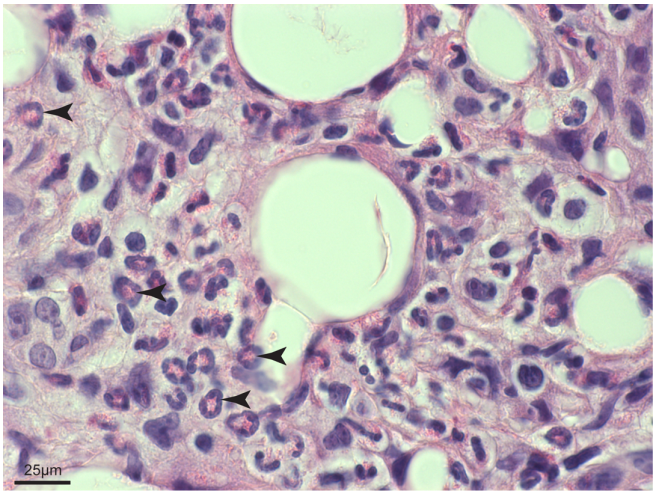

Figure 6.11 Eosinophil population within 60577 HGSOC tumours. H&E staining of a 60577 tumour viewed under x63 objective. Arrows indicate eosinophils identified by eosinophilic cytoplasmic granules and nuclear morphology. Scale bar, 25µm.

To validate the flow cytometry findings, I stained tumour tissue sections with anti-F4/80 and anti-CD206 antibodies. I observed F4/80^{+} eosinophils (Figure 6.12A) in tissue sections, as expected from the flow cytometry data these cells were CD206-negative (Figure 6.12B). This result validates the flow cytometry findings and has implications for F4/80 as a generally applicable pan-macrophage marker in these murine models.

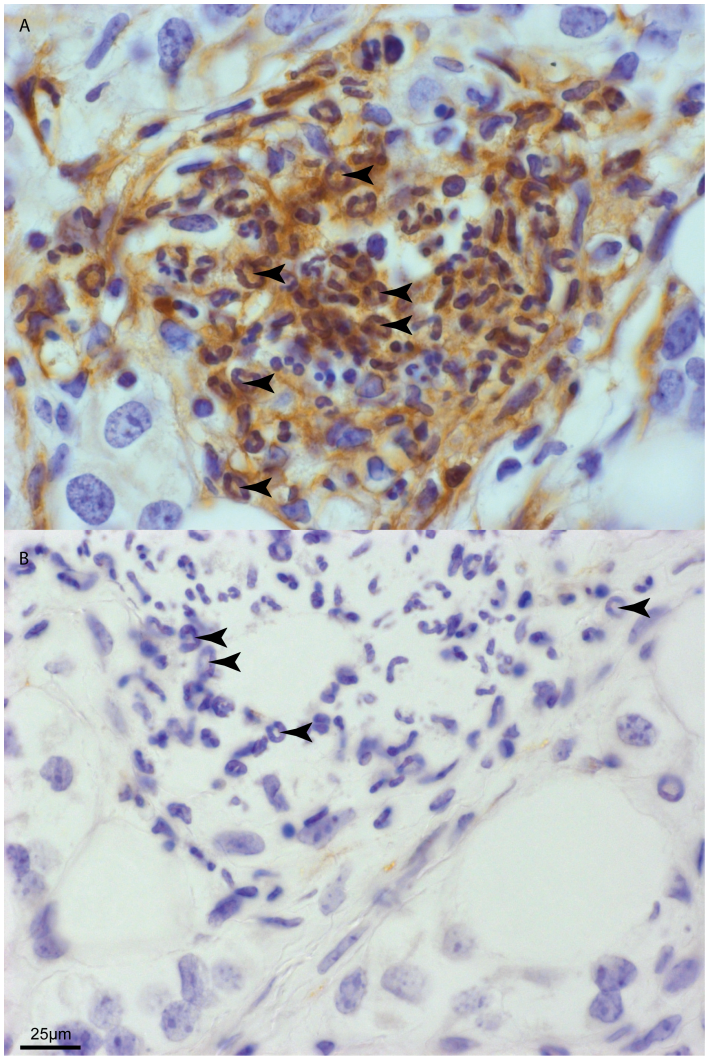

Figure 6.12 Demonstration of eosinophils in a 60577 murine HGSOC tumour. A F4/80 **B** CD206 staining of the same area of a 60577 tumour section. Arrows indicate eosinophils based on nuclear morphology. Scale bar, 25µm.

In further experiments, I found eosinophil populations in all three murine models. To ensure that TAMs are gated separately from the eosinophil population I have therefore defined TAMs by flow cytometry as $CD45^{+}Ly6C^{-}Ly6G^{-}F4/80^{+}CD11b^{+}$MHC Class II^{+} cells (Figure 6.10H), this allowed clear separation of eosinophils from TAMs. Through this thesis I have ensured separation of eosinophils from the TAM population in all flow cytometry analyses performed.

6.1 The effect of chemotherapy on TAM cell number in murine HGSOC

6.1.1 60577 model

To examine the effects of carboplatin chemotherapy in this model, mice were treated with carboplatin 20mg/kg intra-peritoneally (i.p.) commencing twenty-one days after 60577 cell injection. Mice were injected once weekly for three weeks. Flow cytometry was used to assess the omental TME compared to vehicle-treated controls at time points

forty-eight hours and seven days following each dose of carboplatin (Figure 6.13A).

I observed striking reductions in the TAM population within carboplatin treated tumours compared to vehicle controls, both when TAMs were quantified as a percentage of the CD45$^+$ population (Figure 6.13A) and as cells/mg of tissue (Figure 6.13B). Expressing the data as cells/mg of tissue showed incremental decreases in TAM cell number in carboplatin treated tumours over the two-week experiment. This suggests evolving effects of carboplatin treatment. Interestingly, only forty-eight hours following the first dose of carboplatin, I observed a significant reduction in TAM density in carboplatin-treated compared to control tumours. Two weeks after the start of treatment TAM cell number corresponded to that of the healthy omentum (Figure 6.13B).

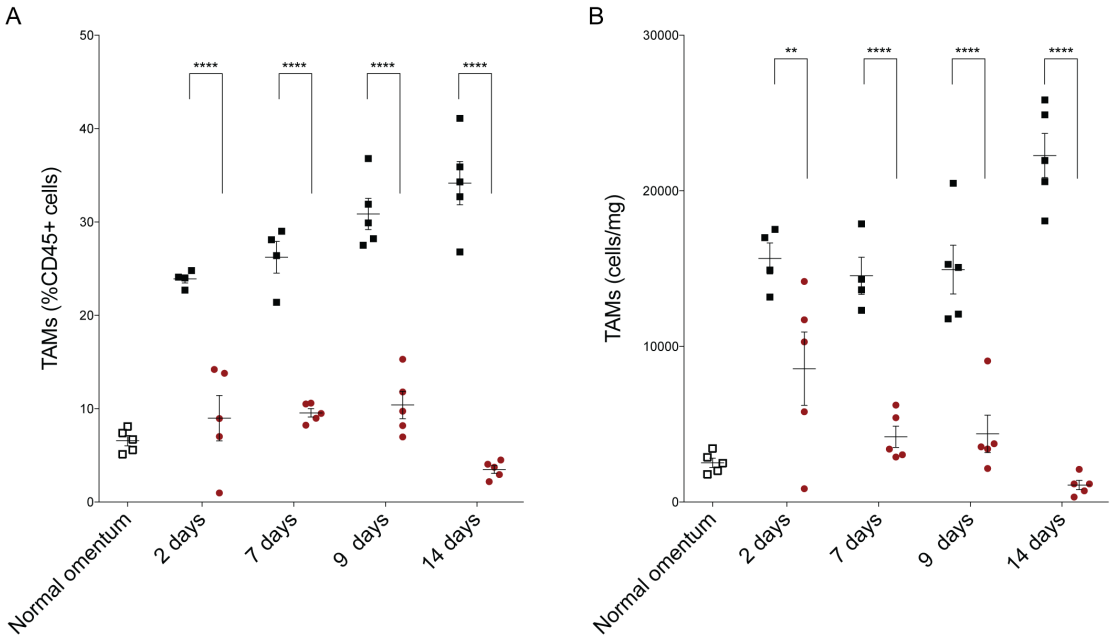

Figure 6.13 Effect of carboplatin on TAM density in the 60577 model. Flow cytometry data relating to the immunostained stromal vascular fractions derived from omental tumours treated with carboplatin (red circles), vehicle alone (black squares) or healthy omental controls (unfilled squares). **A** TAM frequency is expressed as a percentage of the CD45$^+$ population and **B** as cells/mg of tissue. Data relate to a single experiment, five carboplatin treated mice, four-five vehicle-treated mice per time point and ten healthy omental controls; cells from healthy omental controls were combined and stained as five separate samples, the mean for each group is shown. Error bars represent SEM. Significant two-way ANOVA p-values are shown; **<0.01, ****<0.0001. Experiment performed twice.

To further validate the results obtained by flow cytometry, I sought to confirm these findings by staining omental tissue sections with an anti-F4/80 antibody. There was a significant reduction of the percentage F4/80$^+$ area in carboplatin treated compared to vehicle-treated controls at the day fourteen time point (Figure 6.14). As previously determined, F4/80 is not a specific marker for macrophages in these models, therefore I also stained for CD206, a marker predominantly expressed on macrophages and

immature dendritic cells[314]. There was also a significant reduction of $CD206^+$ percentage area in carboplatin treated compared to vehicle controls at fourteen day time point (Figure 6.15, Figure 6.16).

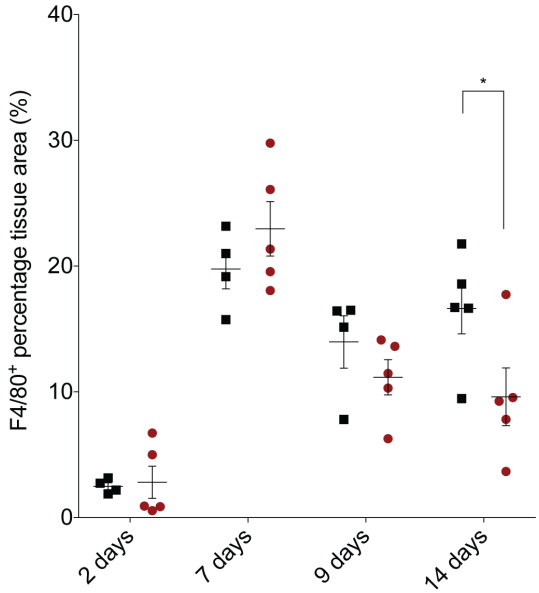

Figure 6.14 Quantification of F4/80 staining by Definiens® digital analysis in 60577 omental tumours. F4/80 staining expressed as percentage positive area of the biopsy. Data quantified relates to a single experiment, five carboplatin treated mice (red circles), four-five vehicle-treated mice (black squares), at a time points following two doses of carboplatin treatment, the mean for each group is shown. Error bars represent SEM. Significant two-way ANOVA p-value is shown; *<0.05.

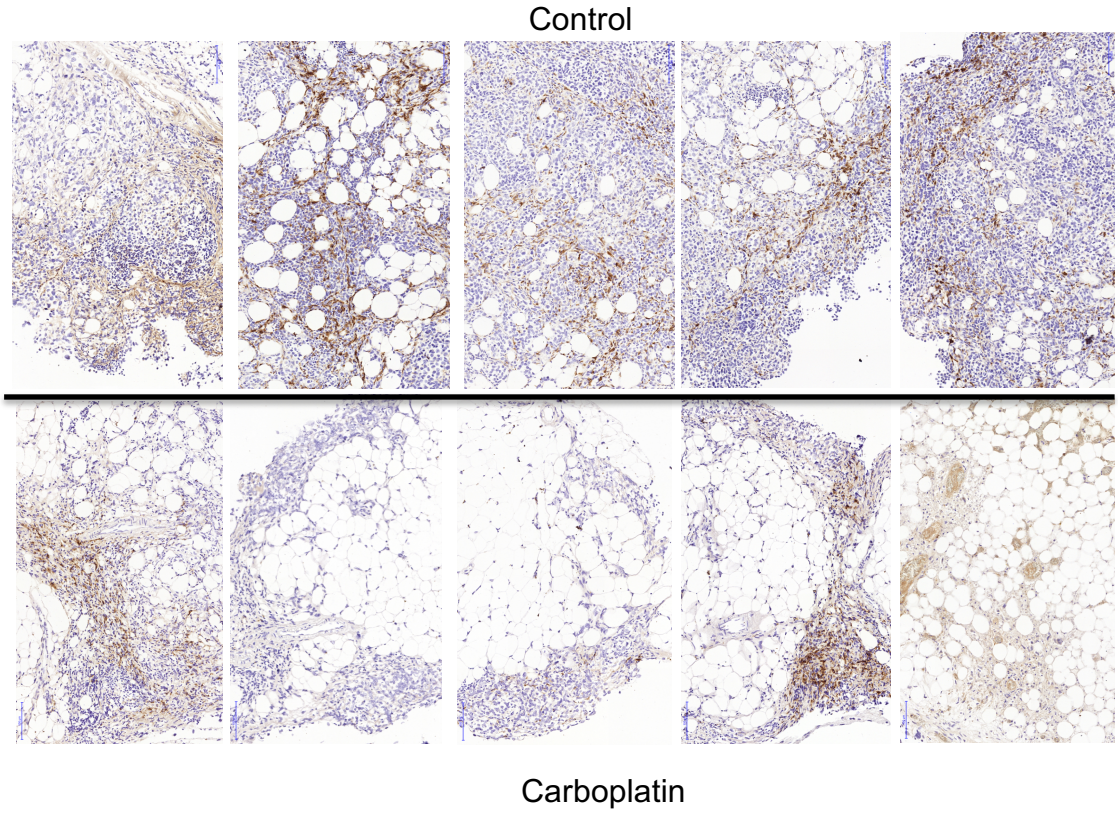

Figure 6.15 60577 omental tumour biopsies stained with an anti-CD206 antibody. Representative images from mice treated with carboplatin (bottom row) and vehicle controls (top row) fourteen days after the start of treatment. Scale bar: 100µm.

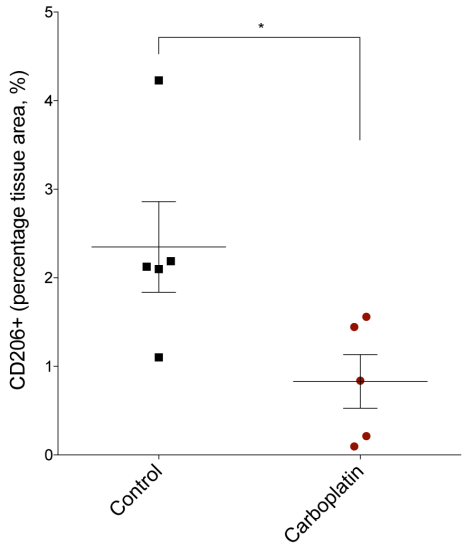

Figure 6.16 Quantification of CD206 staining by Definiens® digital analysis in 60577 omental tumours. Data relates to a single experiment, five carboplatin treated mice, five vehicle-treated mice, at a time point fourteen days following the start of treatment, the mean for each group is shown. Error bars represent SEM. Student's *t*-test p-values is shown; *<0.05.

Taken together these results show that carboplatin treatment depletes TAM from 60577 model omental tumours. This process was rapid and resulted in densities of TAM similar to healthy omenta fourteen days following the start of treatment.

Current standard first line chemotherapy for HGSOC is the combination of carboplatin and paclitaxel. Therefore an analogous experiment was conducted using paclitaxel at a dose of 10mg/kg i.p. (Figure 6.2B). Assessment of TAM density both as percentage of the $CD45^+$ cell infiltrate and as cells/mg of tissue demonstrated no significant difference between paclitaxel treated and vehicle-treated control (Figure 6.17). These data show that carboplatin but not paclitaxel depleted TAM in this model.

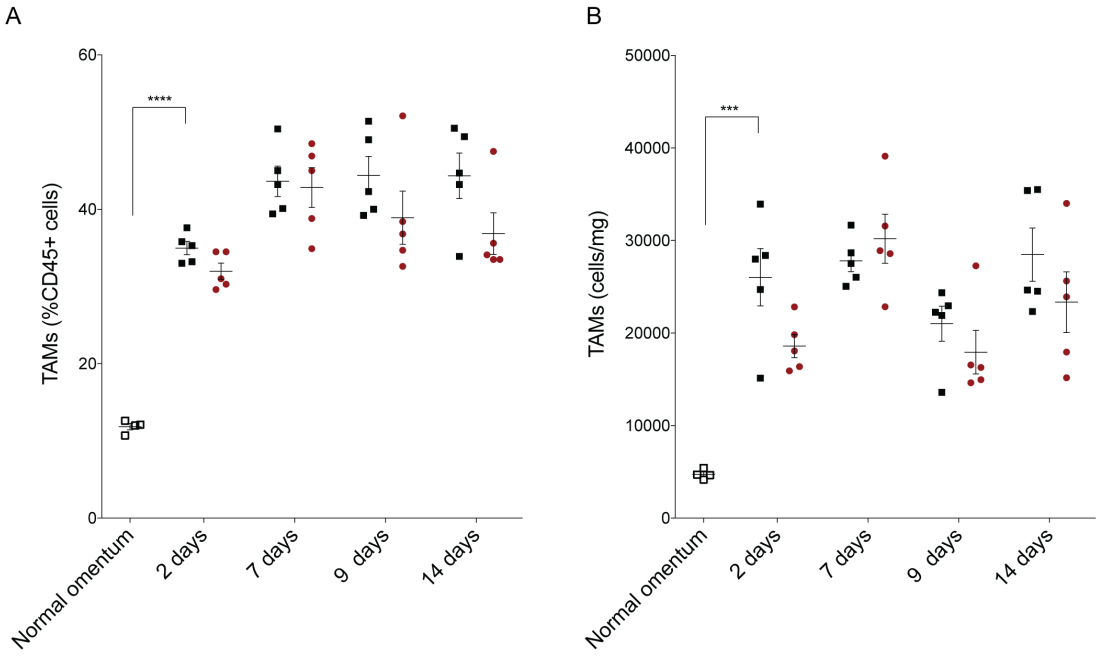

Figure 6.17 Effect of paclitaxel on TAM density in the 60577 model. Flow cytometry data relating to the immunostained stromal vascular fractions derived from omental tumours treated with paclitaxel (red circles), vehicle alone (black squares) or healthy omental controls (unfilled squares). **A** TAM frequency is expressed as a percentage of the $CD45^+$ population and **B** as cells/mg of tissue. Data relate to a single experiment, five paclitaxel treated mice, five vehicle-treated mice per time point and ten healthy omental controls; cells from healthy omental controls were combined and stained as four separate samples, the mean for each group is shown. Error bars represent SEM. Student's t-test p-value shown to compare means between normal omentum and control tumours at the start of treatment; ***p<0.001, p****<0.0001.

6.1.2 30200 model

To extend my assessment to the effects of chemotherapy on TAMs in murine HGSOC, I next treated 30200 tumour-bearing mice with either paclitaxel 10mg/kg i.p., carboplatin 20mg/kg i.p., the combination of paclitaxel and carboplatin or vehicle alone. Assessment of TAM density after the third dose of chemotherapy demonstrated striking and significant reductions in TAM density in carboplatin and combination treated mice compared to vehicle-treated controls (Figure 6.18). Interestingly, and in support of my previous observations in the 60577 model, there were no differences in TAM density in tumours treated with paclitaxel alone compared to vehicle-treated controls (Figure 6.18).

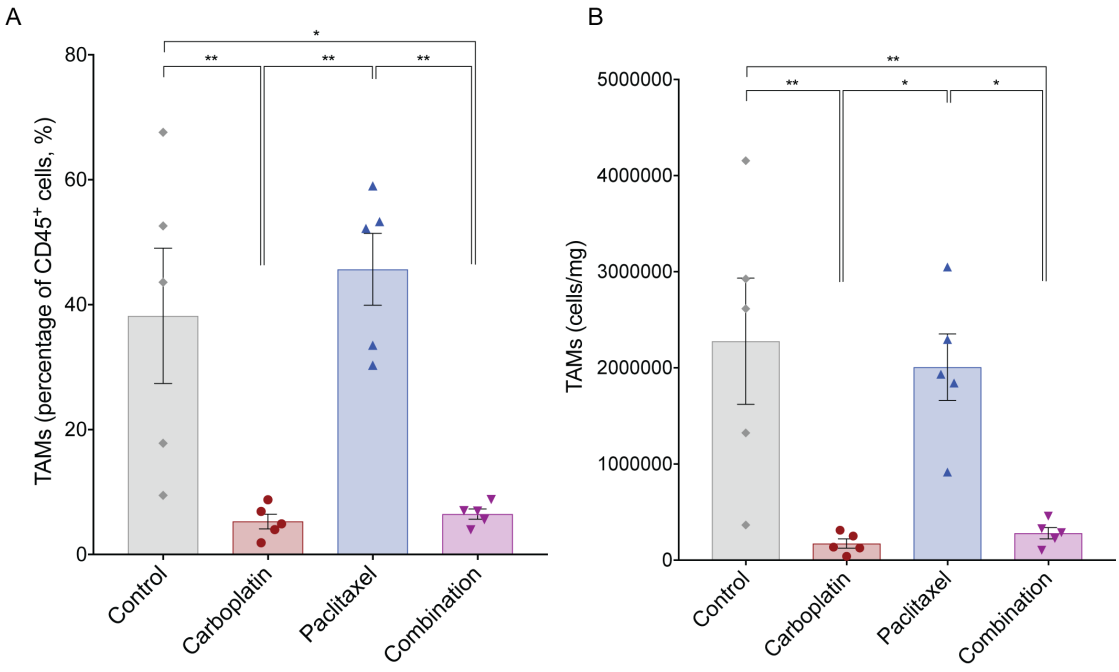

Figure 6.18 Effect of chemotherapy on TAM frequency in the 30200 model. Flow cytometry data relating to the immunostained stromal vascular fractions derived from omental tumours treated with three once-weekly doses of carboplatin, paclitaxel, carboplatin + paclitaxel or vehicle alone. **A** TAM frequency is expressed as a percentage of the total CD45$^+$ cell infiltrate. **B** TAM density expressed as cells/mg of tissue. Data relate to a single experiment, five mice per group, the mean for each group is shown. Error bars represent SEM. Significant one-way ANOVA p-values are shown; *p <0.05, **p<0.01.

6.1.3 HGS2 model

Finally, I assessed the effects of carboplatin treatment in the HGS2 model. Mice were culled seven days after a third dose of carboplatin (Figure 6.2D). As seen in Figure 6.19 the differences between carboplatin treated and vehicle controls at this time point, with this number of samples, was not statistically significant. However, in keeping with effects seen in the 60577 and 30200 models, there was a trend to a reduction (p=0.1) in TAM cell number after carboplatin treatment compared to vehicle-treated controls.

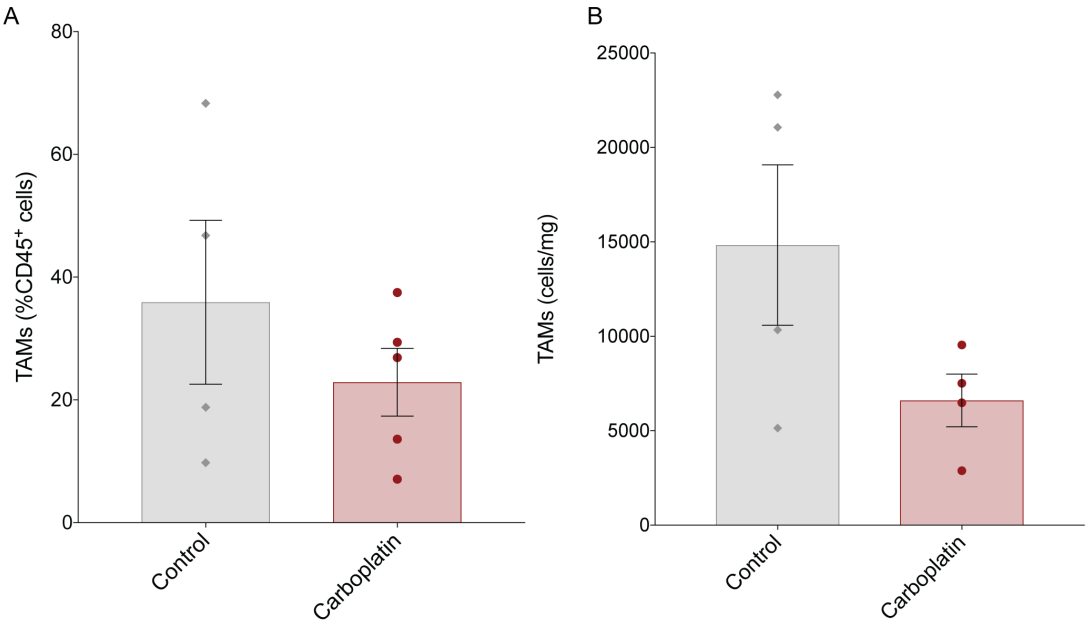

Figure 6.19 Effect of carboplatin on TAM density in the HGS2 model. Flow cytometry data relating to the immunostained stromal vascular fractions derived from omental tumours treated with carboplatin (red circles) or vehicle alone (grey diamonds). **A** TAM frequency is expressed as a percentage of the $CD45^+$ population and **B** as cells/mg of tissue. Data relate to a single experiment. The mean for each group is shown. Error bars represent SEM.

In summary, these data suggest that carboplatin treatment depletes macrophages from murine omental HGSOC tumours. This finding is in contrast to the effects of paclitaxel treatment. The results are also consistent with the reduction in TAM in the malignant cell areas post-NACT in human HGSOC.

6.2 Examining the phenotype of TAM before and after chemotherapy

6.2.1 60577 model

Although the time points following chemotherapy assessed in murine and human tumours differed, the data overall showed a reduction of TAM following carboplatin treatment. To understand this further, I set out to determine in the mouse models if the reduction in TAM was due to loss of certain populations of TAM or a global loss of all TAM subtypes, using a range of markers (CD206, PDL1 and MHC Class II). CD206 and PDL1 were used as markers of an alternatively activated or immunosuppressive macrophage phenotype. Class II MHC was used as a marker of classical activation.

Both $CD206^+$ and $PDL1^+$ TAMs were significantly decreased in carboplatin compared to vehicle-treated tumours as a percentage of the $CD45^+$ population and as cells/mg of tissue (Figure 6.20). By day fourteen the number of $PDL1^+$ and $CD206^+$ TAMs approximated the numbers seen in normal omental tissue (Figure 6.20C, D).

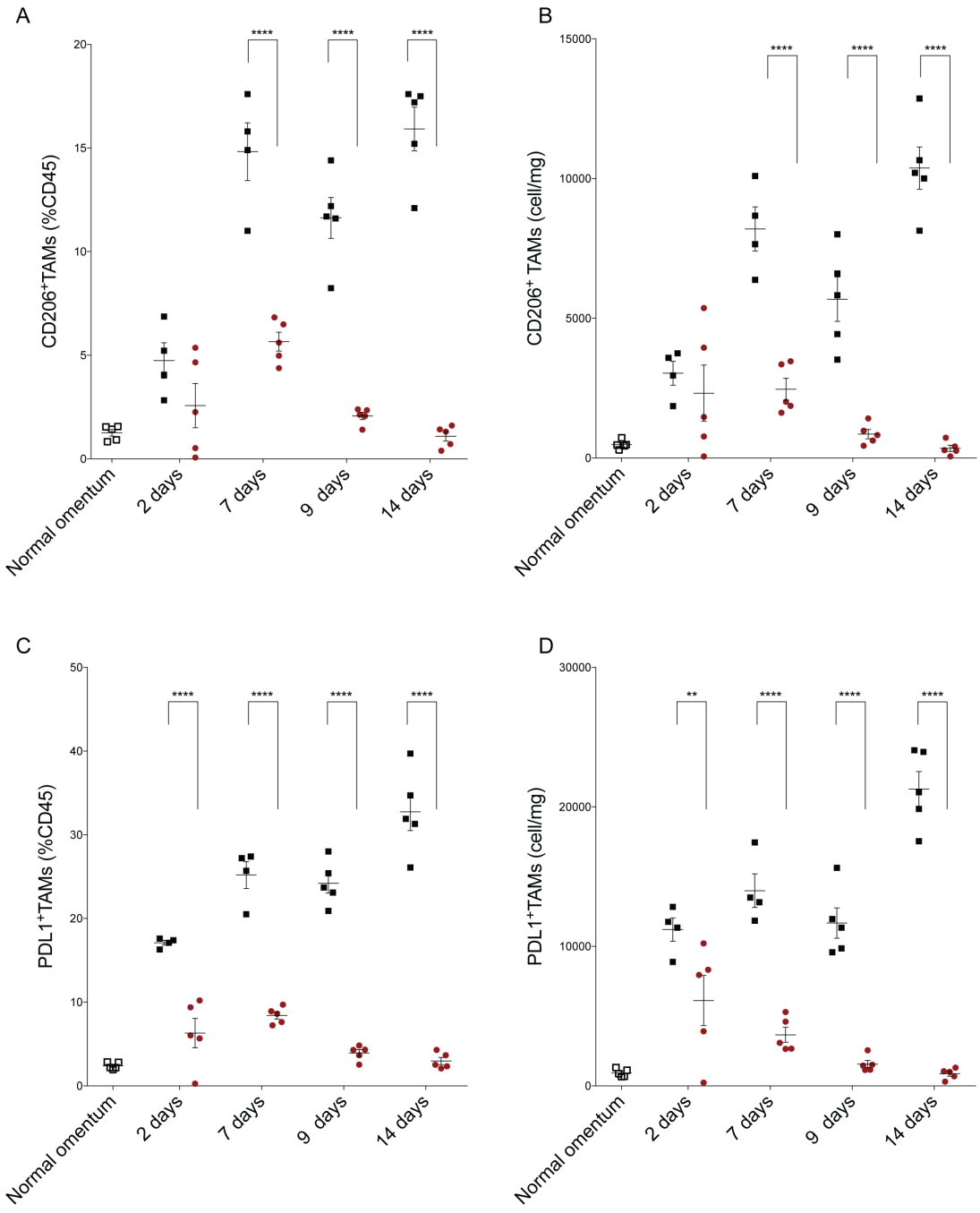

Figure 6.20 Effect of carboplatin on CD206$^+$TAM and PDL1$^+$TAM density in the 60577 model. Flow cytometry data relating to immunostained stromal vascular fractions derived from omental tumours treated with carboplatin (red circles), vehicle alone (black squares) or healthy omental controls (unfilled squares). **A** CD206$^+$TAM frequency is expressed as a percentage of the CD45$^+$ population and **B** as cells/mg of tissue. **C** PDL1$^+$TAM frequency is expressed as a percentage of the CD45$^+$ population and **D** as cells/mg of tissue. Data relate to a single experiment, five carboplatin treated mice, four-five vehicle-treated mice per time point and ten healthy omental controls; cells from healthy omental controls were combined and stained as five seperate samples, the mean for each group is shown. Error bars represent SEM. Significant two-way ANOVA p-values are shown; **p <0.01, ****p <0.0001.

I next assessed the frequency of MHC Class II-high expressing TAMs (MHC Class II$^+$) and CD86$^+$TAM, both markers associated with a proinflammatory 'anti-tumour' TAM phenotype. Here again I observed significant decreases in the numbers of TAMs expressing both these markers as a percentage of the CD45$^+$ population and as cells/mg of tissue (Figure 6.21).

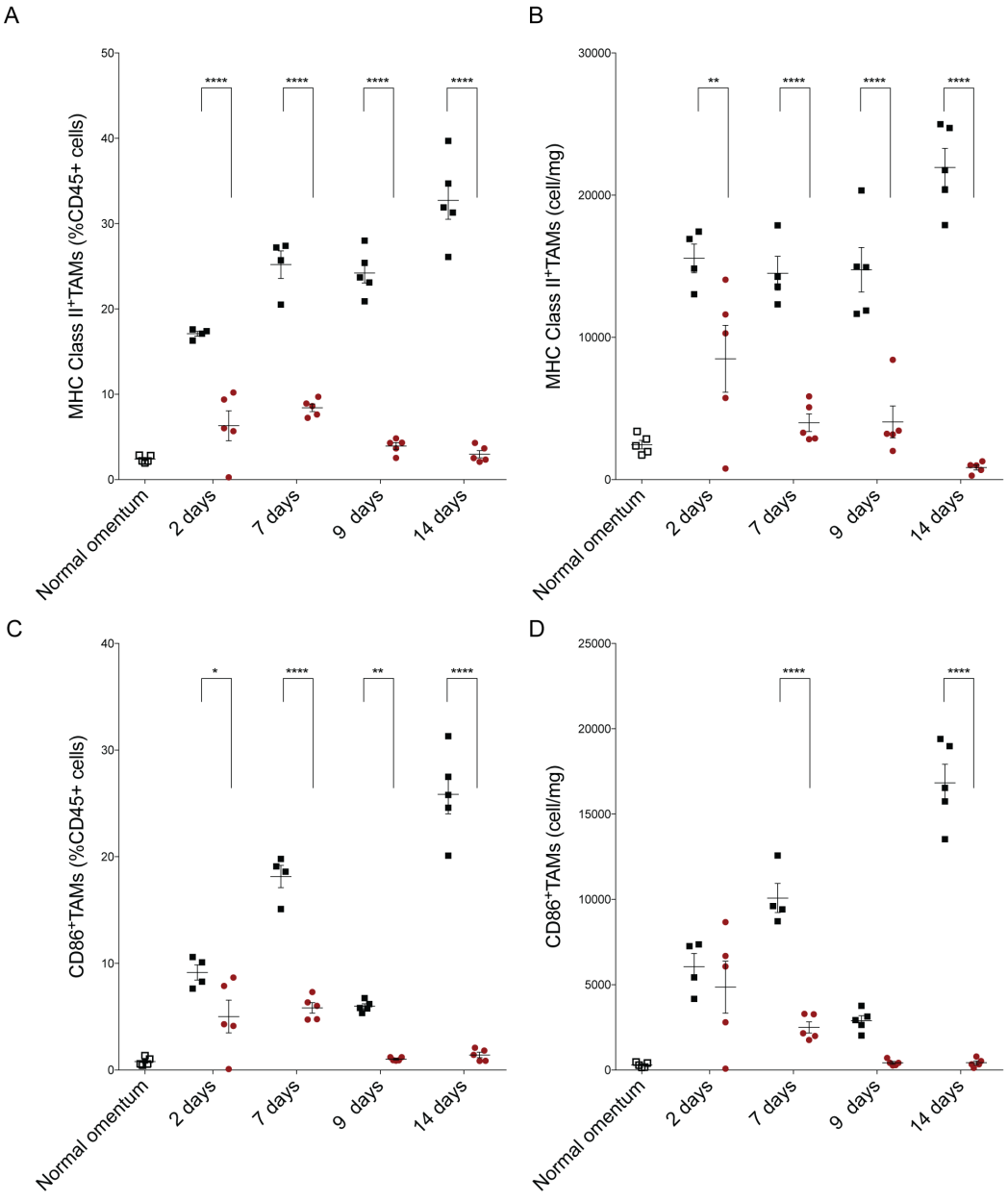

Figure 6.21 Effect of carboplatin on MHC Class II$^+$TAM and CD86$^+$TAM density in the 60577 model. Flow cytometry data relating to the immunostained stromal vascular fractions derived from omental tumours treated with carboplatin (red circles), vehicle alone (black squares) or healthy omental controls (unfilled squares). **A** MHC Class II$^+$TAM frequency is expressed as a percentage of the CD45$^+$ population and **B** as cells/mg of tissue. **C** CD86$^+$TAM frequency is expressed as a percentage of the CD45$^+$ population and **D** as cells/mg of tissue. Data relate to a single experiment, five carboplatin treated mice, four-five vehicle-treated mice per time point and ten healthy omental controls; cells from healthy omental controls were combined and stained as five separate samples, the mean for each group is shown. Error bars represent SEM. Two-way ANOVA p-values are shown; *<0.01, **<0.01, ****<0.0001.

These data suggest that carboplatin treatment results in a rapid depletion of TAM expressing both pro- and anti-inflammatory markers. This may reflect a depletion of multiple TAM subpopulations, rather than depletion of a specific subpopulation of TAM defined by expression of a single marker.

6.2.2 30200 model

In agreement with my observations in the 60577 model, I observed significant reductions in CD206, PDL1 and MHC Class II-high expressing TAMs as a percentage of the total $CD45^+$ cell infiltrate and as cells/mg of tissue (Figure 6.22) in the 30200 experiment. These data suggest that carboplatin either alone or in combination with paclitaxel depletes TAM expressing a broad range of macrophage markers.

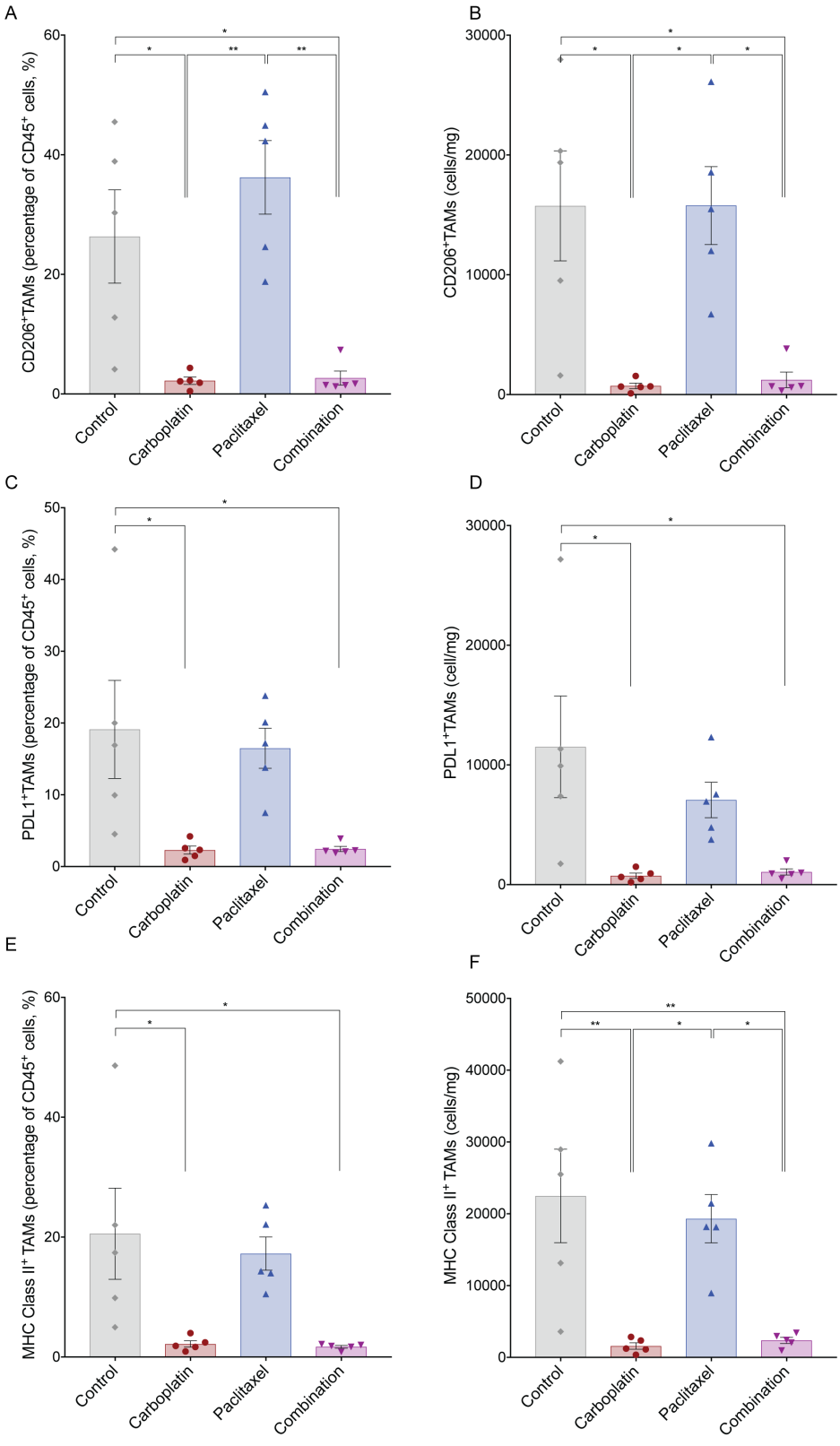

Figure 6.22 Effect of chemotherapy on TAM populations in the 30200 model. Flow cytometry data relating to the immunostained stromal vascular fractions derived from omental tumours treated with three once-weekly doses of carboplatin, paclitaxel, carboplatin + paclitaxel or vehicle alone. **A**, **C**, **E** CD206$^+$TAMs, PDL1$^+$TAMs and MHC Class II$^+$TAMs frequency is expressed as a percentage of the total CD45$^+$ cell infiltrate, **B**, **D**, **F** CD206$^+$TAMs, PDL1$^+$TAMs and MHC Class II$^+$TAM frequency is expressed as cells/mg of tissue. Data relate to a single experiment, five mice per group, the mean for each group is shown. Error bars represent SEM. Significant one-way ANOVA p-values are shown; *p <0.05, **p <0.01.

6.2.3 HGS2 model

Finally, I preformed the same analysis in the HGS2 model. As described above, I did not find significant reductions in overall TAM density in this model. There were no significant differences in $CD206^+$, $PDL1^+$ (Figure 6.22) and MHC Class II-high (MHC Class II^+) TAMs (Figure 6.23) as a percentage of the $CD45^+$ cell infiltrate and as cells/mg of tissue following carboplatin treatment compared to vehicle-treated controls. There were however, non-significant reductions in all markers assessed, which, in the context of the changes seen in the previous two models would suggest a conserved effect across all three murine HGSOC models.

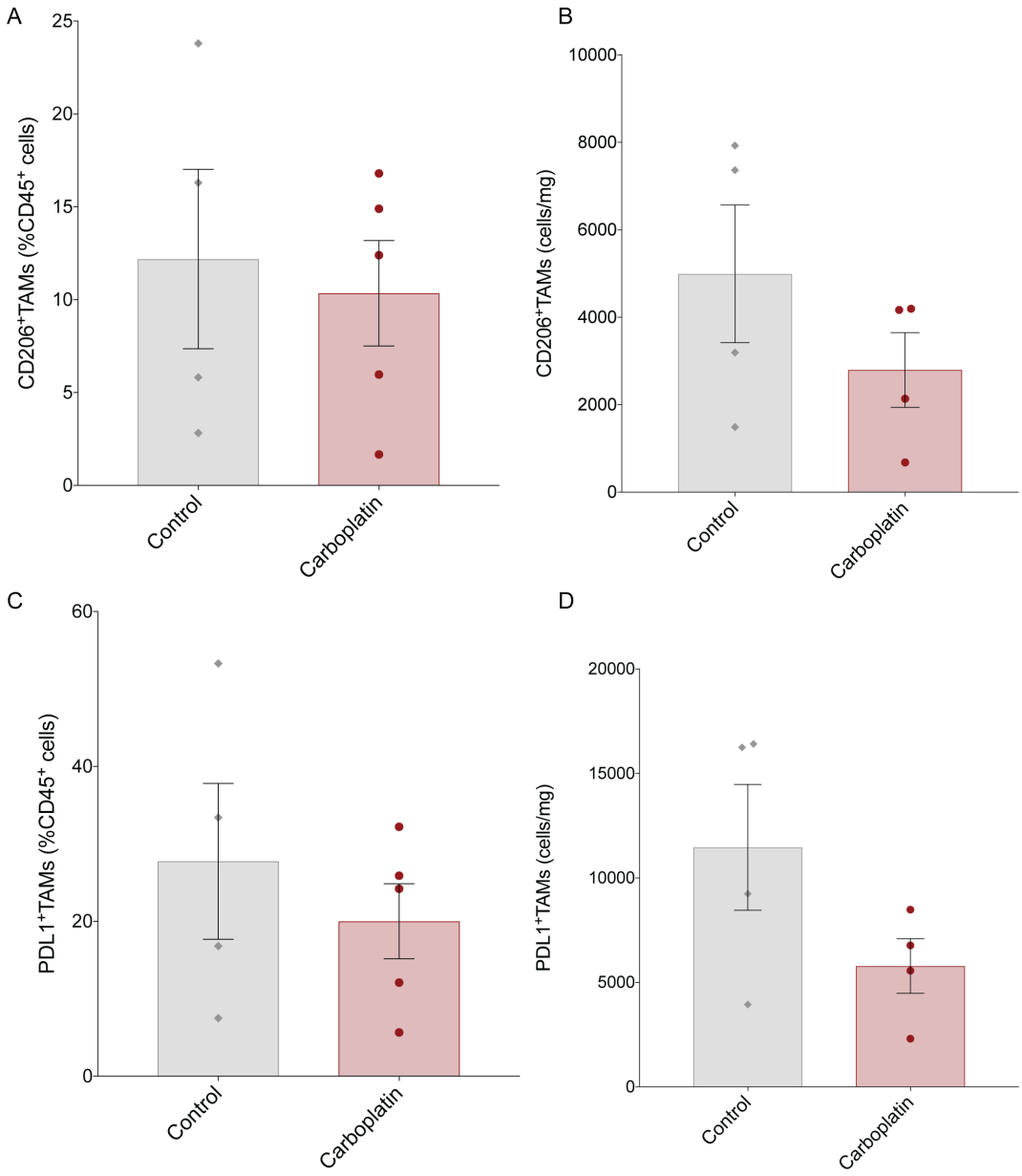

Figure 6.23 Effect of carboplatin on TAM density in the HGS2 model. Flow cytometry data relating to the immunostained stromal vascular fractions derived from omental tumours treated with carboplatin (red circles) or vehicle alone (grey diamonds). **A, C** CD206$^+$TAM and PDL1$^+$TAM frequency is expressed as a percentage of the CD45$^+$ population and **B**, **D** as cells/mg of tissue. Data relates to a single experiment. The mean for each group is shown. Error bars represent SEM.

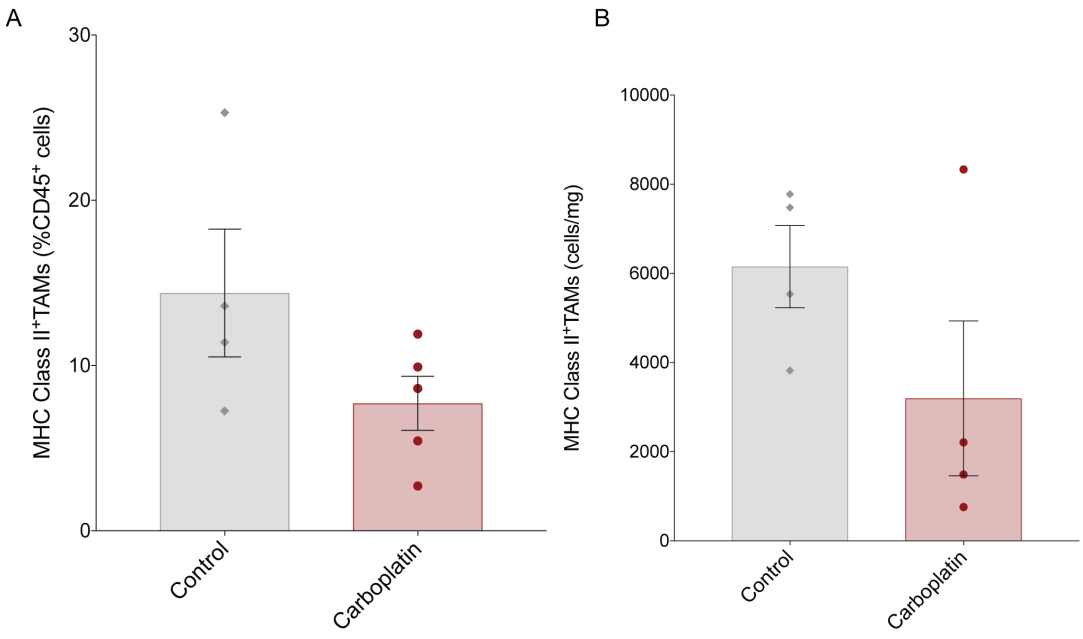

Figure 6.24 Effect of carboplatin on TAM density in the HGS2 model. Flow cytometry data relating to the immunostained stromal vascular fractions derived from omental tumours treated with carboplatin (red circles) or vehicle alone (grey diamonds). **A** MHC Class II$^+$TAM frequency is expressed as a percentage of the CD45$^+$ population and **B** as cells/mg of tissue. Data relates to a single experiment. The mean for each group is shown. Error bars represent SEM.

Overall, these data demonstrate that carboplatin but not paclitaxel treatment results in reductions of TAM populations of murine HGSOC omental tumours. This supports my findings in human HGSOC, where I observed reductions in the density of TAMs within malignant cell areas following NACT compared to matched untreated samples. Within the murine models the reduction in TAM cell number is due to the loss of TAM that express markers associated with both an alternatively and classically activated phenotype.

6.3 TAM phenotype after chemotherapy

In human HGSOC I demonstrated changes in TAM phenotype following NACT as assessed by decreased surface expression of CD163 and trends to reductions in the scavenger receptors CD206 and CD209. I therefore wanted to assess the phenotype of the remaining TAM after carboplatin and paclitaxel treatment in murine tumours. TAM phenotype was assessed by comparing the expression of various activation markers by FC. This was under taken in two ways: by quantifying the percentage of the marker-positive TAMs within the TAM population and by mean fluorescence intensity (MFI) of the various markers within the TAM population. This is in contrast to the data presented in section 6.6 which assessed for changes in the proportion of TAMs defined by a particular marker within the entire CD45$^+$-immune cell microenvironment of HGSOC.

6.3.1 60577 model

To characterise the effect of chemotherapy on TAM phenotype in 60577 tumours I assessed the expression of myeloid polarisation makers as a percentage of the TAM population and by mean florescence intensity (MFI) rather than the entire $CD45^+$ population as described in 6.6. Interestingly, comparing carboplatin treated tumours with vehicle-treated controls I found significant reductions in the expression of $CD206^+$ and $PDL1^+$ both as the percentage of positive cells within the TAM population and by MFI (Figure 6.25A, B). The data showed significant differences between carboplatin treated and vehicle controls after the second dose of carboplatin (day 9).

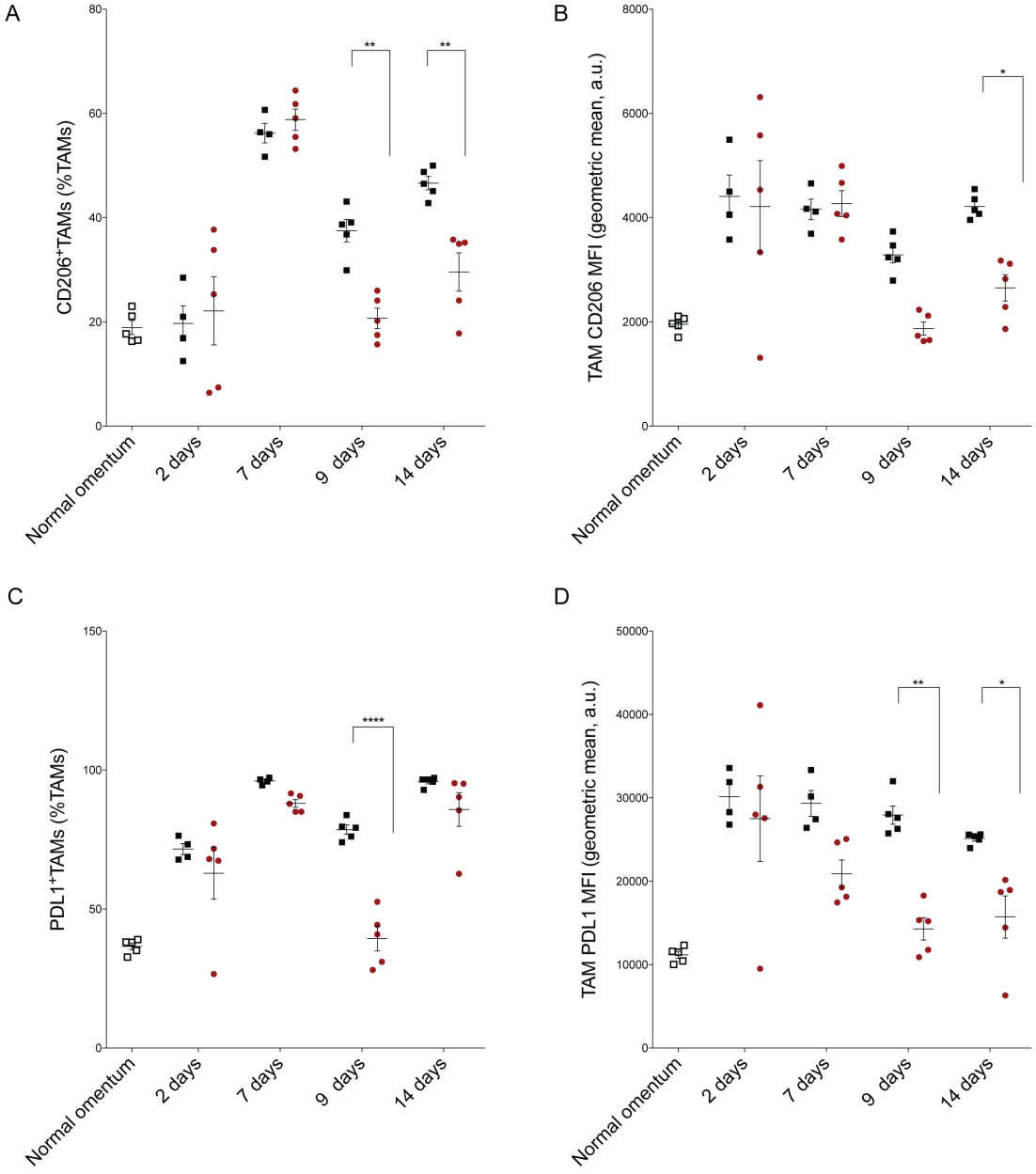

Figure 6.25 Effect of carboplatin on TAM phenotype in the 60577 model. Flow cytometry data relating to the immunostained stromal vascular fractions derived from omental tumours treated with carboplatin (red circles), vehicle alone (black squares) or healthy omental controls (unfilled squares). **A** CD206^{+}TAM frequency is expressed as a percentage of the total TAM population and **B** CD206 MFI. **C** PDL1^{+}TAM frequency is expressed as a percentage of the total TAM population and **D** PDL1 MFI. Data relates to a single experiment, five carboplatin treated mice, four-five vehicle-treated mice per time point and ten healthy omental controls; cells from healthy omental controls were combined and stained as five seperate samples, the mean for each group is shown. Error bars represent SEM. Significant two-way ANOVA p-values are shown; *<0.05, **<0.01, ****<0.0001.

Given the decreases in markers associated with an anti-inflammatory and immunosuppressive TAM phenotype, I assessed for possible reciprocal changes in pro-inflammatory (classically activated) TAM markers. I found significant reductions in both MHC Class II and CD86 expression in TAMs treated with carboplatin compared to

vehicle-treated tumours (Figure 6.26).

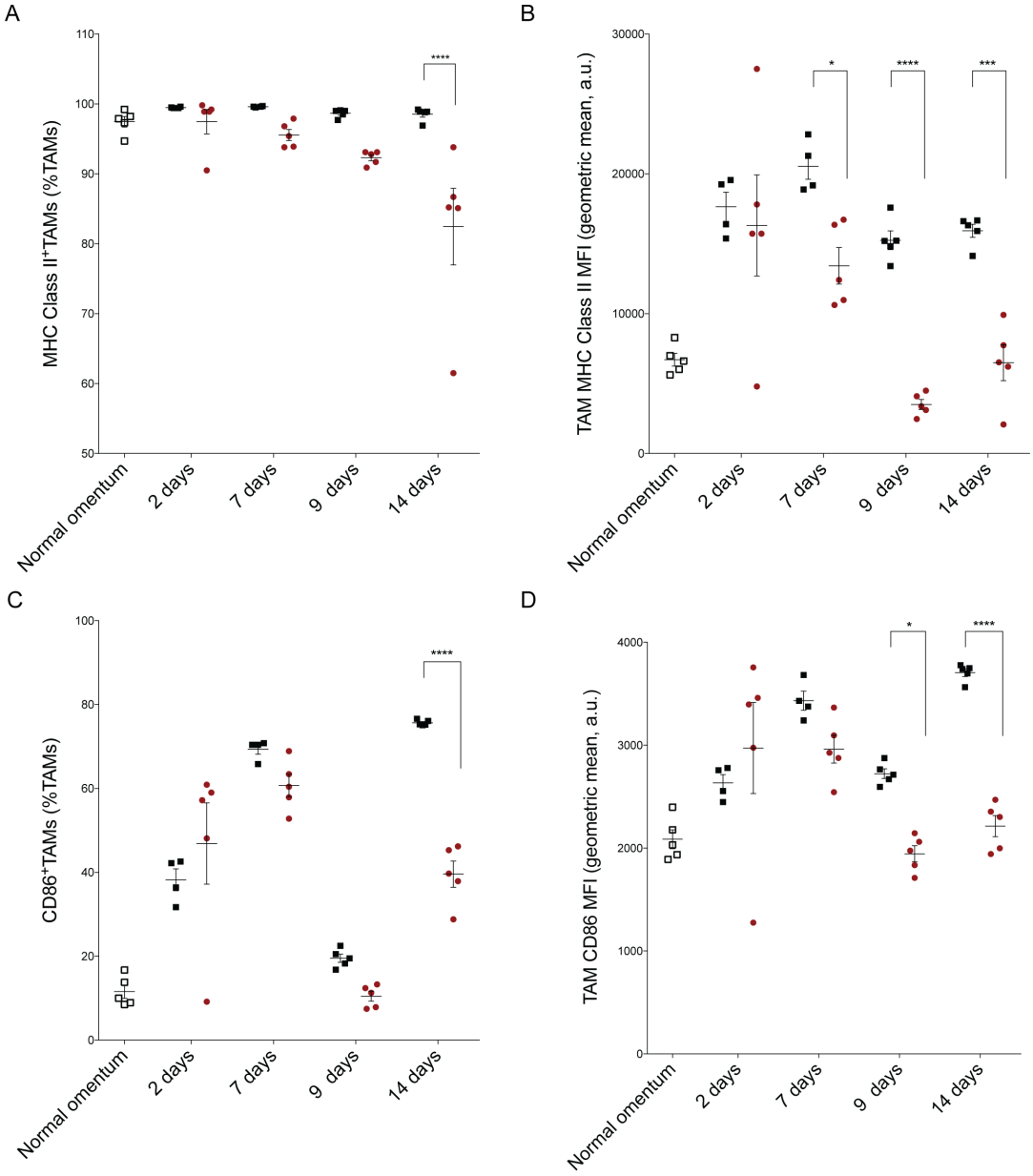

Figure 6.26 Effect of carboplatin on TAM phenotype in the 60577 model. Flow cytometry data relating to the immunostained stromal vascular fractions derived from omental tumours treated with carboplatin (red circles), vehicle alone (black squares) or healthy omental controls (unfilled squares). **A** MHC Class II^{+}TAM frequency is expressed as a percentage of the total TAM population and **B** MHC Class II MFI. **C** CD86^{+}TAM frequency is expressed as a percentage of the total TAM population and **D** CD86 MFI. Data relates to a single experiment, five carboplatin treated mice, four-five vehicle-treated mice per time point and ten healthy omental controls; cells from healthy omental controls were combined and stained as five separate samples, the mean for each group is shown. Error bars represent SEM. Significant two-way ANOVA p-values are shown; *<0.05, ***<0.001, ****<0.0001.

In summary these data show changes in macrophage activation markers in the remaining TAM population following carboplatin treatment compared to vehicle-treated controls. Assessing single markers within the entire TAM population, I observed significant reductions in both markers of classical and alternative macrophage activation. Overall, these data would support a change in phenotype distinct from the classical M1

(classically activated)/M2 (alternatively activated) paradigm after carboplatin treatment.

I next assessed the effects of paclitaxel treatment on TAM phenotype in this model. Comparing between paclitaxel treated and control tumours I found a significant increase in $CD206^{+}$TAM two weeks after treatment started (Figure 6.27). There was a significant reduction in $PDL1^{+}$TAM in paclitaxel treated tumours forty-eight hours after treatment, however this was not seen at later time points. There were no significant changes in the expression of MHC Class II or CD86 expression.

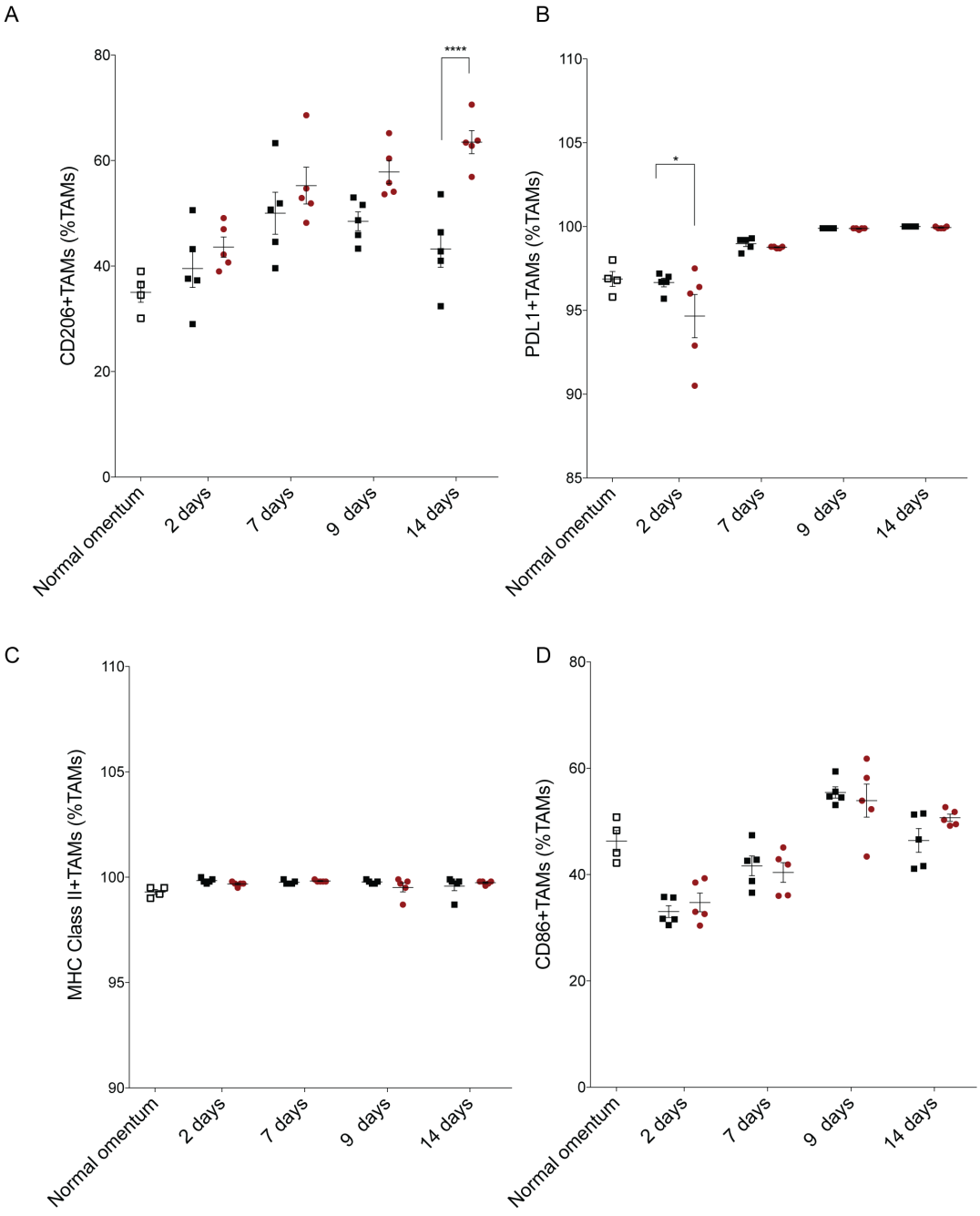

Figure 6.27 Effect of paclitaxel on TAM phenotype in 60577 model. Flow cytometry data relating to the immunostained stromal vascular fractions derived from omental tumours treated with paclitaxel (red circles), vehicle alone (black squares) or healthy omental controls (unfilled squares). **A** $CD206^+$TAM **B** $PDL1^+$TAM **C** MHC Class II^+TAM **D** $CD86^+$TAM frequency is expressed as a percentage of the TAM population. Data relates to a single experiment, five paclitaxel treated mice, five vehicle-treated mice per time point and ten healthy omental controls; cells from healthy omental controls were combined and stained as four separate samples, the mean for each group is shown. Error bars represent SEM.

These data would suggest that paclitaxel may increase $CD206^+$ expression within TAMs possibly suggesting an increase in an anti-inflammatory phenotype. However, there were no concomitant changes in MHC Class II or CD86 expression to support a classical phenotype switch. These data are clearly different from the changes in TAM phenotype seen in response to carboplatin treatment.

6.3.2 30200 model

I next assessed the effects of chemotherapy on TAM phenotype in 30200 tumours. I found a reduction in the expression of $CD206^{+}$TAMs as a percentage of the TAM population and by MFI in carboplatin and combination (carboplatin + paclitaxel) treated tumours compared to paclitaxel and vehicle-treated tumours. The differences were statistically significant when comparing carboplatin *vs* paclitaxel and combination *vs* paclitaxel treated tumours (Figure 6.28A, B). There were no clear differences in PDL1 expression on TAM assessed by MFI or as a percentage of positive cells. (Figure 6.28 C, D).

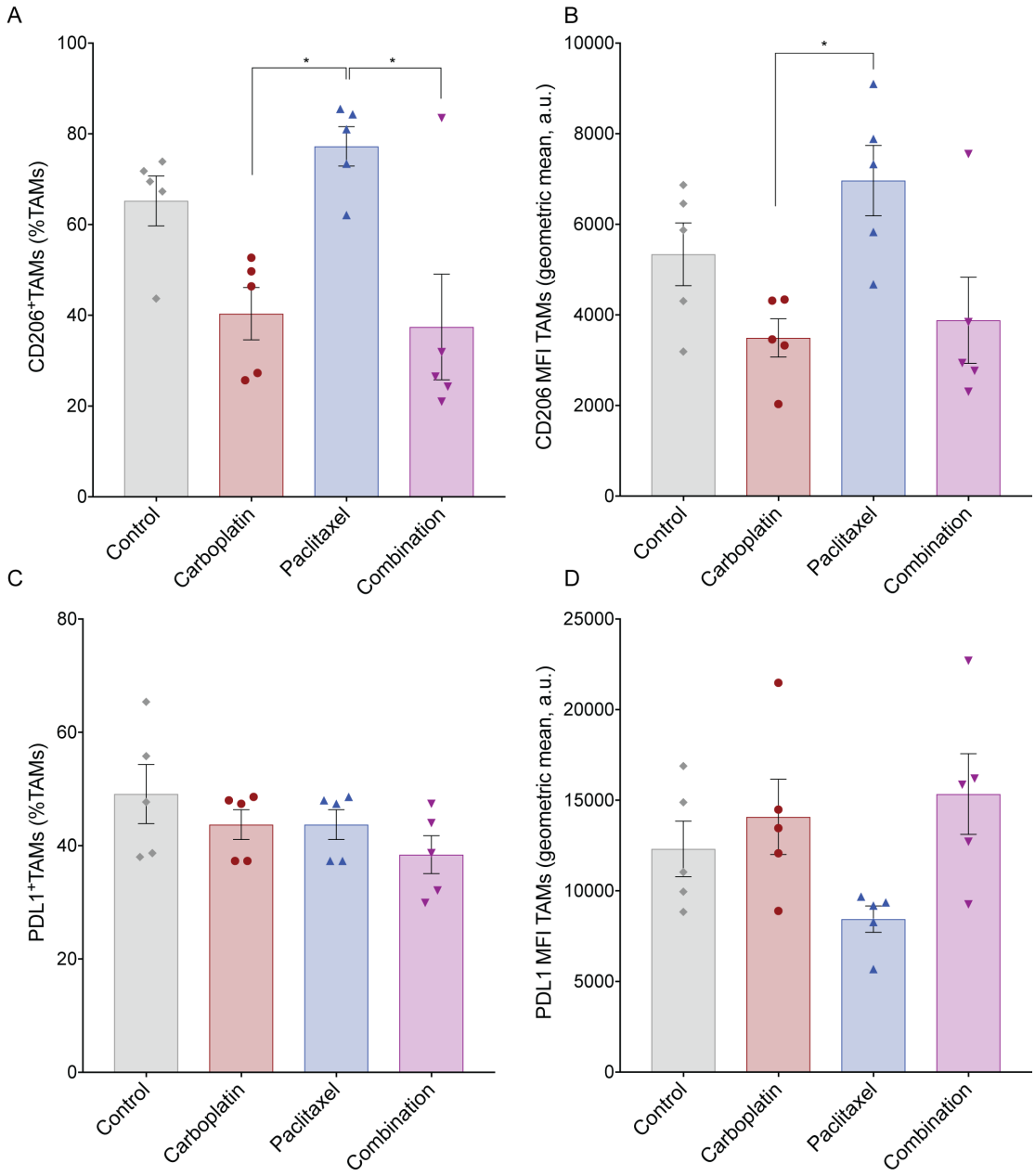

Figure 6.28 Effect of chemotherapy on TAM phenotype in the 30200 model. Flow cytometry data relating to the immunostained stromal vascular fractions derived from omental tumours treated with three once-weekly doses of carboplatin, paclitaxel, carboplatin + paclitaxel or vehicle alone. **A**, **C** CD206^{+}TAM, PDL1^{+}TAM frequency is expressed as a percentage of the TAM population. **B**, **D** CD206, PDL1 MFI. Data relates to a single experiment, five mice per group, the mean for each group is shown. Error bars represent SEM. Significant one-way ANOVA p-values are shown; *p <0.05.

Assessment of MHC Class II and CD86 TAM surface expression showed fewer clear changes than observed in the 60577 model. The percentage of MHC Class II-high TAM decreased after single agent carboplatin and paclitaxel treatment, however, this was not statistically significant. There was a significant reduction in the percentage MHC Class II-high TAMs in combination treated compared to vehicle-treated tumours (Figure 6.29A). However, MHC Class II MFI showed no difference between chemotherapy treated and control tumours (Figure 6.29B). CD86 decreased, though not significantly, both as the

percentage of positive cells and by MFI after carboplatin and combination treatment compared to vehicle-treated and paclitaxel treated tumours (Figure 6.29C, D).

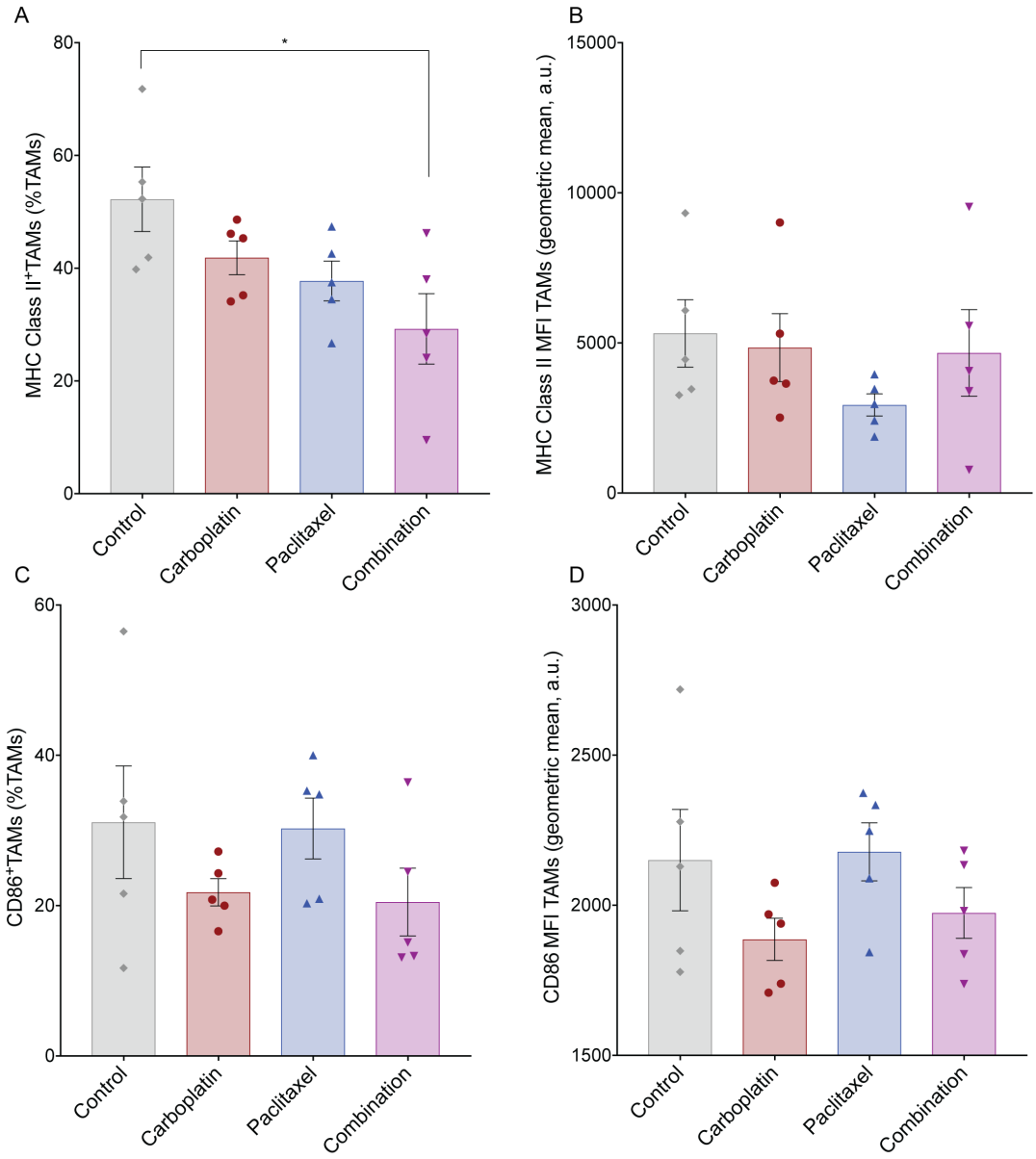

Figure 6.29 Effect of chemotherapy on TAM phenotype in the 30200 model. Flow cytometry data relating to the immunostained stromal vascular fractions derived from omental tumours treated with three once-weekly doses of carboplatin, paclitaxel, carboplatin + paclitaxel or vehicle alone. **A**, **C** MHC Class II^{+}TAM, CD86^{+}TAM frequency is expressed as a percentage of the TAM population, **B**, **D** MHC Class II, CD86 MFI. Data relates to a single experiment, five mice per group, the mean for each group is shown. Error bars represent SEM. Significant one-way ANOVA p-values are shown; *p <0.05.

Overall, these data suggest that in the 30200 model carboplatin treatment, but not paclitaxel treatment, altered the phenotype of the TAMs remaining in the tumour compared to vehicle-treated controls. As seen in the 60577 model, I observed reduced expression of both CD206 and MHC Class II following carboplatin treatment. Reductions in alternatively activated markers seen in both these models mirrors changes in TAM

phenotype seen in human HGSOC post-NACT.

6.3.3 HGS2 model

Finally, I assessed for a change in phenotype with the TAM population (Figure 6.30) in the HGS2 model. Overall there were no significant differences in the expression of TAM activation markers between carboplatin treated and untreated tumours. However, in contrast to the experiments in the 30200 and 60577 models there was a trend to an increase in the alternatively activated markers CD206 and PDL1 (Figure 6.30).

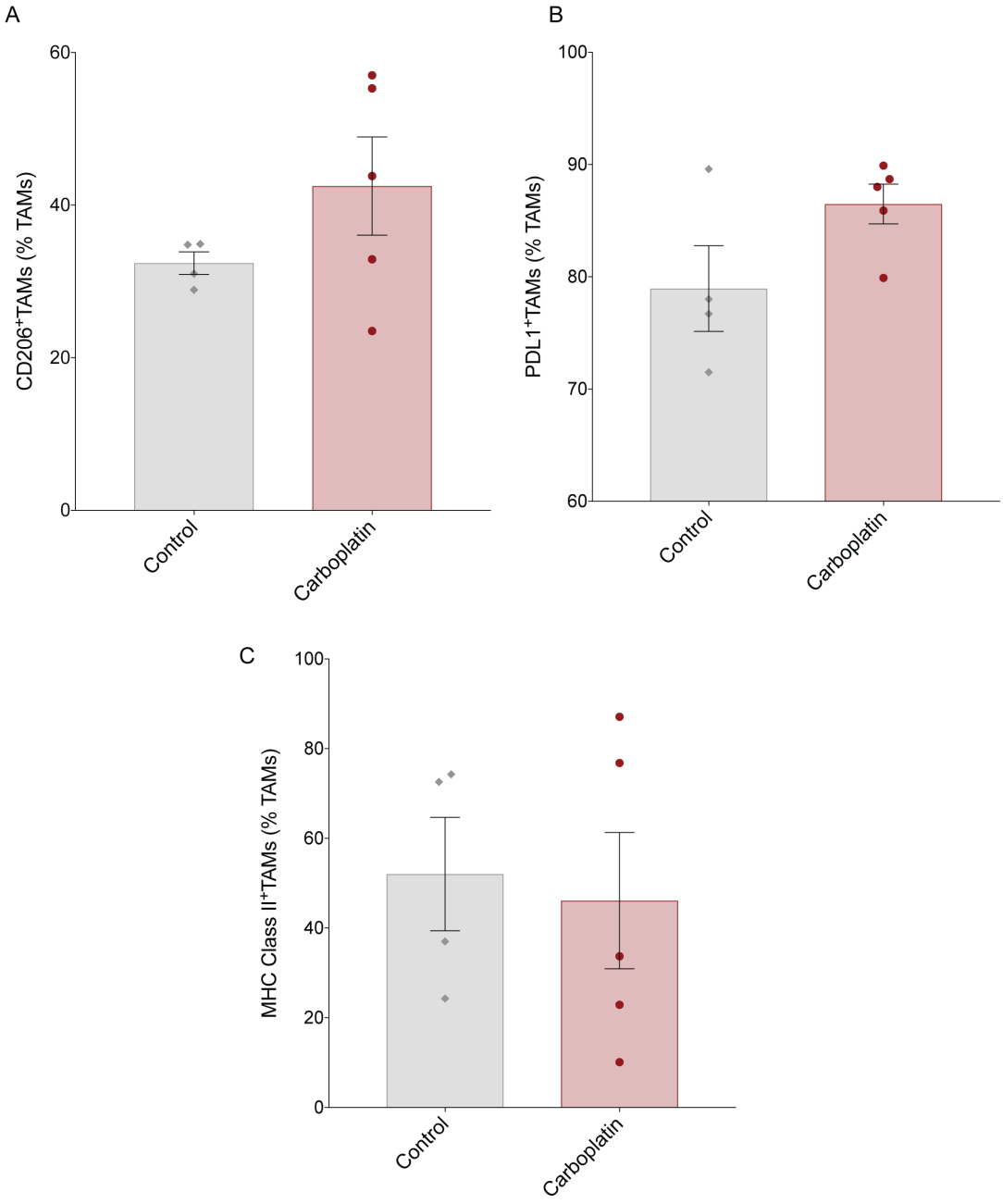

Figure 6.30 Effect of carboplatin on TAM phenotype in the HGS2 model. Flow cytometry data relating to the immunostained stromal vascular fractions derived from omental tumours treated with carboplatin (red circles) or vehicle alone (grey diamonds). **A** CD206^{+}TAM **B** PDL1^{+}TAM **C** MHC Class II^{+}TAM frequency is expressed as a percentage of the TAM population. Data relates to a single experiment. The mean for each group is shown. Error bars represent SEM.

6.4 tSNE analysis of myeloid populations

Dimensionality reduction using the tSNE (t-distributed stochastic neighbour embedding) algorithm allows visualisation of multidimensional data such as FC data in two dimensions. I used tSNE for two reasons *i*) to validate the manual gating applied to the FC data described previously and *ii*) to investigate subpopulations of macrophages

within healthy omentum, in murine HGSOC tumours and tumours treated with carboplatin.

6.4.1 tSNE validation of manual TAM gating

Data relating to the $CD45^+$ population of all tumours in the 60677 carboplatin time-course experiment (Figure 6.2A) were concatenated and the tSNE algorithm was applied. This produced the tSNE plot shown in Figure 6.31A. I then applied the manual gating (Figure 6.9) to the tSNE analysis (Figure 6.31B). The algorithm clustered TAMs as a discrete island. Analysing the TAM population through the experimental time-course shows the selective depletion of this population within carboplatin treated tumours compared to vehicle-treated controls (Figure 6.31D).

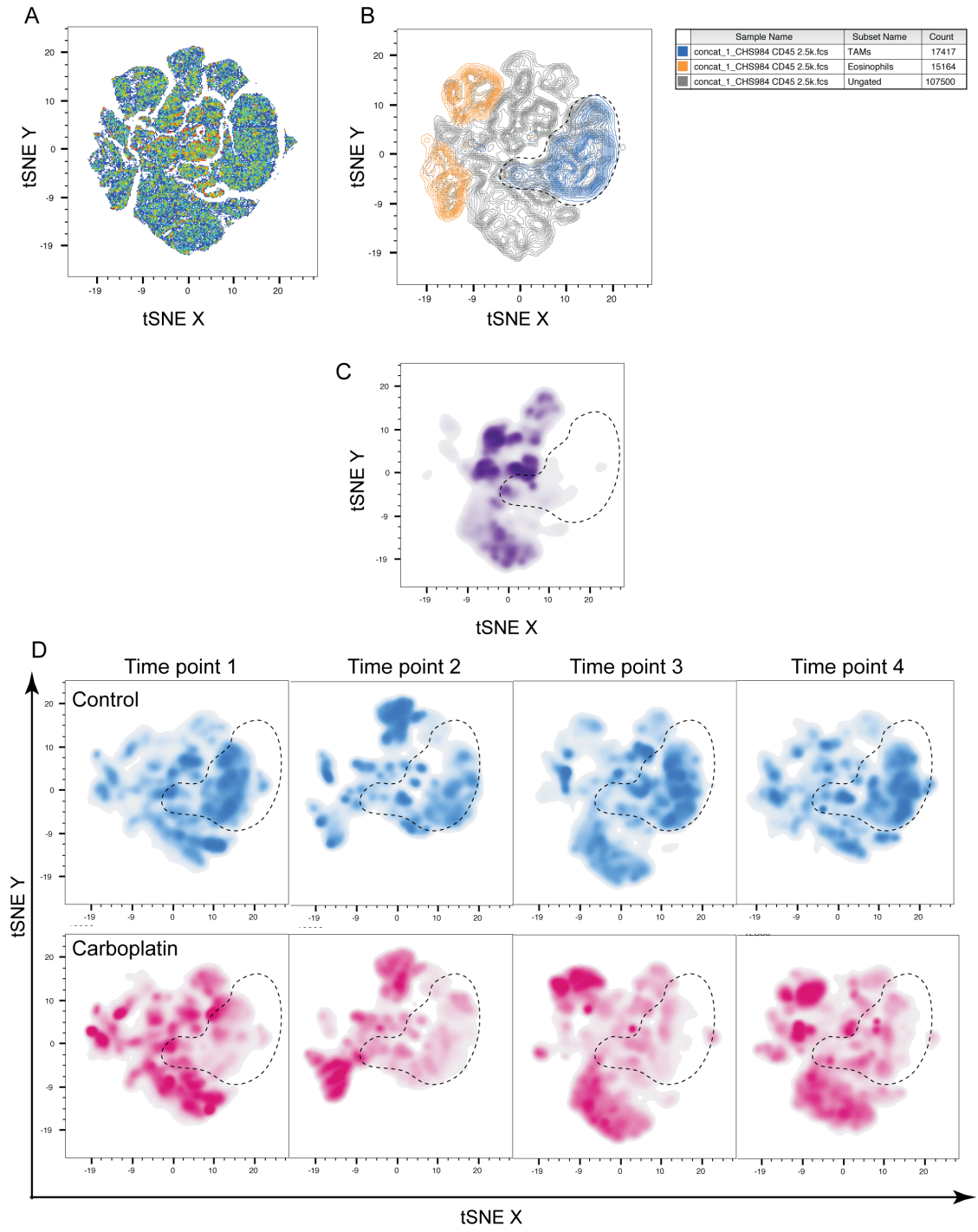

Figure 6.31 tSNE analysis of the 60577 model. A tSNE plot showing data relating to $CD45^+$ population of all samples in the experiment. **B** Manual gating for TAMs ($CD45^+Ly6G^-Ly6G^-CD11b^+F4/80^+MHC\ Class\ II^+$ cells) applied to data (blue overlay), manual gating for eosinophils is also shown (orange overlay). **C** tSNE plot showing data relating to $CD45^+$ population of normal omentum. **D** tNSE plots showing data relating to $CD45^+$ population for control (blue) and carboplatin treated tumours (red) at each of the four time points assessed. Dashed line overlay indicates TAM population.

I performed a similar analysis for the 30200 experiment, which assessed both the effects of carboplatin and paclitaxel. Figure 6.32A shows the tSNE plot for the $CD45^+$ population of all samples in the experiment. Applying the manual gating for TAMs, again showed these cells to cluster as a discrete island (Figure 6.32B). Carboplatin and the combination

of carboplatin and paclitaxel treatment depleted this population compared to paclitaxel single-agent or vehicle-treated tumours (Figure 6.32C). These data confirm the manual gating strategy and TAM depletion following carboplatin but not paclitaxel treatment.

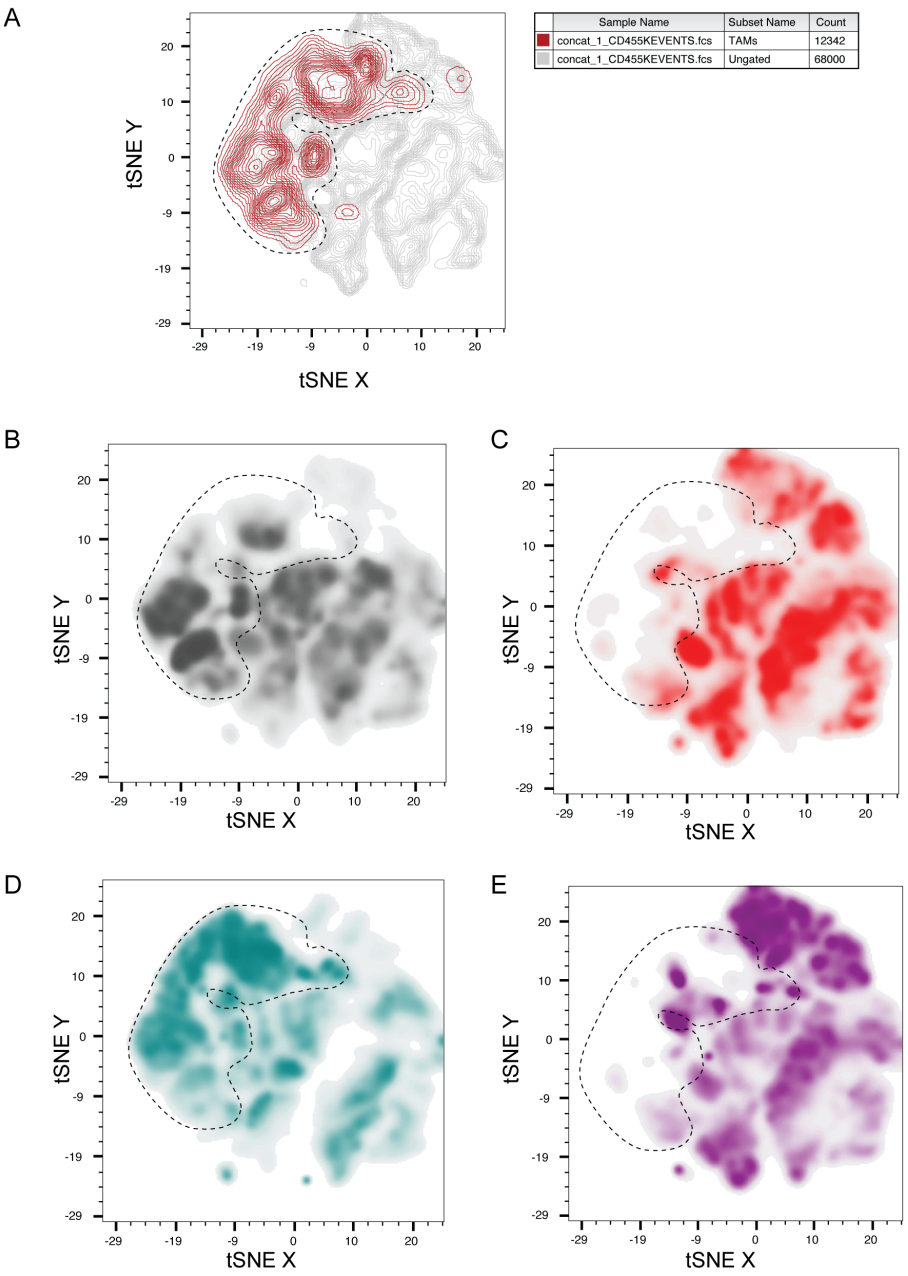

Figure 6.32 tSNE analysis of the 30200 model. A tSNE plot showing data relating to $CD45^+$ population of all samples in the experiment, manual gating for TAMs ($CD45^+Ly6G^-Ly6G^-CD11b^+F4/80^+MHC\ Class\ II^+$ cells) applied to data (red overlay). tSNE plot showing data relating to $CD45^+$ population for **B** vehicle-treated, **C** carboplatin treated, **D** paclitaxel treated and **E** combination (carboplatin + paclitaxel) treated tumours. Dashed line overlay indicates the TAM population.

6.4.2 tSNE analysis of TAM subpopulations

The phenotype analyses presented so far have been limited by the assessment of individual markers assessed within the entire TAM population. tSNE allows for unbiased

clustering of the data, based on differences in fluorescence intensity of multiple markers at single-cell resolution. I applied this approach to define subpopulations within the TAM compartment ($CD45^+Ly6C^-Ly6G^-F4/80^+CD11b^+$ cells) using data from all markers in the panel. It was possible to track these subpopulations within heathy omentum, untreated and carboplatin treated tumours over four times points during a two week treatment course. Given the previous findings of phenotype changes not clearly described by pro-inflammatory and anti-inflammatory markers, I hoped assessment of multiple markers at single-cell resolution would provide a better understanding of the changes in TAM phenotype.

Within the TAM cluster of the tSNE plot I defined 11 discrete nodes produced by the algorithm (Figure 6.33A). I named these nodes 'modules' 1-11. As can be seen in Figure 6.33, each module contained cells with a different expression profile for the markers in the panel, e.g. module 1 cells were F4/80-high, CD206-high, whereas modules 9 and 10 were F4/80-low yet obviously differed in MHC Class II, CD80 and CD86 expression. Figure 6.33B shows a heat map summarising the expression of all the myeloid markers within the panel across the eleven modules. These data show that within the entire TAM population, there is a great deal of complexity in the expression of a small number of myeloid surface markers. Such complexity was not captured by assessing individual marker expression within the entire TAM population.

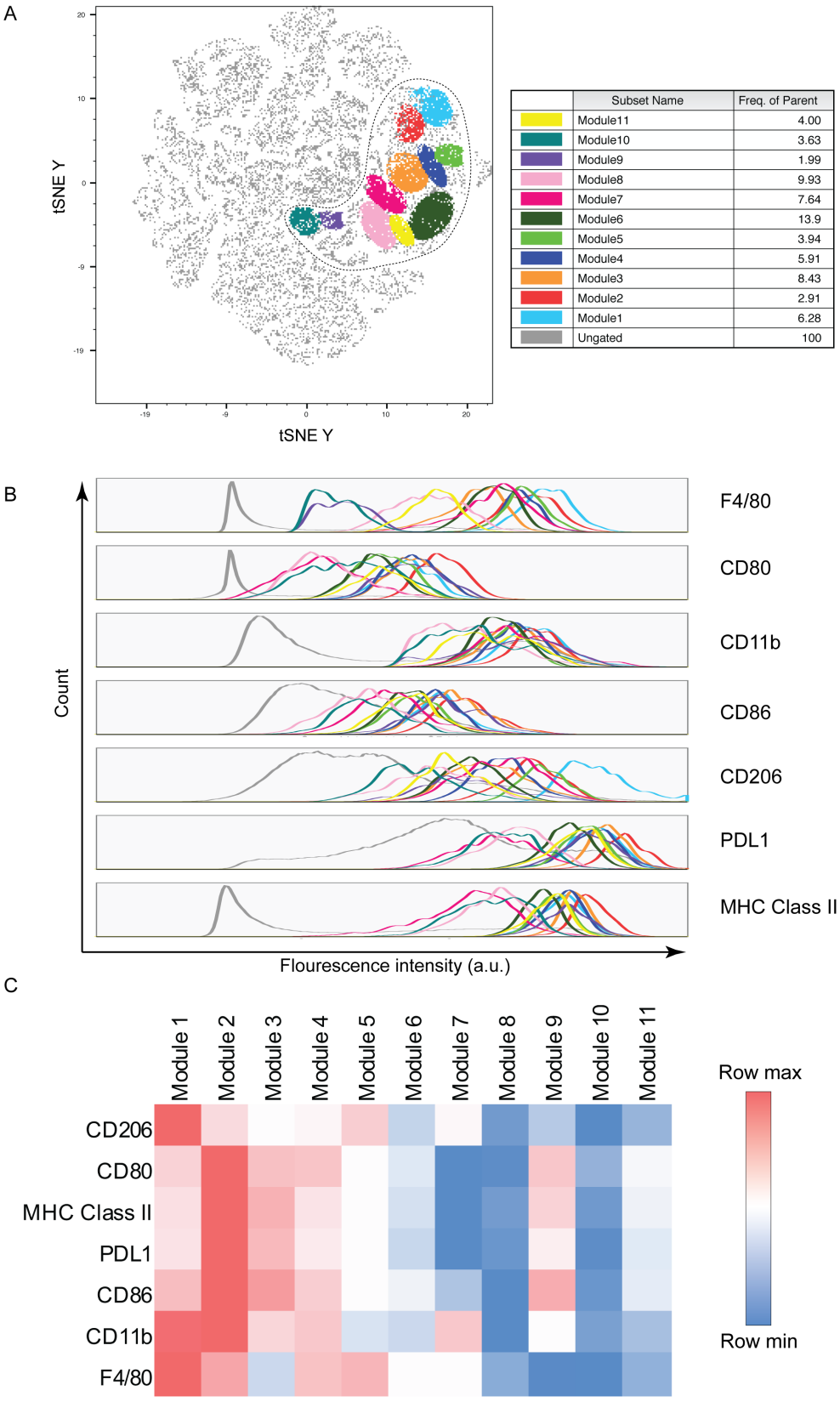

Figure 6.33 tSNE analysis of TAM subpopulations in 60577 tumours. A Definition of 11 modules based on tSNE clustering of data within TAM population, individual modules overlay the tSNE plot and have been assigned a unique colour. **B** Histograms for each module (colours as per A) showing fluorescence intensities for each marker are shown. **C** heatmap summarising MFI values for all markers assessed across all eleven modules.

I then assessed the eleven modules in the macrophage compartment of healthy omentum and in carboplatin and control tumours at four time points following carboplatin treatment in 60577 tumours (Figure 6.34). Within healthy omentum the predominant subpopulations of cells were represented by modules 8 and 10. These tissue-resident macrophages of the omentum were MHC Class II-low and differed in expression of F4/80 with subtle differences in CD206 expression. Control tumours had striking changes in the TAM infiltrate compared to healthy omentum. Marked expansion of several other populations was seen, characterised by high MHC Class II and F4/80 expression. Thus, the repertoire of TAM subpopulations was more diverse in tumours compared to healthy tissue. Serial assessment of TAM subpopulations in control tumours, showed a gradual expansion of module 6, expressing intermediate levels of all markers in the panel. In advanced tumours, module 6 was the predominate population of TAM in 60577 omental tumours.

With carboplatin treatment there was depletion of modules 4, 5 and 6. Following treatment, the most abundant population was module 8, which was also highly expressed in the healthy omentum. Therefore, carboplatin selectively depletes TAM populations that are recruited or expand in the tumour, whilst preserving some of the populations that are within healthy omentum. Interestingly and in keeping with my data so far, depleted TAMs expressed intermediate levels of CD206 and MHC Class II – this may explain the concomitant reduction of both of these markers observed when the TAM population is assessed globally. Following carboplatin treatment, the remaining TAM subpopulations more closely resemble the healthy omentum than untreated tumours.

In summary, these data show a complex group of TAM subpopulations within murine HGSOC in the 60577 model. Comparing these subpopulations between non-diseased and diseased omenta show recruitment or expansion of TAM populations distinct from the tissue-resident macrophages of the heathy omentum. Carboplatin treatment restructured the TAM compartment.

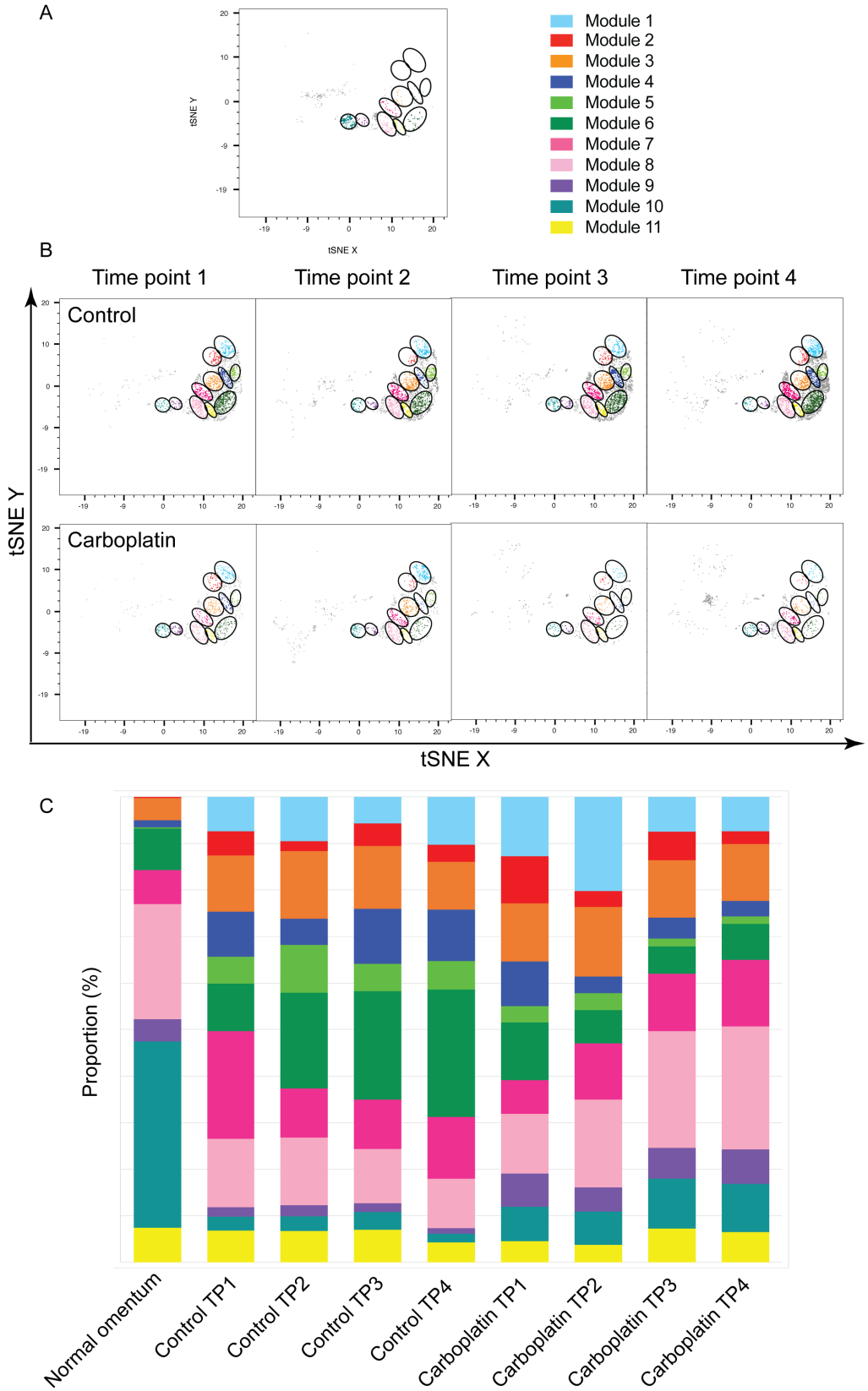

Figure 6.34 Assessment of TAM subpopulations with carboplatin treatment in 60577 tumours. tSNE plot with TAM modules overlaid for **A** normal omentum and **B** control and carboplatin treated tumours though the four time points assessed. **C** Bar plot showing the proportion of each module of the TAM population for normal omentum, vehicle-treated and carboplatin treated tumours at each of the four time points assessed. *TP1*: Time point 1 – two days after treatment started, *TP2*: Time point 2 – seven days after treatment started, *TP3*: Time point 3 – nine days after treatment started, *TP4*: Time point 4 – fourteen days after treatment started.

6.5 Increased TAM death post-chemotherapy

6.5.1 Assessment of TAM viability

The data presented above suggest carboplatin results in loss of TAMs from the TME of murine HGSOC. Two main processes may be responsible for this effect i) TAM recruitment may be reduced, ii) carboplatin treatment may result in increased TAM death. To investigate the possibility that TAMs are being killed by carboplatin treatment, I assessed non-viable TAMs as a percentage of the total TAM population. This demonstrated significantly more non-viable TAMs in carboplatin treated compared to control tumours (Figure 6.35) at all time points. This finding replicated an identical analysis within the human setting after NACT (Chapter 5; Figure 5.7).

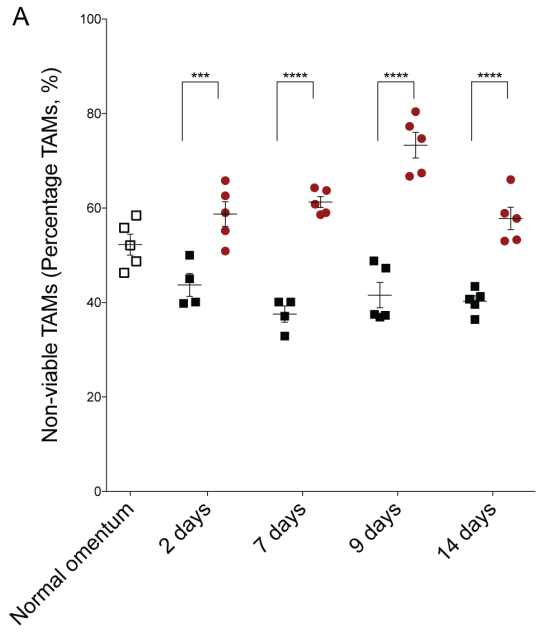

Figure 6.35 Assessment of non-viable TAMs at time points after carboplatin treatment in the 60577 model. Flow cytometry data relating to the immunostained stromal vascular fractions derived from omental tumours treated with carboplatin (red circles), vehicle alone (black squares) or healthy omental controls (unfilled squares). Non-viable TAM frequency is expressed as a percentage of the total TAM population. Data relate to a single experiment, five carboplatin treated mice, four-five vehicle-treated mice per time point and ten healthy omental controls; cells from healthy omental controls were combined and stained as five separate samples, the mean for each group is shown. Error bars represent SEM. Significant two-way ANOVA p-values are shown; ***<0.001, ****<0.0001.

This suggests that carboplatin treatment increases TAM death within the omental TME; this could be a mechanism for the depletion of TAM following carboplatin treatment.

6.6 Effect of chemotherapy on lymphocyte populations

Given the importance of myeloid-T cell interactions in mediating responses to chemotherapy in other cancer types[222] I wished to characterise the effects of

chemotherapy on lymphocyte populations in the omental tumour microenvironment. Figure 6.36 shows the flow cytometry gating strategy.

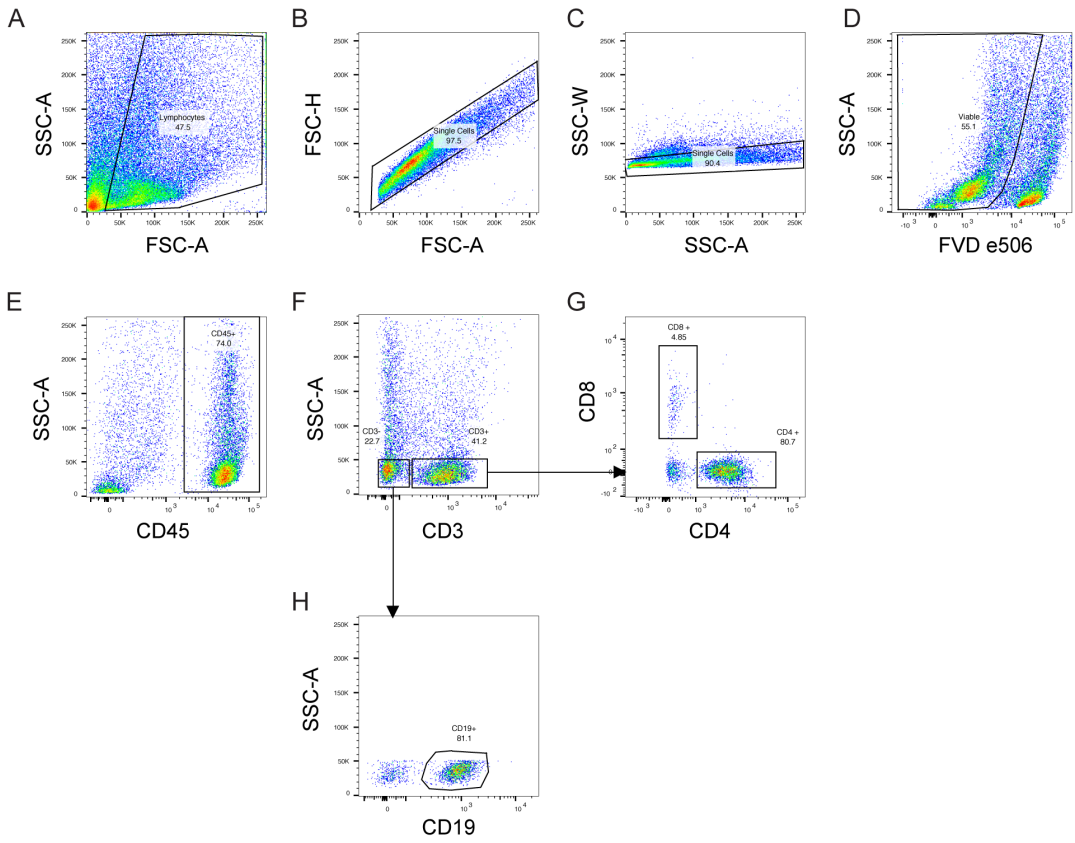

Figure 6.36 Multicolour flow cytometry gating strategy to characterise lymphocyte populations in mouse models. Density plots showing the immunostained stromal vascular fraction from a mouse omental tumour. **A** Gating to exclude cellular debris, **B**, **C** sequential gating to exclude doublet cells, **D** sequential gating to exclude non-viable cells, **E** sequential gating for $CD45^+$ cells, **F** sequential gating for $CD3^-$ and $CD3^+$ cells. **G** $CD3^+$ cells gated for $CD4^+$ and $CD8^+$ cells, further assessment of activation markers was made within these gates. **H** $CD3^-$ cells gated for $CD19^+$ cells. *SSC-A*: side scatter area, *SSC-W*: side scatter width, *FSC-A*: forward scatter area, *FSC-H*: forward scatter height.

6.6.1 60577 model

There was a significant increase in the $CD3^+$, $CD3^+CD4^+$ populations expressed as a percentage of $CD45^+$ cells (Figure 6.37A, C). However, there were no significant differences when these data were expressed as cells/mg of tissue (Figure 6.37B, D). This discrepancy is likely explained by the selective depletion of the TAM population, resulting in changes to the relative density of lymphocytes compared within the $CD45^+$ population but not affecting the $CD3^+$ and $CD3^+CD4^+$ cell number in the tissue overall. $CD3^+CD8^+$ cells decreased in the tissue overall as well as within the $CD45^+$ population (Figure 6.37E, F). There were also decreases in the $CD3^-CD19^+$ B cell population expressed as a percentage of $CD45^+$ cells (Figure 6.38A).

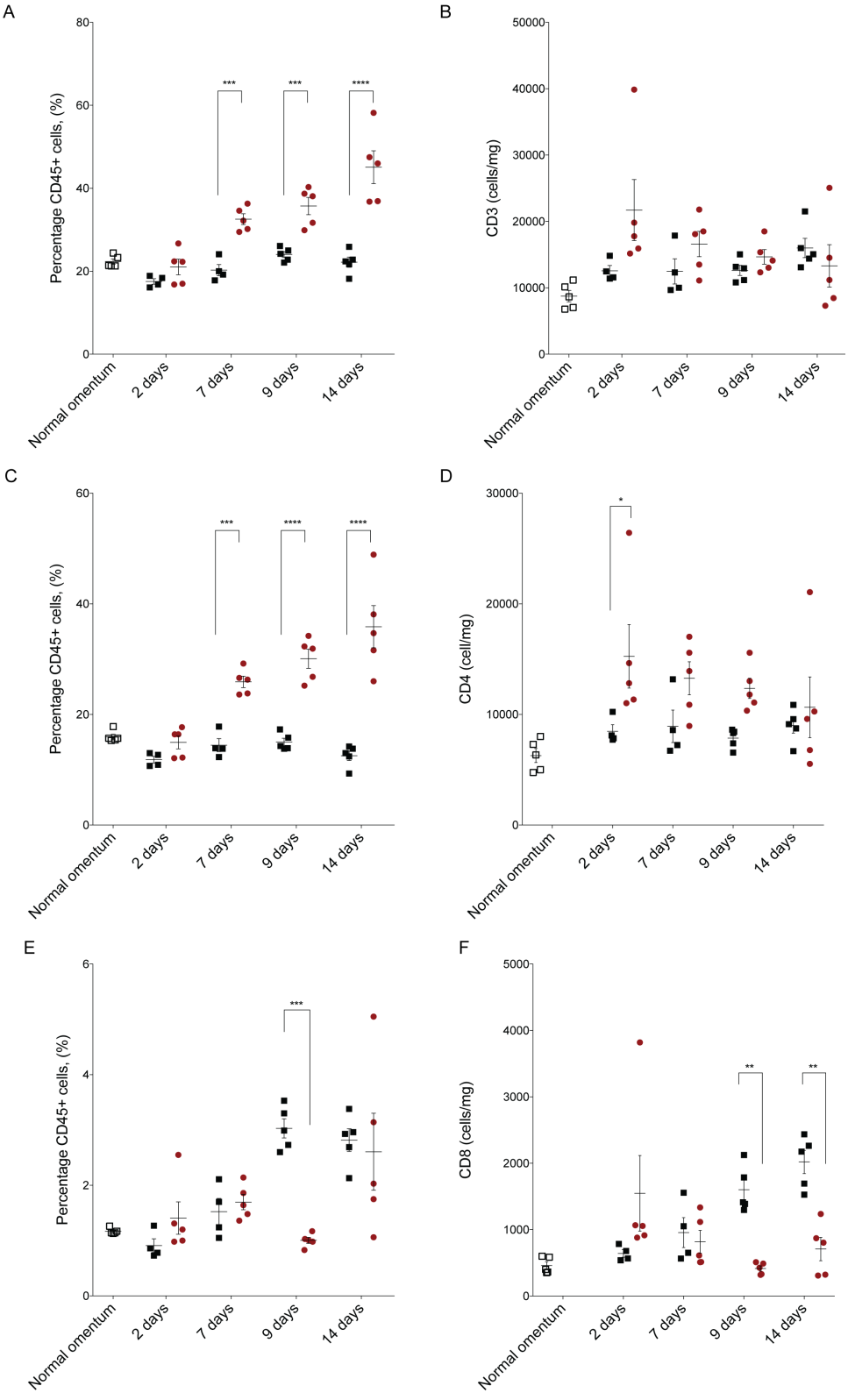

Figure 6.37 The effect of carboplatin treatment on T lymphocyte densities in 60577 tumours. Flow cytometry data relating to the immunostained stromal vascular fractions derived from omental tumours treated with carboplatin (red circles), vehicle alone (black squares) or healthy omental controls (unfilled squares). **A**, **C**, **E** $CD3^+$, $CD3^+CD4^+$, $CD3^+CD8^+$ frequency is expressed as a percentage of the $CD45^+$ population and **B**, **D**, **F** as cells/mg of tissue. Data relates to a single experiment, five carboplatin treated mice, four-five vehicle-treated mice per time point and ten healthy omental controls; cells from healthy omental controls were combined and stained as five seperate samples, the mean for each group is shown. Error bars represent SEM. Significant two-way ANOVA p-values are shown; *<0.05, ***<0.001, ****<0.0001.

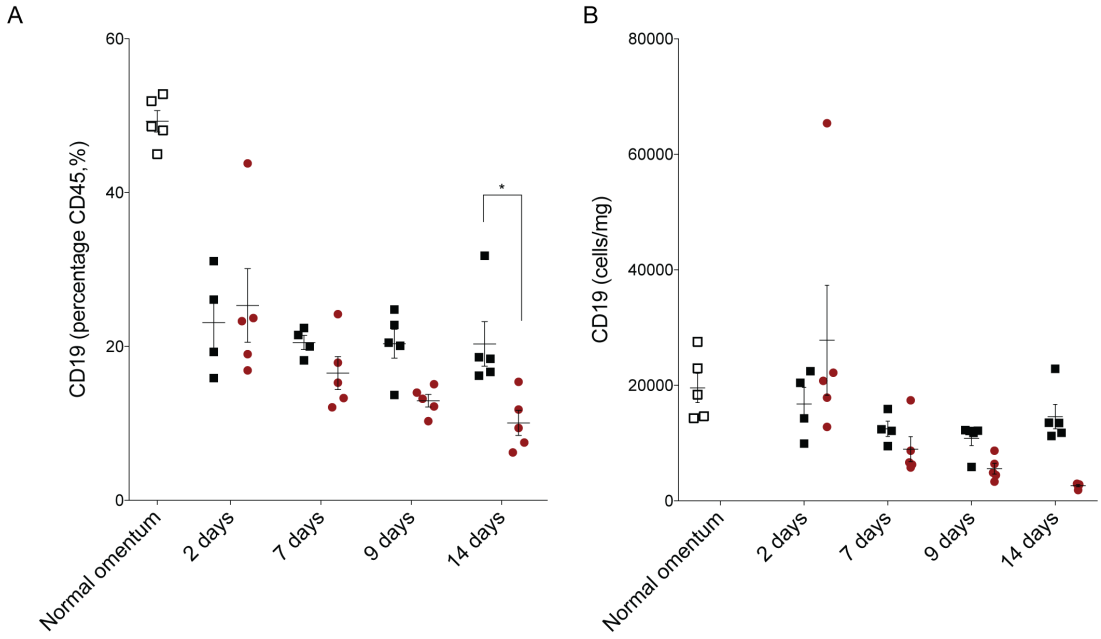

Figure 6.38 The effect of carboplatin treatment on B lymphocyte density in 60577 tumours. Flow cytometry data relating to the immunostained stromal vascular fractions derived from omental tumours treated with carboplatin (red circles), vehicle alone (black squares) or healthy omental controls (unfilled squares). **A** $CD3^{-}CD19^{+}$ frequency is expressed as a percentage of the $CD45^{+}$ population and **B** as cells/mg of tissue. Data relate to a single experiment, five carboplatin treated mice, four-five vehicle-treated mice per time point and ten healthy omental controls; cells from healthy omental controls were combined and stained as five separate samples, the mean for each group is shown. Error bars represent SEM. Significant two-way ANOVA p-values are shown; *p <0.05.

6.6.2 30200 model

In support of my observations in the 60577 model $CD3^{+}$ and $CD3^{+}CD4^{+}$ cells expressed as a percentage of the $CD45^{+}$ cells increased in carboplatin and combination treated tumours compared to vehicle and paclitaxel treated tumours. There were significant differences in $CD3^{+}$ and $CD3^{+}CD4^{+}$ cell number expressed as a percentage of $CD45^{+}$ cell infiltrate between carboplatin and paclitaxel treated tumours (Figure 6.39A, C). However, as before, this difference was not seen when I expressed the data as cells/mg of tissue (Figure 6.39B, D). In contrast there was a significant decrease in the $CD3^{+}CD8^{+}$ population compared to vehicle and paclitaxel treated tumours expressed as cell/mg of tissue (Figure 6.39F). There were no significant differences in frequency of $CD3^{-}CD19^{+}$ B cells between the treatment groups (Figure 6.40).

Overall these data would suggest relative changes in the cell number of $CD3^{+}$ and $CD3^{+}CD4^{+}$ as a percentage of the $CD45^{+}$ with a decrease in the $CD3^{+}CD8^{+}$ populations.

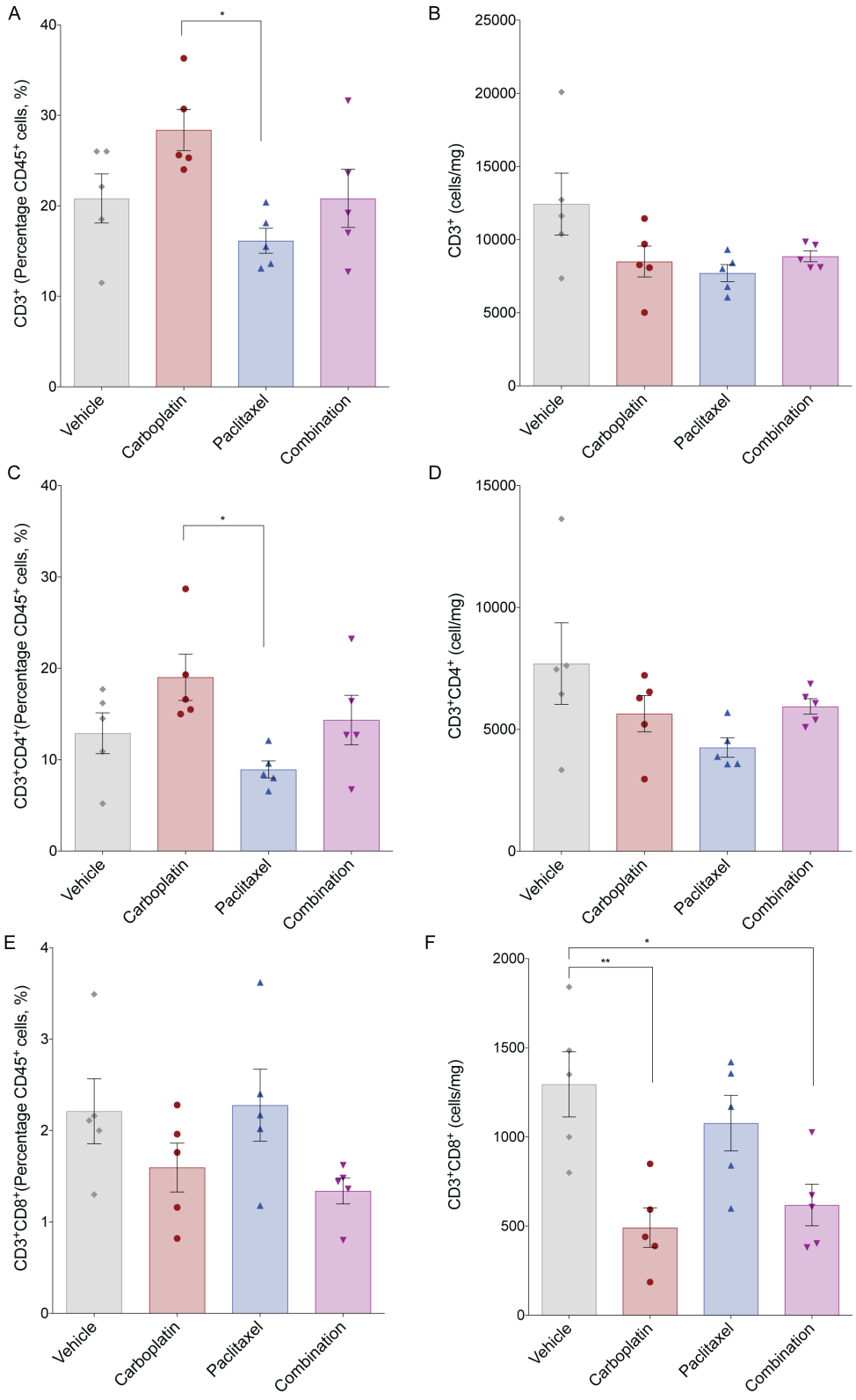

Figure 6.39 Effect of chemotherapy on T lymphocyte densities in the 30200 model. Flow cytometry data relating to the immunostained stromal vascular fractions derived from omental tumours treated with three once-weekly doses of carboplatin, paclitaxel, carboplatin + paclitaxel or vehicle alone. **A**, **C**, **D** $CD3^+$, $CD3^+CD4^+$, $CD3^+CD8^+$ cell frequency is expressed as a percentage of the $CD45^+$ population **B**, **D**, **F** $CD3^+$, $CD3^+CD4^+$, $CD3^+CD8^+$ expressed as cells/mg of tissue. Data relates to a single experiment, five mice per group, the mean for each group is shown. Error bars represent SEM. Significant one-way ANOVA p-values are shown; *<0.05, **<0.01.

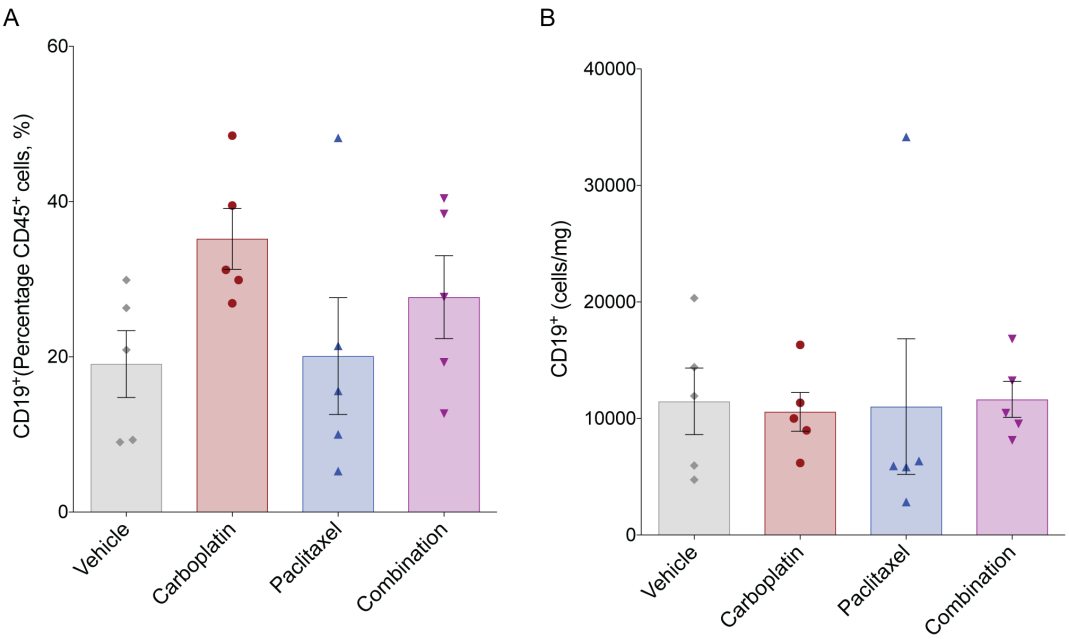

Figure 6.40 Effect of chemotherapy on B lymphocyte density in the 30200 model. Flow cytometry data relating to the immunostained stromal vascular fractions derived from omental tumours treated with three once-weekly doses of carboplatin, paclitaxel, carboplatin + paclitaxel or vehicle alone. $CD19^+$ cell frequency expressed as **A** the percentage of $CD45^+$ cells and **B** as cells/mg of tissue. Data relates to a single experiment, five mice per group, the mean for each group is shown. Error bars represent SEM.

6.6.3 HGS2 model

There were no significant differences in the densities of $CD3^+$, $CD3^+CD4^+$, $CD3^+CD8^+$ (Figure 6.41) or $CD3^-CD19^+$ lymphocytes (Figure 6.42) between carboplatin treated and vehicle-treated tumours.

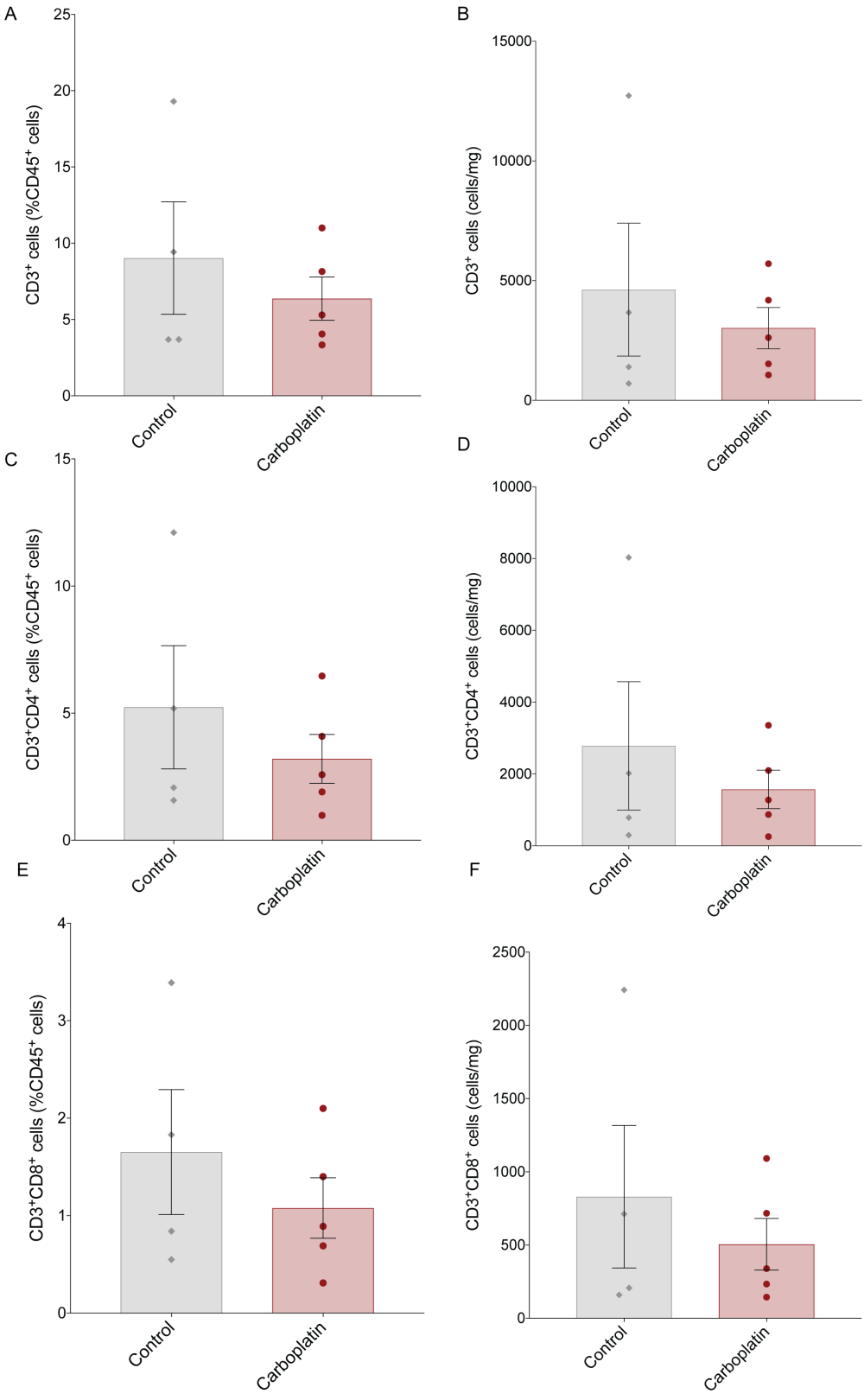

Figure 6.41 Effect of carboplatin on T lymphocyte density in the HGS2 model. Flow cytometry data relating to the immunostained stromal vascular fractions derived from omental tumours treated with carboplatin (red circles) or vehicle alone (grey diamonds). **A** $CD3^+$, **C** $CD3^+CD4^+$, **E** $CD3^+CD8^+$ frequency is expressed as a percentage of the $CD45^+$ population and **B**, **D**, **F** as cells/mg of tissue. Data relates to a single experiment. The mean for each group is shown. Error bars represent SEM.

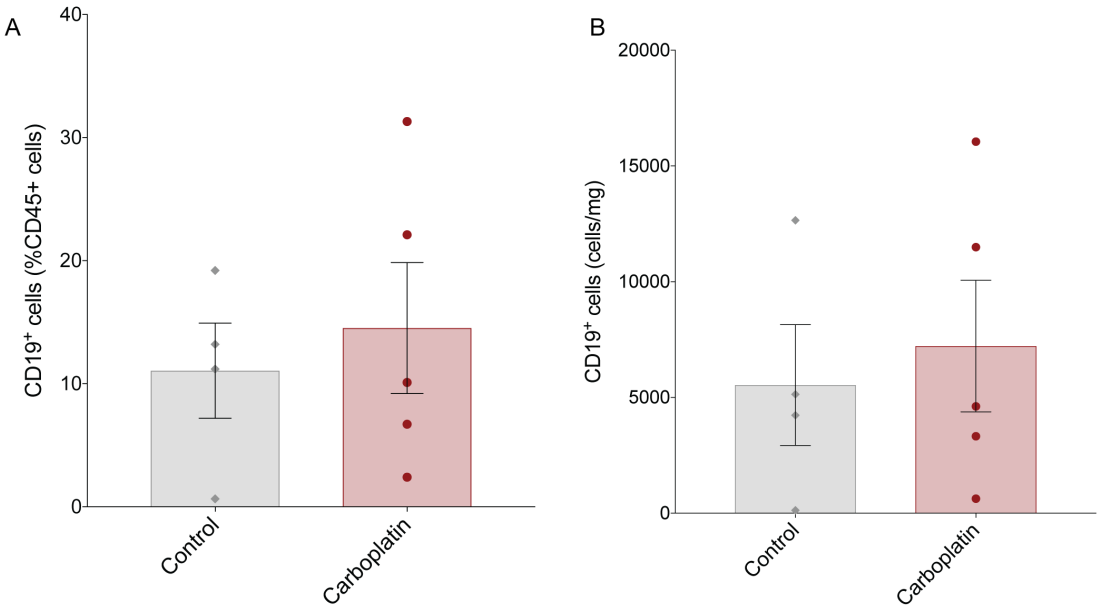

Figure 6.42 Effect of carboplatin on B lymphocyte cell number in the HGS2 model. Flow cytometry data relating to the immunostained stromal vascular fractions derived from omental tumours treated with carboplatin (red circles) or vehicle alone (grey diamonds). **A** $CD3^{-}CD19^{+}$ frequency is expressed as a percentage of the $CD45^{+}$ population and **B** as cells/mg of tissue. Data relates to a single experiment. The mean for each group is shown. Error bars represent SEM.

6.7 Summary and comparision to human data (Chapters 3-5)

The following bullet points summarise the key changes in immune cell infiltrate and phenotype with chemotherapy treatment in human and murine HGSOC.

- In both human and murine HGSOC there was a decrease in TAM cell number.
- In both murine and human HGSOC there was an increase in non-viable TAM following carboplatin treatment.
- Macrophage surface expression of alternatively activated markers decreased following NACT in patients and following carboplatin in the 60577 model.
- In the 30200 tumours there was a trend to a reduction in TAM expression of alternatively activated markers; in HGS2 tumours there was no difference in alternatively activated marker expression after carboplatin treatment.
- The murine TAM response to paclitaxel was different to carboplatin, with increases in CD206 expression in 60577 and a trend to increase in 30200 and HGS2.

Table 6.1 summarises the changes in immune cell density and phenotype observed in human and murine HGSOC omental metastases before and after chemotherapy that I have obtained in this thesis and from the published work of others in our lab.

	Human	60577	30200	HGS2
Chemotherapy	**NACT**	**Carboplatin**	**Carboplatin**	**Carboplatin**
TAM frequency (IHC)	decreased in malignant cell areas	decreased	decreased	
Viable TAM frequency (FC)	unchanged	decreased	decreased	unchanged - trend to decrease
Non-viable TAM frequency (FC)	increased	increased		
DC populations	cDCs increased			
CD163	decreased			
CD206	unchanged - trend to decrease	decreased	unchanged - trend to decrease	unchanged - trend to increase
PDL1		decreased	unchanged	unchanged - trend to increase
CD209	unchanged - trend to decrease			
CD86		decreased	unchanged - trend to decrease	
MHC Class II	unchanged	decreased	unchanged - trend to decrease	unchanged
CX3CR1	decreased			
CD3+	unchanged - Böhm *et al.*	increased	unchanged - trend to increase	unchanged
CD3+CD4+	unchanged - Böhm *et al.*	increased	unchanged - trend to increase	unchanged
CD3+CD8+	unchanged - Böhm *et al.*	decreased	decreased	unchanged
CD3-CD19+	unchanged - trend to increase Montfort *et al.*	decreased	unchanged - trend to increase	unchanged

Table 6.1 Table summarising mouse model and human experimental data. Difference between chemotherapy treated and untreated / vehicle-treated control HGSOC tumours; increases denoted by red shading, decreases denoted by blue shading, no data indicated by grey shading. Significant differences noted with dark shading, statistically non-significant trends noted with light shading. Human lymphocyte data from Böhm *et al.*[113] and Montfort *et al.*[114].

6.8 Discussion

In this chapter I used three murine models that recapitulate the genetic and mutational profile of human HGOSC and tissue location (Maniati *et al.* submitted). The sensitivity of the murine cell lines to carboplatin and paclitaxel *in vitro* was within the ranges for human HGSOC cell lines reported in the literature, however these vary widely[309]. One large study assessed the sensitivity of a panel of thirty-six human ovarian cancer cell lines to single-agent chemotherapy, with IC_{50} values in the range 9-270μM for carboplatin and 2-110nM for paclitaxel[309]. Furthermore, 60577 sensitivity to cisplatin has been tested with a reported IC_{50} value of 167μM[272]. When designing experiments to treat mice with chemotherapy I chose the dose of 20mg/kg for carboplatin and 10mg/kg for paclitaxel based on a literature review[315]. Carboplatin dosing in humans is based on the Cavert *et al.* formula[316] and typical human doses of carboplatin are in the range 200-350mg/m^2 (based on the area under curve [AUC] 5 target). The standard human dose of paclitaxel is 175mg/m^2. Using the surface area calculations as described by Freireich *et al.*, a dose of 20mg/kg approximates 60mg/m^2 and 10mg/kg approximates 30mg/m^2 in mice[317]. Despite the carboplatin dose used to treat mice being lower than an equivalent human dose, tumours showed obvious responses. In initial experiments, paclitaxel was administered to mice at higher concentrations, however this was associated with toxicity (severe weight loss), necessitating dose reduction to 10mg/kg.

Reflecting human HGSOC, the three BRCA deficient models tested in this thesis were sensitive to treatment with carboplatin or the combination of carboplatin with paclitaxel. Paclitaxel administered at a dose of 10mg/kg i.p., did not significantly increase survival compared to vehicle-treated controls. Histological assessment of paclitaxel treated tumours showed no discernible morphological changes compared to vehicle-treated tumours (data not shown). This suggests that the 60577 and 30200 models are not sensitive to paclitaxel *in vivo*, or that the dose of paclitaxel used was too low to produce a cytotoxic effect.

The dose of carboplatin and paclitaxel chosen to treat mice is lower than the standard equivalent human dose. However, these drugs are administered intravenously to patients rather than i.p., as in the case of the mice. Intraperitoneal administration of chemotherapy in ovarian cancer (including the combination of cisplatin and paclitaxel) has been shown to improve survival[52,53,318] in patients compared to conventional intravenous administration. Indeed, intraperitoneal administration of carboplatin increases the local concentration by 20-fold, whereas for paclitaxel it can achieve a 1000-fold increase in concentration[68]. Therefore i.p. treatment is likely to be more effective at

lower doses than intravenous administration and provides some justification for using lower equivalent doses of chemotherapy in mice. In initial experiments (data not shown) I used a higher dose of paclitaxel (19 mg/kg), however, at this dose I observed significant weight loss in mice necessitating a dose reduction to 10mg/kg in further experiments. Toxicity may have been due to the ethanol / cremophor vehicle in which paclitaxel is formulated. This vehicle, necessary to solubilise this highly hydrophobic molecule, is a cause of toxicity when paclitaxel is administered to patients[64].

Carboplatin was highly effective when administered to tumour bearing mice at 20mg/kg i.p. and resulted in clinical resolution of ascites and significantly enhanced survival compared to vehicle-treated mice. These finding are reflected in the clinical data which shows the greater benefit from platinum-based chemotherapy compared to paclitaxel alone. A Phase 3 clinical trial showed significantly improved response rates and progression free survival to the combination of cisplatin (a first generation platinum drug) and paclitaxel or cisplatin alone compared to single-agent paclitaxel[319]. Furthermore, the combination of carboplatin and paclitaxel is non-inferior to treatment with cisplatin and paclitaxel[320].

Tumours from all three models had abundant TAM populations. A key difference consistently noted between mouse and human tumours was the degree of TAM infiltration; murine TAM populations represented 25-35% compared to 10-25% of $CD45^+$ cells in human untreated HGSOC. Murine TAM expressed high levels of CD206 and PDL1, however there was also expression of CD86 and MHC Class II at high levels. These findings were in keeping with the expression of activation makers in human omental HGSOC TAM which also expressed CD163, CD206, and CD209 at high levels, yet were also MHC Class II high. It was encouraging that the TAM phenotype was comparable between mouse and human HGSOC.

The reported effects of chemotherapy on the TME of other preclinical models are variable; with some studies showing TAM recruitment[215–223] and others showing no change or depletion. Overall, in this series of experiments I show that carboplatin can deplete TAM; in contrast, paclitaxel did not affect TAM cell number. I found no evidence for TAM recruitment in any model in response to carboplatin or paclitaxel treatment.

Next, I determined if carboplatin-associated TAM depletion was the result of loss of TAMs defined by a particular surface marker. In the 60577 and 30200 models I found significant reductions of TAM expressing both alternative/immunosuppressive (CD206, PDL1) and classical activation (MHC Class II, CD86) markers. This and my findings in

human tumours, suggestive of increased TAM cell death post-chemotherapy (Figure 4.7), led me to examine if increased cell death could explain TAM depletion in murine tumours. Therefore, I quantified the percentage of non-viable TAM within the total TAM population. At all time points, there were significantly more non-viable TAM in carboplatin treated tumours compared to vehicle-treated controls (Figure 6.35). Therefore, I conclude that carboplatin may increase TAM cell death in both human and murine HGSOC.

The concept of myeloid cell death in response to chemotherapy has not been reported in the context of carboplatin, yet has been reported following treatment with trabectedin. Trabectedin, also a DNA binding molecule, has been found to trigger the activation of caspase-8-mediated apoptosis selectively in monocytes[212]. In preclinical models, depletion of macrophages from the TME of tumours was found to be a key anti-tumour mechanism of this drug. This aspect of the thesis will be explored further in Chapter 9, where I will move into the *in vitro* setting to test the effects of carboplatin on macrophages.

Within human samples I found a significant reduction in TAM density by CD68 immunohistochemistry within malignant cell areas in a cohort of matched pre and post-chemotherapy HGSOC samples (Figure 3.2). However, within the stroma and within the biopsy overall there were no significant differences in TAM density. Human samples were assessed at a time point three-four weeks following a dose of chemotherapy. In the mouse models I have assessed earlier time points. A further factor that may account for the differences in the TAM response in human and murine tumours, is that murine tumours exhibited a less developed stroma compared to human samples. Therefore, it may be that the models recapitulate the malignant cell islands of human HGSOC most accurately. Further assessment of immune cell compartment of murine tumours pre and post-chemotherapy is needed and this is an objective of future work planned to extend this thesis (Chapter 10).

Assessing the phenotype of TAM remaining in the TME, I found reductions in both MHC Class II and CD206 TAMs following carboplatin treatment in 60577 and 30200 tumours. Within the HGS2 model the changes in TAM phenotype where not significantly different between treated and untreated tumours. This suggests a change in TAM phenotype as the result of carboplatin treatment distinct from overall changes within the M1 (classically activated)/M2 (alternatively activated) model. Importantly there are similarities, comparing the changes in TAM phenotype in the murine models to the changes observed in human HGSOC samples. In patients I found a reduction of surface

expression of the $CD163^+$ post-chemotherapy yet no changes in the MHC class II expression (Table 6.1). Therefore, the similarities observed between human and murine TAM responses are most likely as the result of the effects of carboplatin rather than paclitaxel.

In the 60577 and 30200 models $CD3^+$ and $CD3^+CD4^+$ cells increased as a percentage of the $CD45^+$ population. These changes were not however reflected when the data were expressed as cells/mg of tissue. The reason for this discrepancy may be due to the changes in the F4/80 population, as described previously. $CD8^+$ cells decreased both as a percentage of the $CD45^+$ population and as cells/mg of tissue. Within the HGS2 model no changes were seen in the lymphocyte compartment. Although I have not studied the lymphocyte populations within the human HGSOC samples, previous work carried out in our lab has assessed the effects of NACT on T and B lymphocytes. NACT did not significantly affect the density of T cells, yet in good responders (CRS3), there was an enhanced Th1 response signature[113]. Furthermore, NACT promoted anti-tumour B cell reponses[114]. These findings have been further supported by work in the laboratory of Brad Nelson who also assessed TILs in the omentum of matched HGSOC samples. This detailed IHC-based assessment showed significant increases in $CD3^+$, $CD8^+$ and $CD20^+$ cells and near-significant trends to increased $CD4^+$ lymphocytes following NACT[118]. Comparing the responses observed within the murine models with these data and those provided by others[115] suggest that these models may also replicate aspects of the human lymphocyte response to chemotherapy. Study of the lymphocyte populations in murine HGSOC in response to chemotherapy by IHC is planned in future work building on the data presented in this thesis.

TAM exist as a spectrum of activation states defined by changes in not one but hundreds of genes[120]. Therefore, assessing the expression of a single surface proteins will not detect phenotypic complexity. To explore my data in more detail I applied the tSNE algorithm to allow assessment of all the markers in the flow cytometry panel at single-cell resolution. tSNE was applied to murine FC data. The design of the antibody panel prevented the use of tSNE to assess TAM subpopulations in human samples. tSNE was not part of mainstream FC analysis when the project was started and as such the design of the panel did not take the use of this approach into consideration.

tSNE confirmed TAM depletion and validated the manual gating strategy applied to the murine FC data. Within the TAM population tSNE defined subpopulations (modules 1-11) in healthy omentum, control and carboplatin treated tumours. Through a time-course experiment it was possible to observe re-structuring of TAM subpopulations through

disease progression and in response to treatment. Using this approach, clear differences in TAM subpopulations were found between healthy, untreated and carboplatin treated tumours. Within healthy omentum tissue-resident macrophages were F4/80-low, CD11b-low, MHC Class II low (modules 8 and 10). This observation is supported by elegant studies in murine pancreatic cancer, where tissue-resident macrophages were defined by low expression of MHC Class II[139]. Within tumours, TAM phenotypes were more complex then tissue-resident macrophages, with the addition of populations not appreciated in the healthy omentum. Expansion of subpopulations co-expressing high levels of F4/80 and MHC Class II (modules 1-3) were seen, suggesting these cells are recruited or expand within the tissue. Additionally, through two weeks of tumour progression there was expansion of F4/80-intermediate, MHC-intermediate, CD206-intermediate TAMs (modules 4-6). These are the dominate TAM populations in advanced tumours. Interestingly, with carboplatin treatment these subpopulations are selectively depleted. This provides an explanation for the reduction in both MHC Class II and CD206 markers found within the whole TAM population as assessed by conventional FC analysis (Figure 6.25, Figure 6.26).

Compared to untreated tumours, carboplatin treated tumours were enriched for MHC-low F4/80-low (module 8 and 10) TAM, regarded as the tissue resident population of healthy omentum. However, in contrast to healthy omentum there is also expansion of F4/80-high, MHC Class II-high cells (modules 1-3). These populations are opposed in terms of phenotype markers. It is tempting to consider that these cells may be functionally distinct. In Chapter 8 I will target TAM following chemotherapy in this model, this may help to gain an understanding of the roles of these cells in the post-chemotherapy TME.

Building on the data presented in this chapter, in Chapter 7 I generate a murine model of HGSOC relapse and characterise the phenotype of the TAM population in these tumours.

Chapter 7
TAMs at relapse in murine HGSOC

7.1 Background

Despite three-quarters of HGSOC patients responding to first line chemotherapy, the five-year survival rate is 40%, a figure that has not changed for thirty years[29]. In patients who present with stage III or IV disease, the five-year survival drops to 20% and 4% respectively[4]. A majority of patients relapse within eighteen months of primary treatment with increasingly chemo-resistant disease. Strategies to prevent tumour regrowth after chemotherapy are crucial to improving outcome[4].

In chapter 6 I described the effects of carboplatin and paclitaxel treatment on tumour growth and mouse survival in the pre-clinical models of HGSOC. Here I describe a continuation of these experiments which have resulted in the generation of a murine model that replicates the relapse of HGSOC. This relapse model, or others like it, offer the potential to learn more about the TME of relapsed HGSOC and provides a clinically relevant platform to test therapeutic interventions.

In all the murine survival experiments presented in this thesis a human endpoint was used to determine when tumour-bearing mice were culled. Survival endpoint was based on 'moderate' severity as per the Home Office Project License. The survival endpoint for mice was defined as a change in general health, specifically 15% body weight loss over 72 hours or 20% over any time period, or inability to ambulate, or hunched posture, or difficulty breathing or signs of hypothermia as well as signs of ascites or palpable tumours exceeding an estimated size of 1cm diameter. In survival experiments assessment of mice was made twice daily by the same individual to limit inter-observer variability. Furthermore, in the majority of cases survival determinations were made by a trained animal technician who was not directly involved in the experimental design.

7.2 Generating a relapse model of HGSOC

The 60577 model appeared to most closely mimic human platinum sensitive disease, with clinical resolution of ascites and a significantly extended treatment free interval of at least six weeks (Figure 6.5A). Therefore, I followed a cohort of five carboplatin treated mice long-term to see if they relapsed. Mice continued to live with no signs of disease until four months following the last treatment when the first mouse of the cohort started to show abdominal distension secondary to ascites development. Subsequently, all mice demonstrated evidence of disease and were culled at a humane end point. Figure 7.1A shows mouse survival for this experiment, carboplatin treated mice had a median survival of 190 days *vs* 40 days for control mice (log-rank p=0.0005). This experiment was repeated as shown in Figure 7.1B, the median survival of carboplatin-treated mice

was 142 days *vs* 35 days for control mice (log-rank p=0.0023).

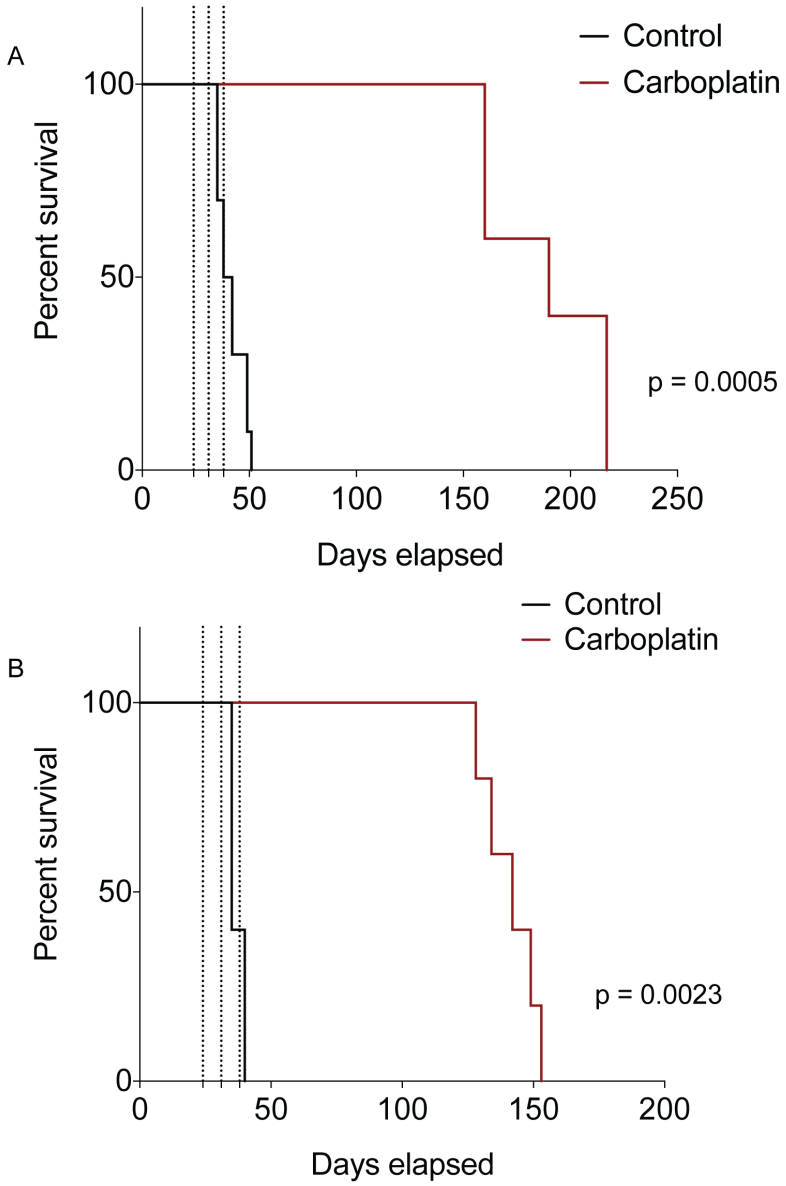

Figure 7.1 Effect of chemotherapy on survival in the 60577 model. Kaplan-Meier curves comparing mice treated with three once-weekly carboplatin i.p. injections (red line) or 0.9% NaCl (black line). Dashed lines indicate carboplatin treatments. Control and treated mice were in separate experiments. **A**, **B** show data derived from two independent experiments. Data relate to seven vehicle-treated control mice and ten carboplatin treated mice. Log-rank (Mantel-Cox) p-value is shown.

Mice typically showed clinical signs of disease relapse approximately fourteen days prior to reaching the humane end point. At autopsy, mice had clear evidence of significant tumour burden including macroscopically identifiable omental tumours and large volume ascites. This is in contrast to mice culled at six weeks following chemotherapy, which showed no macroscopic evidence of disease or ascites. Figure 7.2 shows the omental weights of mice reaching a humane end point due to relapse compared to vehicle-treated tumours, omental weight was significantly increased in relapsed disease (0.16g *vs* 0.04g p = 0.01).

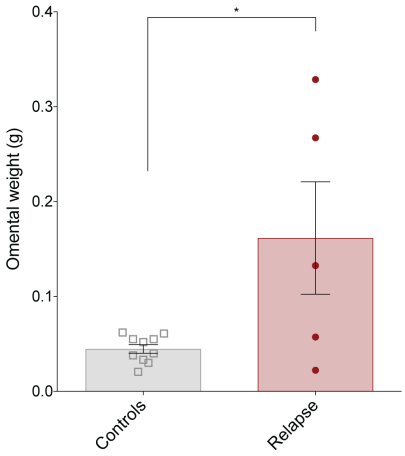

Figure 7.2 Omental weight of relapsed 60577 tumours. Omental weight of tumours from mice culled at end point following tumour relapse after carboplatin treatment. Data relate to ten vehicle-treated control mice and five carboplatin treated mice. Endpoint controls were in a separate experiment, the mean for each group is shown. Student's *t*-test p-value is shown; *<0.05.

7.3 Characterising TAM populations in relapsed tumours

I performed multicolour flow cytometry on the relapsed omental tumours. I compared the relapsed tumours to vehicle-treated tumours resected at a humane end point. TAM density as a percentage of the $CD45^+$ population was comparable between these groups (Figure 7.3). TAM phenotype at relapse closely resembled the surface marker expression profile of vehicle-treated tumours at end point (Figure 7.4A, B, C). There was, however, a statistically significant increase in $CD206^+$ TAM as a percentage of the TAM population at relapse compared to vehicle-treated tumours at end point (67.5% *vs* 28.7%, p = 0.0016), (Figure 7.4A).

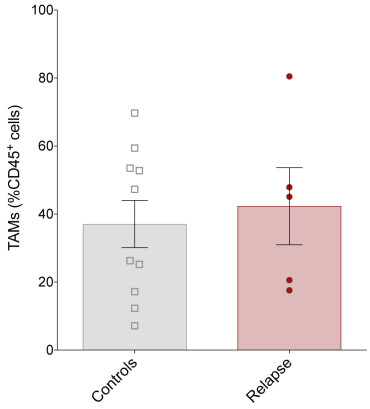

Figure 7.3 TAM cell number in relapsed 60577 tumours. Flow cytometry data relating to the immunostained stromal vascular fractions derived from relapsed omental tumours treated with carboplatin or vehicle. Data relate to five mice in the relapse group and 10 vehicle-treated mice sacrificed at a humane end point. Endpoint controls were in a separate experiment, the mean for each group is shown. Error bars represent SEM.

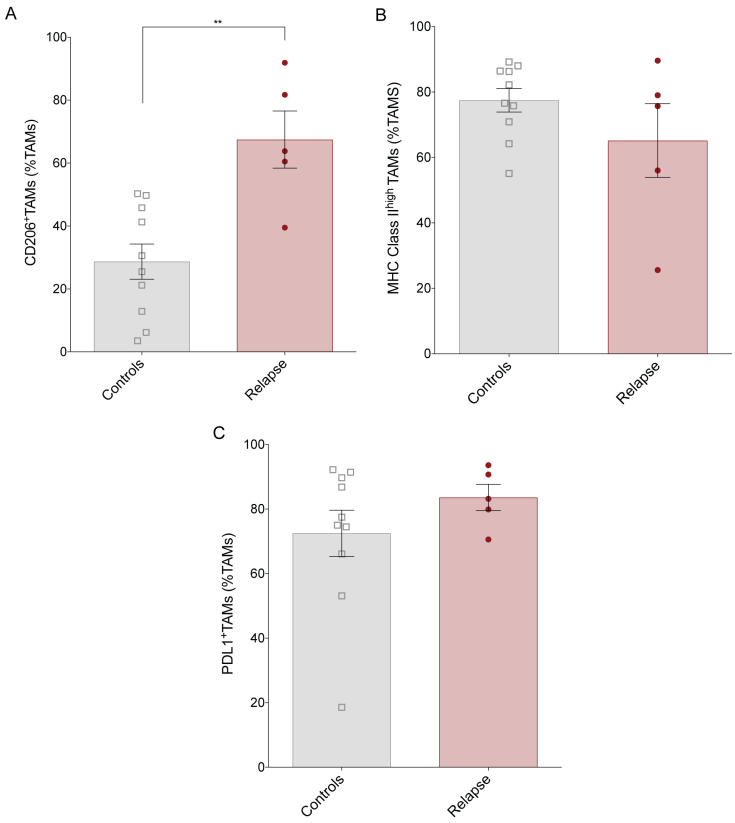

Figure 7.4 TAM surface marker expression in relapsed 60577 tumours. Flow cytometry data relating to the immunostained stromal vascular fractions derived from relapsed omental tumours treated with carboplatin or vehicle controls. **A** frequency of CD206^{+}TAMs expressed as a percentage of the TAM population. **B** frequency of MHC Class 2^{+}TAMs expressed as a percentage of the TAM population **C** frequency of PDL1^{+}TAMs expressed as a percentage of the TAM population. Data relate to five mice in the relapse group and ten mice in the vehicle-treated control group, sacrificed at a humane end point. Endpoint vehicle-treated control tumours were in a separate experiment, the mean for each group is shown. Error bars represent SEM. Significant one-way ANOVA with Turkey's correction p-values are shown; *<0.05, **<0.01.

Lymphocyte populations were also assessed (Figure 7.5). I observed no difference in lymphocyte cell number in relapsed tumours compared to vehicle-treated tumours at end point.

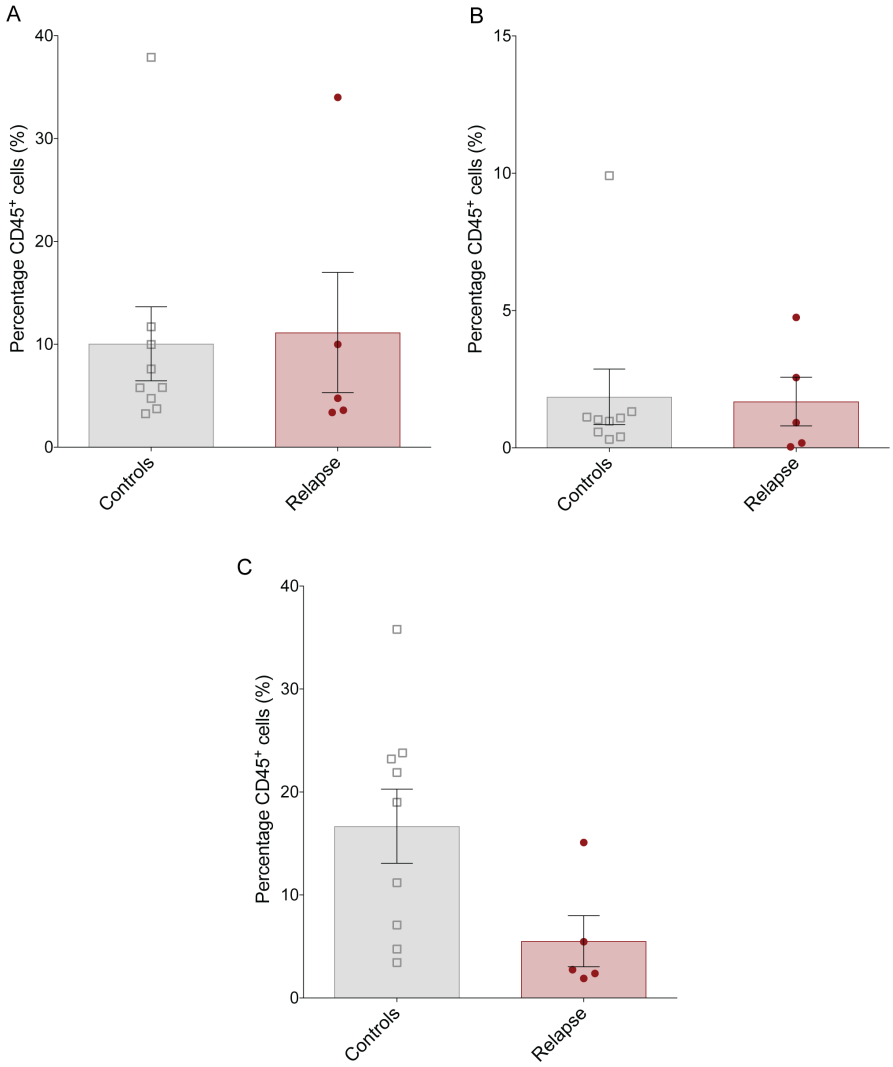

Figure 7.5 Lymphocyte cell number in relapsed 60577 tumours. Flow cytometry data relating to the immunostained stromal vascular fractions derived from relapsed omental tumours treated with carboplatin or vehicle controls. **A** frequency of $CD3^+CD4^+$ expressed as a percentage of the $CD45^+$ population. **B** frequency of $CD3^+CD8^+$ expressed as a percentage of the $CD45^+$ population. **C** frequency of $CD3^-$ $CD19^+$ expressed as a percentage of the $CD45^+$ population. Data relate to five mice in the relapse group and ten mice in the vehicle-treated control group, sacrificed at a humane end point. Endpoint controls were in a separate experiment, the mean for each group is shown. Error bars represent SEM.

Therefore relapsed tumours, following a long treatment-free interval, had a TME that was very similar, in terms of myeloid and lymphocyte cell number, to vehicle-treated tumours.

7.4 Discussion

To explore the possibility of HGSOC relapse following carboplatin treatment, a cohort of mice were followed up long-term. Four-six months following the last dose of chemotherapy all mice developed signs of tumour progression and developed ascites. Median survival following carboplatin treatment was determined in two separate experiments and ranged from 142 – 190 days *vs* 35 – 40 days for vehicle-treated mice.

I then characterised the immune infiltrate in the relapsed tumours. Interestingly, there were no differences in TAM or lymphocyte cell number in vehicle-treated tumours and tumours at relapse. Comparing this to the data relating to early time points following carboplatin treatment (Chapter 6) suggests re-accumulation of both TAM and lymphocyte populations as tumours re-grow in the omentum. TAM surface expression of CD206 was significantly increased in relapse tumours compared to vehicle-treated controls. All other surface markers assessed were not significantly different between the experimental groups. Therefore, I conclude that an immunosuppressive TAM phenotype is re-established at relapse. Kreuzinger *et al.* defined an immune transcriptomic signature in matched relapsed and primary human HGSOC tumours, finding that in some relapsed tumours this signature was concordant with the primary tumours, whereas others were discordant[92]. Thus, this mouse model of relapse may recapitulate the human setting of concordant TMEs within relapse and primary disease.

The results obtained so far lead to the hypothesis that preventing the re-accumulation of TAM after chemotherapy may delay or prevent HGSOC relapse. In the next chapter I will target TAM, using small molecule inhibitors of colony stimulating factor receptor 1 (CSF-1R), both as single agents and in combination with chemotherapy. I will ask the question: 'Can targeting TAM following chemotherapy prevent relapse of HGSOC?'.

Chapter 8
Targeting TAM by CSF-1R inhibition in HGSOC

8.1 Background

The CSF-1-CSF-1R axis is a survival and differentiation pathway for cells of the myeloid lineage and therefore represents a key strategy for targeting TAMs[138]. As described in Chapter 1, numerous CSF-1R-targeting approaches have been developed and have shown promise in a range of pre-clinical models[237]. Multiple clinical trials are currently in progress testing TAM-targeting agents in combination with conventional treatment modalities and immunotherapies[135,237].

In Chapters 6 and 7 I have shown that carboplatin can deplete TAMs in murine HGSOC and that TAM populations repopulate relapsed tumours. This led me to hypothesise that targeting TAM following chemotherapy could delay relapse. To test this hypothesis I have used orally bioavailable CSF-1R inhibitors (CSF-1Ri) administered to tumour-bearing mice with established tumours and also following chemotherapy. The murine model of HGSOC relapse (described Chapter 7) provides an appropriate system to test this approach.

8.2 CSF-1Ri treatment of murine models of HGSOC

In this thesis I have used two small molecule inhibitors of CSF-1R; AZD7507, provided by AstraZeneca and BLZ945 developed by Novartis, which was obtained commercially. AZD7507 and BLZ945 are both selective and potent inhibitors of CSF-1R kinase activity. The reported biochemical IC_{50} values are 3nM for AZD7507 and 1nM BLZ945; both have negligible activity against other kinases[215,251].

8.2.1 AZD7507 treatment of the 60577 model

To examine the effect CSF-1Ri in the 60577 model, AZD7507 was administered orally to mice for twelve days twice daily, commencing twenty-one days after 60577 cell injection. At this time point tumours have formed within the omentum, therefore this recapitulates the clinical situation of treating established tumours. CSF-1Ri and vehicle-treated controls were culled twelve hours following the last dose of AZD7507 and the tumour microenvironment was assessed by FC. Figure 8.1 show a schematic outline of the experimental approach.

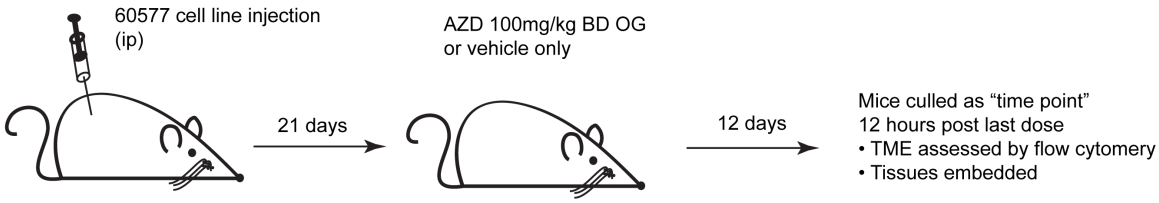

Figure 8.1 Schematic outline of an experiment assessing the effect of AZD7507 treatment on the 60577 model. Significant experimental time points and treatment scheduling is shown. AZD7507 dosing based on Candido *et al.*[251] *BD: twice a day, OG: oral gavage*.

An effective AZD5707 dose, resulting in TAM depletion and increased survival of KPC-tumour bearing mice, has been defined in our lab[251]. I therefore decided to use the same dosing schedule in my experiments. As expected, TAMs ($CD45^+Ly6C^-Ly6G^-CD11b^+F4/80^+$ cells) were significantly decreased by AZD7507 treatment in the omentum both when expressed as a percentage of the $CD45^+$ cell population and as cells/mg of tissue (Figure 8.2). However, the depletion observed was not complete, in keeping with the findings of others[140,251].

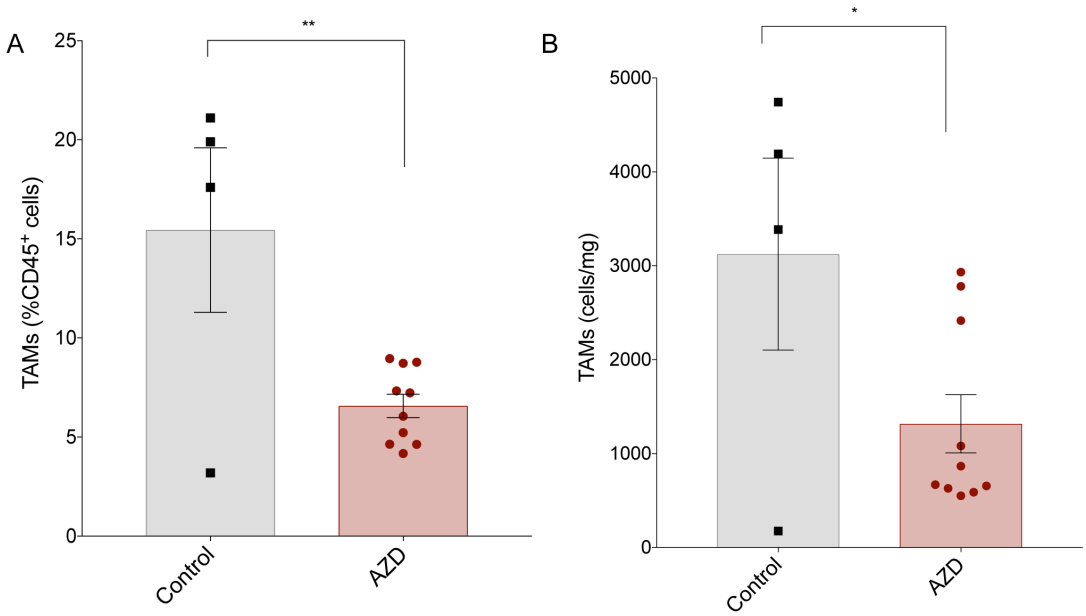

Figure 8.2 The effect of AZD7507 treatment on TAM density. Flow cytometry data relating to the immunostained stromal vascular fractions derived from 60577 omental tumours treated with AZD7507 (red circles) or vehicle alone (black squares). **A** TAM ($CD45^+Ly6C^-Ly6G^-CD11b^+F4/80^+$ cell) frequency is expressed as a percentage of the $CD45^+$ population and **B** as cells/mg. Data relate to a single experiment with ten AZD7507 treated mice and four vehicle-treated mice, the mean for each group is shown. Error bars represent SEM. Student's *t*-test p-values; *<0.05, **<0.01.

To assess if the observed TAM depletion was due to loss of a specific TAM population defined by classically (MHC Class II) or alternatively activated (CD206) surface markers, I assessed these markers as a percentage of the $CD45^+$ tumour infiltrate and as cells/mg

of tissue. TAMs expressing both of these markers were significantly decreased by AZD7507 treatment compared to vehicle-treated controls (Figure 8.3).

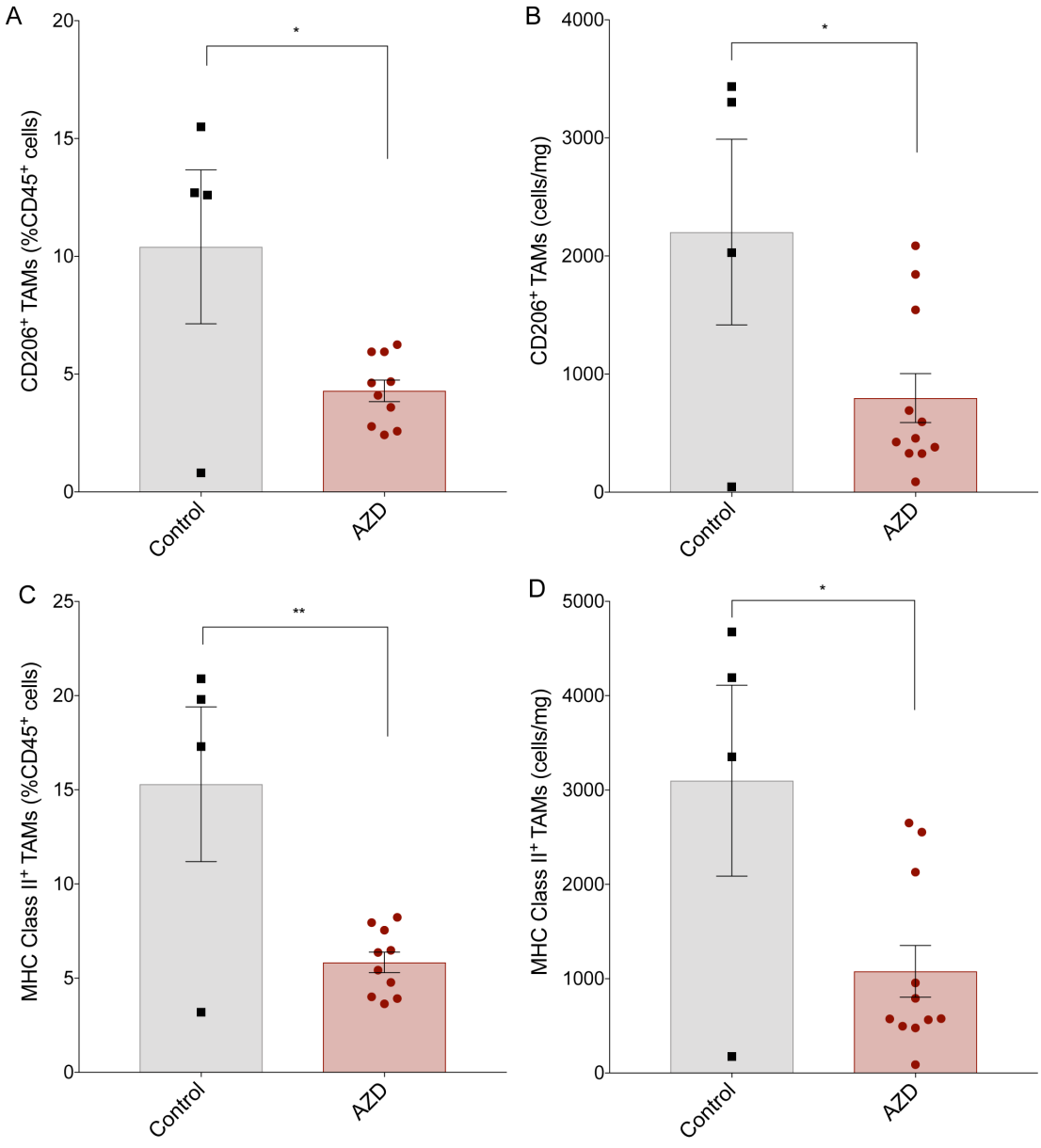

Figure 8.3 The effect of AZD7507 treatment on MHC Class II$^+$ and CD206$^+$ TAM density. Flow cytometry of immunostained stromal vascular fractions derived from omental tumours treated with AZD7507 (red circles) or vehicle alone (black squares). **A** CD206+TAM frequency is expressed as a percentage of the CD45$^+$ population and **B** as cells/mg. **C** MHC Class II$^+$TAM frequency is expressed as a percentage of the CD45$^+$ population and **D** as cells/mg. Data relate to a single experiment, ten AZD7507 treated mice and four vehicle-treated mice, the mean for each group is shown. Error bars represent SEM. Student's *t*-test p-values; *<0.05, **<0.01.

Several studies have suggested that as well as depleting TAMs, CSF-1Ri may affect TAM phenotype[215,216]. To assess for a change in TAM phenotype following AZD7507 treatment I measured CD206 and MHC Class II-high (MHC Class II$^+$) expression as the percentage of positive cells within the TAM population and by MFI. Figure 8.4 A and B show no significant differences in CD206 expression between the AZD7507 and vehicle-treated groups. However, there was a significant decrease in MHC Class II expression both expressed as percentage of positive cells and by MFI (Figure 8.4 C and D). This

implies a change of overall TAM phenotype in the remaining cells.

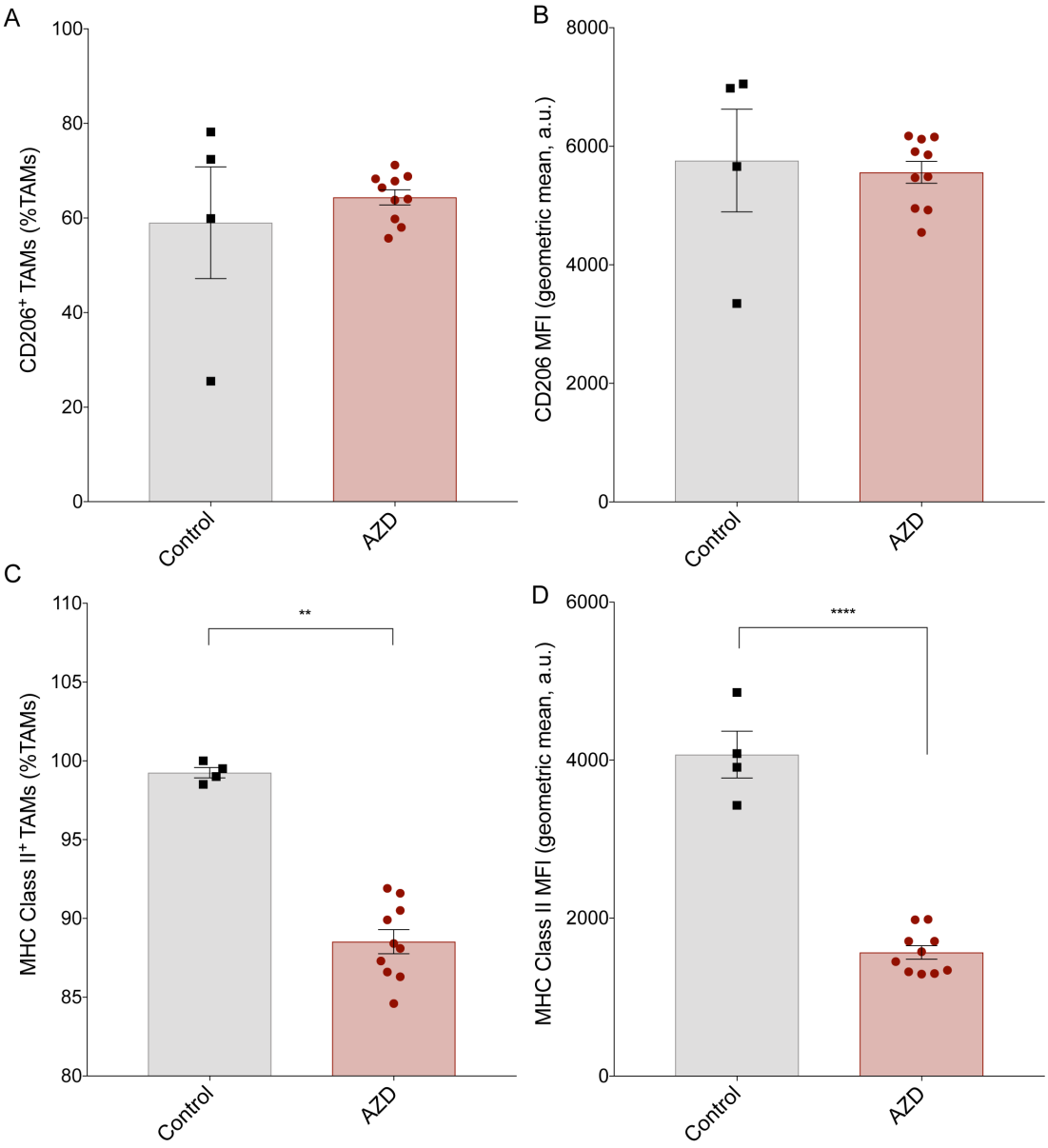

Figure 8.4 The effect of AZD7507 treatment on TAM phenotype. Flow cytometry data of the immunostained stromal vascular fractions derived from omental tumours treated with AZD7507 (red circles) or vehicle alone (black squares). **A** CD206$^+$TAM as a percentage of the TAM population and **B** as MFI. **C** MHC Class II$^+$TAM as a percentage of the TAM population and **D** as MFI. Data relate to a single experiment, ten AZD7507 treated mice and four vehicle-treated mice, the mean for each group is shown. Error bars represent SEM. Student's *t*-test p-values are shown; **<0.01, ****<0.001.

TAM depletion may result in changes to other cell types in the TME[222,239,251]. As seen in Figure 8.5 I was unable to detect any change in the total CD3$^+$, or CD8$^+$ T lymphocyte populations. I did observe a significant decrease in the CD4$^+$ population following AZD7507 treatment as a percentage of the CD45$^+$ population, however, this was not significant when assessed as cells/mg of tissue (Figure 8.5). There was also a significant decrease in CD19$^+$ B lymphocytes following AZD7507 treatment compared to vehicle-

treated tumours (Figure 8.6).

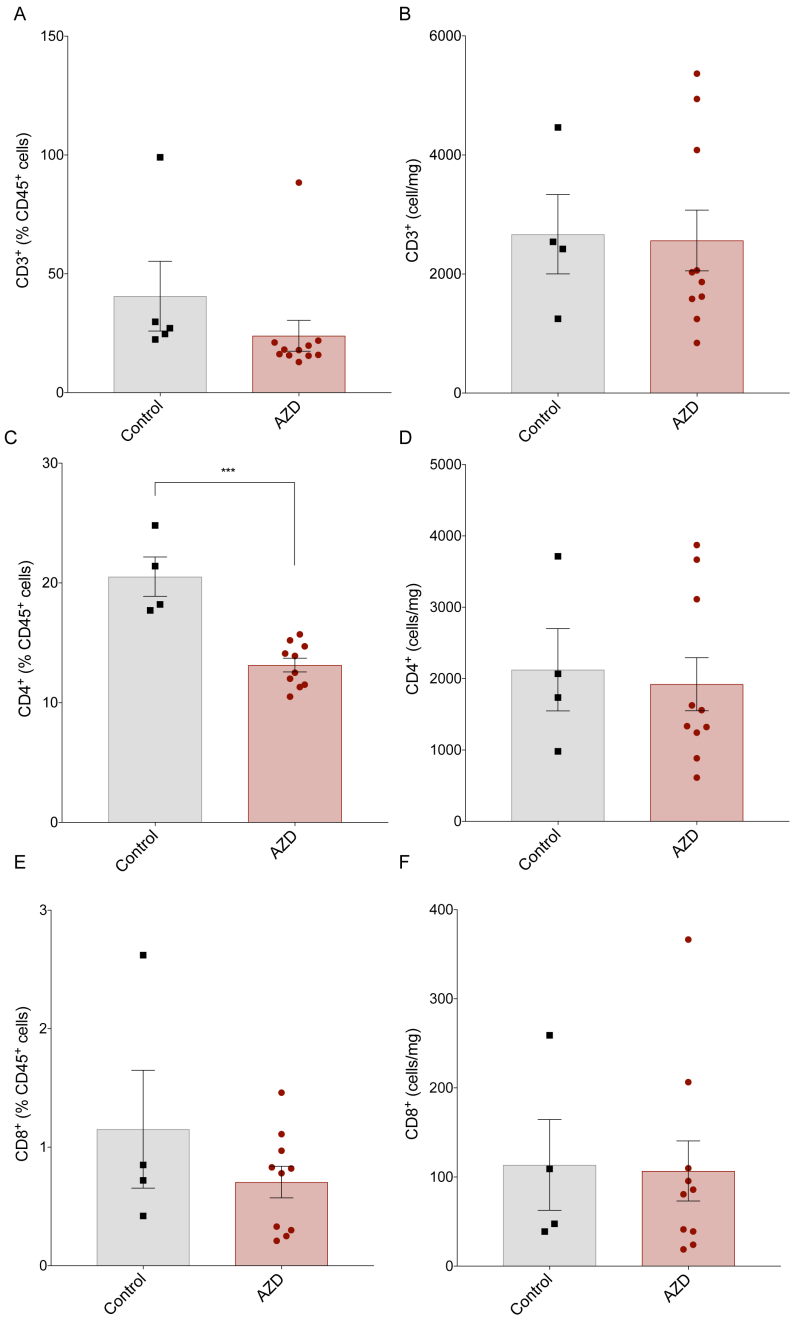

Figure 8.5 The effect of AZD7507 treatment on T lymphocyte populations. Flow cytometry of immunostained stromal vascular fractions derived from 60577 omental tumours treated with AZD7507 (red circles) or vehicle alone (black squares). **A** $CD3^+$ **C** $CD3^+CD4^+$ **E** $CD3^+CD8^+$ as a percentage of the $CD45^+$ population and **B** $CD3^+$, **D** $CD3^+CD4^+$, **F** $CD3^+CD8^+$ as cells/mg of tissue. Data relate to a single experiment, ten AZD7507 treated mice and four vehicle-treated mice, the mean for each group is shown. Error bars represent SEM. Student's *t*-test p-values are shown; ***<0.001.

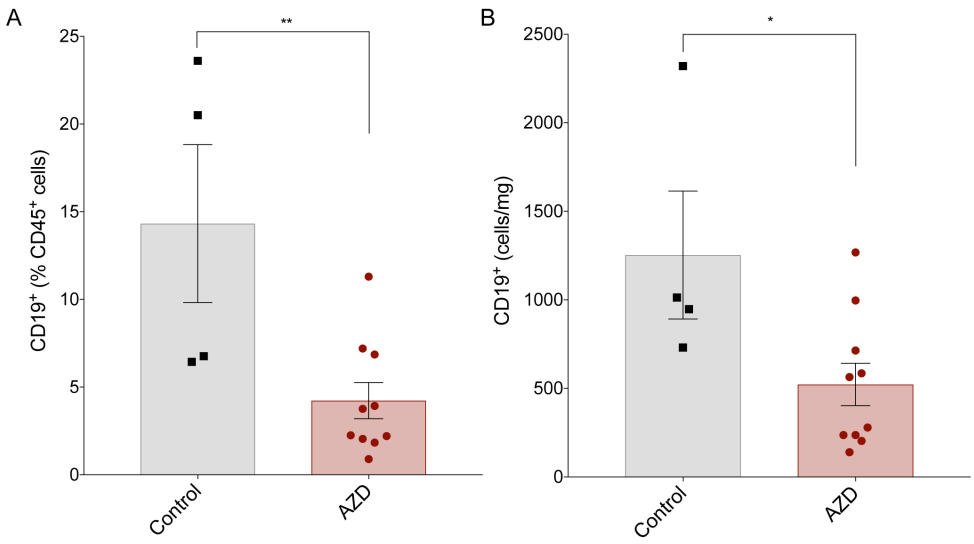

Figure 8.6 The effect of AZD7507 treatment on B lymphocyte populations. Flow cytometry data relating to the immunostained stromal vascular fractions derived from omental tumours treated with carboplatin (red circles) or vehicle alone (black squares). **A** $CD19^+$ cells as a percentage of the $CD45^+$ population and **B** as cells/mg of tissue. Data relate to a single experiment, ten AZD7507 treated mice and four vehicle-treated mice, the mean for each group is shown. Error bars represent SEM. Student's *t*-test p-values; *<0.05, **<0.01.

In this initial experiment the original plan had been to treat mice for fourteen days, however, as several of the AZD7507 treated mice developed large volume ascites and reached a humane end point before this time point, the experiment was terminated after twelve days of treatment. This suggests that AZD7507 may not improve survival in this model. Mouse post-mortem findings demonstrated well developed tumours and large volume ascites in all AZD7507 treated mice as well as vehicle controls. Assessment of the omental weight in AZD7507-treated mice showed no statistical difference in tumour weight, again suggesting that AZD7507 did not alter tumour growth in this model (Figure 8.7).

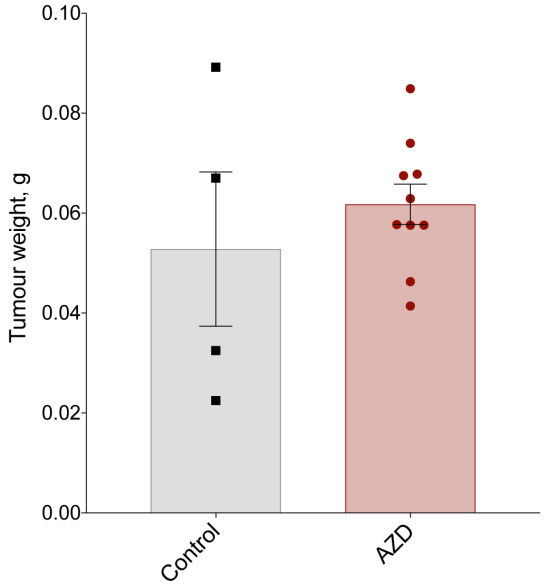

Figure 8.7 The effect of AZD7507 treatment on tumour weight in the 60577 model. Omental weight from mice treated with AZD7507 (red circles) or vehicle alone (black squares). Data relate to a single experiment, ten AZD7507 treated mice and four vehicle-treated mice, the mean for each group is shown. Error bars represent SEM.

To formally assess the effects of AZD7507 treatment on survival in the 60577 model I performed a second experiment. Mice were either pre-treated with AZD7507 for forty-eight hours prior to cell injection, or AZD7507 was started, in mice bearing established tumours, twenty-one days following cell injection. Mice in each group were continuously treated with AZD7507 or vehicle alone until a humane endpoint was reached. There was no difference in survival between AZD7507-treated and vehicle-treated controls when the treatment was started immediately prior to tumour cell injection nor after twenty-one days (Figure 8.8A). Furthermore, there was no difference in the mean omental weight between AZD7507-treated and vehicle-treated controls under either treatment regimen (Figure 8.8B). Therefore, in this model, global TAM depletion with CSF-1Ri did not affect murine HGSOC survival when administered in the context of an established tumour or before tumour development. Given that the phenotype of TAMs change following chemotherapy it will be important to assess the effects of TAM depletion following chemotherapy. Later in this Chapter I will assess the effects of CSF-1Ri-mediated TAM depletion at different time points following chemotherapy.

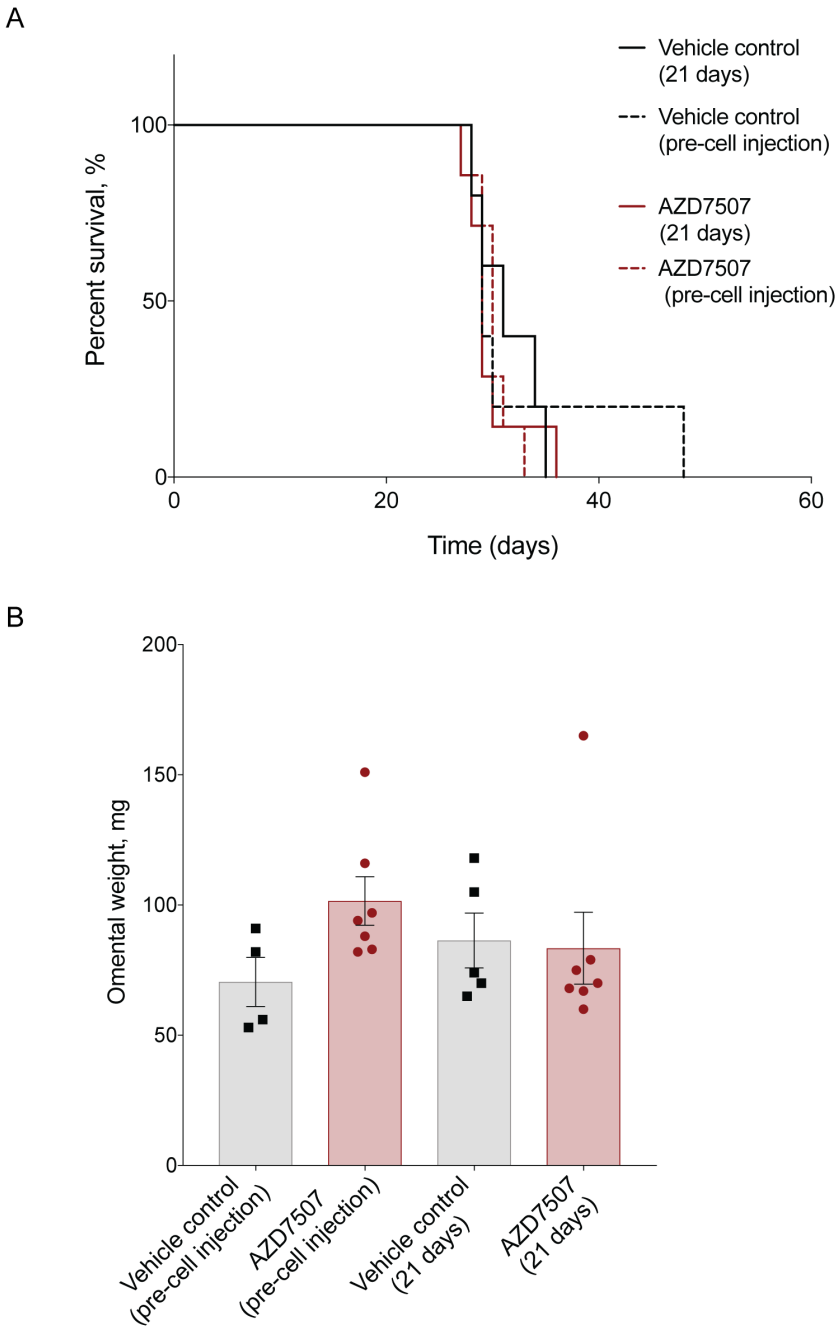

Figure 8.8 The effect of AZD7507 treatment on survival and tumour weight in the 60577 model. A Kaplan Meier curves showing survival of mice treated with AZD7507 started forty-eight hours before 60577 cell injection (red dashed line), AZD7507 started twenty-one days after 60577 cell injection (red line), vehicle-treated mice started forty-eight hours before 60577 cell injection (back dashed line) and vehicle-treated mice started twenty-one days after 60577 cell injection (black line). **B** Omental weight from mice treated with AZD7507 (red circles) or vehicle control (black squares). Data relate to a single experiment, four-seven mice per group, the mean for each group is shown. Error bars represent SEM.

8.2.2 BLZ945 treatment of the 60577 model

I next assessed the effects of BLZ945 in the 60577 murine model. BLZ945 was obtained commercially. Due to high cost of this compound, initially I only obtained enough drug to treat four mice for four days. BLZ945 treated tumours were compared to vehicle-treated tumours at a time point 12 hours following the last treatment. Figure 8.9 shows a schematic outline for this experiment. BLZ945 has not been previously used in the lab, in view of the expense of this compound, I used doses that have proved effective in the treatment of tumour-bearing mice described in the literature[215,321].

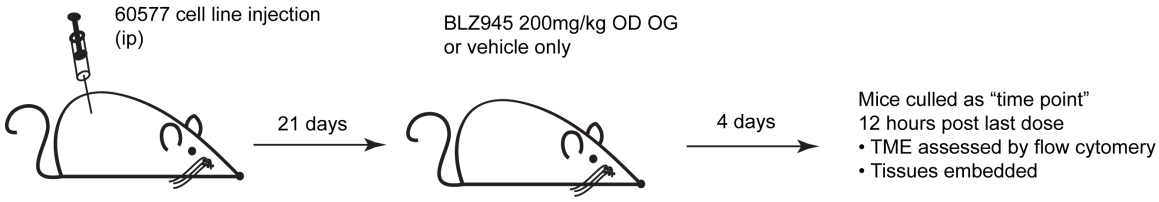

Figure 8.9 Schematic outline of an experiment assessing the effect of BLZ945 on the 60577 model. Significant experimental time points and treatment scheduling is shown. *OD: once a day, OG: oral gavage*.

After four days of treatment with BLZ945, there was a significant decrease in the TAM density in BLZ945 treated tumours compared to vehicle-treated controls (Figure 8.10).

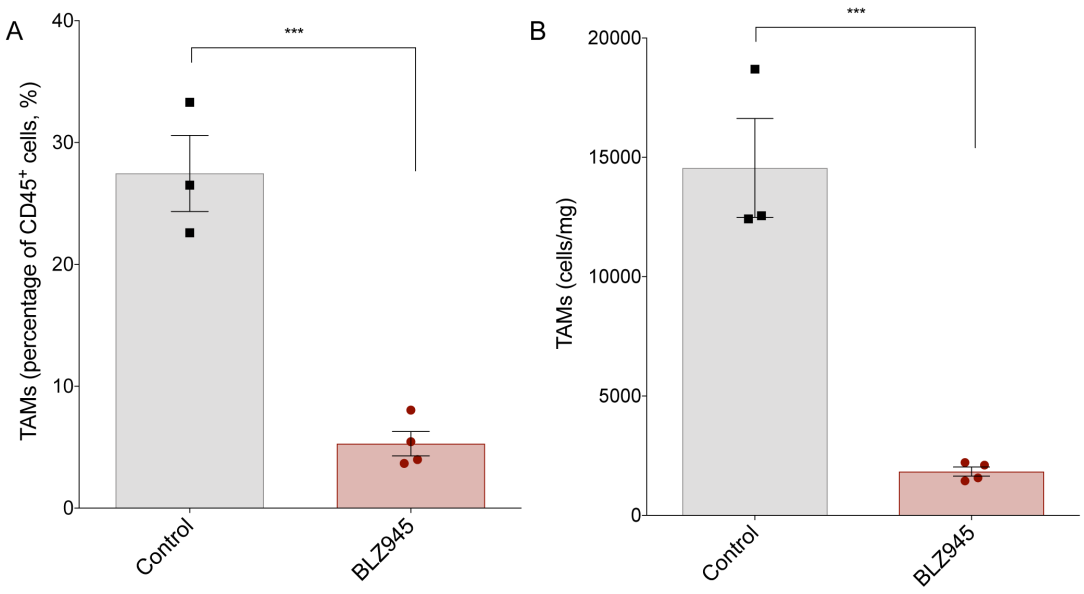

Figure 8.10 The effect of BLZ945 treatment on TAM cell number. Flow cytometry data relating to the immunostained stromal vascular fractions derived from omental tumours treated with BLZ945 (red circles) or vehicle alone (black squares). **A** TAM frequency is expressed as a percentage of the $CD45^+$ population and **B** as cells/mg. Data relate to a single experiment, four BLZ945 treated mice and three vehicle-treated mice, the mean for each group is shown. Error bars represent SEM. Student's *t*-test p-values are shown; ***<0.001.

As seen previously in experiments using AZD7507, FC analysis showed there was a

significant reduction in TAMs expressing the surface markers CD206, MHC Class II as well as PDL1 (Figure 8.11) both when quantified as cells/mg of tissue and as a percentage of the CD45$^+$ immune cell infiltrate.

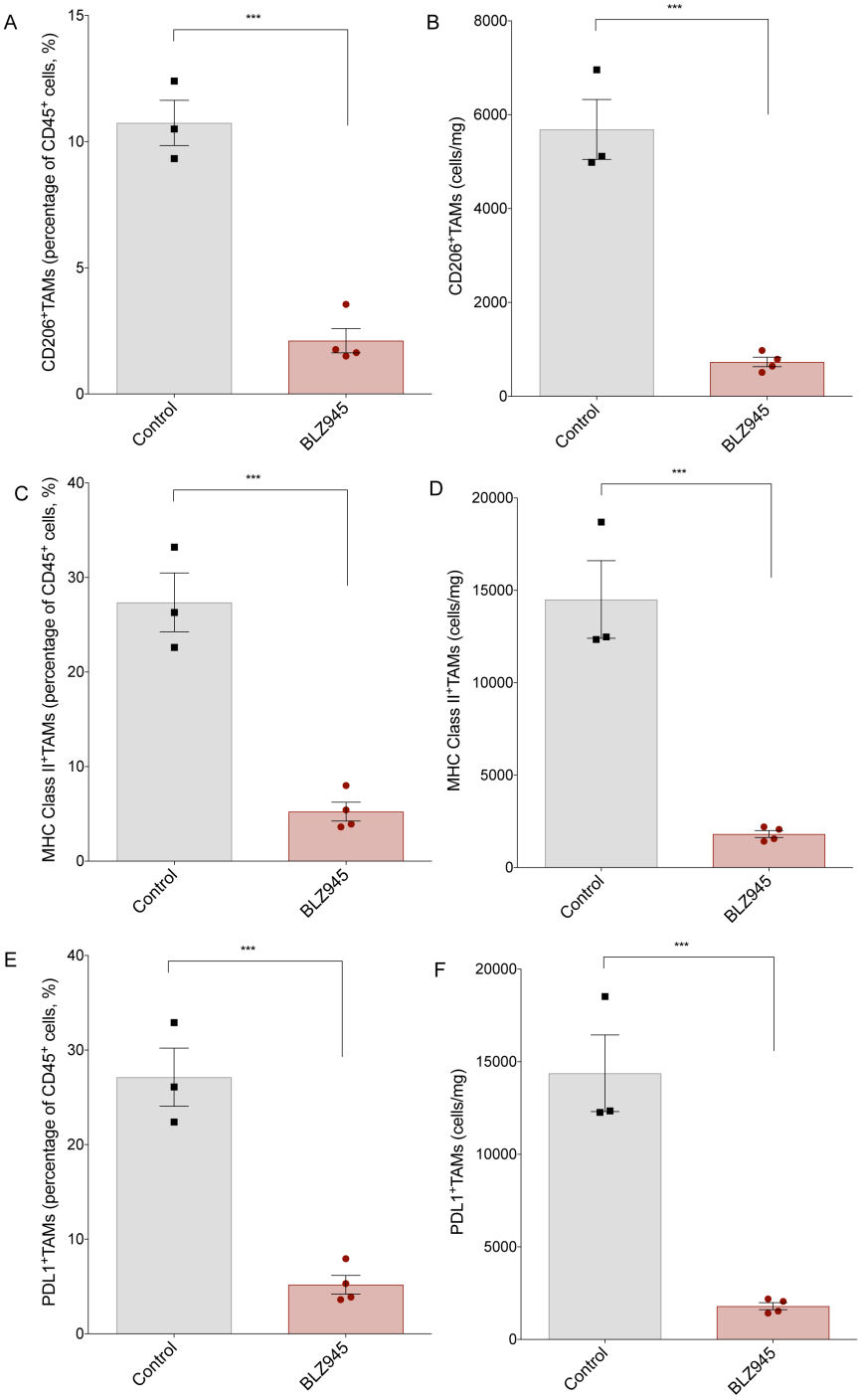

Figure 8.11 The effect of BLZ945 treatment on MHC Class II$^+$ and CD206$^+$ TAM cell number. Flow cytometry data relating to the immunostained stromal vascular fractions derived from omental tumours treated with BLZ945 (red circles) or vehicle alone (black squares). **A** CD206$^+$TAM frequency is expressed as a percentage of the CD45$^+$ population and **B** as cells/mg. **C** MHC Class II$^+$TAM frequency is expressed as a percentage of the CD45$^+$ population and **D** as cells/mg. **E** PDL1$^+$TAM frequency is expressed as a percentage of the CD45$^+$ population and **F** as cells/mg. Data relate to a single experiment, four BLZ945 treated mice and three vehicle-treated mice, the mean for each group is shown. Error bars represent SEM. Student's *t*-test p-values are shown; *<0.05, **<0.01.

I next looked for any change in TAM phenotype after BLZ945 treatment. Interestingly, as observed with AZD7507 treatment of this model, I found significant reductions in MHC Class II expression with no changes in CD206 expression (Figure 8.12).

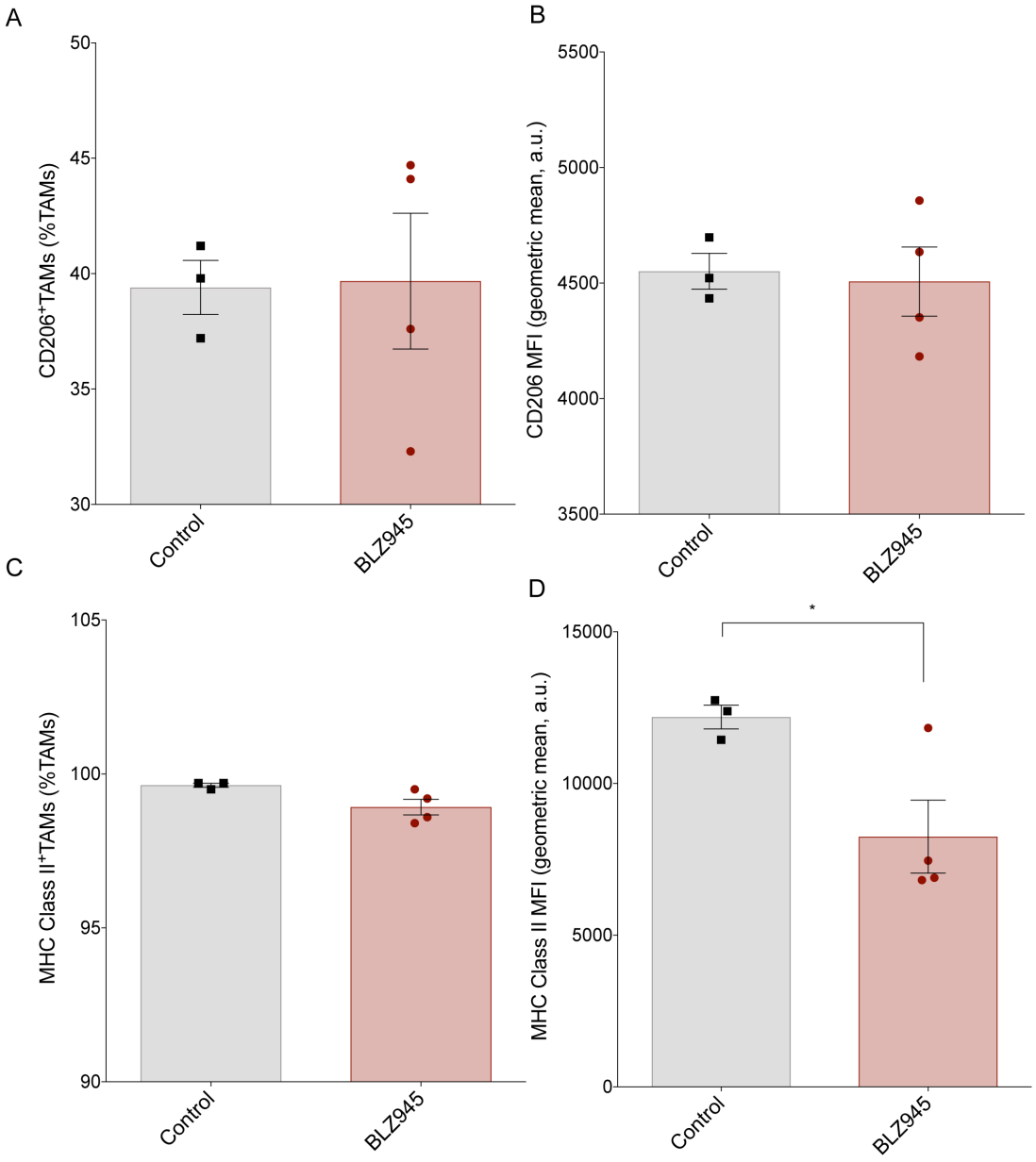

Figure 8.12 The effect of BLZ945 treatment on TAM phenotype. Flow cytometry data relating to the immunostained stromal vascular fractions derived from omental tumours treated with BLZ945 (red circles) or vehicle alone (black squares). **A** CD206$^+$TAM percentage of the TAM population and **B** as MFI. **C** MHC ClassII$^+$TAM percentage of the TAM population and **D** as MFI. Data relates to a single experiment, four BLZ945 treated mice and three vehicle-treated mice, the mean for each group is shown. Error bars represent SEM. Student's *t*-test p-values are shown; *<0.05.

Assessments of the lymphocyte populations showed significant decreases in the CD3$^+$ and CD3$^+$CD4$^+$ populations (Figure 8.13) but no significant changes in CD3$^+$CD8$^+$ cell number (Figure 8.13). As seen with AZD7507 treatment, there was a significant decrease in CD19$^+$ cells in BLZ945 treated compared to vehicle-treated tumours (Figure 8.14).

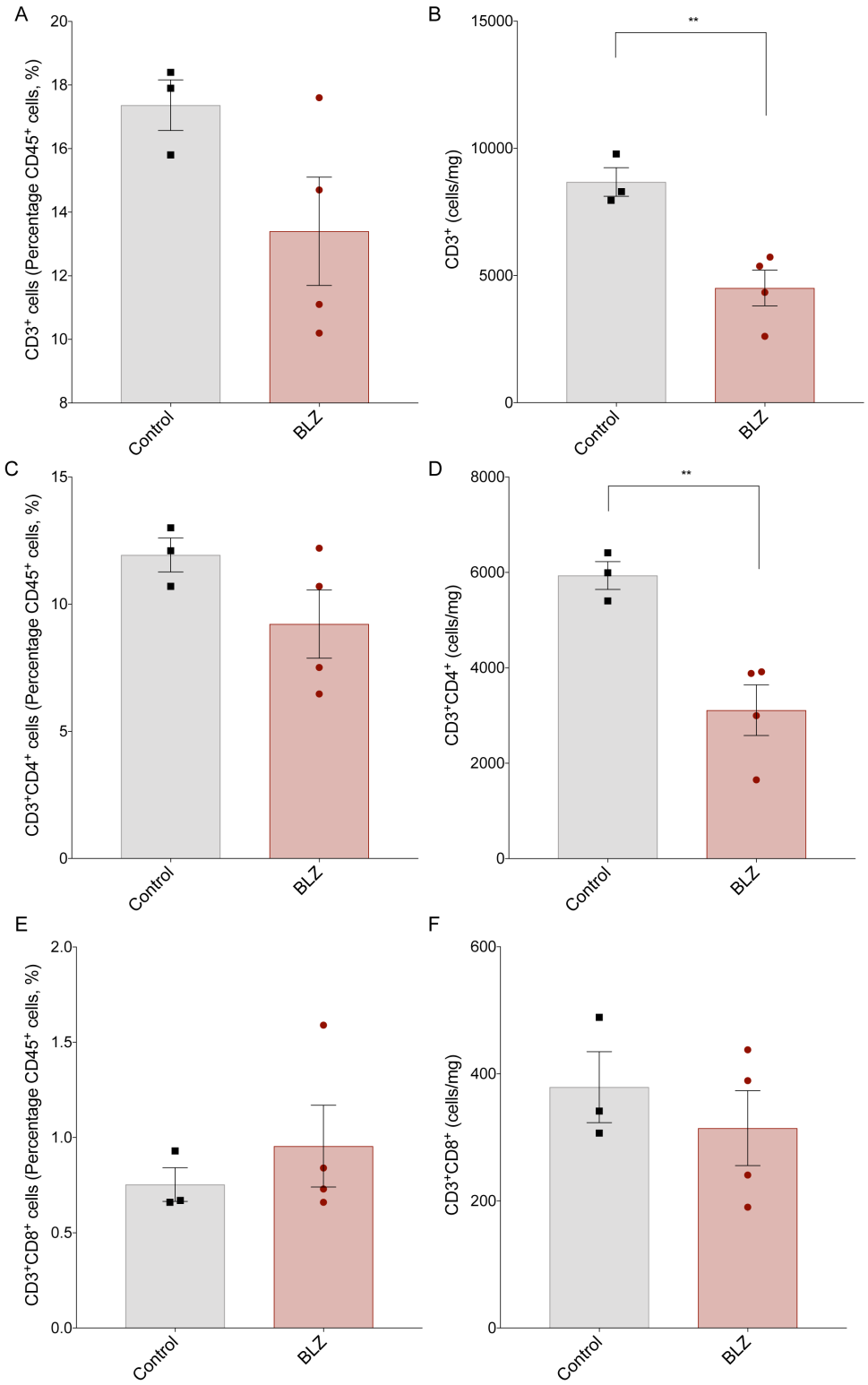

Figure 8.13 The effect of BLZ945 treatment on T lymphocyte populations. Flow cytometry data relating to the immunostained stromal vascular fractions derived from omental tumours treated with BLZ945 (red circles) or vehicle alone (black squares). **A** $CD3^+$ **C** $CD3^+CD4^+$ **E** $CD3^+CD8^+$ as a percentage of the $CD45^+$ population and **B** $CD3^+$, **D** $CD3^+CD4^+$, **F** $CD3^+CD8^+$ as cells/mg of tissue. Data relate to a single experiment, four BLZ945 treated mice and three vehicle-treated mice, the mean for each group is shown. Error bars represent SEM. Student's *t*-test p-values; **<0.01.

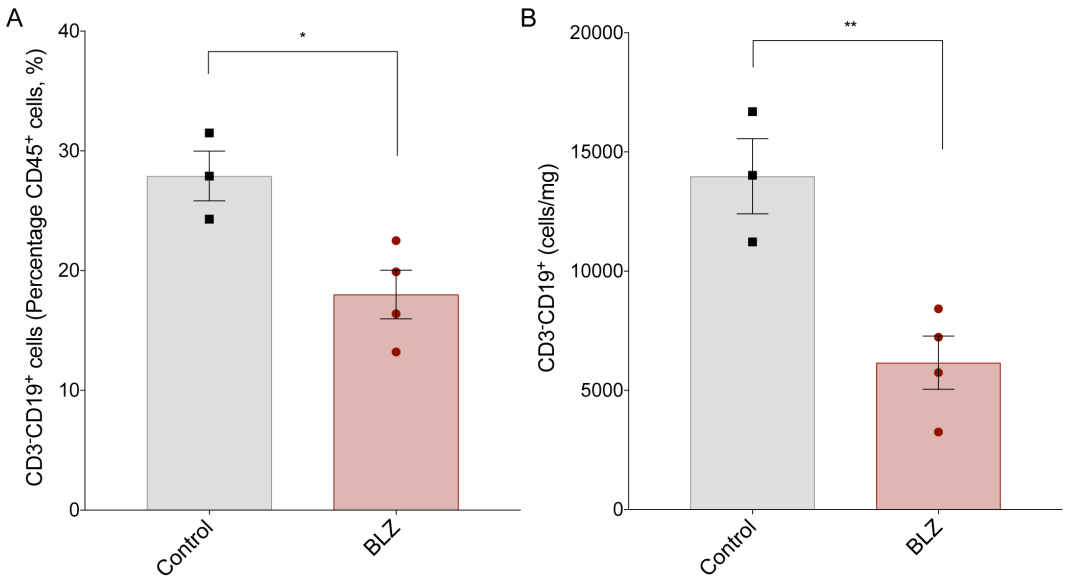

Figure 8.14 The effect of BLZ945 treatment on the B lymphocyte population. Flow cytometry data relating to the immunostained stromal vascular fractions derived from omental tumours treated with BLZ945 (red circles) or vehicle alone (black squares). **A** $CD19^+$ cells as a percentage of the $CD45^+$ population and **B** as cells/mg of tissue. Data relate to a single experiment, four BLZ945 treated mice and three vehicle-treated mice, the mean for each group is shown. Error bars represent SEM. Student's *t*-test p-values are shown; *<0.05, **<0.01.

There were no significant differences in omental weight between BLZ945 treated and vehicle controls (Figure 8.15), as might be expected after only four days on treatment.

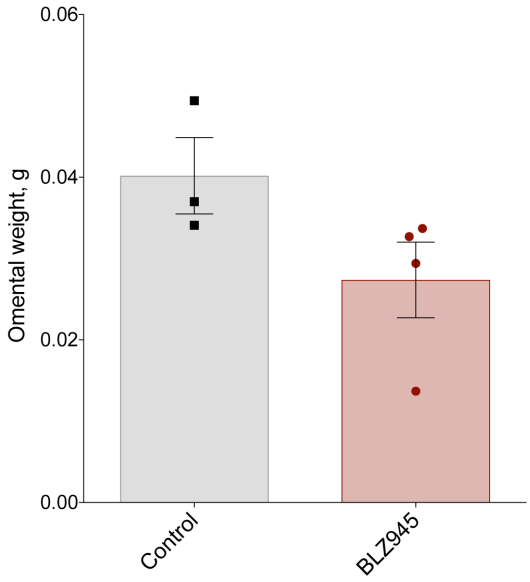

Figure 8.15 The effect of BLZ945 treatment on tumour weight in the 60577 model. Fresh omental weight from mice treated with BLZ945 (red circles) or vehicle alone (black squares). Data relates to a single experiment, four BLZ945 treated mice and three vehicle-treated mice, the mean for each group is shown. Error bars represent SEM.

8.2.3 Summary: CSF-1Ri treatment of 60577 tumours

Overall these data show no reduction in tumour size or survival benefit of CSF-1Ri TAM depletion in the 60577 model. However, both AZD7507 and BLZ945 reduced the density of TAMs in 60577 tumours. Surface expression of MHC Class II on TAM was significantly reduced whereas CD206 expression remained unchanged and highly expressed. CSF-1Ri treatment also resulted in changes to tumour infiltrating lymphocyte populations with significant reductions of $CD4^+$ T cells and $CD19^+$ B cells following treatment with either inhibitor. At post mortem there were no obvious macroscopic changes in the amount or sites of peritoneal dissemination in CSF-1Ri-treated mice compared to vehicle-treated controls.

8.3 CSF-1Ri treatment of HGSOC relapse

An overarching aim of this thesis is to determine if there is any value in targeting TAMs in metastatic HGSOC. Treating 60577 tumours with AZD7507 alone did not change survival or tumour size. Therefore, targeting TAM before chemotherapy may not be helpful. The findings presented in Chapters 3 and 6 suggest that TAMs were depleted in human and mouse HGSOC following carboplatin treatment. Therefore CSF-1Ri treatment co-administered with chemotherapy may not further modify the TME. I decided instead to test the effect of CSF-1Ri following carboplatin chemotherapy. I hypothesised that the period following chemotherapy may represent a 'window of opportunity' to target TAMs, preventing TAM re-accumulation, with the aim of delaying HGSOC relapse. The relapse 60577 model of HGSOC provided a suitable system to test this hypothesis.

8.3.1 Effect of CSF-1Ri on survival to relapse

To assess the effects of CSF-1Ri on tumour regrowth post-chemotherapy, mice were treated with three once-weekly doses of carboplatin, then following an interval of ten weeks from the last dose of carboplatin, they were treated with AZD7507 for three weeks. This corresponded with the first mouse reaching a humane end point due to recurrent disease. I chose to start treatment at ten weeks following carboplatin because in previous experiments in the 60577 relapse model mice had started to reach endpoint at approximately thirteen weeks following completion of carboplatin treatment (Chapter 7). Figure 8.16 shows a schematic representation of this experiment.

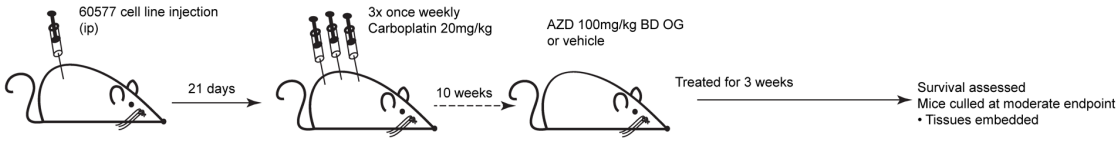

Figure 8.16 Schematic outline of an experiment assessing the effects of AZD7507 on HGSOC relapse. Significant experimental time points and treatment scheduling are shown. *BD: twice a day, OG: oral gavage*.

The main objective of this experiment was to study the effect of AZD7507 compared to vehicle-treated mice on overall survival. As shown in Figure 8.17 there was no significant difference in survival between AZD7507 and vehicle-treated controls. All mice in the experiment developed recurrent disease with evidence of omental tumours and large volume ascites at endpoint.

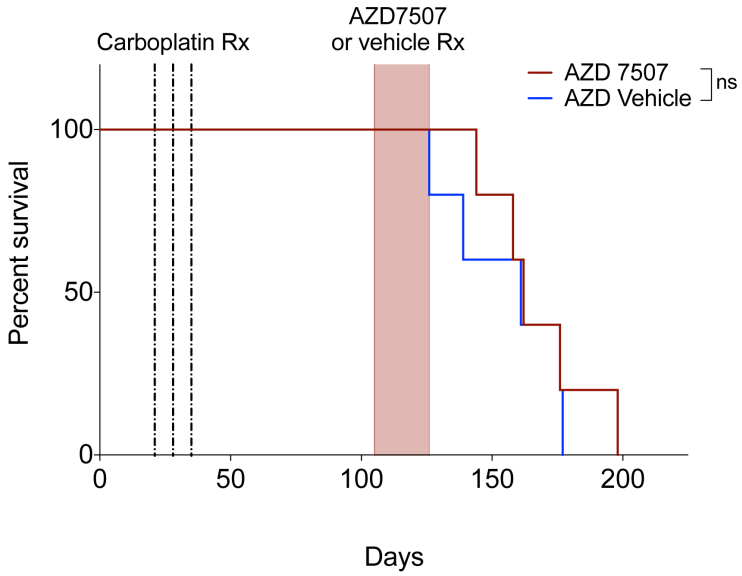

Figure 8.17 The effect of AZD7507 treatment on survival to relapse. Kaplan Meier curves showing AZD7507 treated mice (red line) and vehicle-treated controls (blue line). Carboplatin tretaments are indicated (dashed lines), the period of AZD7507 or vehicle tretament is indicated (red shading). Data from a single experiment are shown. Log-rank (Mantel-Cox) test p-value is shown; ns=non-significant.

Given that TAM reaccumulate in relapsing tumours (see Chapter 7), I next asked if initiating CSF-1Ri treatment sooner than ten weeks following chemotherapy would change outcome. Therefore, I treated mice with either AZD7507 or BLZ945 starting four weeks after carboplatin treatment. This time point was chosen as previous studies showed only small foci of malignant cells in the omentum at a time point six weeks following carboplatin treatment. Therefore, I assumed that TAM would not have reaccumulated in the omentum at this earlier time point. Figure 8.18 shows the schematic outline of this experiment.

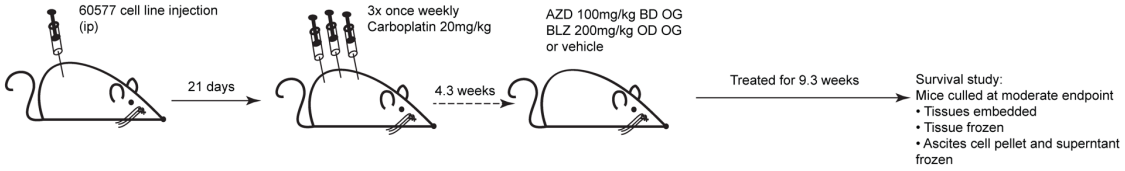

Figure 8.18 Schematic outline of experiment assessing the effect of AZD7507 and BLZ945 on HGSOC relapse. Significant experimental time points and treatment scheduling are shown. *OD: once a day, BD: twice a day, OG: oral gavage*.

Contrary to expectations, when treatment was started four weeks after completion of carboplatin, administration of either AZD7507 or BLZ945 significantly reduced time to relapse and survival compared to vehicle only treated controls (Figure 8.19). The median survival in AZD7507-treated mice was 126 days *vs* 149 days for vehicle-treated controls p=0.001; BLZ945-treated mice median survival was 135 days *vs* 150 days for vehicle-treated controls p=0.016.

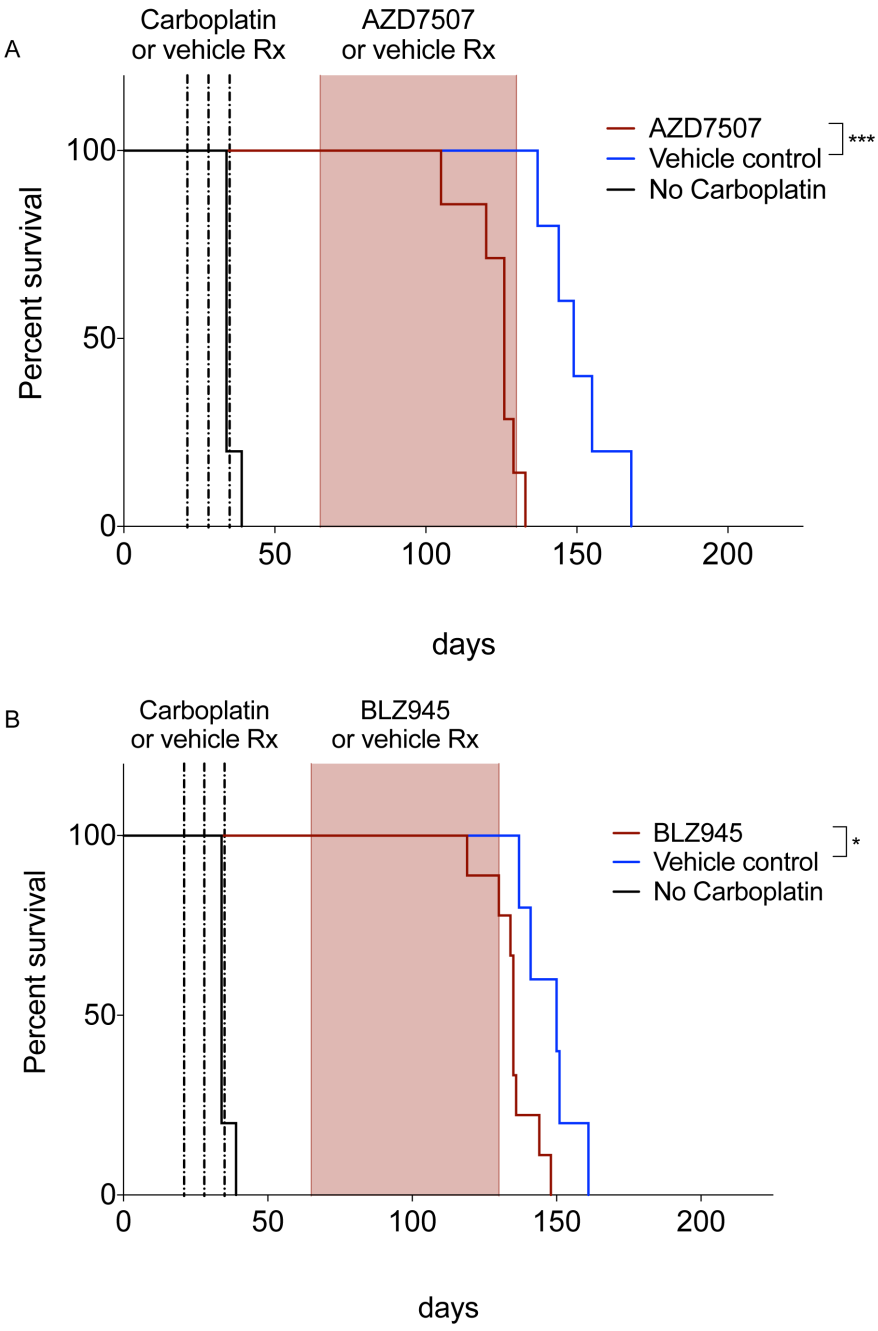

Figure 8.19 The effects of AZD7507 and BLZ945 tretament on survival to relapse in the 60577 model commensed four weeks following carboplatin treatment. Kaplan Meier curves showing **A** AZD7507 or **B** BLZ945 treated mice (red line), vehicle-treated controls (blue line) and mice not treated with chemotherapy (black line). Carboplatin or vehicle tretaments are indicated (dashed lines), the period of AZD7507 or vehicle tretament is indicated (red shading). Data from a single experiment is shown. Log-rank (Mantel-Cox) test p-value is shown; *<0.05, ***<0.001.

To further explore this result an experiment was performed in which mice were treated with AZD7507 for 12 weeks starting immediately after completion of carboplatin treatment. Again, mice treated with AZD7507 starting immediately after chemotherapy had a shortened overall survival compared to vehicle-treated controls (Figure 8.20). This experiment was performed with the assistance of Dr. Chiara Berlato, Barts Cancer Institute. Analysis of flow cytometry data relating to this experiment is ongoing.

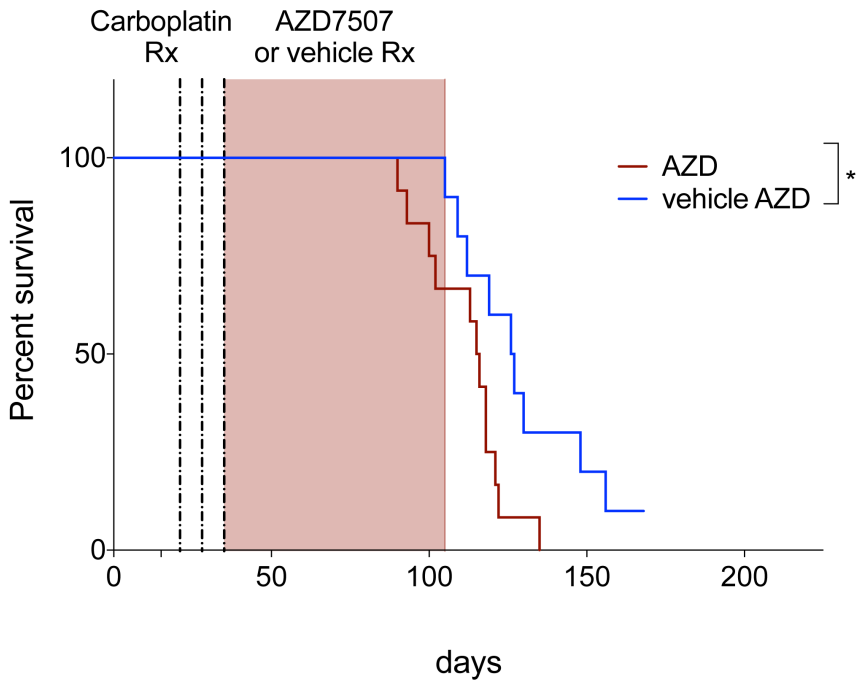

Figure 8.20 The effects of AZD7507 tretament on survival to relapse in the 60577 model commensed immedialy following carboplatin tretament. Kaplan Meier curves showing AZD7507 treated mice (red line) and vehicle-treated controls (blue line). Carboplatin tretaments are indicated (dashed lines), the period of AZD7507 or vehicle tretament is indicated (red shading). Data from a single experiment are shown. Log-rank (Mantel-Cox) test p-value is shown; *<0.05.

Overall this series of experiments suggest that TAM populations are modified by carboplatin treatment to take on roles which limit tumour growth. Therefore, depletion of TAMs soon after, or immediately following the completion of carboplatin treatment explains the detrimental effects of CSF-1Ri on murine survival.

8.3.2 Assessment of TAM density in CSF-1Ri treated tumours by immunohistochemistry

To confirm TAM depletion in the relapse model secondary to AZD7507 and BLZ945 treatment, I measured F4/80 expression by IHC within omental tumours in the survival experiments (Figure 8.21). This confirmed significant reductions in F4/80$^+$ infiltrate in BLZ945 treated mice compared to vehicle controls. The data relating to AZD7507 treated *vs* vehicle controls were not statistically significant (p=0.08), although the difference

between means was very similar to BLZ945 treated tumours. This is likely due to small numbers in the AZD7507 control group.

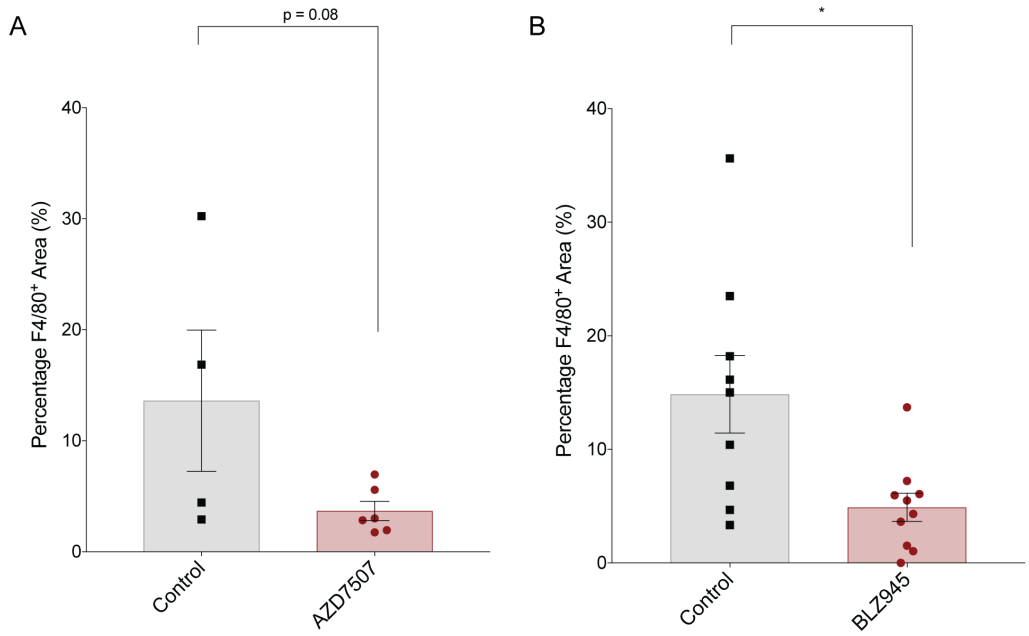

Figure 8.21 Validation of TAM depletion with CSF-1Ri in relapsed HGSOC. Quantification of F4/80 staining by Definiens® digital analysis in relapsed tumours. **A** AZD7507 (red circles) and vehicle-treated controls (black squares). **B** BLZ945 (red circles) and vehicle-treated controls (black squares). F4/80 staining expressed as percentage positive area of the biopsy. Data quantified relate to a single experiment, the mean for each group is shown. Error bars represent SEM. Student's *t*-test p-values are shown; *<0.05.

These results add further weight to the interim conclusions from both the human and murine studies in the previous chapters. I hypothesise that after chemotherapy TAM may contribute to a microenvironment that attempts to limit tumour growth and development. Partial depletion of these TAM may be detrimental.

8.4 Discussion

In this chapter I report a series of experiments that were conducted to assess the value of targeting TAM with CSF-1Ri in metastatic HGSOC. Treatment of the 60577 model with CSF-1Ri as a single-agent did not alter survival (Figure 8.8). Furthermore, there were no differences in tumour weight after twelve days of AZD7507 treatment compared to vehicle-treated controls (Figure 8.7). I next treated tumour-bearing mice after chemotherapy with both AZD7507 and BLZ945. Counter to expectations, starting either CSF-1Ri four weeks after carboplatin treatment significantly decreased overall survival (Figure 8.19). Furthermore, starting AZD7507 treatment immediately following carboplatin treatment also significantly decreased overall survival compared to vehicle treatment controls (Figure 8.20). Therefore, CSF-1Ri treatment following carboplatin seems to be harmful. This surprising result shows that chronic CSF-1Ri treatment may deplete or repolarise populations of TAMs which restrain tumour progression.

Alternatively, chronic CSF-1Ri-mediated TAM depletion may induce compensatory changes in the TME with recruitment of other tumour promoting cells e.g. granulocytes; or the changes observed in lymphocyte cell number may be responsible. CSF-1Ri resulted in overall reductions in $CD4^+$ T cells and $CD19^+$ B cells. Tumour infiltrating lymphocytes are the cell type most robustly associated with a good prognosis in ovarian cancer[34]. Furthermore, work in our lab has shown B cells in HGSOC are associated with an antitumoral immune landscape[114]. Therefore, although CSF-1Ri treatment significantly reduced TAM density, the changes observed in the lymphocyte populations could also explain reductions in overall survival in mice treated with CSF-1Ri post-chemotherapy.

AZD7507 and BLZ945 treatment resulted in reduction of TAM cell density (Figure 8.2, Figure 8.10), showing that effective doses of these compounds were being used. However, higher concentrations may have resulted in further depletion. This could be tested in future experiments. The remaining TAMs showed reduced expression of MHC Class II with preserved high CD206 expression. Therefore, in addition to TAM depletion CSF-1Ri treatment may have altered the overall phenotype of the remaining macrophage population, towards an alternatively activated state. This finding agrees with Mitchem *et al.* who showed specific depletion of MHC Class II-high TAM by CSF-1Ri; in this study the depleted cells also expressed high levels of F4/80 and were able to phagocytose tumour cells. Therefore, in this model CSF-1Ri treatment may have skewed TAM towards a tumour promoting phenotype. Furthermore, in several systems MHC Class II-low macrophages have been associated with poor prognosis and a profibrotic phenotype[139,322].

Human studies in a number of cancers types support my data, which have shown that following chemotherapy high TAM density was associated with improved survival[181,188]. Di Caro *et al.* showed that chemotherapy modified the association of TAM density with clinical outcome in PDAC; prior to chemotherapy TAM were immunosuppressive and high TAM density associated with poor outcome, following chemotherapy TAM density predicted improved survival. Taken together, these data show that chemotherapy may directly or indirectly change macrophage function towards antitumoral functions.

Initiating CSF-1Ri treatment at a later time point, ten weeks compared to immediately after or four weeks post-carboplatin, was not associated with differences in survival to relapse (Figure 8.17). Hence it is possible that the 'positive' effects of carboplatin on TAMs may exist for a relatively short period of time following the completion of treatment.

Therefore, the ideal time to intervene with TAM-modifying therapy may be immediately post-chemotherapy with the aim of further stimulating the anti-tumour activities of TAM rather than depleting them with a CSF-1Ri. It can be envisaged that a brief period of CSF-1Ri treatment just before chemotherapy, rather than a long-term treatment, as in my experiments, may alter the interaction of the TAM population with chemotherapy. It may be that such an approach would reduce TAM-mediated immunosupression which may enhance the 'immuno-stimulatory' effects of chemotherapy.

In both the patient biopsies and mouse models I found evidence for direct, or indirect, *in vivo* cytotoxic activity of carboplatin on TAMs. In the final chapter I have investigated this further using *in vitro* models.

Chapter 9
Carboplatin activates inflammatory cell death in macrophages

9.1 Introduction

In the data presented so far in this thesis I have described the effects of NACT or on TAMs in human and murine HGSOC. These data show that chemotherapy results in: *i*) a change in TAM phenotype with down regulation of CD206 and scavenger receptors, *ii*) upregulation of inflammasome, TLR and IL1β signalling pathways (so far only in human TAM) *iii*) significant reductions in TAM and *iv*) increases in non-viable TAM. I conclude that carboplatin may induce TAM cell death as well as promote an inflammatory TAM phenotype. A unifying mechanism linking these latter two processes could be the activation of pyroptosis. This led me to ask the question – 'can carboplatin induce pyroptosis in macrophages?'.

Pyroptosis is an inflammatory form of cell death characterised by cell membrane lysis and the release of the proinflammatory cytokines IL1β and IL-18[323,324]. This process is mediated by the activation of pro-inflammatory caspases (capase-1/11 in the mouse and caspase-1/4/5 in humans) which occurs following the assembly of specific multiprotein signalling platforms called inflammasomes. In the canonical pathway, inflammasome assembly, with resultant cleavage and activation of caspase-1 mediates cleavage of the repressor domain from the pore forming domain (PFD) of gasdermin D (GSDMD)[323,325]. This results in the assembly of gasdermin pores in the cell membrane causing the cell to swell and lyse[326]. This event facilitates the release of the inflammatory cytokines. Non-canonical activation of pyroptosis can also occur via gasdermin D cleavage by caspases-4/5/11. In humans gasdermin D is one of six gasdermin family members[323]. Several other gasdermins form pores upon cleavage of the PFD. One of these, gasdermin E (DFNA5) is activated by cleaved caspase-3[327]. Therefore, caspase-3 has recently been shown to activate pyroptosis via this alternative pathway.

In view of the data summarised above, I assessed the effects of carboplatin treatment on macrophage viability, phenotype, inflammasome assembly and activation of pyroptosis using human monocyte derived macrophages.

9.2 Assessments of the effect of chemotherapy on human HGSOC cell lines *in vitro*

To define relevant *in vitro* concentrations of carboplatin to use in experiments on macrophages, I first tested the sensitivity of three human HGSOC cell lines (AOCS1, G164 and G33) to carboplatin (Figure 9.1). All three cell lines had a similar response to carboplatin with IC_{50} of 55.56μM (AOCS), 123.8μM (G164), 189.6μM (G33); these are within the ranges reported for the sensitivity of other ovarian cancer cell lines to

carboplatin[309]. Furthermore, IC_{50} carboplatin values were similar to those of the murine HGSOC cell lines (86.1μM -155.4μM) (Figure 6.1).

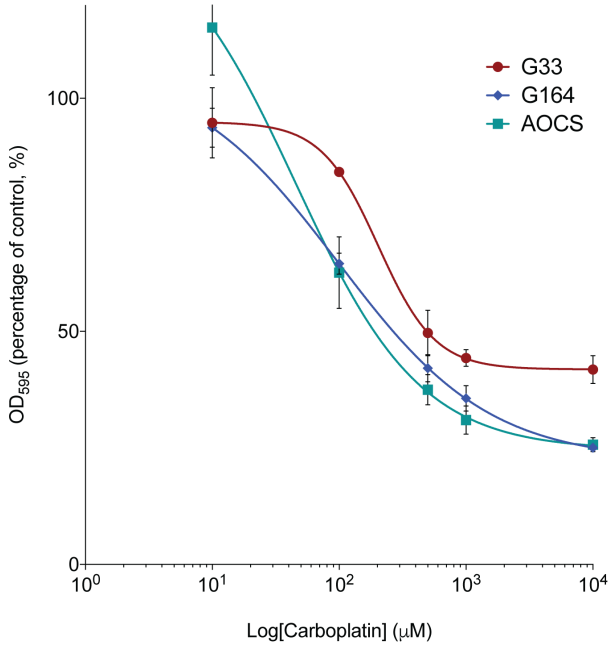

Figure 9.1 Testing the sensitivity of human HGSOC cell lines to carboplatin. G33 (red line), G164 (blue line) and AOCS1 (green line) cells were cultured in media containing varying concentrations of carboplatin for forty-eight hours. Cells were then fixed and stained with crystal violet. Crystal violet staining was quantified by spectrophotometry. OD_{595} measurements presented as the mean with error bars representing SEM from three experiments, normalised to media-only control for carboplatin. IC_{50} values: G33=203.1μM, G164=98.63μM and AOCS1=45.1μM.

9.3 The effects of chemotherapy on macrophages *in vitro*

Next I tested the effects of chemotherapy on human macrophages (Figure 9.2 and Figure 9.3). Macrophages were differentiated from $CD14^+$ human monocytes by culture in the presence of h-MSCF (CSF-1) for seven days and then polarised *in vitro* to either M1/classically activated or M2/alternatively activated phenotypes with LPS/IFNγ or IL-4/IL-10 respectively. The cells were then treated with carboplatin at different concentrations for forty-eight hours, cell viability and phenotype were assessed by flow cytometry. Macrophages were killed by carboplatin at concentrations in the range 50-200μM. This is within the range of IC_{50} value for the human HGSOC cell lines tested (Figure 9.1). The IC_{50} was lower for M1/classically activated macrophages (93μM) than M2 (203μM) polarised macrophages.

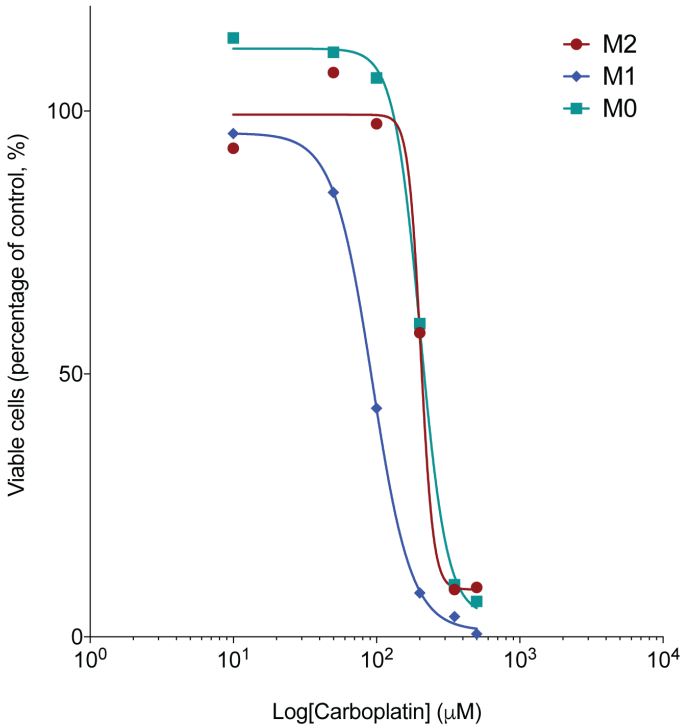

Figure 9.2 Assessing the effects of carboplatin on macrophage viability *in vitro*. Human $CD14^+$ monocytes derived from leucocyte cones were differentiated in media containing h-MCSF for seven days prior to being polarised to M1/classically activated (blue line) and M2/alternatively activated (red line) phenotypes with LPS/IFNγ and IL-4/IL-10 respectively, M0 (green line) cells received no additional stimulation. Cells were cultured in media containing varying concentrations of carboplatin for forty-eight hours. Data represent viable cells expressed as the percentage of single cells, normalized to the media only control for each stimulation condition. Data relate to a single experiment. IC_{50} values: M0=201.7μM, M1=93.5μM and M2=203.3μM.

I then assessed a range of phenotype markers in viable macrophages after carboplatin treatment. The surface expression of CD206, CD163 and PDL1 on M2-polarised macrophages decreased with increasing concentrations of carboplatin compared to untreated cells (Figure 9.3). HLA-DR surface expression also decreased, although only at higher carboplatin concentrations than those that caused changes in other markers (Figure 9.3). These data suggest a change in macrophage phenotype from an alternatively to a classically activated phenotype by carboplatin treatment. Furthermore, these data recapitulate the findings in mouse and human HGSOC tumours where carboplatin decreased both CD206 and CD163 on TAMs.

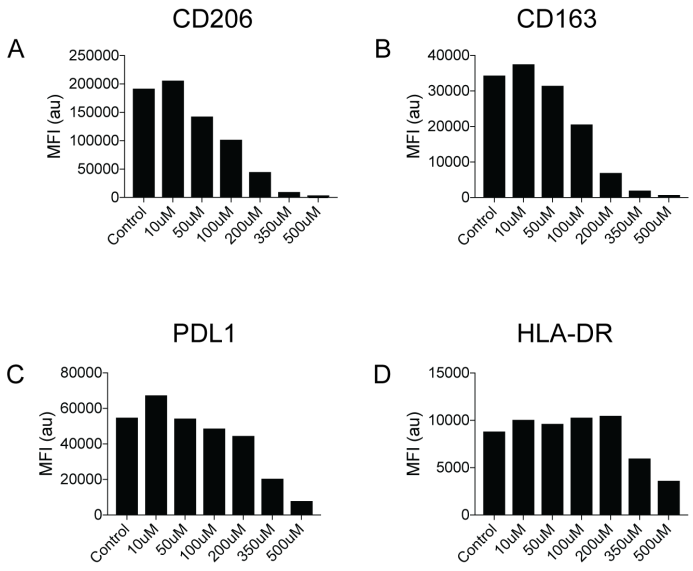

Figure 9.3 Assessing the effects of carboplatin chemotherapy on macrophage phenotype *in vitro*. Human $CD14^+$ monocytes derived from leucocyte cones were differentiated in media containing h-MCSF for seven days prior to being polarised to an M2 phenotype with IL-4/IL-10. Cells were cultured in media containing varying concentrations of carboplatin for forty-eight hours. Flow cytometry was performed to assess expression of cell surface markers. Data represent MFI of **A** CD206, **B** CD163 and **C** PDL1 and **D** HLA-DR in viable macrophages. Data relate to a single experiment.

In summary, these preliminary data show a direct effect of carboplatin on macrophages in culture, independent of the presence of malignant cells and their responses to carboplatin treatment. Carboplatin seems to kill macrophages at concentrations similar to the IC_{50} of carboplatin on human HGSOC cell lines *in vitro*. This experiment was repeated using macrophages polarised with conditioned media from human HGSOC cell lines rather than using IL-4/IL-10 as shown above. This experiment (data not shown) supported the data presented here, however, further replicates of these experiments are needed and will be undertaken in planned future work.

9.4 Assessment of cell death markers in human HGSOC

These data, coupled with my findings of increased non-viable TAM following chemotherapy in both mouse and human tumours (Figure 4.7, Figure 6.35), led me to look for evidence of TAM death in human HGSOC sections. I performed dual-colour IHC for CD68 and Pax-8 on human HGSOC biopsies and in consecutive sections I stained for cleaved caspase-3 as a marker of apoptosis. Interestingly, there was clear overlap of the cleaved caspase-3 and CD68 staining patterns. The areas of most obvious overlap were within post-chemotherapy 'macrophage lakes' described in Chapter 3 (Figure 9.4).

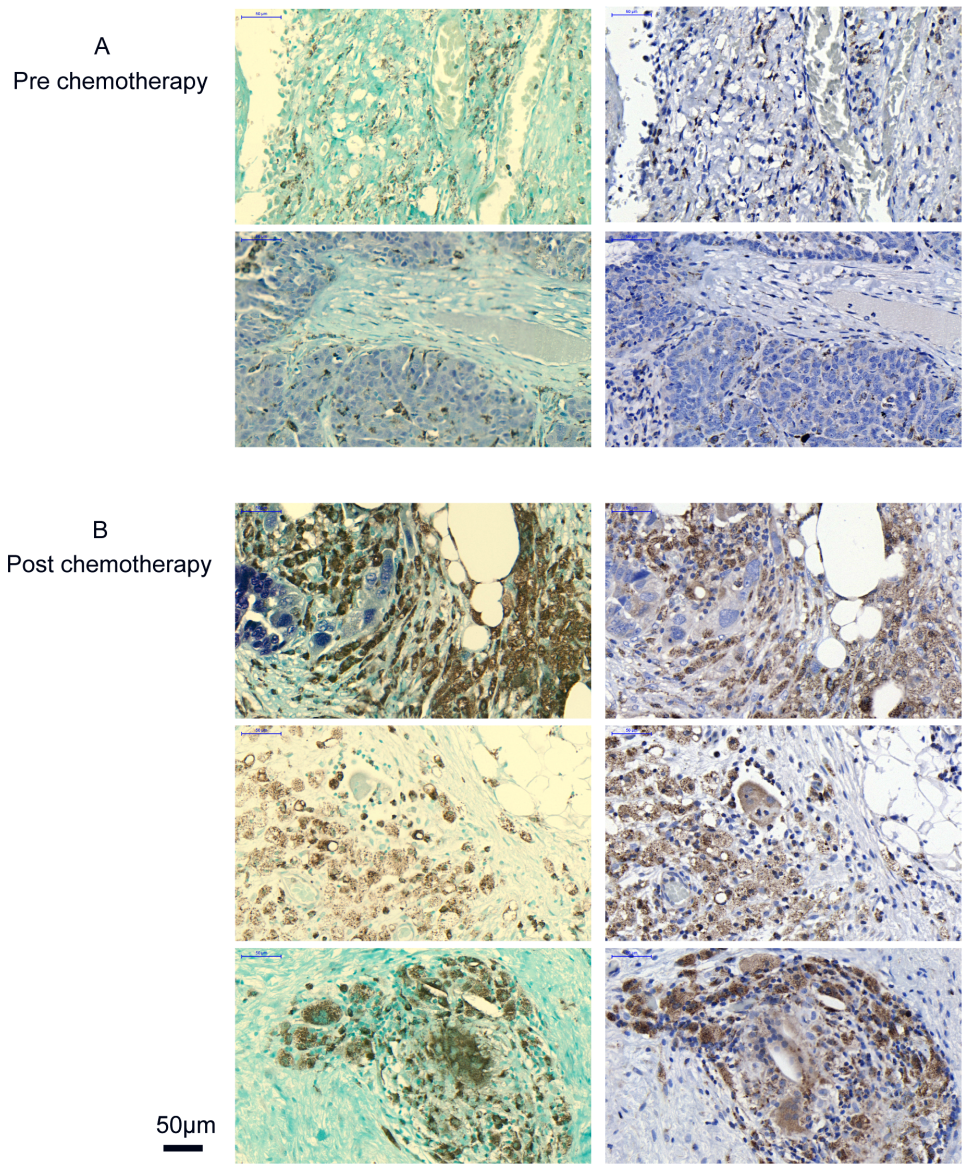

Figure 9.4 CD68, Pax-8 and cleaved caspase-3 evaluated in HGSOC omental metastases pre and post-chemotherapy. Representative staining of four HGSOC omental biopsies **A** pre chemotherapy and **B** post-chemotherapy. For each sample consecutive sections have been stained. *Left column:* CD68 (brown), Pax-8 (purple) green counterstaining. *Right column:* Cleaved caspase-3 (brown), blue counterstaining. Scale bar: 50µm.

Despite the fact that cleaved caspase-3 is frequently regarded as a marker of apoptosis, assessment of cell and nuclear morphology suggested that the cleaved caspase-3^{+} cells were not apoptotic. Also, the distribution of the staining would be highly unusual for apoptosis which usually shows positivity within individual cells rather than in large clusters of cells as seen in Figure 9.4. To further explore this finding, I performed a TUNEL (terminal deoxynucleotidyl transferase dUTP nick end labelling) assay on sections containing cleaved caspase-3^{+} macrophage lakes. This technique recognises fragmented DNA within the nucleus, a classical feature of apoptosis. In keeping with the morphological appearances of these cells, they did not appear to be TUNEL positive suggesting that they were not undergoing apoptosis (Figure 9.5).

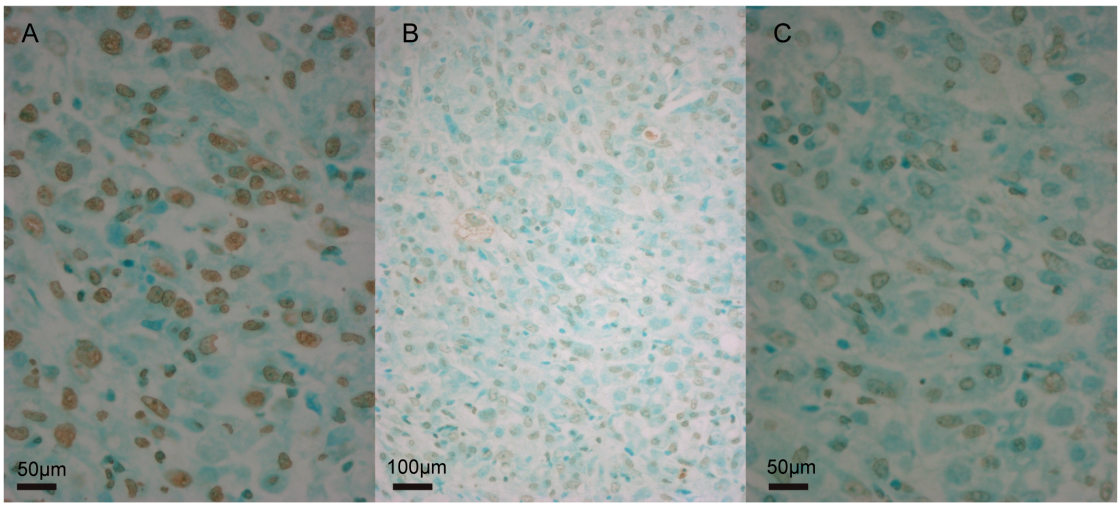

Figure 9.5 TUNEL staining within 'macrophage lakes' post-chemotherapy. Representative example of staining result. **A** positive control, tissue incubated with DNAase for 20mins prior to TUNEL staining. **B** Post-chemotherapy HGSOC biopsy showing area within a 'macrophage lake' shown at x20 magnification. **C** as **B** x40. Scale bar: 100µm, 50µm.

The data presented so far show that carboplatin can kill TAM and that post-NACT TAM express high levels of cleaved of caspase-3 compared to untreated tumours. In Chapter 4 I showed that the top upregulated pathways in post-NACT human TAM were 'inflammasome' and 'IL1β signalling', hence I hypothesised that TAM may be undergoing inflammatory forms of cell death such as pyroptosis in tumours.

It has recently been established that caspase-3 cleavage can activate pyroptosis by the cleavage of gasdermin E[327]. However, canonical activation of pyroptosis is via inflammasome assembly, resulting in caspase-1 mediated cleavage of gasdermin D. To test if there was an activation of the inflammasome in macrophages as the result of carboplatin stimulation, I performed a proximity ligation assay (PLA)[328] to test for the interaction of NLRP3 (NOD-, LRR- and pyrin domain-containing 3) and ASC (apoptosis-associated speck-like protein containing a CARD) in macrophages treated with 250µM and 500µM carboplatin (Figure 9.6 and Figure 9.7). There was a significant increase in the number of PLA signals/cell in macrophages treated with 250µM and 500µM carboplatin compared to untreated cells (Figure 9.7). These data show that carboplatin treatment results in formation of the NLRP3 inflammasome complex and support the pathway analysis of the TAM RNA-sequencing data as described above.

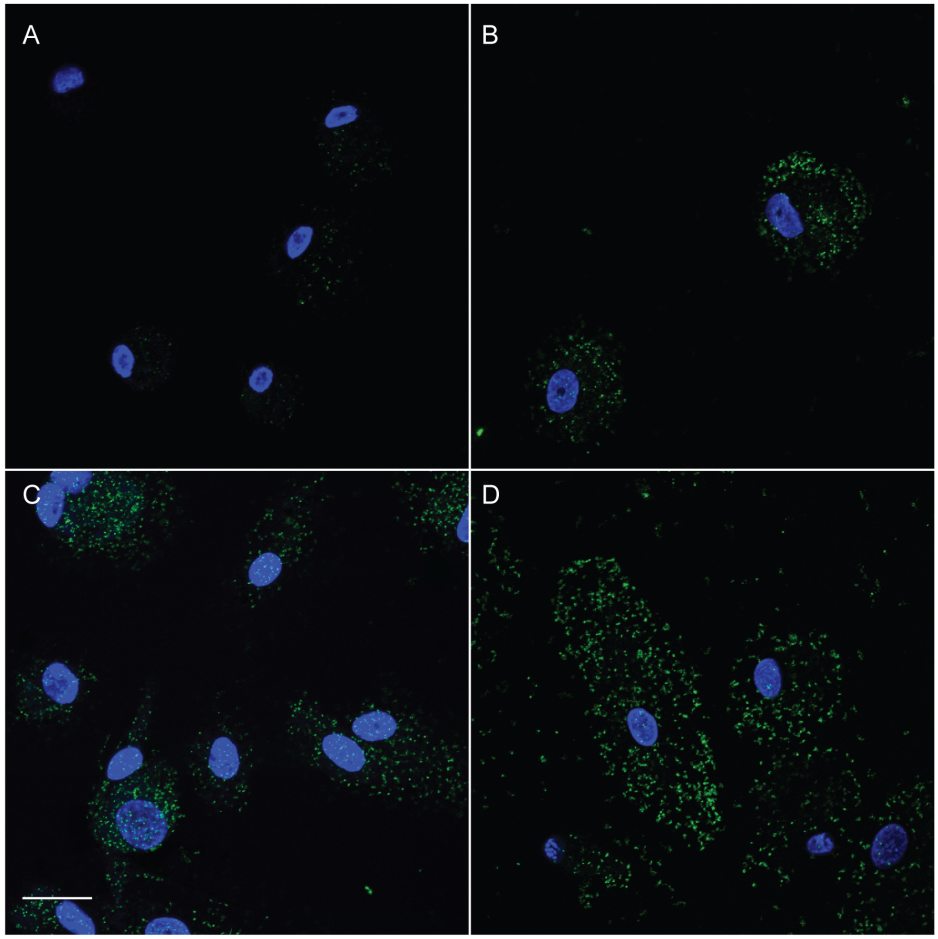

Figure 9.6 PLA assay. Image shows representative examples of PLA assay performed on M2-differentiated macrophages. **A** media only control, **B** LPS/nigericin treated cells (positive control), **C** cells treated with carboplatin 250μM and **D** cell treated with carboplatin 500μM for twenty-four hours. Green specks indicate NLRP3 inflammasome complexes. Scale bar: 25μM.

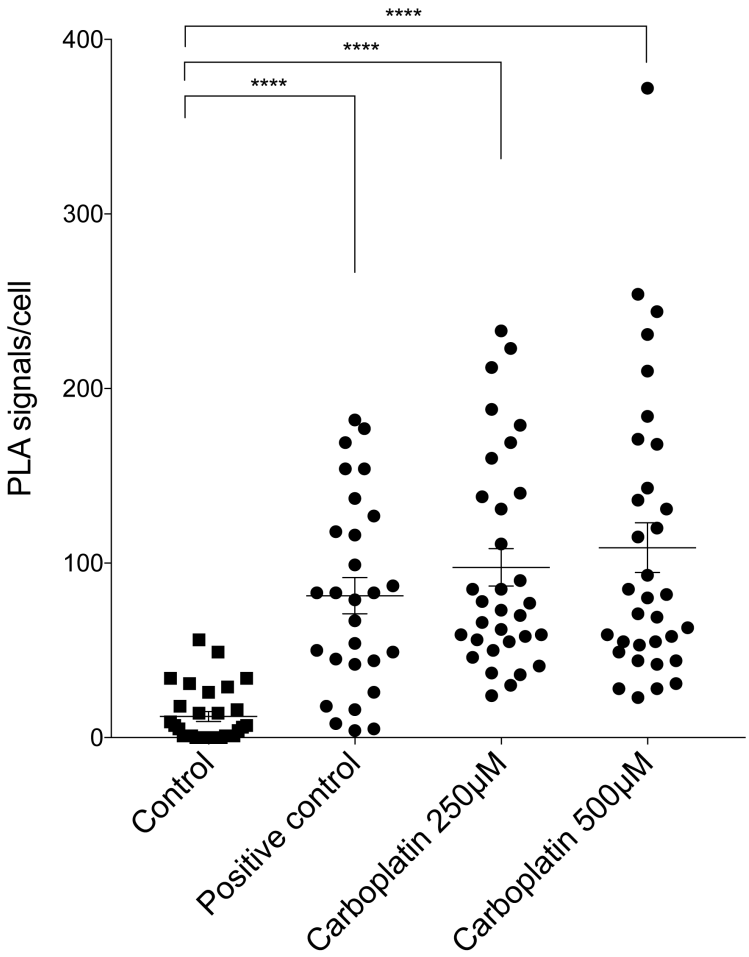

Figure 9.7 Quantification of PLA signals. Quantification of PLA signal per cell in untreated controls, positive control (LPS/nigericin treated cells), and carboplatin treated macrophages at concentrations of 250μM and 500μM applied for twenty-four hours. Data relate to a single experiment, PLA signals quantified in twenty-five – thirty-five cells per group, the mean for each group is shown. Error bars represent SEM. One-way ANOVA p-values are shown; ****<0.0001.

To assess inflammasome activation in human HGSOC omental metastases, I conducted immunofluorescent staining for CD68 and NLRP3 in biopsy samples obtained from untreated tumours and after NACT. I found increased expression of NLRP3 in CD68 positive cells (Figure 9.8) further supporting the concept of inflammasome activation post-chemotherapy.

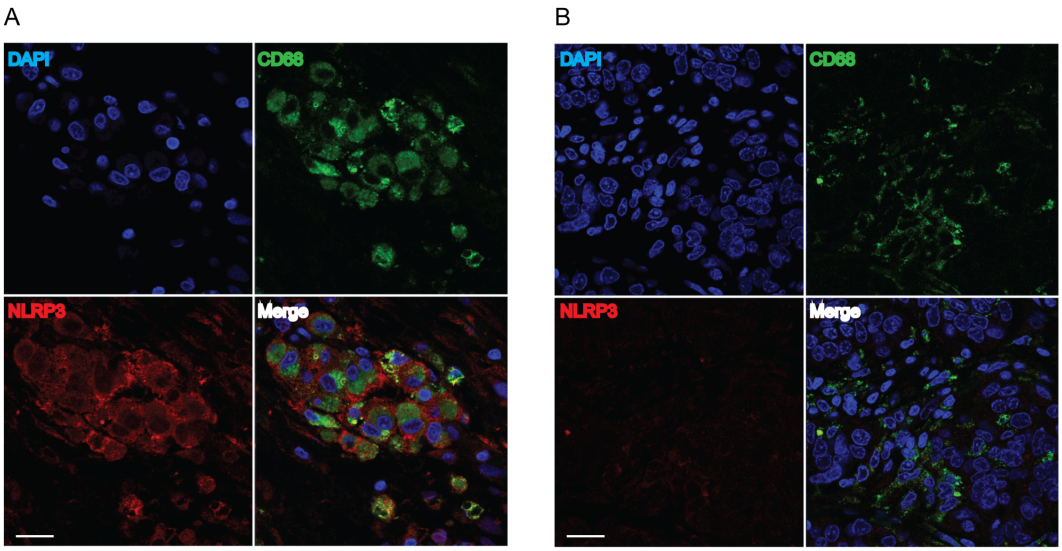

Figure 9.8 Assessment of NLRP3 expression in human HGSOC omental metastases. Immunofluorescent staining of HGSOC omental metastases from a patient **A** treated with interval cytoreductive surgery and **B** treated by primary cytoreductive surgery. *Top-left:* nuclei stained blue with DAPI, *top-right:* CD68 staining (green), *bottom-left:* NLRP3 staining (red) and *bottom-right:* merged view. Scale bar: 10um.

As I found increased cleaved caspase-3 in TAM after chemotherapy, I wished to further explore the possibility of caspase-3 cleavage after chemotherapy in macrophages. Given that cleaved caspase-3 is able to activate pyroptosis via the cleavage of DFNA5, I also measured cleavage of DFNA5 in the cells using western blot of macrophage lysates. Figure 9.9 shows carboplatin induced cleavage of caspase-3 and DFNA5 in M2 polarised macrophages *in vitro*. This provides evidence of non-canonical activation of pyroptosis in macrophages in response to carboplatin treatment.

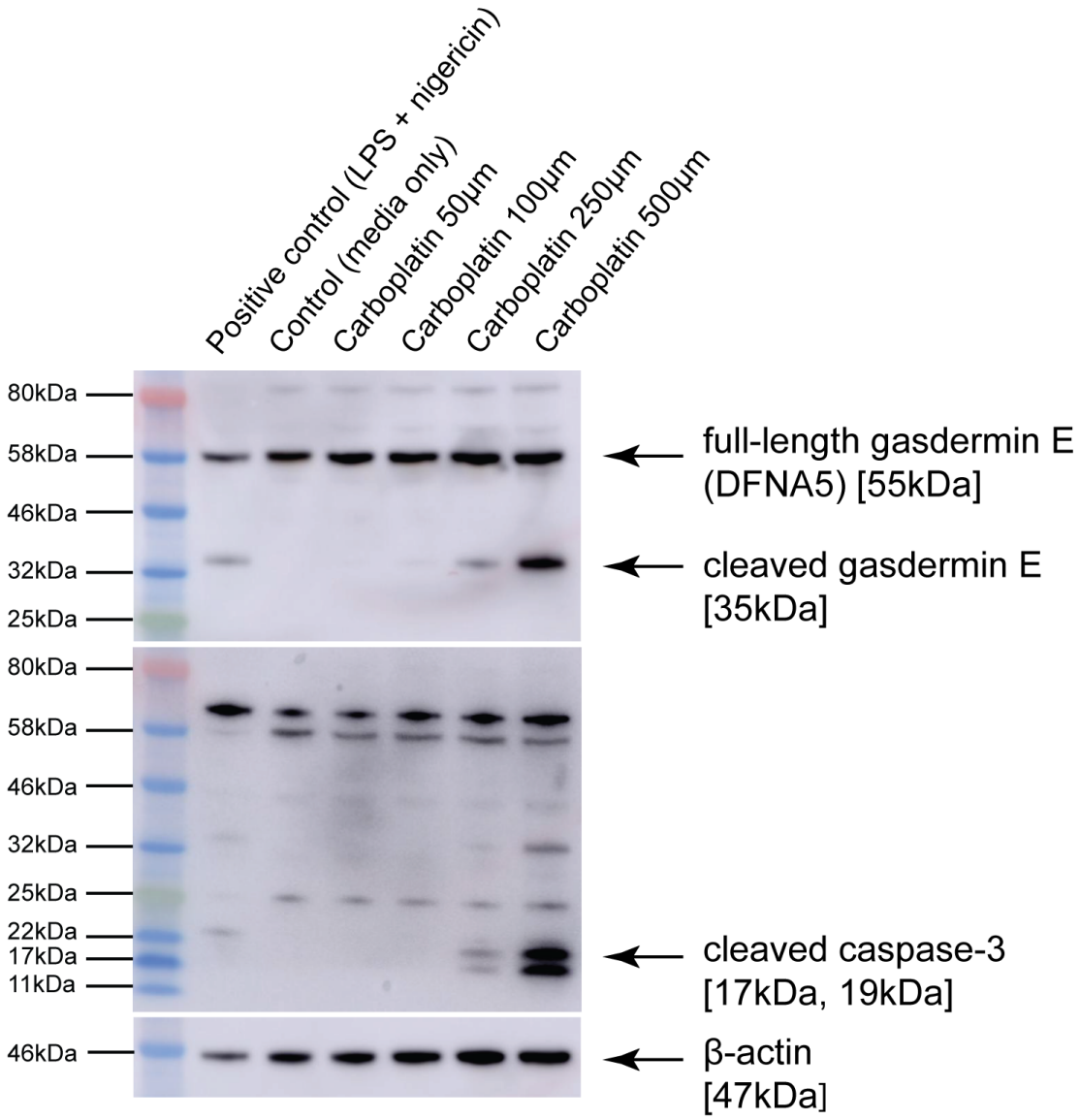

Figure 9.9 Cleavage of DFNA5 and caspase-3 with carboplatin treatment of M2 monocyte-derived macrophages. Monocytes were cultured for seven days with h-MCSF. The differentiated macrophages were stimulated with IL4/IL-10 additional three days. Cell were incubated with varying concentrations of carboplatin for twenty-four hours or LPS/nigericin as a positive control. Data relate to a single experiment.

As pyroptosis is associated with proinflammatory cytokine release, especially IL1β and IL-18, I measured cytokine secretion in macrophages cultured with and without carboplatin using an MSD V-Plex assay. As can be seen in Figure 9.10, carboplatin treatment of macrophages increased the secretion of multiple cytokines, including IL1β. Uncontrolled cytokine release adds further support for inflammatory cell death in TAMs following carboplatin treatment.

In conclusion, I have found evidence that carboplatin triggers the cleavage and activation of gasdermin E, leading to NLRP3 inflammasome assembly, pyroptosis and release of pro-inflammatory cytokines.

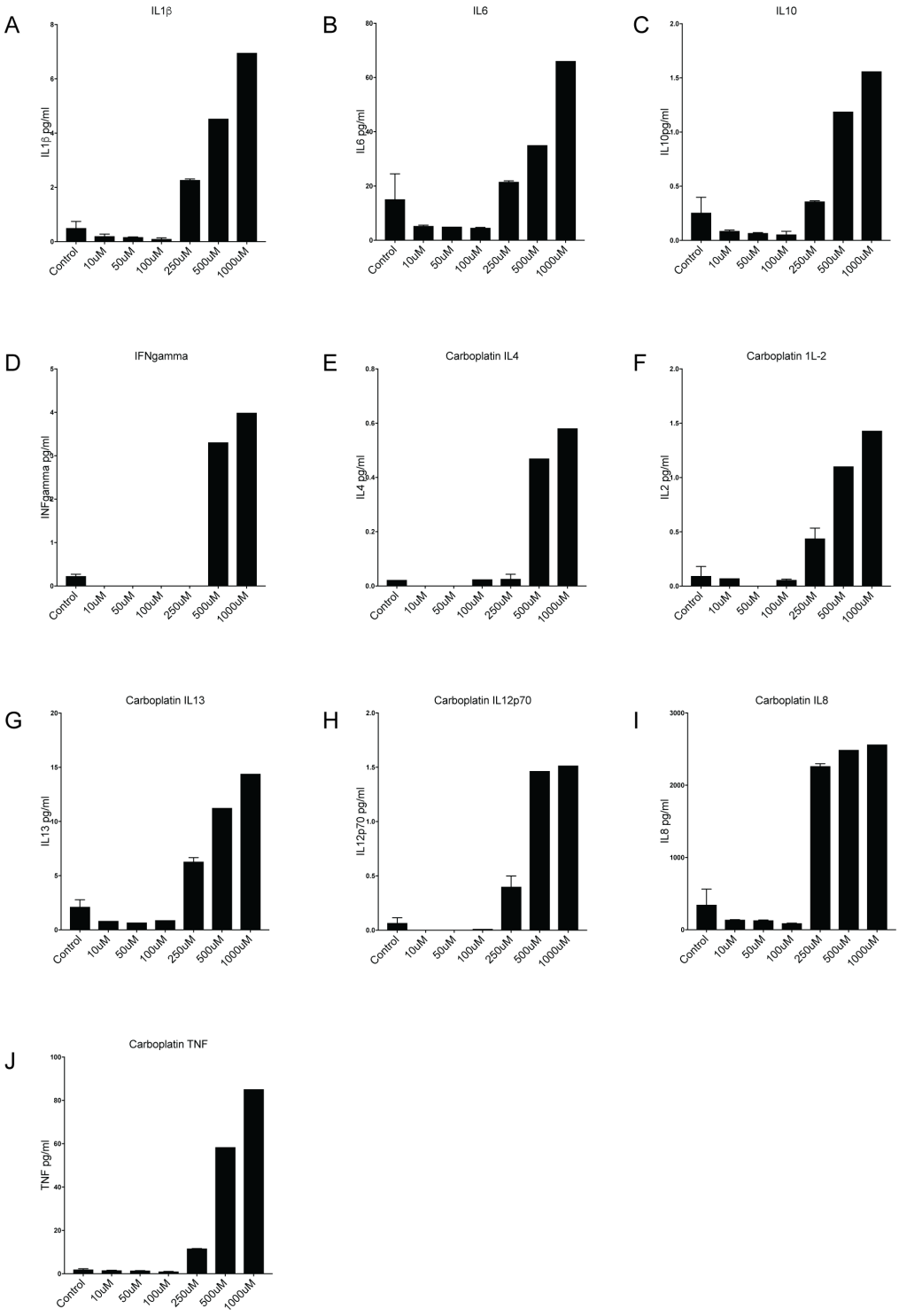

Figure 9.10 Macrophage cytokine secretion following carboplatin treatment. Monocytes were cultured for seven days with h-MCSF. The differentiated macrophages were stimulated with IL4/IL-10 additional three days. Cell were incubated with varying concentrations of carboplatin for twenty-four hours or left untreated. Ten cytokines (**A**-**J**) were measured by performing an MSD V-Plex assay. Data relate to a single experiment.

9.1 Discussion

I this chapter I report a preliminary series of experiments on macrophages differentiated from $CD14^+$ human monocytes. It is well described that these cells can be successfully polarised to M1/classically activated or M2/alternatively activated states *in vitro* with the cytokines IFN/LPS and IL-4/IL-10 respectively[120]. I assessed the effects of carboplatin treatment on cell death and macrophage phenotype *in vitro*. Interestingly, I found significant increases in macrophage cell death with carboplatin treatment. This effect was noted at concentrations of carboplatin approximating the IC_{50} concentration for three HGSOC cell lines. These findings substantiate my findings of increased cell death within the TAM population of both human and mouse HGSOC after carboplatin treatment. Furthermore, these data show a direct effect of carboplatin on macrophages.

As described previously, the sensitivity of cell lines to carboplatin reported in the literature varies widely. The IC_{50} values obtained for three human HGSOC cell lines are within the range described in the literature[309], although direct comparison is limited by different assays and culture conditions[329]. A source of variability in my data is that two different methods were used to assess cell viability in macrophages and in malignant cells. Macrophages were assessed via flow cytometry, and malignant cells were assessed by crystal violet staining of adherent cells. Therefore, this limits comparisons between the concentrations of carboplatin used to treat malignant cells and macrophages. This work will be extended and repeated (see Future plans, Chapter 10). However, I conclude that carboplatin does affect macrophages directly and can change cell phenotype and induce death at concentrations approximating those that produce responses in human HGSOC cell lines *in vitro*.

Given these findings, I wanted to measure cell death in human HGSOC biopsies. I found post-chemotherapy TAM to express high levels of cleaved caspase-3 (Figure 9.4). Cleaved caspase-3 is a common marker for apoptosis, yet the morphology of the cells, the nuclear features and the distribution of the staining were not typical of this mode of cell death. Furthermore, the TUNEL assay was negative in sections that contained high cleaved caspase-3 positivity (Figure 9.5) suggesting that cleaved $caspase\text{-}3^+$, $CD68^+$ cells were not apoptotic. There are no other markers that can be used to reliably assess cell death in fixed paraffin embedded tissue. Therefore, I was not able to conclusively determine if there was an increase in TAM cell death in tissue sections. However, cleaved caspase-3 activates pyroptosis, via cleavage of gasdermin E. This fitted well with the pathways analysis of human TAM post-NACT showing inflammasome activation.

To explore the possibility that carboplatin can induce inflammasome activation in macrophages, I performed the PLA assay for the NLRP3/ASC complex in cultured M2/alternatively-differetiated macrophages. This showed NLRP3 inflammasome assembly in carboplatin treated macrophages. However, only two concentrations of carboplatin were used (250μM and 500μM). I sought to confirm these *in vitro* findings in human tissue samples by co-staining tissues for NLP3 and CD68. Qualitative assessment of this staining suggested an upregulation of NLRP3 expression following chemotherapy. These data support the RNA-sequencing data and suggest inflammasome activation in macrophage following carboplatin treatment.

To explore a role for cleaved caspase-3 in activating pyroptosis, I measured cleavage of caspase-3 and gasdermin E in macrophage lysates by western blot. I found cleavage of caspase-3 and gasdermin E at carboplatin concentrations of 250-500μM. Furthermore, an MSD assay showed a strong increase in the secretion of multiple cytokines in carboplatin treated compared to untreated cells. This further supports carboplatin activated pyroptosis in macrophages.

The data presented in the chapter are preliminary but my interim conclusion is that some macrophages treated with carboplatin die as the result of activation of pyroptosis. This would explain macrophage depletion and phenotype changes described previously in this thesis.

Chapter 10
Summary of findings, discussion and future plans

HGSOC has a poor survival; this is due to the failure of chemotherapy, administered in combination with radical cytoreductive surgery, to control this disease. Frequently patients will respond well to chemotherapy and undergo surgical clearance of all macroscopic disease, yet still relapse within a short time frame. Survival has not been meaningfully impacted in the last twenty years; this highlights the need for new therapeutic strategies to combat HGSOC. Immunotherapies have shown success in treating a subset of cancers, in some cases with dramatic and durable responses. Extending the use of immunotherapies more widely is a current challenge facing this area of science. An in depth understanding of the tumour microenvironment of HGSOC and how this evolves under the effects of therapy is essential in the design of effective immunotherapies for this disease.

10.1 Summary of findings

Figure 10.1 is a graphical summary of the significant finding presented in this thesis. I will now discuss how the key points of my thesis relate to aspects of macrophage biology and immunotherapy design in HGSOC.

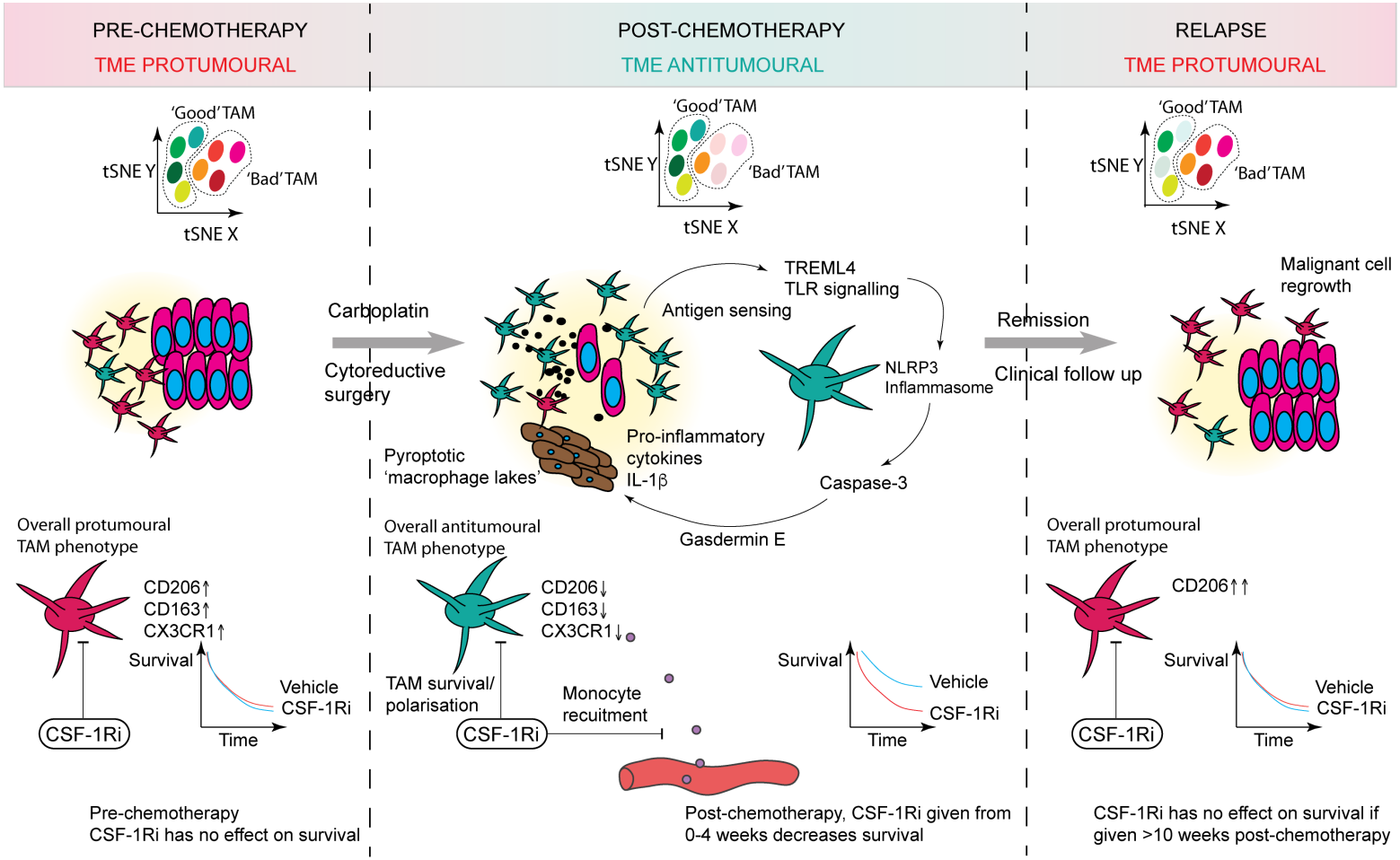

Figure 10.1 Graphical summary and current working hypothesis. Chemotherapy results in a transient restructuring of the TAM populations favouring an anti-tumoural TME. TAM depletion and increased antigen sensing may underlie the changes observed. 'Chronic' CSF-1Ri treatment from 0-4 weeks post-chemotherapy reduced overall survival, suggesting an overall tumour-limiting TAM phenotype soon after chemotherapy in contrast to CSF-1Ri before chemotherapy or at relapse.

10.2 The HGSOC TME post-chemotherapy

Historically, research into the mechanisms of action of chemotherapy has focused on the malignant cells. However, in addition to targeting malignant cells, chemotherapy frequently activates anti-tumour or pro-tumour immune pathways and networks within the wider TME[208]. Understanding the mechanisms underlying these differential effects is important and may identify strategies to boost chemotherapy response and prevent relapse.

I have focused on the myeloid compartment of the HGSOC TME and the data in this thesis show changes in myeloid cell density, location and phenotype in response to first-line chemotherapy. Overall my data suggest that chemotherapy, most notably carboplatin, drives anti-tumour functions in TAMs and increases DC density. There are multiple lines of evidence to support this within both human and murine tumours. By FC I found reductions in TAM alternatively activated surface marker expression and transcriptomic assessment of human TAM showed enrichment of the pathway terms 'inflammasome', 'IL1β signalling' and 'TLR signalling', suggesting inflammatory macrophage activation.

Targeting TAMs *in vivo* using CSF-1Ri in mouse HGSOC models resulted in partial TAM depletion. There was no effect on survival when CSF-1Ri was administered as a single agent during all stages of tumour development or to mice bearing established tumours. In contrast, CSF-1Ri treatment immediately after chemotherapy or four weeks after chemotherapy resulted in a significantly worse survival compared to vehicle-treated controls. Treating mice at a time point ten weeks following the end of chemotherapy did not result in changes to murine survival. These data suggest dynamic changes in TAM phenotype and function in HGSOC through primary chemotherapy and beyond.

These data fit with the findings of others showing that NACT can promote anti-tumour responses within other cell types within the TME of HGSOC, e.g. $CD3^+$ and $CD8^+$ T cell recruitment[330]. Furthermore, in haematological malignancies[203], PDAC[188] and CRC[181], chemotherapy alters TAM phenotype and in this context, high TAM densities post-chemotherapy predict improved patient outcome. For example, following chemotherapy Di Caro *et al.* show that high density of TAMs associates with extended survival, yet the converse was true before chemotherapy[188].

The roles of TAMs in HGSOC are not clear. This study contributes data from high-fidelity murine models to suggest that TAM depletion may not impact ovarian cancer growth and

progression (Figure 8.8). Moughon *et al.* depleted TAMs in the ID8 HGSOC model[248] using the CSF-1Ri GW2580. GW2580 treatment decreased alternatively activated macrophage density in ascites and reduced ascites volume secondary but survival differences were not reported[248]. Data assessing of the role of TAM in the context of human ovarian cancer is limited. Lan *et al.* showed that patients with tumours richly infiltrated with $CD163^+$ TAMs to have significantly reduced progression-free and overall survival[194]. TAM CD206/CD68 ratio predicts worse PFS[193], and, correspondingly, a high M1 (classically activated)/M2 (alternatively activated) ratio associated with improved survival[195]. Furthermore, Zhang *et al.* showed a high intra-tumoural, as opposed to stromal or whole tissue, M1 (classically activated)/M2 (alternatively activated) phenotypic ratio was associated with improved survival[196] suggesting localisation as well as phenotype to be clinically relevant. However, it should be noted that these studies are predominantly in mixed cohorts of ovarian cancer subtypes and the effects of chemotherapy on macrophage phenotype was not considered. Therefore, although these data are limited to small studies assessing TAM phenotype using a limited range of markers and in mixed cohorts of 'ovarian cancer' patients, they suggest that the TAM phenotype may be important in determining patient outcome.

TAMs do not function in isolation but in concert with a range of other cells within the TME. Although this has not been assessed in this work, understanding the networks that TAMs form with other cell types is likely to provide further insight into the effects of immunity on tumour growth and the response of HGSOC to treatment. Understanding changes to the TME under the influence of treatment is important as it may provide insights into the design of immunotherapeutic strategies for HGSOC.

10.3 TAM diversity and chemotherapy

I have explored the effects of chemotherapy on TAM by considering changes in TAM phenotype, in the bulk population (by RNA-seq and FC) and at single-cell resolution (via tNSE analysis of FC data). TAM exist as a spectrum of phenotypes in tumour microenvironments[331], tSNE analysis supports this view. I was able to define multiple TAM subpopulations using a relatively small number of macrophage activation markers. Gaining an appreciation of TAM subpopulations through resolving marker expression at single-cell level with tSNE provided a greater understanding of TAM heterogeneity that was not appreciated when comparing the changes of single markers within the bulk TAM population. For example, using this approach I observed that populations expressing markers at intermediate levels decreased, which correlates with my changes assessing the TAM population globally. Interestingly, tSNE shows that chemotherapy altered the relative proportions of TAM subpopulations in murine HGSOC. Tracking TAM

subpopulations though chemotherapy treatment showed, that although there was overall TAM depletion, the proportion of TAM subpopulations expressing markers representative of different functional states also changed.

These data, taken together with CSF-1Ri treatment of the post-chemotherapy TME, suggests that chemotherapy sculpts the relative proportions of anti-tumoural *vs* pro-tumoral TAM. Further single-cell approaches will greatly help in the understanding of TAM biology where the complexity of myeloid cell phenotypes will greatly exceed that seen simplistic *in vitro* systems. Single-cell RNA-sequencing (scRNA-seq) and CyTOF will be important in further defining TAM diversity in HGSOC. Application of tNSE to human FC data has been hampered by the configuration of the panel of antibodies used. However, use of these techniques represents a natural extension of this project. Furthermore, tSNE assessment of the myeloid populations depleted by CSF-1Ri will be undertaken in murine tumours.

10.4 How does chemotherapy affect TAMs?

The data presented in this thesis suggest TAMs can be affected by chemotherapy either directly or as a result of the effects on the malignant cells.

Given the *in vitro* and *in vivo* sensitivity of human and the murine HGSOC to carboplatin, the microenvironment that TAMs find themselves in will change rapidly and given the plasticity of this cell type it is not surprising that differences in TAM phenotype and functions are appreciated. Immunogenic cell death is well characterised in response to many cytotoxic drugs[332]. In this process malignant cells responding to chemotherapy emit signals either as the result of membrane lysis releasing intracellular molecules or by upregulation of surface proteins. These signals, known as DAMPs include ATP, HMGB1 and calreticulin[332]. I found the most significantly upregulated gene in macrophages after chemotherapy exposure was *TREML4*. This molecule is highly expressed on macrophages and dendritic cells and is able to bind dead and apoptotic cells[297]. Furthermore, treml4 can facilitate the presentation of tumour antigens to $CD4^+$ and $CD8^+$ T cells, resulting in enhanced antitumor immunity. This suggests that TAMs are responding to and interacting with dead/dying tumour cells in the HGSOC microenvironment i.e. that there is immunogenic cell death in the TME of HGSOC. Furthermore, the increase in DCs seen post-chemotherapy further supports the concept of chemotherapy mediating engagement of anti-tumour immunity in response to tumour antigens.

It is important to model the diversity of human HGSOC treatment response. In this thesis

I attempt to capture this diversity by studying three murine models that differ in their transcriptomic profiles (Maniati *et al.* manuscript submitted). These models also differ in their responses to carboplatin; 60577 was the most sensitive and HGS2 the least sensitive. Interestingly, TAM response to chemotherapy associated with the response of malignant cells to chemotherapy. 60577 showed significant TAM responses to carboplatin, both in phenotype and cell number, in contrast to HGS2, which showed non-significant changes. Furthermore, the TAM response to carboplatin compared to paclitaxel, to which murine tumours were not sensitive to as single-agent therapy, were very different. Alternatively activated marker expression was increased in paclitaxel treated tumours, compared to decreases following carboplatin treatment. Although more data are needed, these observations point to TAM response being linked to malignant cell response.

In patients with HGSOC 'good' responses to chemotherapy are associated with dense fibro-inflammatory infiltrates in combination with malignant cell destruction[280]. I show that macrophages 'lakes' form in response to chemotherapy, the association of these with nests of residual malignant cells suggests a response to dead/dying malignant cells. Further support for chemotherapy response determining HGSOC TME immune activation comes from findings in our lab where tumours that responded well (CRS3) compared to those that did not (CRS2) were significantly enriched a Th1 T cell signiture[113].

Using scRNA-seq and CyTOF approaches, Gubin *et al.* show the evolution of the TME of murine T3 sarcoma tumours in response to successful immune-checkpoint therapy[331]. They demonstrate significant TME restructuring, with depletion of CX3CR1^{+}TAM subpopulations and increases in subpopulations characterised by iNOS expression, a marker of classical macrophage activation[331]. These changes were associated with reduction of Treg and increase in effector T cell responses[331]. These changes reflect changes I have documented in the HGSOC TME in response to chemotherapy. This could suggest of the tantalising concept of a common response of the TME driven by a good response in malignant cells, irrespective of treatment modality.

I also provided data to suggest a direct mechanism of action of carboplatin on macrophages. I conducted studies on human macrophages in isolation from other cell types, to assess for any direct effects of chemotherapy. Surprisingly, I found evidence that carboplatin is able to directly target macrophages and resulted in cell death and phenotype changes in the absence of tumour cells. The concentration and time of exposure are important variables to consider in the generalisability of these results to *in*

vivo conditions. However, these initial studies are supported by work showing that trabectedin, which is also a drug that binds DNA (analogous to carboplatin) resulted in death of monocytes via caspase-8 dependant apoptosis[212]. Clearly both direct and indirect mechanisms could be operational in the TME, and the importance of each mechanism may differ in different contexts.

10.5 Targeting TAM in the context of chemotherapy in HGSOC

Despite chemotherapy engaging antitumoral immunity and frequently having dramatic effects of the malignant cells, chemotherapy rarely cures HGSOC. This suggests a partial and or transient immune activation and that combining chemotherapy with approaches to extend antitumor immunity long term could be valuable.

My experiments in murine models suggest that depleting TAM after chemotherapy is not a useful strategy in HGSOC and furthermore, following chemotherapy may actually be harmful. This would suggest that strategies to promote the positive effects of chemotherapy long term in the TME could be of benefit in the tumour and others. There are multiple approaches that have shown success in activating macrophages to anti-tumoural phenotypes in mice. These include the use of TLR agonists, CD40 agonists, PI3Kγ inhibitors[138]. Future work is proposed to assess the effects of TAM activating agents as a therapeutic approach in the treatment of HGSOC.

10.6 Overall summary

Chemotherapy promotes an anti-tumour TAM phenotype distinct from M1 (classically activated)-M2 (alternatively activated)-axis changes. TAM depletion with CSF-1Ri is not a beneficial strategy in this disease. Re-programming of TAM before and/or during chemotherapy, or intervening following chemotherapy to maintain a positive TAM phenotype, may represent more successful ways to harness the potential of TAM-based immunotherapy in HGSOC.

10.7 Future work

10.7.1 Limitations of current work

Chapters 3-5

The small number of human samples that were obtained during the course of the project has limited the analyses. Transcriptomic data were obtained only for bulk TAM populations; sc-RNA would have provided a powerful tool to extend the data presented.

The human matched post-NACT samples were contained in TMAs. Due to small core size these may have not accurately captured the stromal response. I did not have access to larger HGSOC sections matched pre and post-NACT, which would have allowed for more comprehensive assessment of both the malignant cell areas and the stromal response. When assessing the effects of TAM density on survival the small sample number is especially limiting. In addition, it has not been possible to perform multivariate analysis to control for other possible confounding variables.

Within the transcriptomic data I have not been able to validate the RNA findings at protein level. There are a range of molecules of interest that should be validated at protein level by IHC or by RNA scope analysis.

Chapters 6-8

The murine models recapitulate many of the features of human HGSOC; however, there were differences. The stromal areas of the tumours did not appear to be as well developed in mice compared the appearance in human samples. Given that I see differences in the appearance of stromal macrophages in human samples pre and post-NACT this is a potential limitation.

It has not been possible to characterise the TAM response of all models to both carboplatin and paclitaxel. HGS2 has not been characterised in response to paclitaxel and the response of the 30200 model to carboplatin as a single-agent has not been

assessed, although experiments are underway. Furthermore, it has not been possible to fully characterise the responses of the TME to chronic CSF-1Ri treatment in the relapse model, although this will be undertaken (see below).

In this study I have not been able to explore the possible mechanisms by which TAM may become anti-tumoral post-chemotherapy. For example, it could be envisaged that TAM be able to directly phagocytose and kill tumour cells following chemotherapy exposure. *In vitro* experiments will be conducted to assess the effects of chemotherapy on TAM-mediated tumour cell killing.

Chapter 9

The data presented in this chapter are preliminary and will need to be repeated and extended. Although the data produced so far suggest possible activation of the inflammasome and cleavage of gasdermin E these were only seen at concentrations of carboplatin of 250μM applied to cells for twenty-four hours. This is a high concentration of the drug and lower concentrations will need to be assessed.

Furthermore, I have not performed any experiments to assess the effects of carboplatin on macrophages in the presence of malignant cells. Co-culture experiments with human HGSOC cell lines and or in 3-D *in vitro* models are needed to further extend these data.

To address some of the shortcomings described above and to extend the work presented in this thesis, I propose the following experiments:

- tSNE on human samples pre and post-NACT
- scRNA-seq on human myeloid cells from HGSOC (this will be undertaken in the lab as a distinct project)
- Further quantification and validation of RNA-seq data by IHC
- Further analysis of murine tumour immune population pre and post-chemotherapy by IHC
- Analysis of murine tumour immune populations by IHC following CSF-1Ri treatment both as a single-agent and when administered after chemotherapy
- Extend relapse experiments into 30200 / HGS2 models
- Assess the effects of carboplatin on macrophages in 2D/3D co-culture systems with malignant cells
- Look for evidence of inflammasome assembly using PLA assay in human HGSOC sections
- Look for further evidence of pyroptosis in human and mouse tumours pre and

post NACT/carboplatin

- *In vivo* experiments to test the effects of therapeutics that promote anti-tumour macrophage activities following carboplatin treatment
- *In vitro* experiments to assess the effects of chemotherapy on macrophage effector function, including tumour cell killing assays

References

1. Torre, L. A., Bray, F., Siegel, R. L. & Ferlay, J. Global Cancer Statistics , 2012. **65,** 87–108 (2015).
2. Jayson, G. C., Kohn, E. C., Kitchener, H. C., Ledermann, J. A. & Manchester, G. J. Ovarian cancer. *Lancet* **384,** 1376–1388 (2014).
3. Office for National Statistics. Survival rates in England, patients diagnosed 2011-2015 followed up to 2016. 2016. www.statistics.gov.uk/statbase/product.asp?vlnk=14007.
4. CRUK Ovarian Cancer statistics.
5. Redman, C., Duffy, S., Bromham, N. & Francis, K. Recognition and initial management of ovarian cancer : summary of NICE guidance. 1–4 (2011). doi:10.1136/bmj.d2073
6. Kurman, R. J. & Shih, I. M. Molecular pathogenesis and extraovarian origin of epithelial ovarian cancer - Shifting the paradigm. *Hum. Pathol.* **42,** 918–931 (2011).
7. Bowtell, D. D. L. The genesis and evolution of high-grade serous ovarian cancer. *Nat. Publ. Gr.* **10,** 803–808 (2010).
8. Zorn, K. K. Gene Expression Profiles of Serous, Endometrioid, and Clear Cell Subtypes of Ovarian and Endometrial Cancer. *Clin. Cancer Res.* **11,** 6422–6430 (2005).
9. Tothill, R. W. *et al.* Novel molecular subtypes of serous and endometrioid ovarian cancer linked to clinical outcome. *Clin. Cancer Res.* **14,** 5198–5208 (2008).
10. Schwartz, D. R. *et al.* Gene expression in ovarian cancer reflects both morphology and biological behavior, distinguishing clear cell from other poor-prognosis ovarian carcinomas. *Cancer Res.* **62,** 4722–9 (2002).
11. Auersperg, N. The origin of ovarian cancers--hypotheses and controversies. *Front. Biosci. (Schol. Ed).* **5,** 709–19 (2013).
12. Kurman, R. J. Origin and molecular pathogenesis of ovarian high-grade serous carcinoma. *Ann. Oncol.* **24,** x16–x21 (2013).
13. Lee, Y. *et al.* A candidate precursor to serous carcinoma that originates in the distal fallopian tube. *J. Pathol.* **211,** 26–35 (2007).
14. Kuhn, E. *et al.* TP53 mutations in serous tubal intraepithelial carcinoma and concurrent pelvic high-grade serous carcinoma-evidence supporting the clonal relationship of the two lesions. *J. Pathol.* **226,** 421–426 (2012).
15. Li, H.-X. *et al.* Advances in serous tubal intraepithelial carcinoma: correlation with high grade serous carcinoma and ovarian carcinogenesis. *Int. J. Clin. Exp. Pathol.* **7,** 848–57 (2014).

16. Callahan, M. J. *et al.* Primary Fallopian Tube Malignancies in BRCA -Positive Women Undergoing Surgery for Ovarian Cancer Risk Reduction. *J. Clin. Oncol.* **25,** 3985–3990 (2007).
17. Kindelberger, D. W. *et al.* Intraepithelial Carcinoma of the Fimbria and Pelvic Serous Carcinoma: Evidence for a Causal Relationship. *Am. J. Surg. Pathol.* **31,** 161–169 (2007).
18. Marquez, R. T. Patterns of Gene Expression in Different Histotypes of Epithelial Ovarian Cancer Correlate with Those in Normal Fallopian Tube, Endometrium, and Colon. *Clin. Cancer Res.* **11,** 6116–6126 (2005).
19. Karnezis, A. N., Cho, K. R., Gilks, C. B., Pearce, C. L. & Huntsman, D. G. The disparate origins of ovarian cancers: pathogenesis and prevention strategies. *Nat. Rev. Cancer* **17,** 65–74 (2017).
20. Bell, D. *et al.* Integrated genomic analyses of ovarian carcinoma. *Nature* **474,** 609–615 (2011).
21. Venkitaraman, A. R. Linking the Cellular Functions of BRCA Genes to Cancer Pathogenesis and Treatment. *Annu. Rev. Pathol. Mech. Dis.* **4,** 461–487 (2009).
22. Loveday, C. *et al.* Germline RAD51C mutations confer susceptibility to ovarian cancer. *Nat. Genet.* **44,** 475–476 (2012).
23. Loveday, C. *et al.* Germline mutations in RAD51D confer susceptibility to ovarian cancer. *Nat. Genet.* **43,** 879–882 (2011).
24. Meindl, A. *et al.* Germline mutations in breast and ovarian cancer pedigrees establish RAD51C as a human cancer susceptibility gene. *Nat. Genet.* **42,** 410–414 (2010).
25. Rafnar, T. *et al.* Mutations in BRIP1 confer high risk of ovarian cancer. *Nature Genetics* **43,** 1104–1107 (2011).
26. Konstantinopoulos, P. A. *et al.* Gene expression profile of BRCAness that correlates with responsiveness to chemotherapy and with outcome in patients with epithelial ovarian cancer. *J. Clin. Oncol.* **28,** 3555–61 (2010).
27. Ledermann, J. *et al.* Olaparib Maintenance Therapy in Platinum-Sensitive Relapsed Ovarian Cancer. *N. Engl. J. Med.* **366,** 1382–1392 (2012).
28. Fong, P. C. *et al.* Inhibition of Poly(ADP-Ribose) Polymerase in Tumors from BRCA Mutation Carriers. *N. Engl. J. Med.* **361,** 123–134 (2009).
29. Bowtell, D. D. *et al.* Rethinking ovarian cancer II: reducing mortality from high-grade serous ovarian cancer. *Nat. Rev. Cancer* **15,** 668–679 (2015).
30. Norris, E. J. *et al.* Clonal lineage of high grade serous ovarian cancer in a patient with neurofibromatosis type 1. *Gynecol. Oncol. Reports* **23,** 41–44 (2018).
31. Martins, F. C. *et al.* Combined image and genomic analysis of high-grade serous ovarian cancer reveals PTEN loss as a common driver event and prognostic

classifier. *Genome Biol.* **15,** 526 (2014).

32. Leong, H. S. *et al.* Efficient molecular subtype classification of high-grade serous ovarian cancer. *J. Pathol.* **236,** 272–277 (2015).
33. Nelson, B. H. The impact of T-cell immunity on ovarian cancer outcomes. *Immunol. Rev.* **222,** 101–116 (2008).
34. Zhang, L. *et al.* Intratumoral T Cells, Recurrence, and Survival in Epithelial Ovarian Cancer. *N. Engl. J. Med.* **348,** 203–213 (2003).
35. Olaitan, A. *et al.* The surgical management of women with ovarian cancer in the south west of England. *Br. J. Cancer* **85,** 1824–1830 (2001).
36. Tingulstad, S., Skjeldestad, F. E. & Hagen, B. The Effect of Centralization of Primary Surgery on Survival in Ovarian Cancer Patients. **102,** 499–505 (2003).
37. Lheureux, S., Gourley, C., Vergote, I. & Oza, A. M. Epithelial ovarian cancer. *Lancet* **393,** 1240–1253 (2019).
38. Griffiths, C. T. Surgical resection of tumor bulk in the primary treatment of ovarian carcinoma. *Natl. Cancer Inst. Monogr.* **42,** 101–4 (1975).
39. Aletti, G. D., Dowdy, S. C., Podratz, K. C. & Cliby, W. A. Surgical treatment of diaphragm disease correlates with improved survival in optimally debulked advanced stage ovarian cancer. *Gynecol. Oncol.* **100,** 283–287 (2006).
40. Eisenkop, S. M., Friedman, R. L. & Wang, H. J. Complete cytoreductive surgery is feasible and maximizes survival in patients with advanced epithelial ovarian cancer: A prospective study. *Gynecol. Oncol.* **69,** 103–108 (1998).
41. Zivanovic, O. *et al.* The impact of bulky upper abdominal disease cephalad to the greater omentum on surgical outcome for stage IIIC epithelial ovarian, fallopian tube, and primary peritoneal cancer. *Gynecol. Oncol.* **108,** 287–292 (2008).
42. Chi, D. S. *et al.* What is the optimal goal of primary cytoreductive surgery for bulky stage IIIC epithelial ovarian carcinoma (EOC)? *Gynecol. Oncol.* **103,** 559–564 (2006).
43. Tseng, J. H. *et al.* Continuous improvement in primary Debulking surgery for advanced ovarian cancer: Do increased complete gross resection rates independently lead to increased progression-free and overall survival? *Gynecol. Oncol.* **151,** 24–31 (2018).
44. du Bois, A. *et al.* Role of surgical outcome as prognostic factor in advanced epithelial ovarian cancer: A combined exploratory analysis of 3 prospectively randomized phase 3 multicenter trials. *Cancer* **115,** 1234–1244 (2009).
45. Vergote, I. *et al.* Neoadjuvant Chemotherapy or Primary Surgery in Stage IIIC or IV Ovarian Cancer. *N. Engl. J. Med.* **363,** 943–953 (2010).
46. Chang, S.-J., Hodeib, M., Chang, J. & Bristow, R. E. Survival impact of complete cytoreduction to no gross residual disease for advanced-stage ovarian cancer: A

meta-analysis. *Gynecol. Oncol.* **130,** 493–498 (2013).

47. Harter, P. *et al.* A Randomized Trial of Lymphadenectomy in Patients with Advanced Ovarian Neoplasms. *N. Engl. J. Med.* **380,** 822–832 (2019).
48. Sato, S. & Itamochi, H. Neoadjuvant chemotherapy in advanced ovarian cancer: latest results and place in therapy. *Ther. Adv. Med. Oncol.* **6,** 293–304 (2014).
49. Kehoe, S. *et al.* Primary chemotherapy versus primary surgery for newly diagnosed advanced ovarian cancer (CHORUS): An open-label, randomised, controlled, non-inferiority trial. *Lancet* **386,** 249–257 (2015).
50. Vergote, I. B., Van Nieuwenhuysen, E. & Vanderstichele, A. How to Select Neoadjuvant Chemotherapy or Primary Debulking Surgery in Patients With Stage IIIC or IV Ovarian Carcinoma. *J. Clin. Oncol.* **34,** 3827–3828 (2016).
51. Katsumata, N. *et al.* Long-term results of dose-dense paclitaxel and carboplatin versus conventional paclitaxel and carboplatin for treatment of advanced epithelial ovarian, fallopian tube, or primary peritoneal cancer (JGOG 3016): a randomised, controlled, open-label trial. *Lancet Oncol.* **14,** 1020–1026 (2013).
52. Alberts, D. S. *et al.* Intraperitoneal Cisplatin plus Intravenous Cyclophosphamide versus Intravenous Cisplatin plus Intravenous Cyclophosphamide for Stage III Ovarian Cancer. *N. Engl. J. Med.* **335,** 1950–1955 (1996).
53. Markman, M. *et al.* Phase III Trial of Standard-Dose Intravenous Cisplatin Plus Paclitaxel Versus Moderately High-Dose Carboplatin Followed by Intravenous Paclitaxel and Intraperitoneal Cisplatin in Small-Volume Stage III Ovarian Carcinoma: An Intergroup Study of the Gynecol. *J. Clin. Oncol.* **19,** 1001–1007 (2001).
54. Tewari, D. *et al.* Long-Term Survival Advantage and Prognostic Factors Associated With Intraperitoneal Chemotherapy Treatment in Advanced Ovarian Cancer. *Obstet. Gynecol. Surv.* **70,** 505–506 (2015).
55. Walker, J. *et al.* A phase III trial of bevacizumab with IV versus IP chemotherapy for ovarian, fallopian tube, and peritoneal carcinoma: An NRG Oncology Study. *Gynecol. Oncol.* **141,** 208 (2016).
56. Lim, M. C. *et al.* Randomized trial of hyperthermic intraperitoneal chemotherapy (HIPEC) in women with primary advanced peritoneal, ovarian, and tubal cancer. *J. Clin. Oncol.* **35,** 5520–5520 (2017).
57. van Driel, W. J. *et al.* Hyperthermic Intraperitoneal Chemotherapy in Ovarian Cancer. *Obstet. Gynecol. Surv.* **73,** 280–281 (2018).
58. Dilruba, S. & Kalayda, G. V. Platinum-based drugs: past, present and future. *Cancer Chemother. Pharmacol.* **77,** 1103–1124 (2016).
59. Holzer, A. K., Manorek, G. H. & Howell, S. B. Contribution of the Major Copper Influx Transporter CTR1 to the Cellular Accumulation of Cisplatin, Carboplatin,

and Oxaliplatin. *Mol. Pharmacol.* **70,** 1390–1394 (2006).

60. Kalayda, G. V., Wagner, C. H., Buß, I., Reedijk, J. & Jaehde, U. Altered localisation of the copper efflux transporters ATP7A and ATP7B associated with cisplatin resistance in human ovarian carcinoma cells. *BMC Cancer* **8,** 175 (2008).
61. Nakayama, K. Prognostic Value of the Cu-Transporting ATPase in Ovarian Carcinoma Patients Receiving Cisplatin-Based Chemotherapy. *Clin. Cancer Res.* **10,** 2804–2811 (2004).
62. Dasari, S. & Bernard Tchounwou, P. Cisplatin in cancer therapy: Molecular mechanisms of action. *Eur. J. Pharmacol.* **740,** 364–378 (2014).
63. Wani, M. C., Taylor, H. L., Wall, M. E., Coggon, P. & McPhail, A. T. Plant antitumor agents. VI. Isolation and structure of taxol, a novel antileukemic and antitumor agent from Taxus brevifolia. *J. Am. Chem. Soc.* **93,** 2325–2327 (1971).
64. Yang, C.-P. & Horwitz, S. Taxol®: The First Microtubule Stabilizing Agent. *Int. J. Mol. Sci.* **18,** 1733 (2017).
65. Bekier, M. E., Fischbach, R., Lee, J. & Taylor, W. R. Length of mitotic arrest induced by microtubule-stabilizing drugs determines cell death after mitotic exit. *Mol. Cancer Ther.* **8,** 1646–1654 (2009).
66. Sandall, S. *et al.* A Bir1-Sli15 Complex Connects Centromeres to Microtubules and Is Required to Sense Kinetochore Tension. *Cell* **127,** 1179–1191 (2006).
67. Lens, S. M. A. & Medema, R. H. The Survivin/Aurora B Complex: Its Role in Coordinating Tension and Attachment. *Cell Cycle* **2,** 507–510 (2003).
68. Lisio, M.-A., Fu, L., Goyeneche, A., Gao, Z. & Telleria, C. High-Grade Serous Ovarian Cancer: Basic Sciences, Clinical and Therapeutic Standpoints. *Int. J. Mol. Sci.* **20,** 952 (2019).
69. Oza, A. M. *et al.* Standard chemotherapy with or without bevacizumab for women with newly diagnosed ovarian cancer (ICON7): overall survival results of a phase 3 randomised trial. *Lancet Oncol.* **16,** 928–936 (2015).
70. Burger, R. A. *et al.* Incorporation of Bevacizumab in the Primary Treatment of Ovarian Cancer. *N. Engl. J. Med.* **365,** 2473–2483 (2011).
71. Ledermann, J. A. *et al.* Cediranib in patients with relapsed platinum-sensitive ovarian cancer (ICON6): a randomised, double-blind, placebo-controlled phase 3 trial. *Lancet* **387,** 1066–1074 (2016).
72. Matulonis, U. A. *et al.* Cediranib, an Oral Inhibitor of Vascular Endothelial Growth Factor Receptor Kinases, Is an Active Drug in Recurrent Epithelial Ovarian, Fallopian Tube, and Peritoneal Cancer. *J. Clin. Oncol.* **27,** 5601–5606 (2009).
73. Hirte, H. *et al.* A phase 2 study of cediranib in recurrent or persistent ovarian, peritoneal or fallopian tube cancer: A trial of the Princess Margaret, Chicago and California Phase II Consortia. *Gynecol. Oncol.* **138,** 55–61 (2015).

74. Papa, A., Caruso, D., Strudel, M., Tomao, S. & Tomao, F. Update on Poly-ADP-ribose polymerase inhibition for ovarian cancer treatment. *J. Transl. Med.* **14,** 267 (2016).
75. Gelmon, K. A. *et al.* Olaparib in patients with recurrent high-grade serous or poorly differentiated ovarian carcinoma or triple-negative breast cancer: A phase 2, multicentre, open-label, non-randomised study. *Lancet Oncol.* **12,** 852–861 (2011).
76. Ledermann, J. *et al.* Olaparib Maintenance Therapy in Patients With Platinum-Sensitive Relapsed Serous Ovarian Cancer. *Obstet. Gynecol. Surv.* **69,** 594–596 (2014).
77. Pujade-Lauraine, E. *et al.* Olaparib tablets as maintenance therapy in patients with platinum-sensitive, relapsed ovarian cancer and a BRCA1/2 mutation (SOLO2/ENGOT-Ov21): a double-blind, randomised, placebo-controlled, phase 3 trial. *Lancet Oncol.* **18,** 1274–1284 (2017).
78. Mirza, M. R. *et al.* Niraparib Maintenance Therapy in Platinum-Sensitive, Recurrent Ovarian Cancer. *Obstet. Gynecol. Surv.* **72,** 91–92 (2017).
79. Coleman, R. L. *et al.* Rucaparib maintenance treatment for recurrent ovarian carcinoma after response to platinum therapy (ARIEL3): a randomised, double-blind, placebo-controlled, phase 3 trial. *Lancet* **390,** 1949–1961 (2017).
80. Moore, K. *et al.* Maintenance Olaparib in Patients With Newly Diagnosed Advanced Ovarian Cancer. *Obstet. Gynecol. Surv.* **74,** 86–87 (2019).
81. Odunsi, K. Immunotherapy in ovarian cancer. *Ann. Oncol.* **28,** viii1-viii7 (2017).
82. Gaillard, S. L., Secord, A. A. & Monk, B. The role of immune checkpoint inhibition in the treatment of ovarian cancer. *Gynecol. Oncol. Res. Pract.* **3,** 11 (2016).
83. Hamanishi, J. *et al.* Safety and Antitumor Activity of Anti–PD-1 Antibody, Nivolumab, in Patients With Platinum-Resistant Ovarian Cancer. *J. Clin. Oncol.* **33,** 4015–4022 (2015).
84. Disis, M. L. *et al.* Avelumab (MSB0010718C; anti-PD-L1) in patients with recurrent/refractory ovarian cancer from the JAVELIN Solid Tumor phase Ib trial: Safety and clinical activity. *J. Clin. Oncol.* **34,** 5533–5533 (2016).
85. Varga, A. *et al.* Antitumor activity and safety of pembrolizumab in patients (pts) with PD-L1 positive advanced ovarian cancer: Interim results from a phase Ib study. *J. Clin. Oncol.* **33,** 5510–5510 (2015).
86. Matanes, E. & Gotlieb, W. H. Immunotherapy of gynecological cancers. *Best Pract. Res. Clin. Obstet. Gynaecol.* (2019). doi:10.1016/j.bpobgyn.2019.03.005
87. Fujita, K. *et al.* Prolonged disease-free period in patients with advanced epithelial ovarian cancer after adoptive transfer of tumor-infiltrating lymphocytes. *Clin. Cancer Res.* **1,** 501–7 (1995).

88. Worzfeld, T. *et al.* The Unique Molecular and Cellular Microenvironment of Ovarian Cancer. *Front. Oncol.* **7,** 24 (2017).
89. Lloyd, K. L., Cree, I. A. & Savage, R. S. Prediction of resistance to chemotherapy in ovarian cancer: a systematic review. *BMC Cancer* **15,** 117 (2015).
90. Worzfeld, T. *et al.* The Unique Molecular and Cellular Microenvironment of Ovarian Cancer. *Front. Oncol.* **7,** 24 (2017).
91. Patch, A.-M. *et al.* Whole–genome characterization of chemoresistant ovarian cancer. *Nature* **521,** 489–494 (2015).
92. Kreuzinger, C. *et al.* A complex network of tumor microenvironment in human high grade serous ovarian cancer. *Clin. Cancer Res.* clincanres.1159.2017 (2017). doi:10.1158/1078-0432.CCR-17-1159
93. Bristow, R. E., Puri, I. & Chi, D. S. Cytoreductive surgery for recurrent ovarian cancer: A meta-analysis. *Gynecol. Oncol.* **112,** 265–274 (2009).
94. Harter, P. *et al.* Prospective validation study of a predictive score for operability of recurrent ovarian cancer: the Multicenter Intergroup Study DESKTOP II. A project of the AGO Kommission OVAR, AGO Study Group, NOGGO, AGO-Austria, and MITO. *Int. J. Gynecol. Cancer* **21,** 289–295 (2011).
95. Tian, W.-J. *et al.* A Risk Model for Secondary Cytoreductive Surgery in Recurrent Ovarian Cancer: An Evidence-Based Proposal for Patient Selection. *Ann. Surg. Oncol.* **19,** 597–604 (2012).
96. Cowan, R. A. *et al.* A comparative analysis of prediction models for complete gross resection in secondary cytoreductive surgery for ovarian cancer. *Gynecol. Oncol.* **145,** 230–235 (2017).
97. Hanahan, D. & Coussens, L. M. Accessories to the Crime: Functions of Cells Recruited to the Tumor Microenvironment. *Cancer Cell* **21,** 309–322 (2012).
98. Balkwill, F. R., Capasso, M. & Hagemann, T. The tumor microenvironment at a glance. *J. Cell Sci.* **125,** 5591–6 (2012).
99. Dunn, G. P., Old, L. J. & Schreiber, R. D. The Immunobiology of Cancer Immunosurveillance and Immunoediting. *Immunity* **21,** 137–148 (2004).
100. Balkwill, F., Charles, K. A. & Mantovani, A. Smoldering and polarized inflammation in the initiation and promotion of malignant disease. *Cancer Cell* **7,** 211–217 (2005).
101. Palucka, A. K. & Coussens, L. M. The Basis of Oncoimmunology. *Cell* **164,** 1233–1247 (2016).
102. Raspollini, M. R. *et al.* Tumour-infiltrating gamma/delta T-lymphocytes are correlated with a brief disease-free interval in advanced ovarian serous carcinoma. *Ann. Oncol.* **16,** 590–596 (2005).
103. Tomšová, M., Melichar, B., Sedláková, I. & Šteiner, I. Prognostic significance of

CD3+ tumor-infiltrating lymphocytes in ovarian carcinoma. *Gynecol. Oncol.* **108,** 415–420 (2008).

104. Woo, E. Y. *et al.* Regulatory CD4(+)CD25(+) T cells in tumors from patients with early-stage non-small cell lung cancer and late-stage ovarian cancer. *Cancer Res.* **61,** 4766–72 (2001).
105. Curiel, T. J. *et al.* Specific recruitment of regulatory T cells in ovarian carcinoma fosters immune privilege and predicts reduced survival. *Nat. Med.* **10,** 942–949 (2004).
106. Wolf, D. The Expression of the Regulatory T Cell-Specific Forkhead Box Transcription Factor FoxP3 Is Associated with Poor Prognosis in Ovarian Cancer. *Clin. Cancer Res.* **11,** 8326–8331 (2005).
107. Milne, K. *et al.* Systematic Analysis of Immune Infiltrates in High-Grade Serous Ovarian Cancer Reveals CD20, FoxP3 and TIA-1 as Positive Prognostic Factors. *PLoS One* **4,** e6412 (2009).
108. Leffers, N. *et al.* Prognostic significance of tumor-infiltrating T-lymphocytes in primary and metastatic lesions of advanced stage ovarian cancer. *Cancer Immunol. Immunother.* **58,** 449–459 (2009).
109. Sato, E. *et al.* Intraepithelial CD8+ tumor-infiltrating lymphocytes and a high CD8+/regulatory T cell ratio are associated with favorable prognosis in ovarian cancer. *Proc. Natl. Acad. Sci.* **102,** 18538–18543 (2005).
110. Hamanishi, J. *et al.* Programmed cell death 1 ligand 1 and tumor-infiltrating CD8+ T lymphocytes are prognostic factors of human ovarian cancer. *Proc. Natl. Acad. Sci.* **104,** 3360–3365 (2007).
111. Anderson, K. G., Stromnes, I. M. & Greenberg, P. D. Obstacles Posed by the Tumor Microenvironment to T cell Activity: A Case for Synergistic Therapies. *Cancer Cell* **31,** 311–325 (2017).
112. Phuc Dong, H. *et al.* NK-and B-Cell Infiltration Correlates With Worse Outcome in Metastatic Ovarian Carcinoma. *Am J Clin Pathol* **125,** 451–458 (2006).
113. Bo hm, S. *et al.* Neoadjuvant Chemotherapy Modulates the Immune Microenvironment in Metastases of Tubo-Ovarian High-Grade Serous Carcinoma. *Clin. Cancer Res.* **22,** 3025–3036 (2016).
114. Montfort, A. *et al.* A Strong B-cell Response Is Part of the Immune Landscape in Human High-Grade Serous Ovarian Metastases. *Clin. Cancer Res.* **23,** 250–262 (2017).
115. Pölcher, M. *et al.* Foxp3+ cell infiltration and granzyme B+/Foxp3+ cell ratio are associated with outcome in neoadjuvant chemotherapy-treated ovarian carcinoma. *Cancer Immunol. Immunother.* **59,** 909–919 (2010).
116. Peng, J. *et al.* Chemotherapy Induces Programmed Cell Death-Ligand 1

Overexpression via the Nuclear Factor- B to Foster an Immunosuppressive Tumor Microenvironment in Ovarian Cancer. *Cancer Res.* **75,** 5034–5045 (2015).

117. Wouters, M. C. A. *et al.* Treatment Regimen, Surgical Outcome, and T-cell Differentiation Influence Prognostic Benefit of Tumor-Infiltrating Lymphocytes in High-Grade Serous Ovarian Cancer. *Clin. Cancer Res.* **22,** 714–724 (2016).
118. Lo, C. S. *et al.* Neoadjuvant Chemotherapy of Ovarian Cancer Results in Three Patterns of Tumor-Infiltrating Lymphocyte Response with Distinct Implications for Immunotherapy. *Clin. Cancer Res.* **23,** 925–934 (2017).
119. Mantovani, A. & Allavena, P. The interaction of anticancer therapies with tumor-associated macrophages. *J. Exp. Med.* **212,** 435–445 (2015).
120. Murray, P. J. *et al.* Macrophage Activation and Polarization: Nomenclature and Experimental Guidelines. *Immunity* **41,** 14–20 (2014).
121. Wynn, T. A., Chawla, A. & Pollard, J. W. Macrophage biology in development, homeostasis and disease. *Nature* **496,** 445–455 (2013).
122. Zheng, X. *et al.* Redirecting tumor-associated macrophages to become tumoricidal effectors as a novel strategy for cancer therapy. *Oncotarget* **8,** 48436–48452 (2017).
123. Sica, A. & Mantovani, A. Macrophage plasticity and polarization: in vivo veritas. *J. Clin. Invest.* **122,** 787–795 (2012).
124. Mills, C. D., Kincaid, K., Alt, J. M., Heilman, M. J. & Hill, A. M. M-1/M-2 Macrophages and the Th1/Th2 Paradigm. *J. Immunol.* **164,** 6166–6173 (2000).
125. Pollard, J. W. Trophic macrophages in development and disease. *Nat. Rev. Immunol.* **9,** 259–270 (2009).
126. Hanahan, D. & Weinberg, R. A. Hallmarks of cancer: The next generation. *Cell* **144,** 646–674 (2011).
127. Wynn, T. A., Chawla, A. & Pollard, J. W. Macrophage biology in development, homeostasis and disease. *Nature* **496,** 445–55 (2013).
128. Noy, R. & Pollard, J. W. Tumor-Associated Macrophages: From Mechanisms to Therapy. *Immunity* **41,** 49–61 (2014).
129. Cassetta, L. & Pollard, J. W. Targeting macrophages: therapeutic approaches in cancer. *Nat. Rev. Drug Discov.* **17,** 887–904 (2018).
130. Mantovani, A., Biswas, S. K., Galdiero, M. R., Sica, A. & Locati, M. Macrophage plasticity and polarization in tissue repair and remodelling. *Journal of Pathology* **229,** 176–185 (2013).
131. van de Laar, L. *et al.* Yolk Sac Macrophages, Fetal Liver, and Adult Monocytes Can Colonize an Empty Niche and Develop into Functional Tissue-Resident Macrophages. *Immunity* **44,** 755–768 (2016).
132. Bajpai, G. *et al.* The human heart contains distinct macrophage subsets with

divergent origins and functions. *Nat. Med.* **24,** 1234–1245 (2018).

133. Cassetta, L. *et al.* Human Tumor-Associated Macrophage and Monocyte Transcriptional Landscapes Reveal Cancer-Specific Reprogramming, Biomarkers, and Therapeutic Targets. *Cancer Cell* **35,** 588–602.e10 (2019).
134. Zhu, Y. *et al.* Tissue-Resident Macrophages in Pancreatic Ductal Adenocarcinoma Originate from Embryonic Hematopoiesis and Promote Tumor Progression Article Tissue-Resident Macrophages in Pancreatic Ductal Adenocarcinoma Originate from Embryonic Hematopoiesis and Promote. *Immunity* **47,** 323–338.e6 (2017).
135. DeNardo, D. G. & Ruffell, B. Macrophages as regulators of tumour immunity and immunotherapy. *Nat. Rev. Immunol.* 1 (2019). doi:10.1038/s41577-019-0127-6
136. Loyher, P.-L. *et al.* Macrophages of distinct origins contribute to tumor development in the lung. *J. Exp. Med.* **215,** 2536–2553 (2018).
137. Bowman, R. L. *et al.* Macrophage Ontogeny Underlies Differences in Tumor-Specific Education in Brain Malignancies. *Cell Rep.* **17,** 2445–2459 (2016).
138. Mantovani, A., Marchesi, F., Malesci, A., Laghi, L. & Allavena, P. Tumour-associated macrophages as treatment targets in oncology. *Nat. Rev. Clin. Oncol.* **14,** 399–416 (2017).
139. Zhu, Y. *et al.* Tissue-Resident Macrophages in Pancreatic Ductal Adenocarcinoma Originate from Embryonic Hematopoiesis and Promote Tumor Progression. *Immunity* **47,** 323–338.e6 (2017).
140. Pathria, P., Louis, T. L. & Varner, J. A. Targeting Tumor-Associated Macrophages in Cancer. *Trends Immunol.* **40,** 310–327 (2019).
141. Stanley, E. R. & Chitu, V. CSF-1 receptor signaling in myeloid cells. *Cold Spring Harb. Perspect. Biol.* **6,** 1–21 (2014).
142. Qian, B.-Z. & Pollard, J. W. Macrophage Diversity Enhances Tumor Progression and Metastasis. *Cell* **141,** 39–51 (2010).
143. Smith, H. O. *et al.* The clinical significance of inflammatory cytokines in primary cell culture in endometrial carcinoma. *Mol. Oncol.* **7,** 41–54 (2013).
144. Lin, E. Y. *et al.* Macrophages Regulate the Angiogenic Switch in a Mouse Model of Breast Cancer. *Cancer Res.* **66,** 11238–11246 (2006).
145. Wyckoff, J. B. *et al.* Direct visualization of macrophage-assisted tumor cell intravasation in mammary tumors. *Cancer Res.* **67,** 2649–2656 (2007).
146. Schmid, M. C. *et al.* PI3-Kinase γ Promotes Rap1a-Mediated Activation of Myeloid Cell Integrin α4β1, Leading to Tumor Inflammation and Growth. *PLoS One* **8,** e60226 (2013).
147. Schmid, M. C. *et al.* Combined Blockade of Integrin- 4 1 Plus Cytokines SDF-1 or IL-1 Potently Inhibits Tumor Inflammation and Growth. *Cancer Res.* **71,** 6965–

6975 (2011).

148. Kaneda, M. M. *et al.* PI3Kγ is a molecular switch that controls immune suppression. *Nature* **539,** 437–442 (2016).
149. Kaneda, M. M. *et al.* Macrophage PI3K Drives Pancreatic Ductal Adenocarcinoma Progression. *Cancer Discov.* **6,** 870–885 (2016).
150. Gunderson, A. J. *et al.* Bruton Tyrosine Kinase-Dependent Immune Cell Cross-talk Drives Pancreas Cancer. *Cancer Discov.* **6,** 270–285 (2016).
151. Schmid, M. C. *et al.* Receptor Tyrosine Kinases and TLR/IL1Rs Unexpectedly Activate Myeloid Cell PI3Kγ, A Single Convergent Point Promoting Tumor Inflammation and Progression. *Cancer Cell* **19,** 715–727 (2011).
152. Campbell, M. J. *et al.* Proliferating macrophages associated with high grade, hormone receptor negative breast cancer and poor clinical outcome. *Breast Cancer Res. Treat.* **128,** 703–711 (2011).
153. Bottazzi, B. *et al.* A paracrine circuit in the regulation of the proliferation of macrophages infiltrating murine sarcomas. *J. Immunol.* **144,** 2409–12 (1990).
154. Franklin, R. A. *et al.* The cellular and molecular origin of tumor-associated macrophages. *Science (80-.).* **344,** 921–925 (2014).
155. Feng, X. *et al.* Loss of CX3CR1 increases accumulation of inflammatory monocytes and promotes gliomagenesis. *Oncotarget* **6,** 15077–94 (2015).
156. Ruffell, B. & Coussens, L. M. Perspective Macrophages and Therapeutic Resistance in Cancer. *Cancer Cell* **27,** 462–472 (2015).
157. Yeo, E.-J. *et al.* Myeloid WNT7b Mediates the Angiogenic Switch and Metastasis in Breast Cancer. *Cancer Res.* **74,** 2962–2973 (2014).
158. Lin, E. Y. *et al.* Vascular endothelial growth factor restores delayed tumor progression in tumors depleted of macrophages. *Mol. Oncol.* **1,** 288–302 (2007).
159. De Palma, M. *et al.* Tie2 identifies a hematopoietic lineage of proangiogenic monocytes required for tumor vessel formation and a mesenchymal population of pericyte progenitors. *Cancer Cell* **8,** 211–226 (2005).
160. Mazzieri, R. *et al.* Targeting the ANG2/TIE2 Axis Inhibits Tumor Growth and Metastasis by Impairing Angiogenesis and Disabling Rebounds of Proangiogenic Myeloid Cells. *Cancer Cell* **19,** 512–526 (2011).
161. Forget, M. A. *et al.* Macrophage Colony-Stimulating Factor Augments Tie2-Expressing Monocyte Differentiation, Angiogenic Function, and Recruitment in a Mouse Model of Breast Cancer. *PLoS One* **9,** e98623 (2014).
162. Wyckoff, J. *et al.* A Paracrine Loop between Tumor Cells and Macrophages Is Required for Tumor Cell Migration in Mammary Tumors. *Cancer Res.* **64,** 7022–7029 (2004).
163. Goswami, S. *et al.* Macrophages Promote the Invasion of Breast Carcinoma Cells

via a Colony-Stimulating Factor-1/Epidermal Growth Factor Paracrine Loop. *Cancer Res.* **65,** 5278–5283 (2005).

164. Sangaletti, S. *et al.* Macrophage-Derived SPARC Bridges Tumor Cell-Extracellular Matrix Interactions toward Metastasis. *Cancer Res.* **68,** 9050–9059 (2008).
165. Gocheva, V. *et al.* IL-4 induces cathepsin protease activity in tumor-associated macrophages to promote cancer growth and invasion. *Genes Dev.* **24,** 241–255 (2010).
166. Quail, D. F. & Joyce, J. A. Microenvironmental regulation of tumor progression and metastasis. *Nat. Med.* **19,** 1423–1437 (2013).
167. Bonde, A.-K., Tischler, V., Kumar, S., Soltermann, A. & Schwendener, R. A. Intratumoral macrophages contribute to epithelial-mesenchymal transition in solid tumors. *BMC Cancer* **12,** 35 (2012).
168. Rohan, T. E. *et al.* Tumor Microenvironment of Metastasis and Risk of Distant Metastasis of Breast Cancer. *JNCI J. Natl. Cancer Inst.* **106,** 1–11 (2014).
169. Coussens, L. M. & Pollard, J. W. Leukocytes in mammary development and cancer. *Cold Spring Harb. Perspect. Biol.* **3,** 1–22 (2011).
170. Movahedi, K. *et al.* Different tumor microenvironments contain functionally distinct subsets of macrophages derived from Ly6C(high) monocytes. *Cancer Res.* **70,** 5728–5739 (2010).
171. Ruffell, B. *et al.* Leukocyte composition of human breast cancer. *Proc. Natl. Acad. Sci.* **109,** 2796–2801 (2012).
172. Schlecker, E. *et al.* Tumor-Infiltrating Monocytic Myeloid-Derived Suppressor Cells Mediate CCR5-Dependent Recruitment of Regulatory T Cells Favoring Tumor Growth. *J. Immunol.* **189,** 5602–5611 (2012).
173. Adeegbe, D. O. & Nishikawa, H. Natural and Induced T Regulatory Cells in Cancer. *Front. Immunol.* **4,** 1–14 (2013).
174. Savage, N. D. L. *et al.* Human Anti-Inflammatory Macrophages Induce Foxp3+GITR+CD25+ Regulatory T Cells, Which Suppress via Membrane-Bound TGF -1. *J. Immunol.* **181,** 2220–2226 (2008).
175. Denning, T. L., Wang, Y., Patel, S. R., Williams, I. R. & Pulendran, B. Lamina propria macrophages and dendritic cells differentially induce regulatory and interleukin 17–producing T cell responses. *Nat. Immunol.* **8,** 1086–1094 (2007).
176. Borrego, F., Ulbrecht, M., Weiss, E. H., Coligan, J. E. & Brooks, A. G. Recognition of human histocompatibility leukocyte antigen (HLA)-E complexed with HLA class I signal sequence-derived peptides by CD94/NKG2 confers protection from natural killer cell-mediated lysis. *J. Exp. Med.* **187,** 813–8 (1998).
177. Morandi, F. *et al.* Human Neuroblastoma Cells Trigger an Immunosuppressive

Program in Monocytes by Stimulating Soluble HLA-G Release. *Cancer Res.* **67,** 6433–6441 (2007).

178. LeMaoult, J., Krawice-Radanne, I., Dausset, J. & Carosella, E. D. HLA-G1-expressing antigen-presenting cells induce immunosuppressive CD4+ T cells. *Proc. Natl. Acad. Sci.* **101,** 7064–7069 (2004).
179. Noman, M. Z. *et al.* PD-L1 is a novel direct target of HIF-1α, and its blockade under hypoxia enhanced MDSC-mediated T cell activation. *J. Exp. Med.* **211,** 781–790 (2014).
180. Rodriguez, P. C. *et al.* Arginase I Production in the Tumor Microenvironment by Mature Myeloid Cells Inhibits T-Cell Receptor Expression and Antigen-Specific T-Cell Responses. *Cancer Res.* **64,** 5839–5849 (2004).
181. Malesci, A. *et al.* Tumor-associated macrophages and response to 5-fluorouracil adjuvant therapy in stage III colorectal cancer. *Oncoimmunology* **6,** e1342918 (2017).
182. Vesely, M. D., Kershaw, M. H., Schreiber, R. D. & Smyth, M. J. Natural Innate and Adaptive Immunity to Cancer. *Annu. Rev. Immunol.* **29,** 235–271 (2011).
183. Psaila, B. & Lyden, D. The metastatic niche: adapting the foreign soil. *Nat. Rev. Cancer* **9,** 285–293 (2009).
184. Qian, B. *et al.* A Distinct Macrophage Population Mediates Metastatic Breast Cancer Cell Extravasation, Establishment and Growth. *PLoS One* **4,** e6562 (2009).
185. Bingle, L., Brown, N. J. & Lewis, C. E. The role of tumour-associated macrophages in tumour progression: Implications for new anticancer therapies. *Journal of Pathology* **196,** 254–265 (2002).
186. Zhang, Q. *et al.* Prognostic Significance of Tumor-Associated Macrophages in Solid Tumor: A Meta-Analysis of the Literature. *PLoS One* **7,** e50946 (2012).
187. Ino, Y. *et al.* Immune cell infiltration as an indicator of the immune microenvironment of pancreatic cancer. *Br. J. Cancer* **108,** 914–923 (2013).
188. Di Caro, G. *et al.* Dual prognostic significance of tumour-associated macrophages in human pancreatic adenocarcinoma treated or untreated with chemotherapy. *Gut* **65,** 1710–1720 (2016).
189. Colvin, E. K. Tumor-Associated Macrophages Contribute to Tumor Progression in Ovarian Cancer. *Front. Oncol.* **4,** 1–6 (2014).
190. Bellora, F. *et al.* TLR activation of tumor-associated macrophages from ovarian cancer patients triggers cytolytic activity of NK cells. *Eur. J. Immunol.* **44,** 1814–1822 (2014).
191. Kawamura, K., Komohara, Y., Takaishi, K., Katabuchi, H. & Takeya, M. Detection of M2 macrophages and colony-stimulating factor 1expression in serous and

mucinous ovarian epithelial tumors. *Pathol. Int.* **59,** 300–305 (2009).

192. Colvin, E. K. Tumor-associated macrophages contribute to tumor progression in ovarian cancer. *Front. Oncol.* **4,** 137 (2014).
193. Le Page, C. *et al.* BTN3A2 expression in epithelial ovarian cancer is associated with higher tumor infiltrating T cells and a better prognosis. *PLoS One* **7,** (2012).
194. Lan, C. *et al.* Expression of M2-Polarized Macrophages is Associated with Poor Prognosis for Advanced Epithelial Ovarian Cancer. *Technol. Cancer Res. Treat.* **12,** 259–267 (2012).
195. He, Y. F. *et al.* High MUC2 expression in ovarian cancer is inversely associated with the M1/M2 ratio of tumor-associated macrophages and patient survival time. *PLoS One* **8,** 1–14 (2013).
196. Zhang, M. *et al.* A high M1/M2 ratio of tumor-associated macrophages is associated with extended survival in ovarian cancer patients. *J. Ovarian Res.* **7,** 19 (2014).
197. Yuan, X. *et al.* Prognostic significance of tumor-associated macrophages in ovarian cancer: A meta-analysis. *Gynecol. Oncol.* **147,** 181–187 (2017).
198. Reinartz, S. *et al.* Mixed-polarization phenotype of ascites-associated macrophages in human ovarian carcinoma: Correlation of CD163 expression, cytokine levels and early relapse. *Int. J. Cancer* **134,** 32–42 (2014).
199. Finkernagel, F. *et al.* The transcriptional signature of human ovarian carcinoma macrophages is associated with extracellular matrix reorganization. *Oncotarget* **7,** 75339–75352 (2016).
200. Alvaro, T. *et al.* The presence of STAT1-positive tumor-associated macrophages and their relation to outcome in patients with follicular lymphoma. *Haematologica* **91,** 1605–12 (2006).
201. Farinha, P. Analysis of multiple biomarkers shows that lymphoma-associated macrophage (LAM) content is an independent predictor of survival in follicular lymphoma (FL). *Blood* **106,** 2169–2174 (2005).
202. Taskinen, M., Karjalainen-Lindsberg, M.-L., Nyman, H., Eerola, L.-M. & Leppa, S. A High Tumor-Associated Macrophage Content Predicts Favorable Outcome in Follicular Lymphoma Patients Treated with Rituximab and Cyclophosphamide-Doxorubicin-Vincristine-Prednisone. *Clin. Cancer Res.* **13,** 5784–5789 (2007).
203. Kridel, R. *et al.* The prognostic impact of CD163-positive macrophages in follicular Lymphoma: A study from the BC cancer agency and the lymphoma study association. *Clin. Cancer Res.* **21,** 3428–3435 (2015).
204. Ålgars, A. *et al.* Type and location of tumor-infiltrating macrophages and lymphatic vessels predict survival of colorectal cancer patients. *Int. J. Cancer* **131,** 864–873 (2012).

205. Gentles, A. J. *et al.* The prognostic landscape of genes and infiltrating immune cells across human cancers. *Nat. Med.* **21,** 938–945 (2015).
206. Wang, B. *et al.* Association of Intra-tumoral Infiltrating Macrophages and Regulatory T Cells Is an Independent Prognostic Factor in Gastric Cancer after Radical Resection. *Ann. Surg. Oncol.* **18,** 2585–2593 (2011).
207. Colotta, F., Peri, G., Villa, A. & Mantovani, A. Rapid killing of actinomycin D-treated tumor cells by human mononuclear cells. I. Effectors belong to the monocyte-macrophage lineage. *J. Immunol.* **132,** 936–44 (1984).
208. Galluzzi, L., Buqué, A., Kepp, O., Zitvogel, L. & Kroemer, G. Immunological Effects of Conventional Chemotherapy and Targeted Anticancer Agents. *Cancer Cell* **28,** 690–714 (2015).
209. Ma, Y. *et al.* CCL2/CCR2-Dependent Recruitment of Functional Antigen-Presenting Cells into Tumors upon Chemotherapy. *Cancer Res.* **74,** 436–445 (2014).
210. D'Incalci, M., Badri, N., Galmarini, C. M. & Allavena, P. Trabectedin, a drug acting on both cancer cells and the tumour microenvironment. *Br. J. Cancer* **111,** 646–650 (2014).
211. Germano, G. *et al.* Antitumor and Anti-inflammatory Effects of Trabectedin on Human Myxoid Liposarcoma Cells. *Cancer Res.* **70,** 2235–2244 (2010).
212. Germano, G. *et al.* Role of Macrophage Targeting in the Antitumor Activity of Trabectedin. *Cancer Cell* **23,** 249–262 (2013).
213. Iida, N. *et al.* Commensal Bacteria Control Cancer Response to Therapy by Modulating the Tumor Microenvironment. *Science (80-.).* **342,** 967–970 (2013).
214. Vacchelli, E. *et al.* Chemotherapy-induced antitumor immunity requires formyl peptide receptor 1. *Science (80-.).* **350,** 972–978 (2015).
215. Pyonteck, S. M. *et al.* CSF-1R inhibition alters macrophage polarization and blocks glioma progression. *Nat. Med.* **19,** 1264–1272 (2013).
216. Mitchem, J. B. *et al.* Targeting Tumor-Infiltrating Macrophages Decreases Tumor-Initiating Cells, Relieves Immunosuppression, and Improves Chemotherapeutic Responses. *Cancer Res.* **73,** 1128–1141 (2013).
217. Dijkgraaf, E. M. *et al.* Chemotherapy alters monocyte differentiation to favor generation of cancer-supporting m2 macrophages in the tumor microenvironment. *Cancer Res.* **73,** 2480–2492 (2013).
218. Bruchard, M. *et al.* Chemotherapy-triggered cathepsin B release in myeloid-derived suppressor cells activates the Nlrp3 inflammasome and promotes tumor growth. *Nat. Med.* **19,** 57–64 (2013).
219. Jinushi, M. *et al.* Tumor-associated macrophages regulate tumorigenicity and anticancer drug responses of cancer stem/initiating cells. *Proc. Natl. Acad. Sci.*

108, 12425–12430 (2011).

220. Nakasone, E. S. *et al.* Imaging Tumor-Stroma Interactions during Chemotherapy Reveals Contributions of the Microenvironment to Resistance. *Cancer Cell* **21,** 488–503 (2012).
221. Shree, T. *et al.* Macrophages and cathepsin proteases blunt chemotherapeutic response in breast cancer. *Genes Dev.* **25,** 2465–2479 (2011).
222. DeNardo, D. G. *et al.* Leukocyte complexity predicts breast cancer survival and functionally regulates response to chemotherapy. *Cancer Discov.* **1,** 54–67 (2011).
223. Hughes, R. *et al.* Perivascular M2 Macrophages Stimulate Tumor Relapse after Chemotherapy. *Cancer Res.* **75,** 3479–3491 (2015).
224. Berraondo, P. *et al.* Cytokines in clinical cancer immunotherapy. *Br. J. Cancer* **120,** 6–15 (2019).
225. Loberg, R. D. *et al.* Targeting CCL2 with Systemic Delivery of Neutralizing Antibodies Induces Prostate Cancer Tumor Regression In vivo. *Cancer Res.* **67,** 9417–9424 (2007).
226. Moisan, F. *et al.* Abstract 817: Enhancement of paclitaxel and carboplatin therapy by CCL2 blockade in ovarian cancers. *Cancer Res.* **72,** 817–817 (2012).
227. Lu, X. & Kang, Y. Chemokine (C-C Motif) Ligand 2 Engages CCR2 + Stromal Cells of Monocytic Origin to Promote Breast Cancer Metastasis to Lung and Bone. *J. Biol. Chem.* **284,** 29087–29096 (2009).
228. Fridlender, Z. G. *et al.* Monocyte Chemoattractant Protein–1 Blockade Inhibits Lung Cancer Tumor Growth by Altering Macrophage Phenotype and Activating CD8 + Cells. *Am. J. Respir. Cell Mol. Biol.* **44,** 230–237 (2011).
229. Li, X. *et al.* Targeting of tumour-infiltrating macrophages via CCL2/CCR2 signalling as a therapeutic strategy against hepatocellular carcinoma. *Gut* **66,** 157–167 (2017).
230. Bonapace, L. *et al.* Cessation of CCL2 inhibition accelerates breast cancer metastasis by promoting angiogenesis. *Nature* **515,** 130–133 (2014).
231. Pienta, K. J. *et al.* Phase 2 study of carlumab (CNTO 888), a human monoclonal antibody against CC-chemokine ligand 2 (CCL2), in metastatic castration-resistant prostate cancer. *Invest. New Drugs* **31,** 760–768 (2013).
232. Brana, I. *et al.* Carlumab, an anti-C-C chemokine ligand 2 monoclonal antibody, in combination with four chemotherapy regimens for the treatment of patients with solid tumors: an open-label, multicenter phase 1b study. *Target. Oncol.* **10,** 111–123 (2015).
233. Sandhu, S. K. *et al.* A first-in-human, first-in-class, phase I study of carlumab (CNTO 888), a human monoclonal antibody against CC-chemokine ligand 2 in

patients with solid tumors. *Cancer Chemother. Pharmacol.* **71,** 1041–1050 (2013).

234. Nywening, T. M. *et al.* Targeting tumour-associated macrophages with CCR2 inhibition in combination with FOLFIRINOX in patients with borderline resectable and locally advanced pancreatic cancer: a single-centre, open-label, dose-finding, non-randomised, phase 1b trial. *Lancet Oncol.* **17,** 651–662 (2016).
235. Peyraud, F., Cousin, S. & Italiano, A. CSF-1R Inhibitor Development: Current Clinical Status. *Curr. Oncol. Rep.* **19,** 1–10 (2017).
236. Lin, H. *et al.* Discovery of a Cytokine and Its Receptor by Functional Screening of the Extracellular Proteome. *Science (80-.).* **320,** 807–811 (2008).
237. Ries, C. H., Hoves, S., Cannarile, M. A. & Rüttinger, D. CSF-1/CSF-1R targeting agents in clinical development for cancer therapy. *Curr. Opin. Pharmacol.* **23,** 45–51 (2015).
238. Manthey, C. L. *et al.* JNJ-28312141, a novel orally active colony-stimulating factor-1 receptor/FMS-related receptor tyrosine kinase-3 receptor tyrosine kinase inhibitor with potential utility in solid tumors, bone metastases, and acute myeloid leukemia. *Mol. Cancer Ther.* **8,** 3151–3161 (2009).
239. Ries, C. H. *et al.* Targeting tumor-associated macrophages with anti-CSF-1R antibody reveals a strategy for cancer therapy. *Cancer Cell* **25,** 846–859 (2014).
240. Kitamura, T. *et al.* CCL2-induced chemokine cascade promotes breast cancer metastasis by enhancing retention of metastasis-associated macrophages. *J. Exp. Med.* **212,** 1043–1059 (2015).
241. Zhu, X.-D. *et al.* High Expression of Macrophage Colony-Stimulating Factor in Peritumoral Liver Tissue Is Associated With Poor Survival After Curative Resection of Hepatocellular Carcinoma. *J. Clin. Oncol.* **26,** 2707–2716 (2008).
242. Koh, Y. W., Park, C., Yoon, D. H., Suh, C. & Huh, J. CSF-1R Expression in Tumor-Associated Macrophages Is Associated With Worse Prognosis in Classical Hodgkin Lymphoma. *Am. J. Clin. Pathol.* **141,** 573–583 (2014).
243. Ruffell, B. *et al.* Macrophage IL-10 Blocks CD8+ T Cell-Dependent Responses to Chemotherapy by Suppressing IL-12 Expression in Intratumoral Dendritic Cells. *Cancer Cell* **26,** 623–637 (2014).
244. Cassier, P. A. *et al.* CSF1R inhibition with emactuzumab in locally advanced diffuse-type tenosynovial giant cell tumours of the soft tissue: a dose-escalation and dose-expansion phase 1 study. *Lancet Oncol.* **16,** 949–956 (2015).
245. Tap, W. D. *et al.* Structure-Guided Blockade of CSF1R Kinase in Tenosynovial Giant-Cell Tumor. *N. Engl. J. Med.* **373,** 428–437 (2015).
246. Yan, D. *et al.* Inhibition of colony stimulating factor-1 receptor abrogates microenvironment-mediated therapeutic resistance in gliomas. *Oncogene* **36,** 6049–6058 (2017).

247. Butowski, N. *et al.* Orally administered colony stimulating factor 1 receptor inhibitor PLX3397 in recurrent glioblastoma: an Ivy Foundation Early Phase Clinical Trials Consortium phase II study. *Neuro. Oncol.* **18,** 557–564 (2016).
248. Moughon, D. *et al.* Macrophage Blockade Using CSF1R Inhibitors Reverses The Vascular Leakage Underlying Malignant Ascites In Late-Stage Epithelial Ovarian Cancer. *Cancer Res.* 1–12 (2015). doi:10.1158/0008-5472.CAN-14-3373
249. Lyons, Y. A. *et al.* Macrophage depletion through colony stimulating factor 1 receptor pathway blockade overcomes adaptive resistance to anti-VEGF therapy. *Oncotarget* **8,** 96496–96505 (2017).
250. Weizman, N. *et al.* Macrophages mediate gemcitabine resistance of pancreatic adenocarcinoma by upregulating cytidine deaminase. *Oncogene* **33,** 3812–3819 (2014).
251. Candido, J. B. *et al.* CSF1R+Macrophages Sustain Pancreatic Tumor Growth through T Cell Suppression and Maintenance of Key Gene Programs that Define the Squamous Subtype. *Cell Rep.* **23,** 1448–1460 (2018).
252. Balkwill, F. Tumour necrosis factor and cancer. *Nat. Rev. Cancer* **9,** 361–371 (2009).
253. Liebes, L. *et al.* Modulation of monocyte functions by muramyl tripeptide phosphatidylethanolamine in a phase II study in patients with metastatic melanoma. *J. Natl. Cancer Inst.* **84,** 694–9 (1992).
254. Colombo, N. *et al.* Anti-tumor and immunomodulatory activity of intraperitoneal IFN-gamma in ovarian carcinoma patients with minimal residual tumor after chemotherapy. *Int. J. cancer* **51,** 42–6 (1992).
255. Pujade-Lauraine, E. *et al.* Intraperitoneal recombinant interferon gamma in ovarian cancer patients with residual disease at second-look laparotomy. *J. Clin. Oncol.* **14,** 343–350 (1996).
256. Halama, N. *et al.* Tumoral Immune Cell Exploitation in Colorectal Cancer Metastases Can Be Targeted Effectively by Anti-CCR5 Therapy in Cancer Patients. *Cancer Cell* **29,** 587–601 (2016).
257. Beatty, G. L. *et al.* CD40 Agonists Alter Tumor Stroma and Show Efficacy Against Pancreatic Carcinoma in Mice and Humans. *Science (80-.).* **331,** 1612–1616 (2011).
258. Beatty, G. L. *et al.* A Phase I Study of an Agonist CD40 Monoclonal Antibody (CP-870,893) in Combination with Gemcitabine in Patients with Advanced Pancreatic Ductal Adenocarcinoma. *Clin. Cancer Res.* **19,** 6286–6295 (2013).
259. Hoves, S. *et al.* Rapid activation of tumor-associated macrophages boosts preexisting tumor immunity. *J. Exp. Med.* **215,** 859–876 (2018).
260. Mantovani, A. & Longo, D. L. Macrophage Checkpoint Blockade in Cancer —

Back to the Future. *N. Engl. J. Med.* **379,** 1777–1779 (2018).

261. Casey, S. C. *et al.* MYC regulates the antitumor immune response through CD47 and PD-L1. *Science (80-.).* **352,** 227–231 (2016).
262. Advani, R. *et al.* CD47 Blockade by Hu5F9-G4 and Rituximab in Non-Hodgkin's Lymphoma. *N. Engl. J. Med.* **379,** 1711–1721 (2018).
263. Rolny, C. *et al.* HRG Inhibits Tumor Growth and Metastasis by Inducing Macrophage Polarization and Vessel Normalization through Downregulation of PlGF. *Cancer Cell* **19,** 31–44 (2011).
264. Yamamoto, N. & Homma, S. Vitamin D3 binding protein (group-specific component) is a precursor for the macrophage-activating signal factor from lysophosphatidylcholine-treated lymphocytes. *Proc. Natl. Acad. Sci.* **88,** 8539–8543 (1991).
265. Bobbs, A. S., Cole, J. M. & Dahl, K. D. C. Emerging and Evolving Ovarian Cancer Animal Models. *Cancer Growth Metastasis* **8s1,** CGM.S21221 (2015).
266. Roby, K. F. *et al.* Development of a syngeneic mouse model for events related to ovarian cancer. *Carcinogenesis* **21,** 585–591 (2000).
267. Walton, J. *et al.* CRISPR/Cas9-Mediated Trp53 and Brca2 Knockout to Generate Improved Murine Models of Ovarian High-Grade Serous Carcinoma. *Cancer Res.* **76,** 6118–6129 (2016).
268. Walton, J. B. *et al.* CRISPR/Cas9-derived models of ovarian high grade serous carcinoma targeting Brca1, Pten and Nf1, and correlation with platinum sensitivity. *Sci. Rep.* **7,** 16827 (2017).
269. Connolly, D. C. *et al.* Female mice chimeric for expression of the simian virus 40 TAg under control of the MISIIR promoter develop epithelial ovarian cancer. *Cancer Res.* **63,** 1389–97 (2003).
270. Flesken-Nikitin, A., Choi, K. C., Eng, J. P., Shmidt, E. N. & Nikitin, A. Y. Induction of carcinogenesis by concurrent inactivation of p53 and Rb1 in the mouse ovarian surface epithelium. *Cancer Res.* **63,** 3459–3463 (2003).
271. Szabova, L. *et al.* Perturbation of Rb, p53, and Brca1 or Brca2 cooperate in inducing metastatic serous epithelial ovarian cancer. *Cancer Res.* **72,** 4141–4153 (2012).
272. Szabova, L. *et al.* Pathway-Specific Engineered Mouse Allograft Models Functionally Recapitulate Human Serous Epithelial Ovarian Cancer. *PLoS One* **9,** e95649 (2014).
273. Perets, R. *et al.* Transformation of the Fallopian Tube Secretory Epithelium Leads to High-Grade Serous Ovarian Cancer in Brca;Tp53;Pten Models. *Cancer Cell* **24,** 751–765 (2013).
274. Zhai, Y. *et al.* High-grade serous carcinomas arise in the mouse oviduct via

defects linked to the human disease. *J. Pathol.* **243,** 16–25 (2017).

275. Stuckelberger, S. & Drapkin, R. Precious GEMMs: emergence of faithful models for ovarian cancer research. *J. Pathol.* **245,** 129–131 (2018).
276. Perets, R. *et al.* Transformation of the Fallopian Tube Secretory Epithelium Leads to High-Grade Serous Ovarian Cancer in Brca;Tp53;Pten Models. *Cancer Cell* **24,** 751–765 (2013).
277. Vincent, J. *et al.* 5-Fluorouracil Selectively Kills Tumor-Associated Myeloid-Derived Suppressor Cells Resulting in Enhanced T Cell-Dependent Antitumor Immunity. *Cancer Res.* **70,** 3052–3061 (2010).
278. Ko, H. J. *et al.* A combination of chemoimmunotherapies can efficiently break self-tolerance and induce antitumor immunity in a tolerogenic murine tumor model. *Cancer Res.* **67,** 7477–7486 (2007).
279. Suzuki, E., Kapoor, V., Jassar, A. S., Kaiser, L. R. & Albelda, S. M. Gemcitabine selectively eliminates splenic Gr-1+/CD11b + myeloid suppressor cells in tumor-bearing animals and enhances antitumor immune activity. *Clin. Cancer Res.* **11,** 6713–6721 (2005).
280. Böhm, S. *et al.* Chemotherapy Response Score: Development and Validation of a System to Quantify Histopathologic Response to Neoadjuvant Chemotherapy in Tubo-Ovarian High-Grade Serous Carcinoma. *J. Clin. Oncol.* **33,** 2457–2463 (2015).
281. Hacker, N. F. & Rao, A. Surgery for advanced epithelial ovarian cancer. *Best Pract. Res. Clin. Obstet. Gynaecol.* **41,** 71–87 (2017).
282. Newman, A. M. *et al.* Robust enumeration of cell subsets from tissue expression profiles. *Nat. Methods* **12,** 453–457 (2015).
283. Shiao, S. L. *et al.* T H 2-Polarized CD4 + T Cells and Macrophages Limit Efficacy of Radiotherapy. *Cancer Immunol. Res.* **3,** 518–525 (2015).
284. Collin, M. & Bigley, V. Human dendritic cell subsets: an update. *Immunology* **154,** 3–20 (2018).
285. Boyette, L. B. *et al.* Phenotype, function, and differentiation potential of human monocyte subsets. *PLoS One* **12,** e0176460 (2017).
286. Li, J., Srivastava, R. M., Ettyreddy, A. & Ferris, R. L. Cetuximab ameliorates suppressive phenotypes of myeloid antigen presenting cells in head and neck cancer patients. *J. Immunother. Cancer* **3,** 54 (2015).
287. Yeap, W. H. *et al.* CD16 is indispensable for antibody-dependent cellular cytotoxicity by human monocytes. *Sci. Rep.* **6,** 34310 (2016).
288. Sconocchia, G. *et al.* Tumor infiltration by FcγRIII (CD16)+ myeloid cells is associated with improved survival in patients with colorectal carcinoma. *Int. J. Cancer* **128,** 2663–2672 (2011).

289. Adhikary, T. *et al.* Interferon signaling in ascites-associated macrophages is linked to a favorable clinical outcome in a subgroup of ovarian carcinoma patients. *BMC Genomics* **18,** 243 (2017).
290. Ensan, S. *et al.* Self-renewing resident arterial macrophages arise from embryonic CX3CR1 + precursors and circulating monocytes immediately after birth. *Nat. Immunol.* **17,** 159–168 (2016).
291. Italiani, P. & Boraschi, D. From Monocytes to M1/M2 Macrophages: Phenotypical vs. Functional Differentiation. *Front. Immunol.* **5,** 1–22 (2014).
292. Abolhalaj, M. *et al.* Profiling dendritic cell subsets in head and neck squamous cell tonsillar cancer and benign tonsils. *Sci. Rep.* **8,** 1–12 (2018).
293. Reinartz, S. *et al.* A transcriptome-based global map of signaling pathways in the ovarian cancer microenvironment associated with clinical outcome. *Genome Biol.* **17,** 108 (2016).
294. Schumann, T. *et al.* Deregulation of PPARβ/δ target genes in tumor-associated macrophages by fatty acid ligands in the ovarian cancer microenvironment. *Int. J. Cancer* **134,** 13416–13433 (2015).
295. Xue, J. *et al.* Transcriptome-Based Network Analysis Reveals a Spectrum Model of Human Macrophage Activation. *Immunity* **40,** 274–288 (2014).
296. Ford, J. W. & McVicar, D. W. TREM and TREM-like receptors in inflammation and disease. *Curr. Opin. Immunol.* **21,** 38–46 (2009).
297. Hemmi, H. *et al.* A new triggering receptor expressed on myeloid cells (Trem) family member, Trem-like 4, binds to dead cells and is a DNAX activation protein 12-linked marker for subsets of mouse macrophages and dendritic cells. *J. Immunol.* **182,** 1278–86 (2009).
298. Ramirez-Ortiz, Z. G. *et al.* The receptor TREML4 amplifies TLR7-mediated signaling during antiviral responses and autoimmunity. *Nat. Immunol.* **16,** 495–504 (2015).
299. Hemmi, H. *et al.* Treml4, an Ig Superfamily Member, Mediates Presentation of Several Antigens to T Cells In Vivo, Including Protective Immunity to HER2 Protein. *J. Immunol.* **188,** 1147–1155 (2012).
300. Patel, V. P. *et al.* Molecular and Functional Characterization of Two Novel Human C-C Chemokines as Inhibitors of Two Distinct Classes of Myeloid Progenitors. *J. Exp. Med.* **185,** 1163–1172 (1997).
301. Nieman, K. M. *et al.* Adipocytes promote ovarian cancer metastasis and provide energy for rapid tumor growth. *Nat. Med.* **17,** 1498–1503 (2011).
302. Tabariès, S. & Siegel, P. M. The role of claudins in cancer metastasis. *Oncogene* **36,** 1176–1190 (2017).
303. Reinartz, S. *et al.* Cell type-selective pathways and clinical associations of

lysophosphatidic acid biosynthesis and signaling in the ovarian cancer microenvironment. *Mol. Oncol.* 1–17 (2018). doi:10.1002/1878-0261.12396

304. Gordon, S. R. *et al.* PD-1 expression by tumour-associated macrophages inhibits phagocytosis and tumour immunity. *Nature* **545,** 495–499 (2017).
305. De Nardo, D. Toll-like receptors: Activation, signalling and transcriptional modulation. *Cytokine* **74,** 181–189 (2015).
306. Laine, P. S. *et al.* Palmitic acid induces IP-10 expression in human macrophages via NF-κB activation. *Biochem. Biophys. Res. Commun.* **358,** 150–155 (2007).
307. Pearce, O. M. T. *et al.* Deconstruction of a metastatic tumor microenvironment reveals a common matrix response in human cancers. *Cancer Discov.* CD-17-0284 (2017). doi:10.1158/2159-8290.CD-17-0284
308. Liebmann, J. E. *et al.* Cytotoxic studies of pacfitaxel (Taxol®) in human tumour cell lines. *Br. J. Cancer* **68,** 1104–1109 (1993).
309. Bicaku, E. *et al.* In vitro analysis of ovarian cancer response to cisplatin, carboplatin, and paclitaxel identifies common pathways that are also associated with overall patient survival. *Br. J. Cancer* **106,** 1967–1975 (2012).
310. Clark, R. *et al.* Milky spots promote ovarian cancer metastatic colonization of peritoneal adipose in experimental models. *Am. J. Pathol.* **183,** 576–591 (2013).
311. Khan, S. M. *et al.* In vitro metastatic colonization of human ovarian cancer cells to the omentum. *Clin. Exp. Metastasis* **27,** 185–196 (2010).
312. Lee, J. J. *et al.* Human versus mouse eosinophils: “That which we call an eosinophil, by any other name would stain as red”. *J. Allergy Clin. Immunol.* **130,** 572–584 (2012).
313. Skinner, B. M. & Johnson, E. E. P. Nuclear morphologies: their diversity and functional relevance. *Chromosoma* **126,** 195–212 (2017).
314. Karayama, M. *et al.* Macrophage mannose receptor, CD206, predict prognosis in patients with pulmonary tuberculosis. *Sci. Rep.* **8,** 1–9 (2018).
315. Shah, D. K., Veith, J., Bernacki, R. J. & Balthasar, J. P. Evaluation of combined bevacizumab and intraperitoneal carboplatin or paclitaxel therapy in a mouse model of ovarian cancer. *Cancer Chemother. Pharmacol.* **68,** 951–958 (2011).
316. Calvert, A. H. *et al.* Carboplatin dosage: prospective evaluation of a simple formula based on renal function. *J. Clin. Oncol.* **7,** 1748–1756 (1989).
317. Freireich, E. J., Gehan, E. A., Rall, D. P., Schmidt, L. H. & Skipper, H. E. Quantitative comparison of toxicity of anticancer agents in mouse, rat, hamster, dog, monkey, and man. *Cancer Chemother. reports* **50,** 219–44 (1966).
318. Armstrong, D. K. *et al.* Intraperitoneal Cisplatin and Paclitaxel in Ovarian Cancer. *N. Engl. J. Med.* **354,** 34–43 (2006).
319. Muggia, F. M. *et al.* Phase III Randomized Study of Cisplatin Versus Paclitaxel

Versus Cisplatin and Paclitaxel in Patients With Suboptimal Stage III or IV Ovarian Cancer: A Gynecologic Oncology Group Study. *J. Clin. Oncol.* **18,** 106–106 (2000).

320. Ozols, R. F. *et al.* Phase III Trial of Carboplatin and Paclitaxel Compared With Cisplatin and Paclitaxel in Patients With Optimally Resected Stage III Ovarian Cancer: A Gynecologic Oncology Group Study. *J. Clin. Oncol.* **21,** 3194–3200 (2003).
321. Olson, O. C. *et al.* Tumor-Associated Macrophages Suppress the Cytotoxic Activity of Antimitotic Agents Article Tumor-Associated Macrophages Suppress the Cytotoxic Activity of Antimitotic Agents. *CellReports* **19,** 101–113 (2017).
322. Wang, B. *et al.* Transition of tumor-associated macrophages from MHC class IIhi to MHC class IIlow mediates tumor progression in mice. *BMC Immunol.* **12,** 43 (2011).
323. Kovacs, S. B. & Miao, E. A. Gasdermins: Effectors of Pyroptosis. *Trends Cell Biol.* **27,** 673–684 (2017).
324. Yang, Y., Wang, H., Kouadir, M., Song, H. & Shi, F. Recent advances in the mechanisms of NLRP3 inflammasome activation and its inhibitors. *Cell Death Dis.* **10,** 128 (2019).
325. Shi, J. *et al.* Cleavage of GSDMD by inflammatory caspases determines pyroptotic cell death. *Nature* **526,** 660–665 (2015).
326. Shi, J., Gao, W. & Shao, F. Pyroptosis: Gasdermin-Mediated Programmed Necrotic Cell Death. *Trends Biochem. Sci.* **42,** 245–254 (2017).
327. Wang, Y. *et al.* Chemotherapy drugs induce pyroptosis through caspase-3 cleavage of a gasdermin. *Nature* **547,** 99–103 (2017).
328. Annibaldi, A. *et al.* Ubiquitin-Mediated Regulation of RIPK1 Kinase Activity Independent of IKK and MK2. *Mol. Cell* **69,** 566–580.e5 (2018).
329. Damiani, E., Solorio, J. A., Doyle, A. P. & Wallace, H. M. How reliable are in vitro IC50 values? Values vary with cytotoxicity assays in human glioblastoma cells. *Toxicol. Lett.* **302,** 28–34 (2019).
330. Lo, C. S. *et al.* Neoadjuvant Chemotherapy of Ovarian Cancer Results in Three Patterns of Tumor-Infiltrating Lymphocyte Response with Distinct Implications for Immunotherapy. *Clin. Cancer Res.* **23,** 925–934 (2017).
331. Gubin, M. M. *et al.* High-Dimensional Analysis Delineates Myeloid and Lymphoid Compartment Remodeling during Successful Immune-Checkpoint Cancer Therapy. *Cell* **175,** 1014–1030.e19 (2018).
332. Kroemer, G., Galluzzi, L., Kepp, O. & Zitvogel, L. Immunogenic Cell Death in Cancer Therapy. *Annu. Rev. Immunol.* **31,** 51–72 (2013).